Report No. 118
DE/ER/53222-101
UC-20g

Columbia University
in the City of New York

Identification of, and Transition to, the Second Region of Ideal MHD Stability in Tokamaks

Steven Anthony Sabbagh

1990

Work Supported by DE-FG02-86ER53222 and DE-FG02-89ER53297

Plasma Physics Laboratory

Department of Applied Physics

School of Engineering and Applied Science

Columbia University

New York, New York 10027

Identification of, and Transition to, the Second Region of Ideal MHD Stability in Tokamaks

by

Steven A. Sabbagh

Submitted in partial fulfillment of
the requirements for the degree of
Doctor of Philosophy
in the Graduate School of Arts and Sciences

COLUMBIA UNIVERSITY
1990

ABSTRACT

Identification of, and Transition to, the Second Region of Ideal MHD Stability in Tokamaks

Steven Anthony Sabbagh

The second region of ideal MHD stability in tokamaks is studied by considering the behavior of the second region boundary for self-consistently calculated, marginally stable, second region equilibria and the characteristics of numerically computed transport sequences that achieve second stability. Equilibria with pressure profiles, $p(\psi)$, that are marginally stable to the second region on each flux surface are generated numerically. This constraint eliminates $p(\psi)$ as an independent variable, and reduces the predictor variables to the tokamak parameters and the q profile. The primary response functions considered are the plasma figures of merit, β and $\varepsilon\beta_p$, and the normalized pressure gradient, α. Variations of the radial wavenumber in the ballooning equation negligibly affect the second region boundary for these equilibria. The second region boundary is sensitive to variations in the q profile at small aspect ratio, A, and will stabilize or destabilize depending on the balance of higher order $\varepsilon = A^{-1}$ modifications of the normal field line curvature, κ_n. These effects are a competition between the stabilizing geometric magnetic well of the toroidal field component of κ_n and the destabilizing poloidal field component of κ_n. The latter term becomes competitive in high $\varepsilon\beta_p$ plasmas with large Shafranov shifts. Simple analytic models are presented that reproduce the scaling of the marginally stable second region values of α and $\varepsilon\beta_p$, and stability diagrams illustrating the behavior of the high-n unstable region for various parameters are shown. Direct access to the second stability region on a flux surface is obtained when the global shear, S, is below a critical value. This value is well

approximated for all marginally second region stable equilibria by the value of S on the flux surface on which the local shear changes sign on the outboard midplane of the plasma. In addition, equilibria evolving from the first to the second region of stability have been generated by a $1^1/_2$ dimensional transport code. The transport model enhances diffusion on flux surfaces that are unstable to large-n modes. Modification of the q profile by neutral beam driven current reduces the size of the unstable region sufficiently to allow transition to the second region. Auxiliary power requirements for this transition are estimated. Stability of the transition equilibria to both small-n external and internal modes is also examined.

Identification of, and Transition to, the Second Region of Ideal MHD Stability in Tokamaks

TABLE OF CONTENTS

ACKNOWLEDGEMENTS

In the course of education, there are individuals who have a profound effect on the direction that one's career will follow. As an undergraduate, that person was Alan Blaer, whose impeccable care in teaching helped direct me toward studying physics. As a graduate student, that person was Gerald Navratil. Instead of flaunting his prowess, Gerry took the time and care to instill in his students a curiosity and sense of challenge in studying plasma physics. As my advisor, he has not only provided the scientific education needed, but also the exposure required to establish my research in the study of fusion relevant plasma physics. Because of Gerry's unselfish characteristic of allowing me to actively expose our research, I've had the honor to interact with many of the greatest contemporary plasma physicists. Alan Todd, Mike Phillips, and Mike Hughes of Grumman have all played an active role on the work in this thesis, and on my education in plasma physics. In addition, I thank Mike Hughes and his wife Mary for their gracious hospitality during my many dinner visits to their house. Alan Sykes and Tim Hender deserve special thanks for their hospitality on my short visit to the Culham Laboratory, and their interest and support of the present study of the second stability region. Alan also deserves a special thanks for sharing with me some of the unpublished history of second region stability. Gu Yong Fu and Jim Van Dam of the Institute for Fusion Studies have provided interest and physical insight to research in establishing a second region equilibrium, and it was a privilege to combine research with them for the 1988 IAEA meeting. Jesus Ramos of MIT has provided interesting and insightful discussions on second region stability. Martin Peng of ORNL has been very eager in sharing his findings on second region stability. Tom Simonen, Ron Stambaugh, Lang Lao, and Tony Taylor of General Atomics have provided valuable

encouragement. Glenn Bateman, Daren Stotler, Martha Redi, and Bill Tang of PPPL provided much of the theory that formed the transport modelling in the present work. Morrell Chance and J. Manickam of PPPL have graciously shared their vast knowledge and experience in MHD stability calculations. Saving the most familiar for last, Amitava Bhattacharjee, Yurij Baransky, Mike Mauel and Jose Milovich of Columbia University have always been eager to help me find the correct answers when the questions themselves completely eluded me. Finally, Tom Ivers, Andrew Holland, and Nick Rivera are not only my closest colleagues, but also some of my closest friends. Our relationships have transcended Maxwell's equations and enveloped such important matters as a sentimental toast at my wedding, a good game of snooker, and the exhilaration of cycling time trials. This work was supported by the U.S. Department of Energy under grants DE-FG02-86ER53222 and DE-FG02-89ER53297.

This work would have not been possible without the love and support of friends and family. My wife Melina, my love, has always been more concerned about the success of my work than about how quickly it could be completed. She has had the patience to endure the sacrifices that go along with graduate student life. She means the world to me and I look forward to our life together now that this work is complete. Melina's mother, Johanna, deserves special mention as a good friend and adopted parent. Her support has proved to be invaluable. My father, Victor and his wife Lia, have given me the opportunity to pursue graduate study by sacrificing and supporting me through undergraduate school. My brother Raymond should be a co-author to this work. He has been by mentor since I can remember, and his interest and patience in teaching me at a young age about anything I wanted to know, and things that I'd never even heard of was a crucial component in getting to this point in my life. My sister

Irene has also been supportive in every way. She's the hardest working person I know, and when matters are difficult, I use her example for motivation. Tom Rosenbauer and his wife, Becky, have been good friends, and have made my graduate life better by always finding something new and interesting to share. A special mention also must be extended to Cos, who not only taught me how to race a bicycle, but has always been there when I needed someone to keep me pointed in the right direction.

This work is dedicated to the memory of my mother, Simone Sabbagh.

Identification of, and Transition to, the Second Region of Ideal MHD Stability in Tokamaks

A strong imagination brings on the event.

Montaigne, *Essays*,
(from "On the Power of the Imagination.")

1.0 INTRODUCTION

The demonstration of an efficient, experimental fusion power reactor is the ultimate endeavor of thermonuclear fusion research. One technique of providing the conditions necessary to sustain thermonuclear fusion reactions in sufficient quantity to provide net power output is to perform the reactions in a hot plasma, thermally isolated from the colder surroundings, by a strong magnetic field. The tokamak[1] has been the most successful method of magnetically confining a fusion relevant plasma. The basic magnetic field configuration in a tokamak is a superposition of a strong externally applied toroidal magnetic field and a poloidal field created by an induced toroidal current within the plasma itself. The field lines are therefore shaped as a toroidal helix. A vertical magnetic field is externally provided to maintain radial equilibrium.

Overcoming the strong Coulomb repulsion forces between nucleii so that the particles are brought close enough together to fuse in an adequate quantity requires that a sufficiently hot plasma of sufficient density be contained for an adequate time. This criteria is often expressed as the fusion product $P_{\text{fusion}} = n\tau_e T_i$, where n is the plasma

density, τ_e is the energy confinement time, and T_i is the ion temperature. The present milestone in tokamak research is the achievement of scientific breakeven, when the amount of energy generated by fusion reactions equals the amount of energy required to sustain the plasma. The P_{fusion} performance of the large contemporary experimental tokamak devices operating with deuterium plasmas, the TFTR at the Princeton Plasma Physics Laboratory, and the JET, at the Culham Laboratory in England, is within a factor of two away from the breakeven value in an equivalent deuterium-tritium plasma. This seems a small factor when compared to the factor of greater than 10^6 improvement of these devices over the pioneering efforts of the late 1950's. Yet, improvements in P_{fusion} are generally not trivially achieved, and development of methods for increasing this product require an understanding of the physical properties of the plasma that limit it.

The fusion product can be increased by raising the plasma pressure, p, or increasing the confinement time. One method of doing so is to increase the size of the machine. However, when scaling the machine up to values of P_{fusion} required for an experimental test reactor, such as the International Tokamak Experimental Reactor (ITER) design,[2] the technology involved in building and operating such a device is daunting. One key difficulty is that since the plasma pressure stability limit at fixed toroidal field, and the confinement time are observed experimentally to scale linearly with the plasma current in conventional tokamak operation, the extrapolated current needs to be uncomfortably large. This reality has led a part of the tokamak research effort toward finding alternate methods of operating a tokamak plasma with the goal of improving its efficiency. A measure of the efficiency of a magnetic confinement system is the ratio of the plasma stored energy to the applied confining magnetic field energy, $\beta \equiv 2\mu_0 p/B_0^2$, where B_0 is the vacuum toroidal field at the plasma geometric center. At fixed B_0, maximizing β maximizes P_{fusion} and also the fusion power density of a test

reactor, that scales as β^2. Improving β is quite desirable since it would provide an increased margin for breakeven and ignition experiments in the short-term, while allowing designs for future tokamak reactors to become more compact and make more efficient use of the applied magnetic field.

Identification of mechanisms that impose limitations on β in a tokamak is an important research goal. By understanding the deleterious effects that limit β, methods of suppressing or avoiding these effects can be discovered and implemented. Present experiments indicate that a β limit does exist,[3,4] and modeling of the stability indicates that ideal MHD ballooning or kink modes set this limit.[5-7] A simple expression that characterizes this semi-empirical limit is

$$\beta_I = C_t * 10^{-8} \, (I(\mathrm{A}) / a(\mathrm{m}) B_0(\mathrm{T})), \quad 2.8 < C_t < 4.4 \qquad (1.0 - 1)$$

which agrees well with the maximum β values achieved in tokamak experiments when $C_t \sim 3.5$. Here, I is the plasma current, and a is the plasma minor radius. For "conventional" safety factor profiles with $q_0 \sim 1$, the n=1 external kink poses the greatest restriction, hence the lowest values of C_t, while high-n ballooning modes yield the larger values of C_t. Here, q_0 is the safety factor at the magnetic axis and n is the toroidal mode number. Thus, a number of tokamak configurations, including small aspect ratio and elongated plasma cross section, which attempt to maximize the plasma current for a given minor radius, provide high β operation below the β_I limit. These devices operate in the "first region" of ideal MHD stability.

In addition, high β operation may be possible in the theoretically predicted "second region" of MHD stability.[8-14] The existence of such a region stable to high-n ballooning modes is now well established by MHD theory and computation for some

classes of tokamak equilibria. Moreover, theory suggests that the second region may be accessible without passing through an unstable zone, for example, by suitable control of the safety factor profile[15-17] or cross-sectional shaping.[18,19] Several other stabilizing mechanisms have been proposed to facilitate transition to the second region including hot particle stabilization,[20-22] induced rotation[23] and rf ponderomotive stabilization.[24] Operation in the second region has been shown theoretically to exhibit favorable high-n resistive mode stability properties.[25] Restabilization of low-n ideal MHD modes has also been observed for high β equilibria in the high-n mode second stability region.[17] The closure and alignment of mod B surfaces with the poloidal flux surfaces, characteristic of high poloidal beta, β_p, second region equilibria, has additionally been shown to reduce neoclassical transport.[26]

The purpose of the present study is to determine the behavior of the values of both the local pressure gradient and global β variables corresponding to the marginal second region threshold with respect to variations in q profile, aspect ratio, and plasma outer boundary shaping. For this analysis, a database of numerically computed, finite aspect ratio equilibria with pressure profiles that are marginally stable at the second region boundary to high-n ballooning modes has been generated. This procedure provides an accurate quantitative analysis, since finite aspect ratio and finite β effects are self-consistently included. The key physics issues illustrated are the stabilization or destabilization of the second region boundary at low aspect ratio, A, due to the dominance of stabilizing or destabilizing toroidal effects on the normal curvature, and the establishment of local direct access windows, that provide instability-free transition between the first and second stable regions. These important characteristics are then examined using analytically tractable models, and simple formulae summarizing these characteristics are derived.

The predictor and response variables used to determine the behavior of the second region threshold are given in Section 3.1.2. The computational model used to generate the marginally stable second region database is described in Sections 3.1.3 and 3.1.4. A description of the global (S,α) diagrams used to diagnose stability, and the connection with the standard $\beta \sim O(\varepsilon^2)$, (S,α) model[27] is given in Section 3.1.5. Here, $\varepsilon \equiv A^{-1}$. The behavior of the normalized pressure gradient, α, and the global figures of merit, β and, $\varepsilon\beta_p$ corresponding to the marginal second region threshold with respect to variations in the tokamak parameters along with physical explanations of the observed characteristics are reviewed in detail in Section 3.1.6. Analytic models that reproduce the behavior of the marginal second region boundary and local direct access are given in Section 3.1.7.

While the identification of the marginal second region boundary for prescribed pressure and safety factor profiles is a useful roadmap for avoiding instabilities, it is not clear that any particular set of profiles can be established in an experimental device. Therefore, a supplementary stability analysis of plasma equilibria that evolve from the first region to the second region is examined in Section 3.2 for profiles that are established by the solution of plasma transport equations. In this study we employ a flux surface averaged transport code,[28] where the magnetic geometry evolves consistently with the heat and mass diffusion, to analyze the transition to the second region. This code also integrates the infinite-n ballooning equation[27,29] at each flux surface and communicates with the PEST stability code[30,31] for low-n analysis of evolving equilibria. Details of the transition to second stability are shown, and the effects of current programming and aspect ratio are discussed. These transport generated transition equilibria are also analyzed for low-n stability.

The minimization of the requirements to reach the second region is subsequently discussed. The second stability region parameterization and transition are applied to the findings of the few tokamaks that have so far attempted to sustain operation of a second stable region plasma. Of particular interest are the very recent collaborative Columbia-Princeton experiments on TFTR, in which a transition scheme that is very similar to that shown in this thesis is being used to successfully establish a second region equilibrium. Present results using this technique have already provided a record β_p value on TFTR, surpassing a "limiting value" that previously could not be surpassed.[32]

As an introduction to the subsequent material, the fundamental equations that are used to model the plasma are first presented in Section 2.0. Previous research on the discovery and development of the second stable region operation of a tokamak is reviewed in Section 3.0. A summary of the instabilities of interest and the role of local shear reversal in the creation of the second stability region is given in the remainder of chapter 3.0.

---

[1]Artsimovich, L.A., Nuclear Fusion **12** (1972) 215.

[2]Post, D.E., in *Plasma Phys. and Controlled Nucl. Fusion Research* **3** (1989) 233.

[3]Bol, K., Buchenauer, D., Chance, M., et al., Phys. Rev. Lett. **57** (1986) 1891.

[4]Burrell, K.H., Stambaugh, R.D., Angel, T.R., et al., Nuclear Fusion **23** (1983) 536.

[5]Troyon, F., Gruber, R., Saurenmann, H., Semenzato, S., and Succi, S., Plasma Phys. and Cont. Fusion **26 1A** (1984) 209; Phys. Lett. **110A** (1985) 29.

[6]Sykes, A., Turner, M.F., Patel, S., in *Proceedings of the 11th European Conference on Controlled Fusion and Plasma Physics*, Aachen, (European Physics Society, Geneva, Switzerland, 1982) **7d** (1983) 363.

[7]Wesson, J.A., Sykes, A., Nuclear Fusion **25** (1985) 85.

[8]Coppi, B., Ferreira, A., Mark, J.W.-K., Ramos, J.J., Nuclear Fusion **19** (1979) 715.

[9]Coppi, B., Ferreira, A., Ramos, J.J., Phys. Rev. Lett. **44** (1980) 990.

[10]Greene, J.M., Chance, M.S., Nuclear Fusion **21** (1981) 453.

[11]Mercier, C., in *Plasma Physics and Controlled Nuclear Fusion Research* (Proc. 7th Int. Conf. Innsbruck, 1978) Vol. 1, IAEA, Vienna (1978) 701.

[12]Fielding, P.J., Haas, F.A., Phys. Rev. Lett. **41** (1978) 801.

[13]Lortz, D., Nuhrenberg, J., Phys. Lett. **68a** (1978) 49.; Nuclear Fusion **19** (1979) 1207.

[14]Strauss, H.R., Park, W., Monticello, D.A., White, R.B., Jardin, S.C., Chance, M.S., Todd, A.M.M., Glasser, A.H., Nuclear Fusion **20** (1980) 638.

[15]Sykes, A., Turner, M.F., in *Controlled Fusion and Plasma Physics* (Proc. 9th Europ. Conf., Oxford, 1979), UKAEA, Culham Lab., Abingdon (1979) 161.

[16]Coppi, B., Crew, G.B., and Ramos, J.J. Comments on Plasma Physics and Controlled Fusion **8** (1983) 11.

[17]Todd, A.M.M., Phillips, M.W., Chance, M.S., Manickam, J., and Pomphrey, N., in *Plasma Physics and Controlled Nuclear Fusion Research* (Proc. 11th Int. Conf. Kyoto, 1986) Vol. 2, IAEA, Vienna (1986) 37.

[18]Chance, M.S., Jardin, S.C., Stix, T.H., Phys. Rev. Lett. **51** (1983) 1963.

[19]Grimm, R.C., Chance, M.S., Todd, A.M.M., Manickam, J., Okabayashi, M., Tang, W.M., Dewar, R.L., Fishman, H., Mendelsohn, S.L., Monticello, D.A., Phillips, M.W., Reusch, M., Nuclear Fusion **25** (1985) 805.

[20]Rosenbluth, M.N., Tsai, S.T., Van Dam, J.W., Engquist, M.G., Phys. Rev. Let. **51** (1983) 1967.

[21]Miller, R.L., and Van Dam, J.W., Nuclear Fusion **27** (1987) 2101.

[22]Wang, X-H., Bhattacharjee, A., and Van Dam, J.W., Phys. Fluids **31** (1988) 332.

[23]Navratil, G.A. and Marshall, T.C., Comments Plasma Phys. Controlled Fusion **10** (1986) 185.

[24]D'Ippolito, D.A., Myra, J.R., and Francis, G.L., Phys. Rev. Lett. **58** (1987) 2216.

[25]Sykes, A., Bishop, C.M., Hastie, R.J., Plasma Physics and Controlled Fusion **29** (1987) 719.

[26]Crume, E.C., Jr., Beasley, C.O., Jr., Hirshman, S.P., Van Rij, W.I., Phys. Fluids **30** (1987) 1152.

[27]Connor, J.W., Hastie, R.J., Taylor, J.B., Phys. Rev. Lett. **40** (1978) 398; Proc. R. Soc. London Ser. A **365** (1979) 1.

[28]Bateman, G., "Spring College on Plasma Physics, Charged Particle Transport in Plasmas", Int. Centre for Theoretical Physics, Trieste, (1985).

[29]Dobrott, D., Nelson, D.B., Greene, J.M., Glasser, A.H., Chance, M.S., and Frieman, E.A., Phys. Rev Lett. **39** (1977) 943.

[30]Grimm, R.C., Greene, J.M., and Johnson, J.L., Meth. Comp. Phys. **16** (1976) 253.

[31]Chance, M.S., in *Proceedings of the Workshop on Finite β Theory*, Varenna, edited by B. Coppi and W.L. Sadowski (U.S. DOE, Washington, D.C., 1977) CONF-7709167, (1977) 43.

[32]McGuire, K., et al., Plasma Phy. & Controlled Fusion. **30**(1988)1391.

You seem to forget that if one follows one's self-interest one wants to be safe, whereas the path of justice and honour involves one in danger.

Thucydides, *The Peloponnesian War*
(from the Melian Dialogue).

2.0 FUNDAMENTAL EQUATIONS

A magnetically confined plasma that provides the environment for fusion reactions to occur in a tokamak device contains a plethora of interesting physical phenomena. The fundamental processes are simple: the interaction of the charged particles in the plasma amongst themselves, and the externally applied electric and magnetic fields. However, solution of the plasma dynamics at the microscopic level, by the kinetic Klimontovich or Liouville equations[1] is neither possible nor desirable. One of the properties that makes the study of plasmas so intriguing is that the particle behavior is self-consistently collective. This quality allows description of plasma dynamics on many different length and time scales.

In the present work, the equilibrium, stability, and transport properties of high β, second stability region tokamak plasmas that exhibit significant deformation of the confining magnetic field are examined. Useful techniques in modelling such plasmas involve treating the charged particles as an electrically conducting fluid, of either one component, for equilibrium and stability studies, or more components, for transport studies. These methods of describing the plasma relinquish the unnecessary microscopic detail of the full kinetic equations, while maintaining the ability to represent

the macroscopic behavior of interest. In this section, the equations used to model the plasma in the second stability region study are presented.

---

[1]Nicholson, D.R., *Introduction to Plasma Theory*, John Wiley and Sons, New York (1983) 37.

2.0.1 Ideal Magnetohydrodynamics

The equations of magnetohydrodynamics (MHD) model the macroscopic dynamics of the plasma by representing it as a single, electrically conducting fluid. They relate the fluid mass density (approximated as the ion mass density), ρ, the ion fluid velocity, $\mathbf{V}$, the fluid pressure, p, the current carried by the fluid, $\mathbf{J}$, and the electric and magnetic fields, $\mathbf{E}$ and $\mathbf{B}$, by the following set of equations, written in MKS units:

$$\frac{\partial \rho}{\partial t} + \nabla \bullet (\rho \mathbf{V}) = 0 , \qquad \text{(Continuity)} \qquad (2.0.1 - 1)$$

$$\rho \left(\frac{\partial \mathbf{V}}{\partial t} + (\mathbf{V} \bullet \nabla)\, \mathbf{V} \right) = \mathbf{J} \times \mathbf{B} - \nabla p, \qquad \text{(Momentum)} \qquad (2.0.1 - 2)$$

$$\mathbf{E} + \mathbf{V} \times \mathbf{B} = \eta \mathbf{J} , \qquad \text{(Ohm's Law)} \qquad (2.0.1 - 3)$$

$$\nabla \times \mathbf{E} = - \frac{\partial \mathbf{B}}{\partial t} , \qquad \text{(Faraday's Law)} \qquad (2.0.1 - 4)$$

$$\nabla \times \mathbf{B} = \mu_0 \mathbf{J} . \qquad \text{(Ampere's Law)} \qquad (2.0.1 - 5)$$

This system of coupled partial differential equations needs an additional scalar equation to close the system. The usual choice is the equation of state,

$$\frac{\partial}{\partial t}\left(\frac{p}{\rho^{\gamma}}\right)=0\,. \qquad \text{(Adiabatic fluid)} \qquad (2.0.1\text{ - }6)$$

In addition, since all physical magnetic fields are divergence free,

$$\nabla \bullet \mathbf{B} = 0\,. \qquad \text{(No monopoles)} \qquad (2.0.1\text{ - }7)$$

This equation is used as an initial condition for the MHD model. Once established, Faraday's Law insures that this condition is satisfied throughout the plasma evolution.

Finally, the plasma resistivity, η, must be specified. When the plasma is considered a perfectly conducting fluid, $\eta \equiv 0$, the set of equations above constitute the *ideal* MHD equations. They form the basis for a wealth of plasma physics research, including fusion plasma physics. Other than the assumption of small resistivity, the ideal MHD equations are valid only when the modelled plasma displays fluid-like characteristics. The plasma should be highly collisional, so that the velocity distributions of the particles are Maxwellian. Also, length scales of the plasma dynamics must be larger than the ion gyro radius, and the frequencies must be smaller than the ion gyro frequency. These assumptions are valid in fusion relevant plasmas, except high collisionality, which is completely violated. However, by a fortunate coincidence, ideal MHD remains a useful model for describing motions of hot, magnetically confined plasmas. The magnetic field restricts the particle motion perpendicular to the field line, thereby providing a "collisional" or "fluid-like" constraint in the direction perpendicular to the magnetic field. This quality artificially satisfies the high collisionality assumption for perpendicular motions, which are of

primary interest for tokamak physics. Particle dynamics along the field lines are unconstrained, and therefore a kinetic treatment is necessary to model the motion of particles parallel to the magnetic field in low collisionality plasmas.

2.0.1.1 Equilibrium

In the analysis of tokamak stability, the first step is to establish an initial plasma equilibrium state. Consider the ideal MHD equations in steady state without flow. The relevant equations (2.0.1 - 2), (2.0.1 - 5), and (2.0.1 - 7) reduce to

$$\mathbf{J} \times \mathbf{B} = \nabla p \ , \qquad (2.0.1.1 - 1)$$

$$\nabla \times \mathbf{B} = \mu_0 \mathbf{J} \ , \qquad (2.0.1.1 - 2)$$

$$\nabla \bullet \mathbf{B} = 0 \ . \qquad (2.0.1.1 - 3)$$

These are the standard ideal MHD equilibrium equations. By specifying the magnetic field, pressure profile, and the appropriate boundary conditions, Eqs. (2.0.1.1 - 1) - (2.0.1.1 - 3) define the state of force balance between the plasma pressure and the confining magnetic field pressure.

2.0.1.1.1 Axisymmetric Flux Coordinates

Solution of the mathematical expressions that model the plasma behavior is simplified by transforming the appropriate equations into a coordinate system that simplifies the computation of derivatives and conforms to boundary conditions. Toroidal curvilinear axisymmetric flux coordinates are the appropriate coordinates for tokamak modelling.

Eq. (2.0.1.1 - 1) implies that $\mathbf{B} \bullet \nabla p = 0$. Therefore, if the magnetic field forms nested surfaces, p can be thought of as a poloidally radial coordinate that labels toroidal or poloidal magnetic flux. Usually, the poloidal flux per unit radian, $\psi = \Psi / 2\pi$, where Ψ is the poloidal flux, is used as the coordinate and is constant over a particular nested magnetic surface. The other obvious coordinate is the toroidal coordinate, φ, that is ignorable in axisymmetry. The third coordinate, θ, demarcates the poloidal angle. It is determined by a specified Jacobian, $\jmath$. Transformation to the flux coordinates (ψ, θ, φ) provides a more convenient analysis of problems in toroidal geometry. Notice that throughout this work, flux coordinate subscripts will be used to denote partial differentiation, unless otherwise indicated by definitions. Also, prime will denote differentiation with respect to the function's argument. A circumflex is used to denote unit vectors.

Consider the transformation from an orthogonal cylindrical coordinate system (R, Z, ζ) to the toroidal coordinates. Fig. (2.0.1.1.1 - 1) illustrates the geometry described the by the coordinates.

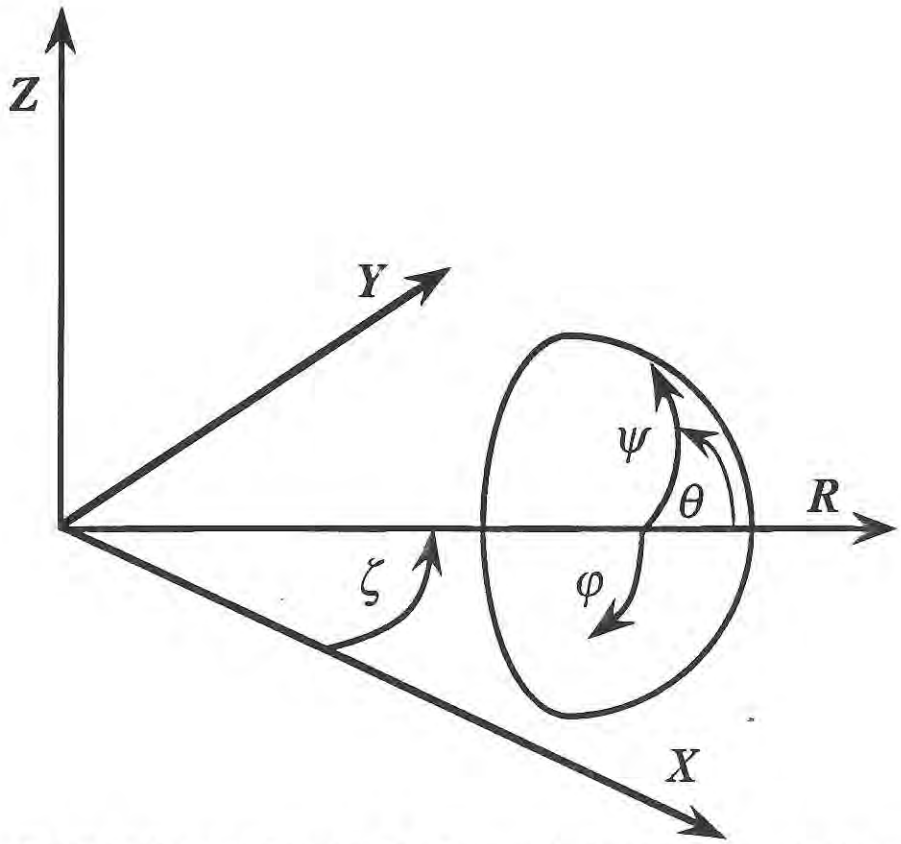

Fig. (2.0.1.1.1 - 1): Geometry of axisymmetric flux coordinates, (ψ, θ, φ), with respect to Cartesian and cylindrical coordinates, (R, Z, ζ).

A point in the Cartesian space is defined by

$$\mathbf{X} = (R\cos(\theta))\,\hat{\mathbf{x}} + (R\sin(\theta))\,\hat{\mathbf{y}} + Z\,\hat{\mathbf{z}}. \qquad (2.0.1.1.1 - 1)$$

In the nomenclature of generalized coordinates, the flux coordinates will form one set of reciprocal basis vectors, the covariant basis vectors, $\mathbf{e}^i$. These can be computed by first establishing the contravariant basis vectors, $\mathbf{e}_i$,

$$\mathbf{e}_1 \equiv \frac{\partial \mathbf{X}}{\partial \psi} = R_\psi\,\hat{\mathbf{R}} + Z_\psi\,\hat{\mathbf{Z}}, \qquad (2.0.1.1.1 - 2)$$

$$\mathbf{e}_2 \equiv \frac{\partial \mathbf{X}}{\partial \theta} = R_\theta\,\hat{\mathbf{R}} + Z_\theta\,\hat{\mathbf{Z}}, \qquad (2.0.1.1.1 - 3)$$

$$\mathbf{e}_3 \equiv \frac{\partial \mathbf{X}}{\partial \varphi} = -R\,\hat{\zeta}. \qquad (2.0.1.1.1 - 4)$$

The covariant basis vectors are then given by $\mathbf{e}^i = (\mathbf{e}_j \times \mathbf{e}_k) / \mathcal{J}$, where

$$\mathcal{J} \equiv \mathbf{e}_1 \bullet (\mathbf{e}_2 \times \mathbf{e}_3) = R\,(R_\psi Z_\theta - R_\theta Z_\psi). \qquad (2.0.1.1.1 - 5)$$

Computed for axisymmetry,

$$\mathbf{e}^1 \equiv \nabla\psi = \frac{R}{\mathcal{J}}\left(Z_\theta \hat{\mathbf{R}} - R_\theta \hat{\mathbf{Z}}\right), \qquad (2.0.1.1.1 - 6)$$

$$\mathbf{e}^2 \equiv \nabla\theta = \frac{R}{\mathcal{J}}\left(-Z_\psi \hat{\mathbf{R}} + R_\psi \hat{\mathbf{Z}}\right), \qquad (2.0.1.1.1 - 7)$$

$$\mathbf{e}^3 \equiv \nabla\varphi = -\frac{\hat{\zeta}}{R}. \qquad (2.0.1.1.1 - 8)$$

The contravariant metric tensor, $\mathbf{g}^{ij} = \mathbf{e}^i \bullet \mathbf{e}^j$, used to transform covariant vector components to their contravariant counterparts is

$$\mathbf{g}^{ij} = \left(\frac{R}{\mathcal{J}}\right)^2 \begin{bmatrix} \left(Z_\theta^2 + R_\theta^2\right) & \left(-Z_\theta Z_\psi - R_\theta R_\psi\right) & 0 \\ \left(Z_\theta Z_\psi + R_\theta R_\psi\right) & \left(Z_\psi^2 + R_\psi^2\right) & 0 \\ 0 & 0 & \left(\frac{\mathcal{J}}{R^2}\right)^2 \end{bmatrix}. \qquad (2.0.1.1.1 - 9)$$

Notice from the form of $\mathbf{g}^{ij}$ that $\nabla\psi$ and $\nabla\theta$ are both orthogonal to $\nabla\varphi$ but not to each other.

Two identities that will be useful in the following section are the definitions of the gradient and the divergence operators,

$$\nabla s = \frac{\partial s}{\partial \theta^i} \mathbf{e}^i, \text{ and} \qquad (2.0.1.1.1 - 10)$$

$$\nabla \bullet \mathbf{s} = \frac{1}{\mathcal{J}} \frac{\partial (\mathbf{s} \bullet \mathbf{e}^i \mathcal{J})}{\partial \theta^i}, \qquad (2.0.1.1.1 - 11)$$

where θ^i represents the flux coordinates, and summation over repeated indices is implied. A more complete list of identities defining operators in these coordinates can be found in the literature containing generalized curvilinear coordinates.[1,2]

---

[1]Borisenko, A.I., and Tarapov, I.E., *Vector and Tensor Analysis with Applications*, Dover, New York (1968) 23.

[2]Bateman, G., *MHD Instabilities*, MIT Press, Cambridge, Mass. (1978) 125.

2.0.1.1.2 Grad-Shafranov Equation

In systems with toroidal axisymmetry, the coupled partial differential equations (p.d.e.s) describing ideal MHD equilibrium (2.0.1.1 - 1) - (2.0.1.1 - 3), can be reduced to a non-linear, two-dimensional, elliptic p.d.e., thereby simplifying the solution procedure. The solution of this form of the equilibrium equation, known as the Grad-Shafranov equation[1-4], is further simplified when considered in the flux coordinate system outlined in the previous section.

The first step in deriving the Grad-Shafranov equation in flux coordinates is to consider the axisymmetric flux coordinate form for the magnetic field,

$$\mathbf{B} = \nabla\varphi \times \nabla\psi + g\,\nabla\varphi\,, \qquad (2.0.1.1.2 - 1)$$

that automatically satisfies Eq. (2.0.1.1 - 3). Currently, g is only assumed to be a function of the poloidal flux coordinates, recalling that it cannot depend on φ due to the axisymmetry. From this form of $\mathbf{B}$, g can easily be identified as RB_t, where B_t is the magnitude of the toroidal component of the magnetic field. The current density can then be computed using Eq. (2.0.1.1 - 2). The result is

$$\mu_0 \mathbf{J} = g^{11}\frac{\partial \nabla\varphi}{\partial\psi} + g^{12}\frac{\partial \nabla\varphi}{\partial\theta} - g^{33}\frac{\partial \nabla\psi}{\partial\varphi} + \nabla^2\psi\,\nabla\varphi\, + \nabla g \times \nabla\varphi\,, \qquad (2.0.1.1.2 - 2)$$

that after the inclusion of the covariant basis vector derivative terms

$$\frac{\partial \nabla\varphi}{\partial\psi} = -\frac{R_\psi}{R}\nabla\varphi, \qquad (2.0.1.1.2 - 3)$$

$$\frac{\partial \nabla\varphi}{\partial\theta} = -\frac{R_\theta}{R}\nabla\varphi, \qquad (2.0.1.1.2 - 4)$$

$$\frac{\partial \nabla\psi}{\partial\varphi} = \frac{R^2 Z_\theta}{\jmath}\nabla\varphi, \qquad (2.0.1.1.2 - 5)$$

reduces to

$$\mu_0 \mathbf{J} = \nabla g \times \nabla\varphi + (RJ_t)\,\nabla\varphi, \qquad (2.0.1.1.2 - 6)$$

where the toroidal current density, J_t, is given by

$$J_t = \frac{R}{\mathcal{J}}\left[\frac{\partial}{\partial\psi}\left(\frac{g^{11}\,\mathcal{J}}{R^2}\right) + \frac{\partial}{\partial\theta}\left(\frac{g^{12}\,\mathcal{J}}{R^2}\right)\right]. \qquad (2.0.1.1.2 - 7)$$

The final step is the evaluation of Eq. (2.0.1.1 - 1). Recalling that p is a flux function, $p \rightarrow p(\psi)$,

$$\mu_0 p'(\psi)\,\nabla\psi = -\,g^{33}\,(g\nabla g + (RJ_t)\nabla\psi) + \left[(\nabla\psi\times\nabla g + g\nabla g)\bullet\nabla\varphi\right]\nabla\varphi. \qquad (2.0.1.1.2 - 8)$$

Note that g must be a flux function, $g \rightarrow g(\psi)$, to restrict the right hand side of this equation to having only a $\nabla\psi$ component, and the result is the Grad-Shafranov equation in axisymmetric flux coordinates,

$$\frac{R^2}{\mathcal{J}}\left[\frac{\partial}{\partial\psi}\left(\frac{|\nabla\psi|^2\,\mathcal{J}}{R^2}\right) + \frac{\partial}{\partial\theta}\left(\frac{(\nabla\psi\bullet\nabla\theta)\,\mathcal{J}}{R^2}\right)\right] = -\,\mu_0 R^2 p'(\psi) - gg'(\psi). \qquad (2.0.1.1.2 - 9)$$

Solution of this equation for ψ requires the specification of the two free functions, $p(\psi)$ and $g(\psi)$, and appropriate boundary conditions. Since the free functions depend on the solution, the full two-dimensional solution of (2.0.1.1.2 - 9) generally requires an iterative technique for solution. Computational solution of this equation however, is simplified since the derivatives and boundary conditions are evaluated in the natural flux coordinates. Also, in lieu of the toroidal field flux function, $g(\psi)$, the magnetic field safety factor, q, is sometimes used as the second free function. In so doing, the relation

$$q(\psi) = \frac{1}{2\pi}\int_0^{2\pi}\frac{\mathbf{B}\bullet\nabla\varphi}{\mathbf{B}\bullet\nabla\theta}\,d\theta' = \frac{g(\psi)}{2\pi}\int_0^{2\pi}\frac{\mathcal{J}}{R^2}\,d\theta' \qquad (2.0.1.1.2 - 10)$$

can be used to eliminate $g(\psi)$ in terms of $q(\psi)$.

As a final note, the cylindrical coordinate form of the Grad-Shafranov equation can be discerned from the flux coordinate form by recognizing that from Eq. (2.0.1.1.1 - 11),

$$\frac{R^2}{\mathcal{J}}\left[\frac{\partial}{\partial\psi}\left(\frac{|\nabla\psi|^2\,\mathcal{J}}{R^2}\right)+\frac{\partial}{\partial\theta}\left(\frac{(\nabla\psi\bullet\nabla\theta)\,\mathcal{J}}{R^2}\right)\right]=R^2\,\nabla\bullet\left(\frac{\nabla\psi}{R^2}\right), \quad (2.0.1.1.2 - 11)$$

that leads to the result,

$$R^2\,\nabla\bullet\left(\frac{\nabla\psi}{R^2}\right)=-\mu_0\,R^2\,p'(\psi)-gg'(\psi). \quad (2.0.1.1.2 - 12)$$

---

[1]Grad, H., and Rubin, H. In *Proceedings of the Second United Nations International Conference on the Peaceful Uses of Atomic Energy*, United Nations, Geneva, 31 (1958) 190.

[2]Shafranov, V.D., Sov. Phys. -JETP 8 (1958) 545.

[3]Laing, E.W., Roberts, S.J., Whipple, R.T., J. Nucl. Energy C 1 (1959) 49.

[4]Shafranov, V.D., Sov. Phys. - JETP 26 (1960) 682.

2.0.1.2 Linear Stability

Early in the research effort to magnetically confine a hot plasma, instabilities were detected that led to degradation or complete loss of the plasma discharge.[1] One of the greatest goals of contemporary experimental magnetic fusion research is to generate fusion relevant plasmas that are stable to modes detrimental to plasma performance.

Therefore, there has been, and still remains, a considerable theoretical effort to demonstrate under what conditions an initially established equilibrium state will return to equilibrium when perturbed, and similarly, under what conditions the plasma will depart from its initial state. This demonstration forms the basis of plasma stability analysis.

While a plasma will exhibit kinetic and resistive instabilities,[2,3] the present work limits the scope to the examination of ideal MHD instabilities, that generally match the driving forces of the plasma against the restoring forces of the confining magnetic field. These instabilities are important to suppress as a first priority, since they are the fastest growing modes that lead to significant loss of confinement or complete collapse of the discharge. In this section, the basic equations that form the foundation for the numerical and computational stability analysis shown throughout the remainder of this work are presented. Additional detail of the derivations can be found in the book by Freidberg.[4]

Since ideal MHD instabilities can be so detrimental to plasma performance, and since their growth rates are fast when measured on a typical experimental timescale, it is generally more important to determine how to avoid these modes entirely, rather than examining their non-linear evolution or saturated states. Therefore, a simplification of the analysis is made by considering a linear stability analysis. The initial state considered is that of ideal MHD equilibrium defined by Eqs. (2.0.1.1 - 1) - (2.0.1.1 - 3). Perturbations of the form $\mathbf{S}(\mathbf{x},t) = \mathbf{S}_0(\mathbf{x}) + \tilde{\mathbf{S}}_1(\mathbf{x},t)$ are introduced on the background equilibrium. The momentum Eq. (2.0.1 - 2) is then linearized, with the result

$$\rho_0 \frac{\partial \tilde{\mathbf{V}}_1}{\partial t} = \mathbf{J}_0 \times \tilde{\mathbf{B}}_1 + \tilde{\mathbf{J}}_1 \times \mathbf{B}_0 - \nabla \tilde{p}_1 . \qquad (2.0.1.2 - 1)$$

The perturbed displacement

$$\tilde{\xi}(\mathbf{x},t) \equiv \int_0^t \tilde{\mathbf{V}}_1(\mathbf{x},t')\, dt' \qquad (2.0.1.2 - 2)$$

is now introduced. The aim is to express Eq. (2.0.1.2 - 1) in terms of $\tilde{\xi}$ and the equilibrium quantities. All perturbations are taken to be zero initially, except for the velocity perturbation. The linearized and time integrated forms of Eqs. (2.0.1 - 1), (2.0.1 - 6) and (2.0.1 - 4) are

$$\tilde{\rho}_1 = - \nabla \bullet (\rho_0 \tilde{\xi}), \qquad (2.0.1.2 - 3)$$

$$\tilde{p}_1 = - \tilde{\xi} \bullet \nabla p_0 - \gamma p_0 \nabla \bullet \tilde{\xi}, \qquad (2.0.1.2 - 4)$$

$$\tilde{\mathbf{B}}_1 = \nabla \times (\tilde{\xi} \times \mathbf{B}_0) \equiv \tilde{\mathbf{Q}}. \qquad (2.0.1.2 - 5)$$

When substituted along with $\tilde{\xi}$ these provide the result,

$$\rho_0 \frac{\partial^2 \tilde{\xi}}{\partial t^2} = \mathbf{F}(\tilde{\xi}) \qquad (2.0.1.2 - 6)$$

where

$$\mathbf{F}(\tilde{\xi}) = \frac{1}{\mu_0}\left[(\nabla \times \mathbf{B}_0) \times \tilde{\mathbf{Q}} + (\nabla \times \tilde{\mathbf{Q}}) \times \mathbf{B}_0\right] + \nabla(\tilde{\xi} \bullet \nabla p_0 + \gamma p_0 \nabla \bullet \tilde{\xi}). \qquad (2.0.1.2 - 7)$$

This equation can be solved as an initial value problem, or as a boundary value problem by Fourier expanding the perturbed quantities and defining boundary conditions for $\tilde{\xi}$. Also, since the force operator, **F**, is self-adjoint, that is, for any two perturbations, $\tilde{\xi}$ and $\tilde{\nu}$, **F** satisfies

$$\int \tilde{\nu} \cdot \mathbf{F}(\tilde{\xi})\, d\mathbf{x} = \int \tilde{\xi} \cdot \mathbf{F}(\tilde{\nu})\, d\mathbf{x}, \qquad (2.0.1.2 - 8)$$

the problem can be considered variationally. A powerful technique that follows, used to determine the plasma stability, is the Energy Principle[5]

Consider equation (2.0.1.2 - 6) with perturbed quantities Fourier expanded in the form $\tilde{\mathbf{S}}_1(\mathbf{x},t) = \mathbf{S}_1(\mathbf{x}) \exp(-i\omega t)$. The resulting Euler equation form,

$$-\omega^2 \rho_0 \xi = \mathbf{F}(\xi), \qquad (2.0.1.2 - 9)$$

can be converted to a variational form in the usual way by taking the dot product with ξ^*, and integrating over space. The result is

$$\omega^2 = \frac{\delta W(\xi^*,\xi)}{\frac{1}{2}\int \rho_0 |\xi|^2\, d\mathbf{x}} \qquad (2.0.1.2 - 10)$$

where the potential energy functional

$$\delta W(\xi^*,\xi) = -\frac{1}{2}\int \xi^* \cdot \mathbf{F}(\xi)\, d\mathbf{x}. \qquad (2.0.1.2 - 11)$$

The Energy Principle now allows determination of the stability of a given equilibrium by the sign of δW. The equilibrium is stable if and only if δW is positive for all displacements that are square integrable with weight factor ρ_0 (finite energy) and satisfy the boundary conditions. Otherwise, the equilibrium is unstable.

The potential energy functional, δW, and the Energy Principle, form the foundation for a large amount of both analytic and numerical stability analyses. They are used in determining the eigenvalues for prescribed eigenfunctions in the PEST stability codes,[6] that are used to determine the stability of small-n modes for the second region transition plasmas in Section 3.2. The δW formulation can also be further simplified when a particular mode of interest allows. An example of this is the establishment of an Euler-Lagrange equation describing large-n ballooning instabilities.[7] Solution of the large-n ballooning equation provides the means by which stability boundaries for these modes are determined in Section 3.1.

---

[1]Krall, N.A., and Trivelpiece, A.W., Principles of Plasma Physics, McGraw-Hill (1973) 12.

[2]Ichimaru, S., *Basic Principles of Plasma Physics: A Statistical Approach*, Benjamin/Cummings, Reading, Mass. 133.

[3]Furth, H.P., Killeen, J., Rosenbluth, M.N., Phys. Fluids, **6** (1963) 459.

[4]Freidberg, J.P., *Ideal Magnetohydrodynamics*, Plenum Press, New York (1987) 231.

[5]Bernstein, I.B., Frieman, E.A., Kruskal, M.D., and Kulsrud, R.M., Proc. R. Soc., London, Ser. A **244** (1958) 17.

[6]Grimm, R.C., Greene, J.M., and Johnson, J.L., Meth. Comp. Phys. **16** (1976) 253.

[7]Connor, J.W., Hastie, R.J., Taylor, J.B., Phys. Rev. Lett. **40** (1978) 396; Proc. R. Soc. (London) A **365** (1979) 1.

2.0.2 Particle and Energy Transport

The ideal MHD model is inadequate for modelling the transport of particles, energy, and magnetic field in a tokamak. Treating the plasma as a combination of interpenetrating electron and ion fluids, the two fluid model allows a reasonable model for tokamak transport for times larger than the Alfvén time, characteristic of ideal MHD.

The magnetic field of a tokamak confines a plasma by reducing plasma particle and energy flow perpendicular to **B**. From a single particle standpoint, individual particles perform Larmor orbits about **B** (the helical magnetic field serves to cancel any net $\nabla \mathbf{B}$ particle drifts) until they collide with other particles, causing particle and energy transport across field lines. On the contrary, there is no such confinement parallel to **B**, along which particles free-stream unless they collide with other particles. This asymmetry of behavior perpendicular and parallel to **B** leads to one of the many imbalances in timescales characteristic of magnetically confined plasmas. In particular, the ratio of the transport timescale parallel to **B**, to the transport timescale perpendicular to **B** is large in a tokamak. Since a magnetic field line wraps around the device forming each magnetic surface, the electron and ion densities and temperatures can each be considered constant on these surfaces on the perpendicular transport timescale.[1] This approximation reduces the general three-dimensional problem into a one-dimensional transport problem, where the appropriate independent variable is the coordinate perpendicular to a magnetic flux surface (along $\nabla \psi$). When evaluating the transport properties of second region equilibria, where flux surfaces are distorted from being circular, the general two-dimensional Grad-Shafranov equation (2.0.1.1.2 - 9) must be determined to evaluate the geometry of the ψ surfaces. The one-dimensional transport

equations are then averaged over the computed ψ surfaces, so that the transport is calculated self-consistently with the magnetic field geometry. This prescription of the plasma transport is known as the $1\frac{1}{2}$ dimensional transport model.[2,3,4] This section describes the steps taken in deriving the flux surface averaged transport equations and how they are combined with the evaluation of ψ to produce the $1\frac{1}{2}$ dimensional model of transport. The review article of Hinton and Hazeltine[5] provides additional detail on the flux surface averaged transport equations as well as a review of transport theory in toroidal geometry, more colloquially known as "neo-classical" transport theory.

The basic equations that constitute the $1\frac{1}{2}$ dimensional transport model can be derived by first formulating the ion and electron fluid equations of particle and energy conservation by taking the even velocity moments

$$\int \mathrm{v}^{\mathrm{i}}\, \mathrm{d}^3\mathrm{v} \quad , \mathrm{i} = 0, 2 \qquad (2.0.2 - 1)$$

of the Fokker-Planck equation,

$$\frac{\partial f_j}{\partial t} + \mathbf{v} \bullet \nabla f_j + \left(\frac{\mathrm{e_j}}{\mathrm{m_j}}\right)(\mathbf{E} + \mathbf{v} \times \mathbf{B}) \bullet \frac{\partial f_j}{\partial \mathbf{v}} = C_j(f_j) \qquad (2.0.2 - 2)$$

where the subscript j pertains to the particle species, $f_j(\mathbf{x},\mathbf{v},t)$ is the particle distribution function, e_j and m_j are the electronic charge and mass of the particles, and $C_j(f_j)$ is the Fokker-Planck collision operator.[6,7] The fluid equations for each species (subscripts omitted) are then

$$\frac{\partial n}{\partial t} + \nabla \bullet (n\,\mathbf{u}) = 0, \qquad (2.0.2 - 3)$$

and

$$\frac{3}{2}\frac{\partial (nT)}{\partial t} + \nabla \bullet \mathbf{Q} = \mathrm{Q} + \mathbf{u} \bullet (\mathbf{F} + e n \mathbf{E}), \qquad (2.0.2 - 4)$$

where

$$n(\mathbf{x},t) = \int f_j(\mathbf{x},\mathbf{v},t)\ \mathrm{d}^3\mathbf{v} \qquad (2.0.2 - 5)$$

is the particle density,

$$n\ \mathbf{u} = \int \mathbf{v}\ f_j(\mathbf{x},\mathbf{v},t)\ \mathrm{d}^3\mathbf{v} \qquad (2.0.2 - 6)$$

is the particle flux,

$$\mathbf{Q} = \frac{\mathrm{m_j}}{2} \int v^2\ f_j(\mathbf{x},\mathbf{v},t)\ \mathrm{d}^3\mathbf{v} \qquad (2.0.2 - 7)$$

is the energy flux,

$$\mathbf{F} = \mathrm{m_j} \int \mathbf{v}\ C_j(f_j)\ \mathrm{d}^3\mathbf{v} \qquad (2.0.2 - 8)$$

is the friction force due to collisions,

$$\mathrm{Q} = \frac{\mathrm{m_j}}{2} \int (\mathbf{v} - \mathbf{u})^2\ C_j(f_j)\ \mathrm{d}^3\mathbf{v} \qquad (2.0.2 - 9)$$

is the energy exchange between species due to collisions, and T is the temperature.

The fluid equations are now averaged over flux surfaces. The flux surface average of a variable h is defined as a volume integral between differentially close magnetic surfaces,

$$\langle h \rangle \equiv \frac{\partial}{\partial V} \int h \, \mathrm{d}^3 \mathrm{v}, \qquad (2.0.2 - 10)$$

where V is the volume enclosed by the appropriate flux surface. By recalling that

$$V \rightarrow V(\psi) = \int_0^{\psi} \int_0^{2\pi} \int_0^{2\pi} \jmath \, d\psi \, d\theta \, d\varphi, \qquad (2.0.2 - 11)$$

this average can be re-written in flux coordinates as

$$\langle h \rangle = \left(\frac{\partial V}{\partial \psi}\right)^{-1} \oint \frac{dS}{|\nabla \psi|} = \frac{\int_0^{2\pi} h \, \jmath \, d\theta}{\int_0^{2\pi} \jmath \, d\theta} . \qquad (2.0.2 - 12)$$

The flux surface label is now chosen to be a function of the toroidal flux, X, specified as

$$\vartheta \equiv \sqrt{\frac{X}{\pi B_0}} . \qquad (2.0.2 - 13)$$

ϑ is then an "effective" radial coordinate, preferred in tokamak transport studies since it will not vary as greatly as ψ during the equilibrium evolution. Notice then that with $V \rightarrow V(\vartheta)$, the volume integral is related to the flux surface average by

$$\int_0^{\vartheta} \frac{\partial V}{\partial \vartheta} \langle h \rangle \, d\vartheta = \int h \, \mathrm{d}^3\mathbf{x} \, . \qquad (2.0.2 - 14)$$

In evaluating the averaged transport equations, it is desirable that particle and energy fluxes be specified relative to the magnetic flux surfaces, that are generally in motion. The following identity will be useful in converting to the flux surface reference frame. The time derivative of a volume integrated quantity on a flux surface is related to the integrated quantity at constant $\mathbf{x}$ by

$$\frac{\partial}{\partial t}\Big|_{\psi} \int h(\mathbf{x},t) \, \mathrm{d}^3\mathbf{x} = \int \frac{\partial h}{\partial t}\Big|_{\mathbf{x}} \mathrm{d}^3\mathbf{x} + \oint \frac{h \, \mathbf{u}^{\psi} \cdot \nabla \psi}{|\nabla \psi|} \, dS \qquad (2.0.2 - 15)$$

where $\mathbf{u}^{\psi}$ is the velocity of the flux surface.

The flux surface averaged particle conservation equation is obtained by integrating Eq. (2.0.2 - 3) over space and converting the integrated divergence by the divergence theorem,

$$\int \frac{\partial n}{\partial t}\Big|_{\mathbf{x}} \mathrm{d}^3\mathbf{x} + \oint \frac{n \, \mathbf{u} \cdot \nabla \psi}{|\nabla \psi|} \, dS = 0 \, . \qquad (2.0.2 - 16)$$

Converting to the flux surface reference frame using Eq. (2.0.2 - 15) and changing variables from ψ to ϑ yields,

$$\frac{\partial}{\partial t}\Big|_{\vartheta} \int n \, \mathrm{d}^3\mathbf{x} + \oint \frac{n \, (\mathbf{u} - \mathbf{u}^{\vartheta}) \cdot \nabla \vartheta}{|\nabla \vartheta|} \, dS = 0 \, . \qquad (2.0.2 - 17)$$

Finally, by using Eqs. (2.0.2 - 12) and (2.0.2 - 14) to convert to flux surface averages, and allowing for sources and sinks of particles, n_s, the result is the flux surface averaged particle transport equation,

$$\frac{\partial}{\partial t}\Big|_{\vartheta}\left[V'(\vartheta)\,\langle n\rangle\right] + \frac{\partial}{\partial \vartheta}\left[\left(V'(\vartheta)\,\langle n\,(\mathbf{u}-\mathbf{u}^{\vartheta})\bullet\nabla\vartheta\rangle\right)\right] = V'(\vartheta)\langle n_s\rangle\,. \qquad (2.0.2-18)$$

The energy transport equation follows similarly, using Eq. (2.0.2 - 4) with the source and sink terms represented by Q_S, as,

$$\frac{3}{2}\frac{\partial}{\partial t}\Big|_{\vartheta}\left[V'(\vartheta)\,\langle nT\rangle\right] + \frac{\partial}{\partial \vartheta}\left[V'(\vartheta)\left(\langle \mathbf{Q}\bullet\nabla\vartheta\rangle - \frac{3}{2}\langle T\,n\,\mathbf{u}^{\vartheta}\bullet\nabla\vartheta\rangle\right)\right] = V'(\vartheta)\langle Q_s\rangle. \qquad (2.0.2-19)$$

The final step is to convert the energy flux to a reference frame relative to the flux surface. This can be done by considering the energy flux as a combination of a diffusive heat flux and a convective heat flux,

$$\langle \mathbf{Q}\bullet\nabla\vartheta\rangle \equiv \langle q_h\rangle + \frac{5}{2}\langle T\,n\,\mathbf{u}\bullet\nabla\vartheta\rangle\,, \qquad (2.0.2-20)$$

and realizing that from Eq. (2.0.2 - 15),

$$\frac{\partial}{\partial t}\Big|_{\vartheta} V'(\vartheta) = \frac{\partial}{\partial \vartheta}\left[\left(V'(\vartheta)\,\langle \mathbf{u}^{\vartheta}\bullet\nabla\vartheta\rangle\right)\right]. \qquad (2.0.2-21)$$

By adding the product of Eq. (2.0.2 - 21) with nT to Eq. (2.0.2 - 19), and compressing the time derivatives, the result is the flux surface averaged energy transport equation,

$$\frac{3}{2} V'(\vartheta)^{-2/3} \frac{\partial}{\partial t}\Big|_{\vartheta} \left[V'(\vartheta)^{5/3} \langle nT \rangle \right] +$$
$$\frac{\partial}{\partial \vartheta}\left[V'(\vartheta) \left(\langle q_h \rangle + \frac{5}{2} \langle T\, n\, (\mathbf{u} - \mathbf{u}^{\vartheta}) \bullet \nabla \vartheta \rangle \right) \right] = V'(\vartheta) \langle Q_s \rangle . \quad (2.0.2 - 22)$$

A brief discussion of the sources, sinks, and transport coefficients employed in the modelling of the second stability region transition will be given in Sections 3.2.1 and 3.2.2.

The third transport equation describes the diffusion of the poloidal magnetic field. Since the poloidal field is non-uniform over a flux surface, an "effective" poloidal field

$$B_{p\,\mathrm{eff}} \equiv \left(\frac{\partial \psi}{\partial \vartheta} \right) \frac{1}{R_0} \quad (2.0.2 - 23)$$

is used. The time evolution equation is given by

$$\frac{\partial B_{p\,\mathrm{eff}}}{\partial t}\Big|_{\vartheta} = \frac{\partial}{\partial \vartheta}\left[\frac{\eta_{\|}\, g(\vartheta)}{\mu_0\, V'(\vartheta) \langle g^{33} \rangle} \frac{\partial}{\partial \vartheta} \left(\frac{V'(\vartheta)\, B_{p\,\mathrm{eff}}}{g(\vartheta)} \langle |\nabla \vartheta|^2\, g^{33} \rangle \right) \right]$$
$$- \frac{\partial}{\partial \vartheta} (\eta_{\|}\, J_{\mathrm{driven}}) \quad (2.0.2 - 24)$$

where $\eta_{\|}$ is the resistivity parallel to **B**, and J_{driven} represents non-inductive current drive, for example, due to neutral beams or diffusion driven bootstrap current.[8] As in the calculation of the standard hydromagnetic equation, Eq. (2.0.2 - 24) is obtained by combining Eqs. (2.0.1 - 3) - (2.0.1 - 5). The detail of the calculation can be found in Ref. [5].

In addition to the flux surface averaged equations, a prescription of the shape of the flux surfaces and the evolution of the toroidal field must be specified. The $1^1/_2$ dimensional transport model exploits the disparity between the transport and ideal MHD timescales to eliminate the inertial term in the MHD momentum equation (2.0.1 - 2), thereby describing the evolution of the plasma as a series of quasi-steady-state equilibria that obey the ideal MHD equilibrium equation (2.0.1.1 - 1). Therefore, the geometry of the flux surfaces used in computing flux surface averaged quantities is determined by solution of the Grad-Shafranov equation. Also, the toroidal field can be determined by solving the flux surface averaged Grad-Shafranov equation for $g(\psi)$. By noticing from Eq. (2.0.2 - 11) that $V'(\psi) = 2\pi \int_0^{2\pi} \jmath d\theta$, the flux surface average of Eq. (2.0.1.1.2 - 9) can be written as

$$\frac{1}{2}\left(g^2(\psi)\right)' \left\langle \frac{1}{R^2} \right\rangle = -\mu_0 p'(\psi) - \frac{1}{V'(\vartheta)} \left(V'(\vartheta)\, R_0 B_{p\,\mathrm{eff}} \left\langle \frac{|\nabla \vartheta|^2}{R^2} \right\rangle \right). \qquad (2.0.2 - 25)$$

Specification of the initial and boundary conditions for n, T, B_t and $B_{p\,\mathrm{eff}}$ (through the specification of the toroidal plasma current) completes the formulation of the transport model, a set of coupled, non-linear, parabolic p.d.e.s. These equations form the basis of the numerical modelling of transport in routines such as the BALDUR[4,9] transport code, used in the analysis of the transition to the second stability region.

---

[1]Shafranov, V.D., J. Nucl. Energy, 8 (1966) 314.

[2]Grad, H., Hu, P.N., Stevens, D.C., Proc. Nat. Acad. Sci. 72 (1975) 3789.

[3]Houlberg, W.A., Hogan, J.T., Nuclear Technology/Fusion 3 (1983) 244.

[4]Bateman, G., Spring College on Plasma Physics, "Charged Particle Transport in Plasmas", Int. Centre for Theoretical Physics, Trieste, (1985).

[5]Hinton, F.L., and Hazeltine, R.D., Rev. Mod. Phys. 48 (1976) 239.

[6]Krall, N.A., and Trivelpiece, A.W., Principles of Plasma Physics, McGraw-Hill (1973) 287.

---

[7]Rosenbluth, M.N., MacDonald, W., and Judd, D., Phys. Rev. **107** (1957) 1.

[8]Bickerton, R.J., Connor, J.W., and Taylor, J.B., Nature Physical Science **229** (1971) 110.

[9]Singer, C.E., et al., BALDUR: A One-dimensional Plasma Transport Code, Princeton Plasma Physics Laboratory Report PPPL-2073.

Here I saw far more people than elsewhere both on the one side and on the other, with great howls rolling weights by main force of chest; they clashed together when they met and then at that point each turned about and rolled his weight back again, shouting: "Why hoard?" and "Why squander?" Thus they returned round the gloomy circle on either hand to the opposite point, shouting at each other again their taunting chorus; then, having reached it, each turned back by his half circle to the other joust.

Dante, *Inferno*, (Canto 7, 1 93-101).

3.0 SECOND STABILITY REGION

The second stability region is a characteristic of short perpendicular wavelength ballooning modes in a tokamak. Here, and throughout this work, perpendicular and parallel refers to the orientation with respect to the magnetic field. At small values of the plasma pressure gradient, $p'(\psi)$, these modes are stable. As $p'(\psi)$ increases in magnitude, ballooning modes are excited in the plasma due to the increased instability drive terms in δW, and a decrease in the magnitude of the local shear of the magnetic field lines on the outboard side of the plasma, where field line curvature is unfavorable.[1] However, as $|p'(\psi)|$ increases further, pressure driven Phirsch-Schluter currents increase the magnitude of the local shear by reversing it in the unfavorable curvature region. This change in the field line structure is stabilizing since a mode needs to bend the field lines to a greater extent at larger shear. This enhanced stability offsets the instability drive terms and restabilizes the mode at large magnitudes of $p'(\psi)$. Plasma equilibria that exist at stable, small $p'(\psi)$ values are called "first region stable", while those existing at stable, large $p'(\psi)$ values are called "second region stable". The unstable gap in $p'(\psi)$ between the first and second region is simply known as the

"unstable" region. Since the instability is thought to create alternate physical effects, such as enhanced transport that would in turn reduce $|p'(\psi)|$ bringing the plasma back to a stable state,[2] equilibria are thought not to be able to exist in steady state in the unstable region. However, there are tokamak equilibria that exhibit favorable stability properties such that no unstable region in $p'(\psi)$ exists, either on a limited group of flux surfaces, or across the entire plasma minor radius. Attaining these equilibria in an experimental device may allow access to large $p'(\psi)$, or large β operation in a tokamak without encountering an unstable region. By theoretically investigating the stability of different classes of equilibria, the most favorable candidates to reach the second region can be ascertained, thereby providing a guide to achievement of a second region equilibrium in an experimental device.

Both Bruno Coppi at MIT and J.B. Taylor at Culham Laboratory, England, claim the discovery of the second stability region. After an experimental review talk of second stability operation in tokamaks given by Mike Mauel of Columbia U. at the 1989 Sherwood theory conference, both Coppi and Taylor stood up and declared that their respective research groups had theoretically established the existence of the second region. The findings of the two groups had been published in 1978, however, the relevant Culham publication of Connor, Hastie, and Taylor[3], did not show the second stable branch of the ballooning mode. Quite seriously, Taylor admitted at the meeting that the Culham group had indeed discovered the second stable branch, but that he himself forced the other researchers to remove the data since he was convinced that the result was a numerical artifact of the model! This was very enlightening, since previously it was puzzling why the results of Ref. [3] did not contain the second stable region, when the model that was used did include it. Nevertheless, Taylor insisted that his group had made the discovery, although he still believes that the second region is a numerical fiction that is not obtainable experimentally.

In a private communication with Alan Sykes at Culham, it was found that Sykes himself had independently found the second region but he didn't quite believe the result, and was reluctant to disclose it. However, a few days later, he was told a rumor of a similar discovery by the Americans, and as put by Sykes, "That day, I discovered the second stability region." As Sykes said during the discussion, it is always easy to discover something when you already know that it exists! With this in mind, a brief summary of previous research on the second stability region is presented in this section, along with a short outline of the physics that causes the appearance of a ballooning stable region at large pressure gradients.

The purpose of the present chapter is to summarize the properties of the instabilities that are most likely to prevent high β tokamak operation The instability drive terms are examined by deriving the "intuitive" form of δW and the large-n ballooning mode formalism is used to examine short perpendicular wavelength modes. The role of local magnetic field shear on the stability of these modes is also examined.

Due to the assumptions made for different analytical and computational models of ballooning stability, the past research on the second region can seem disjoint or contradictory. The review given in this chapter will serve to conglomerate the past results, and illustrate how the self-consistent results of the present study support, contradict, or generalize those of previous studies.

---

[1]Greene, J.M., Chance, M.S., Nuclear Fusion **21** (1981) 453.

[2]Houlberg, W.A., Hogan, J.T., Nuclear Technology/Fusion **3** (1983) 244.

[3]Connor, J.W., Hastie, R.J., Taylor, J.B., Phys. Rev. Lett. **40** (1978) 396.

3.0.1 Historical Overview of Second Region Research

Since the second stability region is a characteristic of the ballooning mode, the foundation of ballooning modes is itself an important point of departure for a review of research. The stability criteria of interchange modes in cylindrical[1], and toroidal[2,3] geometry are logical predecessors of the more general ballooning mode stability studies. A fair amount of analytical research of the interchange mode in toroidal geometry was performed by the Soviets in the late 1960's and early 1970's.[4-7] While ballooning perturbations were not explicitly analyzed, reference is made to the ballooning mode,[8,9] (see Ref. contained in Kadomtsev, et al. 1967), a perturbation that is pronounced toward the outboard side of the plasma where the toroidal field component of the normal field line curvature is unfavorable. An additional insight relevant to the ballooning mode second-stability region is contained in the work of Mikhailovskii (1974), where the possibility of stability at large pressure gradient is explored.[5,6] However, it would be approximately five years until the self-stabilizing nature of the ballooning mode was appreciated. A key reason for the delay was the lack of a published prescription for analyzing large toroidal mode number ballooning modes.

Work of the late 1970's not only provided sophisticated theoretical models for ideal MHD stability, but also a wealth of numerical studies that supplied exact solution of these models. The notable references are that of Grimm, et al.[10] (1975) on the stability of small-n ideal MHD modes (standard reference for the PEST stability code) and the complementary studies of the large-n modes, that use the reduced form of the potential energy functional in the large-n limit to derive the ballooning equation.[11-13] An advantage of the large-n ballooning approximation is the decoupling of the global

stability problem to that of a set of independent local stability problems, each computed on separate flux surfaces. This prescription substantially simplifies both analytical and numerical solutions of ballooning stability in tokamaks. These methods expedited research in ideal MHD stability. The introduction of the "quasimode" prescription of the ballooning mode (Connor, et al. 1978, shortened as CHT) was particularly important, since it provided a method of properly prescribing boundary conditions for the ballooning equation in tokamak plasmas with magnetic field shear. The work of CHT also contained the so-called "(S,α)" model of ballooning stability, appropriate for infinite A, low $\beta \sim O(\varepsilon^2)$, circular boundary equilibria. While this is perhaps the simplest model that displays a ballooning mode second stability region, it has also lead to some confusion concerning ballooning stability, since the results are many times errantly applied to equilibria of finite A, high β, or shaped boundary, to which the model does not apply. As mentioned previously, although the second stability region was discovered by CHT by using the (S,α) model, the result was not published, so that only the first stable branch of the large-n ballooning mode appears in the paper. Numerical work displaying the onset of the low-n kink/ballooning mode[14,15] was also performed, and the work of Todd, et al. (1977) proposed that a ballooning β limit in tokamaks should scale as ε/q^2.

While numerical studies were beginning to map out stability boundaries for both large and small-n instabilities, two important analytical studies associated with high β plasmas were performed.[16,17] The work of Clarke and Sigmar (1977) illustrated that plasmas need not have an equilibrium β limit if the plasma is heated so that the magnetic field fluxes are conserved. This work had temporarily relieved worries that a plasma could not reach high β because of an equilibrium limit, however, this issue is still being debated today. The work of Fielding and Haas (1978) introduced anisotropic pressure in the large-n ballooning equation, and showed that the anisotropy leads to increased

stability of the ballooning mode. Analytical studies also began on determining the stability boundaries of the ballooning mode.[18] The multiple scale analysis of Pogutse and Yurchenko (1978) produced a model of stability appropriate for small magnetic field shear and low β, but for finite ε. The result of this work displayed a "second stability region" for small values of S and α (produced by a term linear in p' and ε) but since terms greater than $O(\varepsilon^2)$ were dropped, the stable region did not extend indefinitely to large pressure gradient. The inclusion of finite ε produced a stable path from the first to "second" stable regions. This stabilizing effect is due to the decrease in the magnitude of κ_n in the unfavorable curvature region at finite ε, and is known more colloquially as the "geometric magnetic well". This effect holds the potential of providing a direct access path to the second region, however, it will be shown that competing effects can also lead to destabilization of the large-n modes when both finite ε *and* large Shafranov shift are included. Published concurrently was a numerical re-evaluation of the (S,α) model by Lortz and Nuhrenberg[19] that clearly shows the second stable branch of the ballooning mode. Recall that since finite ε effects are dropped in this model, no stable path between the first and second region was shown.

The 1978 IAEA meeting (Proc. 7th Int. Conf., Innsbruck) included many papers relevant to future second region studies.[20-23] In a study of localized displacements, Mercier included the prospect of a kidney bean shaped equilibrium as providing enhanced stability properties. Zakharov introduced the shifted circular model of equilibrium to the stability problem and included both finite ε and Shafranov shift, σ. Unfortunately, terms of order $\varepsilon\sigma'(r)$ were dropped. It will be shown in Chapter 3.1 that it is precisely these terms that lead to instability of the large-n modes at low A. Sykes, et al. applied the ideal MHD stability analysis to the JET tokamak, and introduced the stabilizing effect of raising the axis value of q on the ballooning mode. This paper shows the stabilizing effect of q_0 and the characteristic outward shift of the

unstable region as q_0 is raised. This work was extended and presented at the European Physical Society Conference in 1979.[24] This behavior is shown in the present study, and the stabilizing effect of raising q_0 is the main thrust of many present schemes to access the second stable region. However, there remains a confusion of how increasing q_0 physically provides stability. This point is examined in Section 3.1.6 where it is found that the reduction of the global shear *and* the Shafranov shift are the physical stabilizing effects of increased q_0.

An analytical study of ballooning stability at low shear by Lortz and Nuhrenberg[25] was the first to introduce a scaling between the normalized pressure gradient and the global magnetic field shear for the second stability region boundary. The study is similar to the earlier work of Pogutse and Yurchenko (1978), except that terms to $O(\varepsilon^4)$ were retained, and a second stable region extending to large values of pressure gradient was found. In particular, the normalized pressure gradient was found to scale as the square root of the global shear for both the first and second region boundaries. Pogutse, et al.[26] extended their previous work by considering shaped cross sections, with the conclusion that Dee shaping generally helps stabilize the large-n modes, but that elongation alone leads to instability in the central portion of the plasma.

The works of Coppi, et al.[27-29] directly address the existence of the second stability region, and are perhaps the most cited references on the "discovery" of the second stable region. However, it is clear that they are not the first published works on second stability, and this is acknowledged by Coppi. Reference is made to the works of Mercier, Zakharov, Sykes, et al., and Lortz, et al., stating that the second stable branch had been independently observed. However, the earlier work of Mikhailovskii was not mentioned. Coppi's results clearly show a second stable branch of the ballooning mode at large pressure gradient. The shortening of the connection length along the field line in

the destabilizing curvature region is mentioned as a cause for the reduced growth rate of the mode at large values of β. In the Comments article, the infinite A, shifted circular flux surface model of equilibrium is used to demonstrate the existence of the second stability region. The quasimode prescription is not used in the analysis. Instead, a simpler model known as the "disconnected approximation"[30] is used. This model assumes that the eigenfunction is independent of the global magnetic field shear and that the interval of integration is one poloidal period. The perturbation peaks at the outboard side of the plasma and is assumed to be zero on the inboard side, thereby displaying the ballooning character of the mode. Fortunately, these assumptions themselves do not artificially produce the enhanced stability that leads to the formation of the second region, however, the stability boundaries obtained are not quantitatively accurate.

Work of the early 1980's emphasized the effects of tokamak parameters, plasma boundary shape, and plasma profiles on stability. Second region stability was somewhat neglected in the mid 1980's due to the emphasis of the scaling of an instability induced first region β limit. However, methods of direct access to the second region still provided interesting second region research. A particularly important reference on the effects of A on ballooning stability by Monticello, et al.[31] is the first to mention the destabilizing effect of small A on the ballooning mode for flux conserving equilibria. This is a key point of the present work, addressed in Section 3.1.6.1 and is caused by the destabilizing normal curvature term produced by the *poloidal* field. This characteristic has been neglected in almost all prior and subsequent second region studies. The work of Strauss, et al.[32] examined the stability of both large and small-n ballooning modes in high β equilibria. The results showed that a second stable region exists for these modes, and that magnetic field shear can be stabilizing. The work of Greene and Chance[33] is perhaps the most cited reference with regard to the physical effects of the onset of second stability. Accurate, two-dimensional numerical equilibria

are used in this study, providing a quantitatively precise evaluation of the marginal stability boundary. The effect of finite radial wavenumber in the ballooning equation is also discussed, and its choice is found to greatly affect the marginal second stability region boundary. This result is contrary to what is found in the present study, and this discrepancy will be examined in detail in Section 3.1.4.3. As did Coppi, the work of Greene and Chance emphasizes the importance of reducing the connection length in establishing a second region equilibrium. However, the additional physical process of the reversal of the local shear and its effect on the stability of the ballooning mode is introduced and examined. In particular, it is found that as the pressure gradient is increased in the equilibrium, the local value of the magnetic field shear will reverse and exhibit a zero point somewhere in the unfavorable curvature region. This effect leads to ballooning mode instability. However, as the pressure gradient is increased further, the zero point in the local shear migrates into the favorable curvature region. On flux surfaces where this occurs, the ballooning mode restabilizes in the second stability region. This criterion has been used as a simple benchmark for determining whether or not an equilibrium is second region stable.

The work of Sugiyama and Mark[34] (1981) bears the closest resemblance of all prior work to the work of the present study. The ballooning mode stability of equilibria with various q profiles and A was numerically evaluated for a limited set of equilibria, and while the stability is not performed self-consistently, the general results agree with those found in the present work. Increased q is generally seen to increase the plasma stability in the second region. Also shown is the stabilizing effect of the geometric magnetic well at small A and $q_0 > 1$ that is mentioned specifically in the abstract. However, while not mentioned in the abstract, the paper briefly mentions that the small A, $q_0 \sim 1$ configuration is less stable than the larger A case. Besides the work of Monticello mentioned earlier, and the circular results obtained in the numerical studies

of the bean shape by Grimm, et al. discussed later, this is the only reference found that mentions the effect. This will be investigated in detail in the present study.

Analytic work on computing the ballooning mode stability boundaries at small global shear was extended in 1982.[35,36] The work of Mikhailovskii, et al. in particular included a stability criteria computed for finite A, $\beta \sim O(\varepsilon^2)$, circular boundary plasma, and pressure gradients terms retained to fourth order. The result, a necessary condition for stability, repeated here for convenience is

$$\frac{S^2}{2} + \alpha\varepsilon\left(1 - \frac{1}{q^2}\right) - \frac{1}{2}S\alpha^2 + \frac{13}{128}\alpha^4 > 0. \qquad (3.0.1 - 1)$$

The zeroth order term in α represents the stabilizing effect of the magnetic field shear. The linear term in α is the stabilizing effect of the geometric magnetic well. The quadratic term is a destabilizing term due to the coupling of S and α. The new term is the stabilizing fourth order pressure gradient term that produces the second stability region in this model. Therefore, both the second stable region and a method for direct access to it are incorporated in the model.

The global stability of a relaxed second region equilibrium state was examined by Coppi, Crew, and Ramos[37] (1983). One conclusion, although not verified by later numerical work, is the existence of a "second stability" region for the internal kink modes. More important is the consideration of the large-n stability across the entire plasma. The result is illustrated as a diagram, reprinted below for convenience.

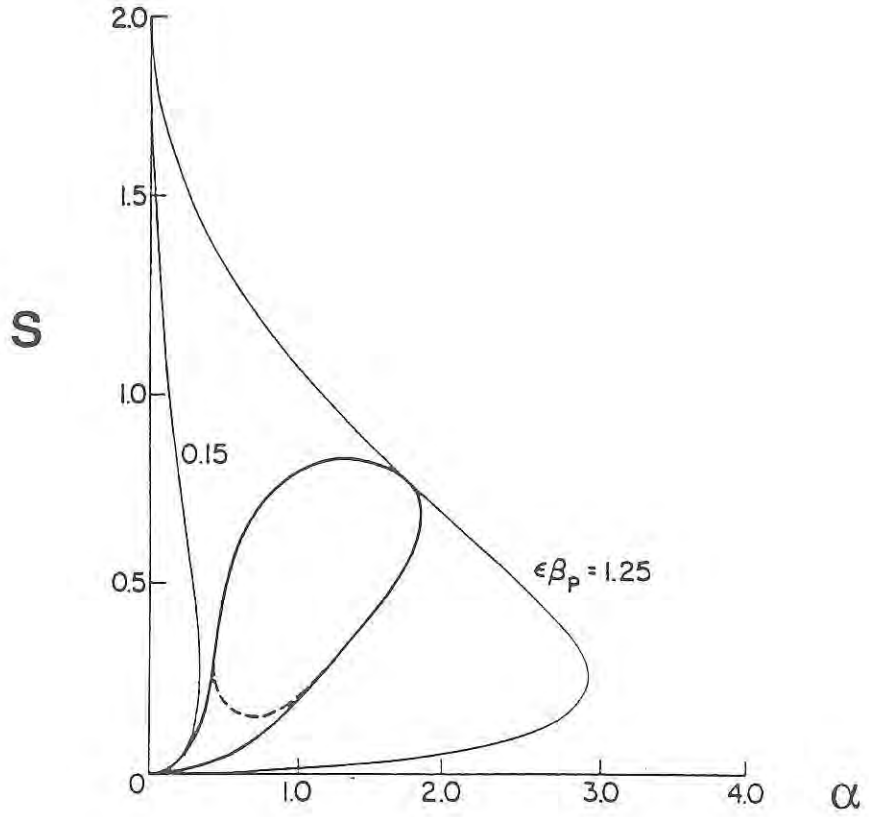

Fig. 3.0.1-1: Stability diagram of Coppi, Crew, and Ramos for the large-n ballooning mode. *The heavy solid line encloses the unstable region obtained for the shifted circular, large A equilibrium model. The light solid lines represent the corresponding marginal equilibria with regard to global stability. The heavy dashed line indicates the effect of increasing q in a finite A configuration.*

Although named a "local" stability diagram, this figure is different than the local "(S,α)" stability diagram of CHT. The key difference is that the standard (S,α) diagram pertains to a specific flux surface, and will vary over the plasma minor radius in a two-dimensional equilibrium. In particular, the plasma stability can improve as S becomes larger, so that no unstable region is detected at all. This is clearly illustrated in Fig. 3.0.1-1 that shows the equilibrium trajectories of both a first and second region equilibrium with zero edge pressure gradients. Therefore, while the standard (S,α) diagram is useful in determining the stability properties of a particular flux surface (local), a diagram similar to Fig 3.0.1 - 1 is useful in determining the stability

properties across the plasma minor radius (global). While the unstable region shown in Fig. 3.0.1-1 will generally differ for self-consistently calculated, two-dimensional equilibria of different β_p, it schematically represents an important diagnostic diagram for global ballooning mode stability. These diagrams will be used throughout the present analysis and will be considered in more detail in Section 3.1.5. In addition to the global examination of the plasma equilibrium, the ability of crossing from the first to the second stability region is mentioned. The point is made that a flux conserving equilibrium with $q_0 > 1.5$ might access the second region without suffering an instability throughout the heating process. This idea follows the pioneering work of Sykes mentioned earlier in increasing the plasma stability by raising q_0. Therefore, this work changed the emphasis of second region research from proving its theoretical existence to showing how it could be accessed in an experimental device.

As with the work of Sykes on the enhanced stability of the $q_0 > 1$ configuration, the pioneering work of Mercier on the enhanced stability of bean shaped plasmas was expanded by the work of Chance, Jardin, and Stix,[38] who showed that a bean shaped plasma of sufficient indentation also has direct access to the second region. Reference to the work of Mercier is made, as well as a numerical shape optimization study of Miller and Moore.[39] The significant stabilizing effects of the bean shape are the externally induced axis shift produced by the indentation and the inherent shortening of the connection length. It is also shown that the bean shape allows the zero point of the local shear to more readily migrate into the favorable curvature region. In particular, the local shear null can appear in the favorable curvature region at low β, before an instability can onset, thereby allowing direct access to the second region on all flux surfaces. The theory was convincing enough to persuade the Department of Energy to support the design and construction of a bean shaped experiment whose goal was to access the second region (PBX).[40] This device, and its successor, PBX-M, have had

limited success and have not yet documented a second region plasma equilibrium. The β limiting mechanism seems to be the kink instability and the vertical instability. Present work is concentrating on methods to further suppress the kink mode with PBX-M's conducting shell, plasma profile modification, and feedback stabilization.

The subsequent numerical stability study of bean shaped tokamaks by Grimm, et al.[41] (1985) provides a detailed analysis of the effects of A, q, and boundary shape variations on the MHD stability of these equilibria. Although the bean shape is not investigated in the present work, the analogous results of the bean shaped study agree with those of the present study. Of particular interest is the increased value of β needed to reach the second region for small A, $q_0 \sim 1$ equilibria. This result is verified in the present work.

The advent of the tokamak β limit of Sykes,[42] and Troyon,[43] discussed briefly in the Introduction led to a large amount of research on the subject of first stable region β limits including methods of increasing β_1 in tokamaks.[44-48] While this work somewhat overshadowed second stability research, some work of the mid 1980's is notable. First, Choe and Freidberg[49] examined the large-n mode stability of the shifted circular, large A, model of equilibrium (Clarke and Sigmar, 1977; Coppi, Crew, and Ramos, 1983) and clearly showed that the effects of flux surface shift without finite ε effects could produce a direct access path to the second region. Also, a generalization of the CHT (S,α) model of stability was used by Bishop[50] to attempt to confirm the proposal that the H-mode of plasma confinement[51-54] could actually be caused by a local access to the second region on the outer plasma flux surfaces. This claim has since received great criticism from experimental evidence that shows H-mode plasmas having edge pressure gradients of first rather than second region magnitudes.[55] While the model used is simple, and does not prove second stability as the cause of the H-mode,

it does illustrate that divertor plasmas may be additional candidates for enhanced ballooning stability and facilitate local direct access to the second region. Recent work by Peng, et al.[56] has investigated more sophisticated models of computing the ballooning stability near a separatrix.

Access to second stability was studied in two papers presented at the 1986 IAEA meeting (Proc. 11th Int. Conf. Kyoto).[57,58] The work of Todd et al. demonstrated a stable trajectory of two-dimensional, numerically generated equilibria with elevated values of q_0 to the second region for ideal MHD modes. External kink modes are stabilized by a conducting shell surrounding the plasma surface. It is also shown that as the plasma enters the second stability region to large-n ballooning modes, the conducting wall may be positioned further away from the plasma surface, illustrating the stabilization of the pressure driven component of the high β kink mode suggested by Coppi, Crew, and Ramos (1983). However, a second stability region to the kink mode is not found without a sufficiently close fitting conducting wall. In addition, small-n internal modes in regions of small shear, more colloquially known as "infernal" modes,[59] are described as being an additional deterrent to second region access since they can be unstable when large-n modes are stable, contrary to the prediction of CHT that large-n modes are the least stable. The work of Yamazaki, et al., discusses the stability of conventional cross-section shapes at elevated q_0 and introduces the "crescent" shape as a candidate for improved ballooning stability

Contemporary research on the second stability region (late 1980's) focussed on accessing the second stable region in experimental devices and improving models that determine the scaling of the second region boundary. While all previous studies on direct access to the second region used plasma pressure and q profiles that were prescribed generically, the independent work of several groups[60-63] considered the

dynamic transition to the second stability region using transport generated profiles that were affected by the plasma stability to define the equilibria. The work of Capes, et al. (1987) used a one-dimensional transport code to generate the profiles for circular boundary equilibria, and a prescribed large-n unstable region is used to provide an obstacle to attaining second stability. By increasing the transport coefficients by a factor of 50 in the unstable region, the initial ohmic first region profiles were limited to the first region during the heating phase unless the global shear was sufficiently small, and the prescribed unstable region was avoided entirely. The analytical and numerical study of Fu, et al. (1987) also used a prescribed unstable region and found that a successful transition could be achieved with the pressure profile crossing the unstable region at sufficiently large auxiliary power. The auxiliary power required to reach the second region is calculated, and is found to scale as the square root of the diffusion enhancement experienced in the unstable region. The work of Sabbagh, et al., (1989) originally performed for a study of transition to the second stability region at large A, (Bhattacharjee, et al., (1987)) is contained in the present work. The results are obtained using a $1^1/_2$ dimensional transport code coupled to a large-n ballooning equation solver to examine the transition to the second region. A significant difference compared to the previous studies is the inclusion of a computed unstable region that changes size during the plasma heating. Transition to the second region is obtained by co-injected neutral beam heating that drives current on the outer flux surfaces. This in turn raises q_0, that reduces the extent of the unstable region, allowing transition to the second region. An additional study of the small-n kink/ballooning mode is performed and the result shows that the kink mode is unstable during the transition and that a conducting wall is needed to stabilize the mode in the second stability region.

Seki, et al.[64] considered the establishment of the core of the plasma reaching the second region to attain high β while the edge pressure gradients remained limited by the

first region boundary. The work of Chance[65] reviewed previous access methods to reach the second region and showed a three-dimensional diagram describing the plasma stability. Alternative techniques of accessing the second region by improved stabilization methods were independently explored. Stabilization of the large-n modes by a population of hot particles,[66,67] induced rotation,[68] and RF ponderomotive stabilization[69] were examined.

Recent studies of the effects of plasma parameters include the work of Llobet et al.[70] and Liu Chen, et al.[71] that independently extended the work of Lortz and Nuhrenberg (1979) by deriving the scaling of the second region stability boundary pressure gradient at large global shear for the CHT (S,α) model of stability. The result of the work shows that α scales as $S^{1.25}$ for the second region boundary for infinite A, low β, equilibria. The work of Mauel[72] examined the stability of infinite A, elongated equilibria of arbitrary axis shift. The result of the study was that elongation alone destabilizes the second region boundary. This result is verified in the present work. The stabilizing effects of low A and high q (geometric magnetic well) are examined in the work of Gerver, et al.[73] The analytic work describing the stabilizing effects are somewhat misleading, since destabilizing terms at low A and $q_0 \sim 1$ are not examined, nor are they seen numerically. They are not shown analytically since the models used order the Shafranov shift as $O(\varepsilon)$, and terms of $O(\varepsilon^2)$ are dropped. Therefore, the destabilizing terms that appear in the lowest order as a product of the shift and the inverse aspect ratio are neglected. This effect is not omitted in the present work, and is discussed in more detail in Chapter 3.1.

A summary of the global β parameter results defining the second region threshold for circular boundary equilibria, contained in the present work, along with a summary of the second region access work of Fu et al. (1987), and Sabbagh, et al.

(1989) was published in the Proceedings of the 12th IAEA meeting (1988 Nice, France).[74] The novel feature of the modelling used to parameterize the second region boundary is that the equilibria are self-consistent and marginally stable at the second region boundary. Also, no physical effects are ordered out of the model. Therefore, the stabilization and destabilization of the ballooning mode at low A is included. The results include a model scaling of the second region boundary value of $\varepsilon\beta_p$, and a comparison of the marginal second region β threshold to the Troyon-Sykes scaling of the first region boundary. For equilibria with $q_0 \sim 1$, the values are shown to follow the scaling with $C_t \sim 17$. The first effort of a large experimental tokamak other than PBX to achieve high β_p plasmas was also presented at the Nice meeting by Simonen, et al.[75] working on the DIII-D tokamak. The experiment was a successful attempt to drive current in DIII-D by neutral beam current drive alone. In so doing, high $\varepsilon\beta_p \sim 1.5$ equilibria with $\beta << \beta_1$ were achieved that may have been near the first and second region coalescence point if the value of q_0, determined by numerical modelling of the equilibria, was about 3.

Interest in the high β_p results of DIII-D and a decrease in research on the first region β limit due to the success and acceptance of the Troyon-Sykes scaling, spurred on second region research. Phillips, Hughes, Todd, et al. have recently examined routes to second stability in TFTR and PBX-M[76] and the relevance of the current profile shape on second region access.[77] An important result of the latter analysis is the re-emphasis of the reduction of the global shear as a method of successfully attaining second region access instead of the more commonly used parameter, q_0, that is not necessarily a good measure of the type of profile required for second region access. Chance and McGuire[78] have also recently re-evaluated second region access by current profile broadening in TFTR. More than five papers presented at the 1989 meeting of the American Physical Society Division of Plasma Physics involved access to the second

stability region. In addition, the first high $\varepsilon\beta_p$ experiments on TFTR designed by a Columbia-Princeton collaboration were presented at this meeting. The preliminary results showed that the previous $\varepsilon\beta_p \sim 0.7$ limit observed in TFTR was exceeded and equilibria with $\varepsilon\beta_p = 1.3$ were established. Preliminary stability analysis of these equilibria shows that β must be raised in these plasmas to place them in the second stable region on all flux surfaces. However, the edge of these plasmas display a direct access window to the second region and some flux surfaces may be slightly into the second stable region. Future experiments hope to achieve high $\varepsilon\beta_p$ plasmas with improved confinement, by either establishing the enhanced confinement or "supershot" regime, operating at higher plasma current, or possibly discovering an enhanced confinement regime in the second stability region.[62,79]

---

[1]Suydam, B.R., In *Proceedings of the Second United Nations International Conference on the Peaceful Uses of Atomic Energy*, United Nations, Geneva **31** (1958) 157.

[2]Mercier, C., Nucl. Fusion **1** (1960) 47.

[3]Greene, J.M., and Johnson, J.L., Plasma Physics **10** (1968) 729.

[4]Kadomtsev, B.B., and Pogutse, O.P., Sov. Phys.-Doklady **11** (1967) 858.

[5]Shafranov, V.D., and Yurchenko, E. I., Sov. Phys.-JETP **26** (1968) 682.

[6]Mikhailovskii, A.B., and Shafranov, V.D., Sov. Phys.-JETP **36** (1974) 88.

[7]Mikhailovskii, A.B., Nucl. Fusion **14** (1974) 483.

[8]Furth, H., Killeen, J., Rosenbluth, M., Coppi, B., 2nd Conference on Plasma Physics, Paper CN21/106, Culham (1965).

[9]Kulsrud, R., 2nd Conference on Plasma Physics, Paper CN21/113, Culham (1965); *Dynamics of Fluids and Plasmas* (S.I. Pai, Ed.) Academic Press (1966) 333.

[10]Grimm, R.C., Greene, J.M., and Johnson, J.L., Meth. Comp. Phys. **16** (1976) 253.

[11]Dobrott, D., Nelson, D.B., Greene, J.M., Glasser, A.H., Chance, M.S., Frieman, E.A., Phys. Rev. Lett. **39** (1977) 943.

[12]Glasser, A.H., in Proceedings of the Finite Beta Theory Workshop, Varenna, edited by B. Coppi and W.L. Sadowski (US DOE, Washington, D.C., 1977), CONF-7709167 (1977) 55.

[13]Connor, J.W., Hastie, R.J., Taylor, J.B., Phys. Rev. Lett. **40** (1978) 396; Proc. R. Soc. (London) A **365** (1979) 1.

[14]Todd, A.M.M., Chance, M.S., Greene, J.M., Grimm, R.C., Johnson, J.L., Manickam, J., Phys. Rev. Lett. **38** (1977) 826.

[15]Bateman, G., and Peng, Y. -K. M. Phys. Rev Lett. **38** (1977) 829.

[16]Clarke, J.F., and Sigmar, D.J., Phys. Rev. Lett. **38** (1977) 70.

[17]Fielding, P.J., and Haas, F.A., Phys. Rev. Lett. **41** (1978) 801.

[18]Pogutse, O.P., and Yurchenko, E.I., JETP Lett. **28** (1978) 318.

[19]Lortz, D. and Nuhrenberg, J., Physics Lett. **68** (1978) 49.

[20]Sykes, A., Turner, M.F., Fielding, P.J., Haas, F.A., in *Plasma Physics and Controlled Nuclear Fusion Research* (Proc. 7th Int. Conf. Innsbruck, 1978) Vol. 1, IAEA, Vienna (1979) 625.

[21]Zakharov, L.E., in *Plasma Physics and Controlled Nuclear Fusion Research* (Proc. 7th Int. Conf. Innsbruck, 1978) Vol. 1, IAEA, Vienna (1979) 683.

[22]Mercier, C., in *Plasma Physics and Controlled Nuclear Fusion Research* (Proc. 7th Int. Conf. Innsbruck, 1978) Vol. 1, IAEA, Vienna (1979) 701.

[23]Coppi, B., Filreis, J., Mark, J.W.-K., in *Plasma Physics and Controlled Nuclear Fusion Research* (Proc. 7th Int. Conf. Innsbruck, 1978) Vol. 1, IAEA, Vienna (1979) 793.

[24]Sykes, A., Turner, M.F., in *Controlled Fusion and Plasma Physics* (Proc. 9th Europ. Conf., Oxford, 1979), UKAEA, Culham Lab., Abingdon (1979) 161.

[25]Lortz, D., and Nuhrenberg, J., Nuclear Fusion **19** (1979) 1207.

[26]Pogutse, O.P., Chudin, N.V., and Yurchenko, E.I., Sov. J. Plasma Phys. **6** (1980) 341.

[27]Coppi, B., Ferreira, A., Mark, J.W.-K., and Ramos, J.J., Nuclear Fusion **19** (1979) 715.

[28]Coppi, B., Ferreira, A., Mark, J.W.-K., and Ramos, J.J., Comments Plasma Phys. **5** (1979) 1.

[29]Coppi, B., Ferreira, A., and Ramos, J.J., Phys. Rev. Lett. **44** (1980) 990.

[30]Coppi, B., Phys. Rev. Lett., **39** (1977) 939.

[31]Monticello, D.,A., Park, W., Jardin, S., Chance, M.S., et al., in *Plasma Physics and Controlled Nuclear Fusion Research* (Proc. 8th Int. Conf. Brussels, 1980) IAEA, Vienna **1** (1981) 227.

[32]Strauss, H.R., Park, W., Monticello, D.A., White, R.B., Jardin, S.C., Chance, M.S., Todd, A.M.M., Glasser, A.H., Nuclear Fusion **20** (1980) 638.

[33]Greene, J.M., Chance, M.S., Nuclear Fusion **21** (1981) 453.

[34]Sugiyama, L., and Mark, J.W.-K., Phys. Lett. **84A** (1981) 123.

[35]Antonsen, T.M., Ferreira, A., and Ramos, J.J., Plasma Physics **24** (1982) 197.

[36]Mikhailovskii, A.B., and Yurchenko, E.I., Plasma Physics **24** (1982) 997.

[37]Coppi, B., Crew, G.B., and Ramos, J.J., Comments Plasma Phys. Controlled Fusion **8** (1983) 11.

[38]Chance, M.S., Jardin, S.C., Stix, T.H., Phys. Rev. Lett. **51** (1983) 1963.

[39]Miller, R., and Moore, R.W., Phys. Rev. Lett. **43** (1979) 765.

[40]Bol, K., et al., Phys Rev. Lett. **57** (1986) 1891.

[41]Grimm, R.C., Chance, M.S., Todd, A.M.M., et al., Nuclear Fusion **7** (1985) 805.

[42]Sykes, A., Turner, M.F., Patel, S., in *Proceedings of the 11th European Conference on Controlled Fusion and Plasma Physics*, Aachen, (European Physics Society, Geneva, Switzerland, 1982) **7d** (1983) 363.

[43]Troyon, F., Gruber, R., Saurenmann, H., Semenzato, S., and Succi, S., Plasma Phys. and Cont. Fusion **26 1A** (1984) 209; Phys. Lett. **110A** (1985) 29.

[44]Wesson, J.A., Sykes, A., Nuclear Fusion **25** (1985) 85.

[45]Yamazaki, K., Amano, T., Naitou, H., Hamada, Y., Azumi, M., Nuclear Fusion **25** (1985) 1543.

[46]Degtyarev, L.M., Drozdov, V.V., Martynov, A.A., Medvedev, S. Yu., Sov. J. Plasma Phys. **11** (1985) 743.

[47]Bespoludennov, S.G., Degtyarev, L.M., Medvedev, S. Yu., Sov. J. Plasma Phys. **21** (1986) 441.

[48]Carreras, B.A., Charlton, L.A., Hogan, J.T., Holmes, J.A., Lazarus, E.A., Cooper, W.A., Hender, T.C., in *Plasma Physics and Controlled Nuclear Fusion Research* (Proc. 11th Int. Conf. Kyoto, 1986) Vol. 2, IAEA, Vienna (1986) 53.

[49]Choe, W.H., and Friedberg, J.P., Phys. Fluids **29** (1986) 1766.

[50]Bishop, C.M., Nuclear Fusion **8** (1986) 1063.

[51]Wagner, F., Becker, G., Behringer, K., et al., Phys Rev. Lett. **49** (1982) 1408.

[52]Ohyabu, N., Stambaugh, R.D., DeBoo, J.C., et al., in *Plasma Science* (Proc. IEEE Int. Conf. San Diego, CA. 1983), IEEE, New York, (1983) 52.

[53]Nagami, M., Kasai, M., Aikawa, H., et al., in *Controlled Fusion and Plasma Physics* (Proc. 11th Europ. Conf. Aachen, 1983). Part I, ECA, Linnich (1983) 115.

[54]Kaye, S.M., Bell, M.G., Bol, K., et al., J. Nucl. Mater. **121** (1984) 115.

[55]Carlstrom, T.N., Ohyabu, N, Burrell, K.H., et al., *Bull. Am. Phys. Soc.* **33** (1988) 1964.

[56]Peng, Y - K. M., Whitson, J.C., *Bull. Am. Phys. Soc.* **34** (1989) 1971.

[57]Todd, A.M.M., Phillips, M.W., Chance, M.S., Manickam, J., and Pomphrey, N., in *Plasma Physics and Controlled Nuclear Fusion Research* (Proc. 11th Int. Conf. Kyoto, 1986) Vol. 2, IAEA, Vienna (1986) 37.

[58]Yamazaki, K., Naitou, H., Amano, T., et al., in *Plasma Physics and Controlled Nuclear Fusion Research* (Proc. 11th Int. Conf. Kyoto, 1986) Vol. 2, IAEA, Vienna (1986) 27.

[59]Manickam, J., Pomphrey, N., and Todd, A.M.M., Nuclear Fusion **27** (1987) 1461.

[60]Capes, H., Mercier, C., Morera, J.P., Nuclear Fusion, **27** (1987) 149.

[61]Fu, G.Y., Van Dam, J.W., Rosenbluth, M.N., in *Theory of Fusion Plasmas* (Proceedings of the Varenna Workshop, Varenna, Italy, 1987) Vol. 1, Editrice Compositori, Bologna (1987) 153.

[62]Bhattacharjee, A., Iacono, R., Marshall, T.C., Mauel, M.E., Navratil, G.A., Paranicas, C., Sabbagh, S.A., Sen, A.K., Van Dam, J.W., Wang, X.-H., Hughes, M.H., Phillips, M.W., Todd, A.M.M., "Second Regime Tokamak Operation at Large Aspect Ratio", Columbia University report #109, June 1987.

[63]Sabbagh, S.A., Hughes, M.H., Phillips, M.W., Todd. A.M.M., Navratil, G.A., Nuclear Fusion **29** (1989) 423.

[64]Seki, S., Tsunematsu, T., Azumi, M., Nemoto, T., Nuclear Fusion **27** (1987) 330.

[65]Chance, M.S., in *Theory of Fusion Plasmas* (Proceedings of the Varenna Workshop, Varenna, Italy, 1987) Vol. 1, Editrice Compositori, Bologna (1987) 87.

[66]Miller, R.L., and Van Dam, J.W., Nuclear Fusion **27** (1987) 2101.

[67]Wang, X-H., Bhattacharjee, A., and Van Dam, J.W., Phys. Fluids **31** (1988) 332.

[68]Navratil, G.A. and Marshall, T.C., Comments Plasma Phys. Controlled Fusion **10** (1986) 185.

[69]D'Ippolito, D.A., Myra, J.R., and Francis, G.L., Phys. Rev. Lett. **58** (1987) 2216.

[70]Llobet, X., Berk, H.L., Rosenbluth, M.N., Phys. Fluids **30** (1987) 2750.

[71]Chen, Liu, Bondeson, A., Chance, M.S., Nuclear Fusion 27 (1987) 1918.

[72]Mauel, M., Phys. Fluids **30** (1987) 3843.

[73]Gerver, M.J., Kesner, J., Ramos, J.J., Phys. Fluids **31** (1988) 2674.

[74]Sabbagh, S.A., Mauel, M.E., Navratil, G.A., Hughes, M.H., Phillips, M.W., Todd, A.M.M., Fu, G.Y., Van Dam, J.W., and Rosenbluth, M.N.,in *Plasma Physics and Controlled Nuclear Fusion Research* (Proc. 12th Int. Conf. Nice, 1988) Vol. 2, IAEA, Vienna (1989) 319.

[75]Simonen, T.S., Matusoka, M., Bhadra, D.K., Chance, M.S., et al. in *Plasma Physics and Controlled Nuclear Fusion Research* (Proc. 12th Int. Conf. Nice, 1988) paper CN-50/E-3-6; Phys. Rev. Lett. **61** (1988) 1720.

[76]Phillips, M.W., Hughes, M.H., Todd, A.M.M, Sherwood Theory meeting (April 3-5, 1989) San Antonio, Texas, paper 3C-2.

[77]Phillips, M.W., Hughes, M.H., Todd, A.M.M, et al., submitted to Phys. Fluids.

[78]Chance, M.S., and McGuire, K.M., European Physical Society meeting, Venice, 1989.

[79]Kesner, J., Nuclear Fusion **29** (1989) 1397.

3.0.2 Modes of Interest

As stated previously, the second region is a characteristic of short $\perp$ wavelength ballooning modes. Therefore, the primary study of the identification of the second region involves the evaluation of the stability boundaries with respect to these modes. There are, of course, other instabilities in tokamaks that may prevent the experimental achievement of second stability to short $\perp$ wavelength modes, and are of interest to the present study. The other modes that are the most dangerous to the goal of reaching second stability in a tokamak are the comparably long $\perp$ wavelength ideal kink/ballooning modes. These instabilities are thought to set the experimentally observed β limits in tokamaks.[1] The stability of these modes will be considered when examining the transition of first region equilibria to the second stable region of short $\perp$ wavelength modes in Chapter 3.2.

While both long $\perp$ wavelength kink/ballooning and short $\perp$ wavelength ballooning instabilities are thought to be the primary causes of β limits in tokamaks, the processes by which β is limited are different for these modes. The short $\perp$ wavelength modes are more localized and are therefore thought to limit β by enhancing plasma transport when unstable. This would lead to a limit of the maximum $|p'(\psi)|$ that could be attained, and therefore, β. However, the global characteristic of the plasma may not be disruptive. This theory of enhanced transport is used in the present study, and may lead to a "soft" β limit in experimental devices. Contrarily, the long $\perp$ wavelength instabilities are global in character, and limit β by terminating the plasma discharge by a disruption once the mode is driven unstable. Therefore, while kink/ballooning modes, and the corresponding β limits have been observed in large tokamaks,[2,3] limits due to the short wavelength modes have not been "observed" in large machines, perhaps since the former are easier to detect. However, if second region equilibria at low current

exhibited improved transport properties by reducing the fluctuation amplitude of microinstabilities,[4] or by forming a reduced transport configuration such as the H-mode,[5] the soft β limit imposed by short $\perp$ wavelength modes may be more prominent, and methods of avoiding it would be of great experimental importance.

A useful way of examining the physical causes of ideal MHD instabilities is to consider the "intuitive" form of δW.[6,7] This can be derived from Eq. (2.0.1.2 - 11) with a few vector decompositions and identities. The steps used in the derivation are shown below. A similar derivation and additional detail related to the boundary terms of δW can be found in Greene and Johnson (1969), and Freidberg.[8] Consider δW given by (2.0.1.2 - 11),

$$\delta W(\xi^*,\xi) = -\frac{1}{2}\int \xi^* \cdot \frac{1}{\mu_0}\left[(\nabla \times \mathbf{B}_0) \times \mathbf{Q} + (\nabla \times \mathbf{Q}) \times \mathbf{B}_0\right] +)$$

$$+ \xi^* \cdot \left[\nabla(\xi \cdot \nabla p_0 + \gamma p_0 \nabla \cdot \xi)\right] dx. \qquad (3.0.2 - 1)$$

This functional is appropriate for the entire plasma-vacuum system. To examine the physical effects of the plasma in creating ideal MHD waves, it is convenient to decompose δW into bulk plasma and surface components. This is performed by converting gradient terms into divergences and using the divergence theorem. Consider the second and fourth terms. A divergence is created in the second term as

$$\frac{1}{\mu_0}\xi^* \cdot (\nabla \times \mathbf{Q}) \times \mathbf{B}_0 = -(\xi^* \times \mathbf{B}_0) \cdot (\nabla \times \mathbf{Q})$$

$$= \nabla \cdot ((\xi^* \times \mathbf{B}_0) \times \mathbf{Q}) + |Q|^2, \qquad (3.0.2 - 2)$$

and similarly for the fourth term,

$$\xi^* \bullet \nabla(\gamma p_0 \nabla \bullet \xi) = \nabla \bullet ((\gamma p_0 \nabla \bullet \xi)\xi^*) - \gamma p_0 |\nabla \bullet \xi|^2 . \qquad (3.0.2 - 3)$$

After converting the volume integrated divergence terms to surface integrals, the result is

$$\delta W = \frac{1}{2} \int \left\{ \frac{|\mathbf{Q}|^2}{\mu_0} + \gamma p_0 |\nabla \bullet \xi|^2 - \xi^* \bullet \left[\frac{\nabla \times \mathbf{B}_0}{\mu_0} \times \mathbf{Q} + \nabla(\xi \bullet \nabla p_0) \right] \right\} d\mathbf{x}$$

$$- \frac{1}{2} \int \xi^* \left(\gamma p_0 \nabla \bullet \xi - \frac{\mathbf{Q} \bullet \mathbf{B}_0}{\mu_0} \right) \bullet d\mathbf{S} . \qquad (3.0.2 - 4)$$

The third term has no component parallel to **B** and can be rewritten. Decomposing the displacement as $\xi = \xi_\perp + \xi_\parallel$, and recognizing $\mathbf{J}_0$ in the third term,

$$- \left(\xi_\perp^* + \xi_\parallel^* \right) \bullet \left[\mathbf{J}_0 \times \mathbf{Q} + \nabla(\xi \bullet \nabla p_0) \right] , \qquad (3.0.2 - 5)$$

the $\xi_\parallel^*$ term vanishes. This can be seen by considering $\xi_\parallel = \xi_\parallel \mathbf{B}_0/|\mathbf{B}_0| \equiv \xi_\parallel \hat{\mathbf{b}}_0$ and evaluating the term,

$$- \xi_\parallel^* \bullet \left[\mathbf{J}_0 \times \mathbf{Q} + \nabla(\xi \bullet \nabla p_0) \right] =$$

$$\frac{\xi_\parallel^*}{|\mathbf{B}_0|} \left[\mathbf{Q} \bullet \mathbf{J}_0 \times \mathbf{B}_0 - \nabla \bullet \left[(\xi \bullet \nabla p_0)\mathbf{B}_0 \right] \right] . \qquad (3.0.2 - 6)$$

Including the ideal MHD equilibrium relation (2.0.1.1 - 1), the definition of **Q** (2.0.1.2 - 5), and some vector identities,

$$\frac{\xi_\parallel^*}{|\mathbf{B}_0|} \left[\left[\nabla \times (\xi \times \mathbf{B}_0) \right] \bullet \nabla p_0 - \nabla \bullet \left[(\xi \bullet \nabla p_0)\mathbf{B}_0 \right] \right] =$$

$$\frac{\xi_\parallel^*}{|\mathbf{B}_0|} \left[\nabla \bullet \left[(\xi \bullet \nabla p_0)\mathbf{B}_0 \right] - \nabla \bullet \left[(\xi \bullet \nabla p_0)\mathbf{B}_0 \right] \right] = 0 . \qquad (3.0.2 - 7)$$

From the remaining $\xi_\perp^*$ projection, the gradient term can be converted to a divergence,

$$- \xi_\perp^* \bullet \nabla(\xi \bullet \nabla p_0) = (\xi \bullet \nabla p_0)\, \nabla \bullet \xi_\perp^* - \nabla \bullet ((\xi \bullet \nabla p_0)\xi_\perp^*) \qquad (3.0.2 - 8)$$

and therefore,

$$\delta W = \frac{1}{2} \int \left(\frac{|Q|^2}{\mu_0} + \gamma p_0 |\nabla \bullet \xi|^2 - \xi_\perp^* \bullet \mathbf{J}_0 \times \mathbf{Q} + (\xi \bullet \nabla p_0)\, \nabla \bullet \xi_\perp^* \right) dx$$

$$+ \frac{1}{2} \int \xi_\perp^* \left(\frac{\mathbf{Q} \bullet \mathbf{B}_0}{\mu_0} - \gamma p_0 \nabla \bullet \xi - (\xi \bullet \nabla p_0) \right) \bullet dS \,. \qquad (3.0.2 - 9)$$

The volume integral in this form of δW is the standard form of the plasma fluid potential energy. The remaining terms are the contribution of the surface and vacuum components of the potential energy. The form of δW given by (3.0.2 - 9) is converted to the form of Greene and Johnson by decomposing $\mathbf{Q}$ and $\mathbf{J}_0$ into perpendicular and parallel components,

$$|Q|^2 = |Q_\perp|^2 + |Q_\parallel|^2 \,, \text{ and}$$

$$\begin{aligned} \xi_\perp^* \bullet \mathbf{J}_0 \times \mathbf{Q} &= \xi_\perp^* \bullet (\mathbf{J}_{0\parallel} \times \mathbf{Q}_\perp + \mathbf{J}_{0\perp} \times \mathbf{Q}_\parallel) \\ &= \mathbf{J}_{0\parallel} (\xi_\perp^* \times \hat{\mathbf{b}}_0) \bullet \mathbf{Q}_\perp + \mathbf{Q}_\parallel \xi_\perp^* \bullet (\mathbf{J}_{0\parallel} \times \hat{\mathbf{b}}_0) \,. \end{aligned} \qquad (3.0.2 - 10)$$

Both $\mathbf{J}_{0\perp}$ and $\mathbf{Q}_\parallel$ can be rewritten. By using (2.0.1.1 - 1),

$$\frac{\mathbf{B}_0 \times \nabla p_0}{|\mathbf{B}_0|^2} = \mathbf{J}_0 - \hat{\mathbf{b}}_0 (\mathbf{J}_0 \bullet \hat{\mathbf{b}}_0) = \mathbf{J}_{0\perp} \,, \qquad (3.0.2 - 11)$$

and

$$\begin{aligned} |\mathbf{B}_0|\, Q_{\parallel} &= \mathbf{B}_0 \bullet \nabla \times (\xi \times \mathbf{B}_0) \\ &= \nabla \bullet ((\xi_\perp \times \mathbf{B}_0) \times \mathbf{B}_0) + (\xi_\perp \times \mathbf{B}_0) \bullet \mu_0 \mathbf{J}_0 \\ &= - \nabla \bullet (|\mathbf{B}_0|^2\, \xi_\perp) + \xi_\perp \bullet (\mathbf{B}_0 \times \mu_0 \mathbf{J}_0) \\ &= - |\mathbf{B}_0|^2\, \nabla \bullet \xi_\perp - \xi_\perp \bullet \nabla |\mathbf{B}_0|^2 - \xi_\perp \bullet \mu_0 \nabla p_0 \,. \end{aligned} \qquad (3.0.2 - 12)$$

By rewriting the equilibrium relation as

$$\mu_0 \nabla p_0 = (\mathbf{B}_0 \bullet \nabla)\mathbf{B}_0 - \frac{1}{2} \nabla |\mathbf{B}_0|^2 \,, \qquad (3.0.2 - 13)$$

and eliminating the gradient of the field energy,

$$Q_{\parallel} = - |\mathbf{B}_0|\, \nabla \bullet \xi_\perp + \frac{\xi_\perp}{|\mathbf{B}_0|} \bullet \left[\mu_0 \nabla p_0 - 2(\mathbf{B}_0 \bullet \nabla)\mathbf{B}_0 \right] . \qquad (3.0.2 - 14)$$

Plugging in (3.0.2 - 14) and (3.0.2 - 11) into (3.0.2 - 10) and substituting the results into (3.0.2 - 9), the new form of the plasma fluid potential energy functional is

$$\begin{aligned} \delta W_f = \frac{1}{2} \int & \frac{|\mathbf{Q}_\perp|^2}{\mu_0} + \frac{|\mathbf{B}_0|^2}{\mu_0} \left| \nabla \bullet \xi_\perp + \frac{2\xi_\perp \bullet (\mathbf{B}_0 \bullet \nabla)\mathbf{B}_0}{|\mathbf{B}_0|^2} \right|^2 + \gamma p_0 |\nabla \bullet \xi|^2) \\ & - 2 \left(\frac{\xi_\perp^* \bullet (\mathbf{B}_0 \bullet \nabla)\mathbf{B}_0}{|\mathbf{B}_0|^2} \right) (\xi_\perp \bullet \nabla p_0) - \frac{J_{0\parallel}}{|\mathbf{B}_0|}\, \xi_\perp^* \times \mathbf{B}_0 \bullet \mathbf{Q}\, dx \,. \end{aligned} \qquad (3.0.2 - 15)$$

Now, introduce the curvature vector, $\kappa \equiv (\hat{\mathbf{b}} \bullet \nabla)\, \hat{\mathbf{b}}$, whose magnitude measures the curvature of the field line. In general, this is different than $(\mathbf{B}_0 \bullet \nabla)\mathbf{B}_0/|\mathbf{B}_0|^2$, since the latter measures the field line curvature and field strength variations. The relation between the two is (i.e. Bateman, p.36)

$$(\mathbf{B} \bullet \nabla)\mathbf{B} = |\mathbf{B}|^2 (\hat{\mathbf{b}} \bullet \nabla) \hat{\mathbf{b}} + \frac{1}{2} \hat{\mathbf{b}} \hat{\mathbf{b}} \bullet \nabla |\mathbf{B}|^2 . \qquad (3.0.2 - 16)$$

The perpendicular projections of these two expressions are the same. Note that for any vector, **P** perpendicular to **B**, $\mathbf{P} \bullet 1/2\ \hat{\mathbf{b}} \hat{\mathbf{b}} \bullet \nabla |\mathbf{B}|^2 = 0$, so that the field energy gradient term drops out, therefore,

$$\mathbf{P} \bullet \frac{(\mathbf{B} \bullet \nabla)\mathbf{B}}{|\mathbf{B}|^2} = \mathbf{P} \bullet \kappa . \qquad (3.0.2 - 17)$$

Equation (3.0.2 - 15) can then be written as

$$\delta W_f = \frac{1}{2} \int \frac{|\mathbf{Q}_\perp|^2}{\mu_0} + \frac{|\mathbf{B}_0|^2}{\mu_0} |\nabla \bullet \xi_\perp + 2\xi_\perp \bullet \kappa|^2 + \gamma p_0 |\nabla \bullet \xi|^2$$

$$- 2 (\xi_\perp^* \bullet \kappa)(\xi_\perp \bullet \nabla p_0) - \frac{\mathbf{J}_{0\parallel}}{|\mathbf{B}_0|} \xi_\perp^* \times \mathbf{B}_0 \bullet \mathbf{Q}_\perp \, dx . \qquad (3.0.2 - 18)$$

The potential energy terms for the three basic ideal MHD waves are now readily apparent. The first term involves the magnetic field perturbation perpendicular to **B**, and is therefore responsible for the shear Alfvén wave. The second term involves magnetic field compression, and is therefore responsible for the fast magnetoacoustic wave. The third term involves the compression of plasma, and is therefore responsible for the plasma acoustic wave.

The last two terms of (3.0.2 - 18) are responsible for driving instabilities, since they are the only non-positive definite terms. The first of these terms involves a coupling of the plasma pressure gradient and the magnetic field line curvature. When this term is negative (destabilizing), the local field line configuration is said to have

"bad" or "unfavorable" curvature. When positive, the term is stabilizing, and the configuration is said to have "good" or "favorable" curvature. The last term is proportional to the magnitude of the parallel current. Therefore, instabilities that are caused primarily by the first term are called pressure driven, while those caused by the second term are called current driven. These instabilities are also distinguished by their localization in the plasma. Unstable modes that appear localized near the surface of the plasma are called external, or free boundary modes, while those that have no surface perturbation are called internal, or fixed boundary modes. In order to minimize the stabilizing effect of the field line bending, the most unstable modes will have long wavelengths along the magnetic field. The relative magnitudes of the wavelengths perpendicular to the field will serve to distinguish the ideal MHD modes of interest, whose characteristics will be examined in the following sections.

---

[1]Troyon, F., Gruber, R., Saurenmann, H., Semenzato, S., and Succi, S., Plasma Phys. and Cont. Fusion **26 1A** (1984) 209; Phys. Lett. **110A** (1985) 29.

[2]Burrell, K.H., Stambaugh, R.D., Angel, T.R., et al., Nuclear Fusion **23** (1983) 536.

[3]Bol, K., Buchenauer, D., Chance, M., et al., Phys. Rev. Lett. **57** (1986) 1891.

[4]Kesner, J., Nuclear Fusion 29 (1989) 1397.

[5]Wagner, F., Becker, G., Behringer, K., et al., Phys Rev. Lett. **49** (1982) 1408.

[6]Furth, H.P., Killeen, J., Rosenbluth, M.N., Coppi, B., in *Plasma Physics and Controlled Nuclear Fusion Research* (Proc. 2nd Int. Conf. Culham, 1964) Vol. 1, IAEA, Vienna (1965) 103.

[7]Greene, J.M., and Johnson, J.L., Plasma Phys. **10** (1968) 729.

[8]Freidberg, J.P., *Ideal Magnetohydrodynamics*, Plenum Press, New York (1987) 255.

3.0.2.1 Long ⊥ Wavelength Kink/Ballooning Instabilities

One of the instabilities that needs to be avoided when achieving high β plasmas is the kink/ballooning mode. This instability is driven by both the plasma pressure gradient and parallel plasma current, and has both long parallel and perpendicular wavelengths. In particular, $\mathbf{k}_{\|} / \mathbf{k}_{\perp} << 1$, where $\mathbf{k}$ is the wave vector, and the perpendicular wavelength is comparable to the plasma minor radius ($\mathbf{k}_{\perp} a = O(1)$). The structure of the mode is more commonly specified by its toroidal mode number, n, given by the Fourier expansion of the perturbation,

$$\xi(\mathbf{x}) = \xi(\psi) \exp(- in\phi) \sum^{m} \exp(im\theta) \; . \qquad (3.0.2.1 - 1)$$

While a mode with a particular n number will exhibit more than one non-zero poloidal harmonic, the dominant, poloidal harmonic is usually used to express the "m" number of the instability. In general, the most unstable modes have small n and small dominant m numbers with the product m=nq corresponding to the first integer q surface in the vacuum. The largest magnitude is found on the outboard side of the tokamak, where the field line curvature is unfavorable. The mode can either be internal or external. At low β, this mode loses its ballooning character and becomes the ideal MHD kink instability. The poloidal projection of the displacement across the plasma cross section for an internal n=4 mode is shown in Fig. 3.0.2.1 - 1.

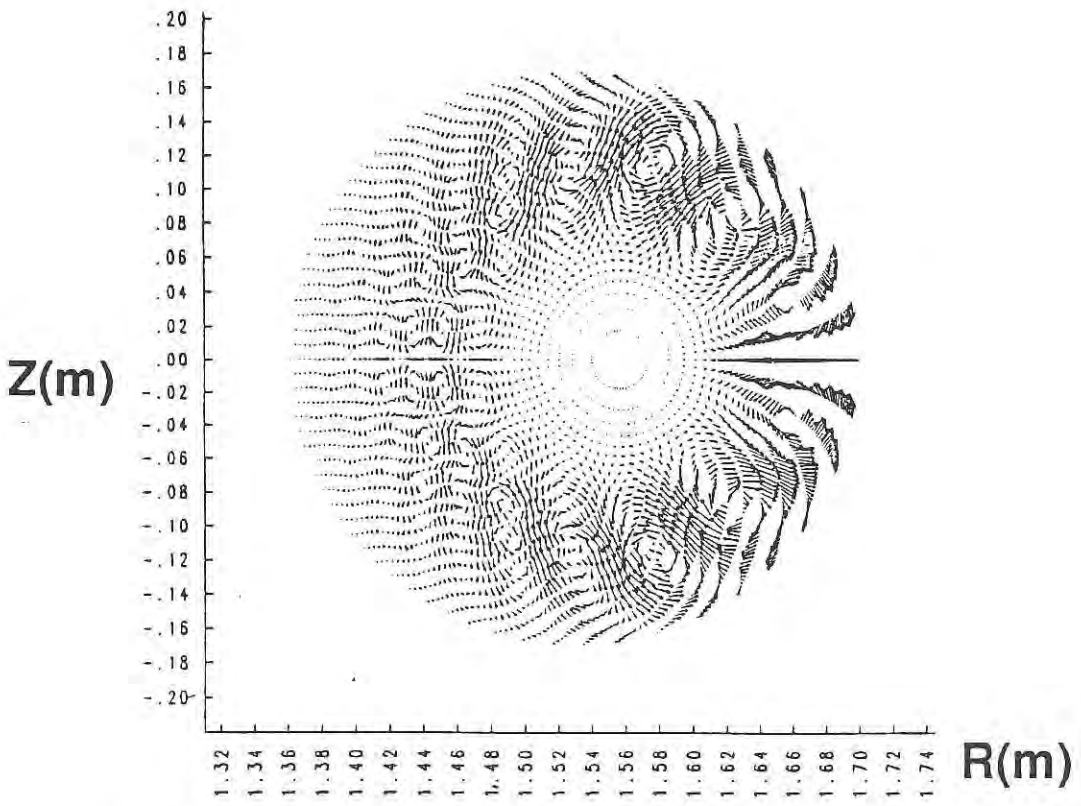

Fig. 3.0.2.1-1: Poloidal projection of unstable eigenvectors for n=4 kink/ballooning mode.

The external kink/ballooning instability usually leads to a bulk motion of the plasma toward the vacuum vessel wall of the tokamak, leading to the abrupt termination of the discharge, and a corresponding "hard" β limit. Several techniques have been suggested to suppress this mode by introducing a close fitting conducting shell around the plasma[1], feedback stabilization[2], or RF ponderomotive stabilization[3]. The primary stabilization technique addressed in the present work is the conducting shell. As this shell is brought closer to the plasma surface, the external current driven component of the perturbation is reduced, and the mode can be stabilized. Also, as the second stability region is entered, the pressure driven component can be reduced. However, even with

the edge perturbation clamped by a conducting wall placed on the plasma surface, the internal kink/ballooning instability can still exist (see Section 3.2.5). Also, since a conducting shell can only stabilize the external mode up to its L/R time, the external mode may also be able to grow on the steady state timescale of the experiment. While conducting wall stabilization has had some success in the PBX-M experiment, a supplementary stabilization technique has not been demonstrated experimentally that has eliminated the high β kink/ballooning instability. Until such a technique is demonstrated, second stability operation may be limited to high β_p operation below the instability threshold of the kink/ballooning mode. While the β limit described by (1.0 - 1) is due to the n=1 mode, the modes with small-n values greater than one are sometimes less stable than the n=1 mode. This behavior is demonstrated in the transition equilibria in Chapter 3.2.

An additional low-n instability associated with high β plasmas is the "infernal" mode. This instability is an internal mode that appears theoretically in plasmas with sufficiently small magnetic field shear. While ballooning modes generally are less stable at large n, when $(\psi q'(\psi))^{-2} > n >> 1$, this trend can reverse,[4,5] and the infernal mode can be unstable even when the infinite-n ballooning modes, examined in the following section, are stable. The effect of this mode has not been determined experimentally.

---

[1]Grimm, R.C., Chance, M.S., Todd, A.M.M, et al., Nuclear Fusion 25 (1985) 805.

[2]Bhattacharjee, A., Iacono, R., Marshall, T.C., Mauel, M.E., Navratil, G.A., Paranicas, C., Sabbagh, S.A., Sen, A.K., Van Dam, J.W., Wang, X.-H., Hughes, M.H., Phillips, M.W., Todd, A.M.M., "Second Regime Tokamak Operation at Large Aspect Ratio", Columbia University report #109, June 1987.

[3]D'Ippolito, D., "Suppression of External Kink Modes in Tokamaks by RF Ponderomotive Effects", 1987 Sherwood Theory Meeting, San Diego, Ca. paper 3B31.

[4]Hastie, R.J., Taylor, J.B., Nuclear Fusion 21 (1981) 187.

[5]Manickam, J., Pomphrey, N., and Todd, A.M.M., Nuclear Fusion 27 (1987) 1461.

3.0.2.2 Short ⊥ Wavelength Ballooning Instabilities

Another class of instabilities that are believed to limit β in tokamaks is the large-n ballooning mode. This instability is driven by the pressure gradient term of δW , and has long parallel and short perpendicular wavelengths ($\mathbf{k}_\perp a >> 1$). The mode is internal and is the toroidal generalization to the cylindrical flute instability, and manifests the ballooning characteristic of the perturbation increasing in the unfavorable curvature region. A schematic illustration of the mode structure is shown in Fig. 3.0.2.2 - 1.

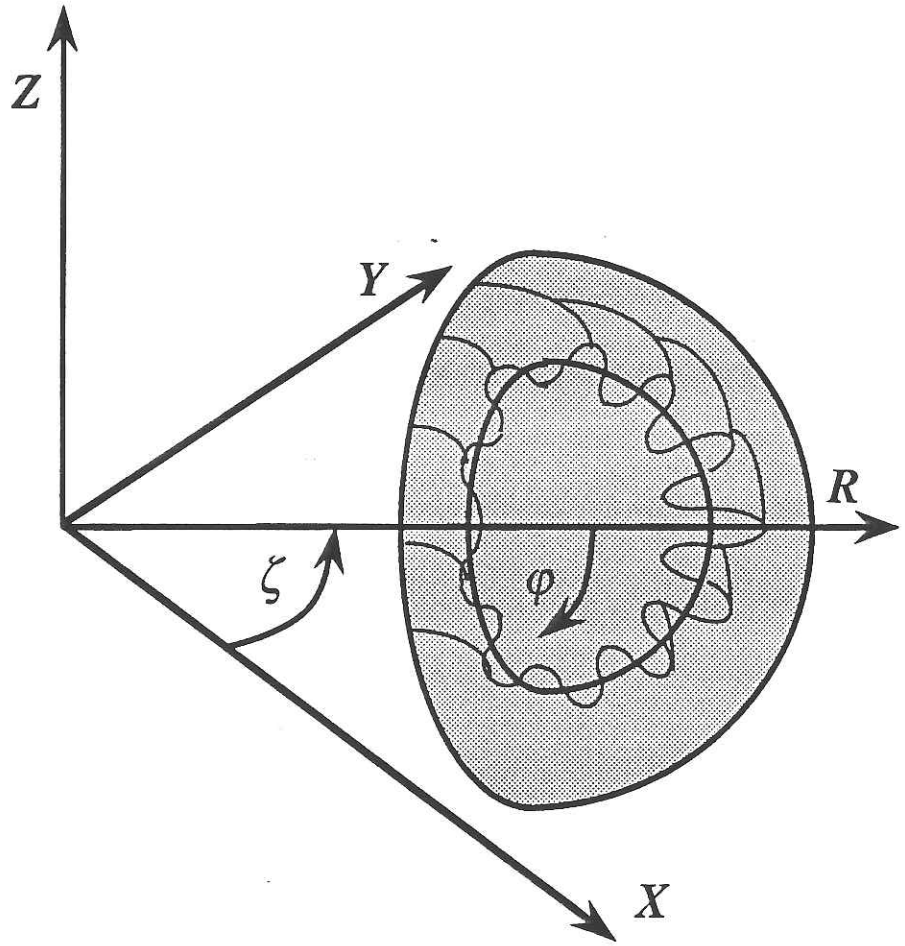

Fig. 3.0.2.2-1: Schematic illustration of mode structure for the large-n ballooning mode in a tokamak. *The fluted perturbation displays the typical ballooning characteristic of having its largest amplitude on the outboard side of the plasma where the field line curvature is unfavorable.*

While the short wavelength nature of the mode makes experimental detection difficult, the appearance of the instability is theoretically associated with some mechanism, such as enhanced particle and energy transport, that would restabilize the mode by decreasing the pressure gradient. Therefore, equilibrium pressure gradients and β would most likely be limited in a non-disruptive, or "soft" manner. Since the mode is internal, conducting walls do not affect its stability, however, several alternate techniques (mentioned in Section 3.0.1) have been proposed to help stabilize the mode. In addition, the mode restabilizes at sufficiently large p', leading to the prospect of high β equilibria that are stable in the "second" stability region.

3.0.3 High-n Expansion, Ballooning Mode Formalism

In the large-n limit, the evaluation of the stability of ideal MHD modes breaks down into the solution of an eigenvalue equation on each flux surface. This limit is generally the least stable and the simplest to evaluate both computationally and analytically. In this section, the large-n ballooning mode formalism is used to reduce δW into the standard Euler-Lagrange form known as the ballooning equation. Evaluation of the plasma equilibrium is necessary input for solution of the ballooning equation. The work of CHT illustrates the standard derivation of the large-n ballooning equation. A somewhat different and more formal approach to the ballooning equation is given by Dewar and Glasser.[1]

An eikonal representation is used to model waves with short perpendicular wavelength and long parallel wavelength. In particular, define

$$\xi_\perp = \bar{\xi}_\perp \exp(iS_e) \equiv \bar{\xi}_\perp \exp(in\Gamma) \; ; \; \mathbf{k}_\perp \equiv \nabla S_e \, , \qquad (3.0.3 - 1)$$

where $\bar{\xi}_\perp$ varies slowly along **B** (on the equilibrium length scale) and ∇S_e is large, so that the exponential varies rapidly perpendicular to **B**. This description allows the amplitude of (3.0.3 - 1) to model the ballooning character of the mode by allowing the slow change of the amplitude as the field line travels from good to bad curvature regions. The eikonal can then be chosen as constant along the field line to all orders,

$$\mathbf{B} \bullet \nabla S_e = 0 \, . \qquad (3.0.3 - 2)$$

The exponential factor models the short perpendicular wavelength of the mode. The eikonal can be evaluated in the tokamak flux coordinates by using (3.0.3 - 2). With **B** given by (2.0.1.1.2 - 1) and the gradient operator by (2.0.1.1.1 - 10),

$$\mathbf{B} \bullet \nabla = \frac{1}{\mathcal{J}} \frac{\partial}{\partial \theta} + \frac{g}{R^2} \frac{\partial}{\partial \varphi} \, . \qquad (3.0.3 - 3)$$

Integrating (3.0.3 - 2) by separation of variables gives

$$S_e = n \, (- \varphi + \int_0^\theta \frac{\mathcal{J} g}{R^2} \, d\theta \, ' + F(\psi)) \, . \qquad (3.0.3 - 4)$$

The toroidal mode number n will serve as an expansion parameter. By taking the $n \rightarrow \infty$ limit, ∇S_e will be a rapidly varying function, thus modeling short $\perp$ wavelength, "large-n" ballooning modes. The arbitrary function $F(\psi)$ is usually absorbed into the integral, and after eliminating g by using (2.0.1.1.2 - 10), the result is

$$S_e = n\left(- \varphi + 2\pi\, q(\psi)\, \frac{\int_{\theta_0}^{\theta} \frac{\mathcal{J}}{R^2}\, d\theta'}{\int_{0}^{2\pi} \frac{\mathcal{J}}{R^2}\, d\theta'} \right). \qquad (3.0.3 - 5)$$

The integration origin, θ_0, is related to the radial wavenumber. This can be seen by evaluating

$$\mathbf{k}_\perp \equiv \nabla S_e = n\nabla\Gamma = n\left(\frac{1}{n}\frac{\partial S_e}{\partial \psi}\nabla\psi + \frac{\mathcal{J}g}{R^2}\nabla\theta - \nabla\varphi\right) \qquad (3.0.3 - 6)$$

with

$$\frac{1}{n}(k_\perp^{\theta_0})_\psi \equiv \frac{1}{n}\frac{\partial S_e}{\partial \psi} = 2\pi\frac{\partial}{\partial \psi}\left(q(\psi)\, \frac{\int_{0}^{\theta} \frac{\mathcal{J}}{R^2}\, d\theta' - \int_{0}^{\theta_0} \frac{\mathcal{J}}{R^2}\, d\theta'}{\int_{0}^{2\pi} \frac{\mathcal{J}}{R^2}\, d\theta'} \right). \qquad (3.0.3 - 7)$$

Therefore, specifying the arbitrary $\theta_0(\psi)$ parameter is equivalent to specifying an offset to the wavevector in the $\nabla\psi$ or radial direction. The additional radial wavenumber is given by the second term in the derivative of (3.0.3 - 7). Although θ_0 is only related to the radial wavenumber, it is referred to as the actual radial "wavenumber" in the literature, therefore, both θ_0 and $(1/n)(k_\perp^{\theta_0})_\psi$ will be noted as the arbitrary radial wavenumber. Note that this is an appropriate form for a general Jacobian. Most authors

specify $\mathcal{J}$, for example, yielding a Hamada coordinate system,[2] with $\mathcal{J} = 1$, or the PEST coordinate system,[3] with $\mathcal{J} \propto R^2$. The latter case gives the arbitrary radial wavenumber

$$\frac{1}{n}(k_{\perp}^{\theta_0})_{\psi} = q'(\psi)\,\theta_0(\psi)\,. \qquad (3.0.3 - 8)$$

Although this result is simpler, it is more convenient for computational reasons to allow $\mathcal{J}$ to be specified, so equations relevant to a general Jacobian should be used. A general Jacobian specification will also be useful when examining the ballooning equation analytically by specifying the inverse transformation of flux coordinates in Chapter 3.1. Therefore, the large-n ballooning equation will be derived below for a general Jacobian.

A dilemma now arises concerning the reality of the model eigenfunction (3.0.3 - 1) that was left unresolved in early analyses of the large-n ballooning mode. Since S_e given by (3.0.3 - 5) is only periodic on rational surfaces, generally it will not produce a physically acceptable eigenfuction due to the lack of periodicity. This problem was solved by Glasser,[4] and more popularly, by Connor, et al.,[5] by adopting the quasimode form of the eigenfunction.[6] By doing so, the problem is extended to an infinite domain in θ and periodicity constraints are relaxed. The resulting eigenfunction is not the physical mode, but rather a "quasimode". The physical mode can be constructed from a linear superposition of quasimodes

$$\xi_{\text{real}}(\psi,\theta) = \sum_{\ell} \xi_{\text{quasi}}(\psi,\theta + 2\pi\ell)\,. \qquad (3.0.3 - 9)$$

A key result of this model is that the eigenvalues of the real mode and the quasimode are identical. The subsequent analysis will assume the quasimode interpretation of the eigenfuction.

The function Γ in (3.0.3 - 1) can be used as a coordinate in the dual coordinate Clebsch representation of the magnetic field. This can be seen by computing **B** in the Clebsch form

$$\mathbf{B} = \nabla\psi \times \nabla\Gamma \qquad (3.0.3 - 10)$$

and realizing that this form reproduces the axisymmetric form of **B** given by (2.0.1.1.2 - 1). Using $\nabla\Gamma$ given by (3.0.3 - 6),

$$\mathbf{B} = \nabla\varphi \times \nabla\psi + \frac{\mathcal{J}g}{R^2}\nabla\psi \times \nabla\theta\text{-}. \qquad (3.0.3 - 11)$$

The second term can be rewritten using

$$\nabla\psi \times \nabla\theta = |\nabla\psi \times \nabla\theta| \frac{\nabla\varphi}{|\nabla\varphi|} = \frac{|\nabla\psi \times \nabla\theta \bullet \nabla\varphi|}{|\nabla\varphi|^2}\nabla\varphi = \frac{R^2}{\mathcal{J}}\nabla\varphi \qquad (3.0.3 - 12)$$

with the result

$$\mathbf{B} = \nabla\varphi \times \nabla\psi + g\,\nabla\varphi\,. \qquad (3.0.3 - 13)$$

The large n expansion of δW proceeds by choosing the minimizing perturbation. First, in systems with magnetic field shear, a displacement that is

incompressible can be found. This choice of eigenfunction minimizes the plasma compression term. Therefore, $\xi_{\|}$ is to be chosen such that

$$\nabla \bullet \xi = 0 \qquad (3.0.3 - 14)$$

is identically satisfied. After substituting the eikonal form of $\xi_{\perp}$, the remaining terms in δW take the form (note zero subscripts denoting equilibrium quantities have been dropped for clarity)

$$\delta W_f = \frac{1}{2} \int \frac{|\mathbf{Q}_{\perp}|^2}{\mu_0} + \frac{|\mathbf{B}|^2}{\mu_0} |\nabla \bullet \xi_{\perp} + i\xi_{\perp} \bullet n\nabla\Gamma + 2\xi_{\perp} \bullet \kappa|^2$$

$$- 2\left(\xi_{\perp}^* \bullet \kappa\right)(\xi_{\perp} \bullet \nabla p) - \frac{\mathbf{J}_{\|}}{|\mathbf{B}|} \xi_{\perp}^* \times \mathbf{B} \bullet \mathbf{Q}_{\perp} \, d\mathbf{x} \, . \qquad (3.0.3 - 15)$$

Expanding the perturbation in powers of n^{-1},

$$\xi_{\perp} = \xi_{\perp 0} + n^{-1}\xi_{\perp 1} + O(n^{-2}), \qquad (3.0.3 - 16)$$

the lowest order contribution is

$$\delta W_f = \frac{n^2}{2\mu_0} \int |\mathbf{B}|^2 |\xi_{\perp 0} \bullet \nabla\Gamma|^2 + O(1) \, . \qquad (3.0.3 - 17)$$

Therefore to minimize δW_f at this order, $\xi_{\perp 0}$ is chosen to be perpendicular to the wavevector, and the lowest order δW_f vanishes. Since it is already perpendicular to **B**, the lowest order perturbation can then be written in the form

$$\xi_{\perp 0} = \xi \frac{\mathbf{B} \times \nabla\Gamma}{|\mathbf{B}||\nabla\Gamma|} \, , \qquad (3.0.3 - 18)$$

and $\mathbf{Q}_{\perp 0}$ can be written as

$$\mathbf{Q}_{\perp 0} \equiv (\nabla \times (\xi_{\perp 0} \times \mathbf{B}))_{\perp} = (\nabla \times \xi \frac{\mathbf{B} \times \nabla \Gamma}{|\mathbf{B}||\nabla \Gamma|} \times \mathbf{B})_{\perp}$$

$$= (\nabla \times (\xi |\mathbf{B}| \frac{\nabla \Gamma}{|\nabla \Gamma|}))_{\perp} = \left(\nabla \left(\frac{\xi |\mathbf{B}|}{|\nabla \Gamma|} \right) \times \nabla \Gamma \right)_{\perp}$$

$$= \left\{ \left[\nabla_{\perp} \left(\frac{\xi |\mathbf{B}|}{|\nabla \Gamma|} \right) + \frac{\mathbf{B}}{|\mathbf{B}|^2} (\mathbf{B} \bullet \nabla) \left(\frac{\xi |\mathbf{B}|}{|\nabla \Gamma|} \right) \right] \times \nabla \Gamma \right\}_{\perp}$$

$$= \frac{\mathbf{B} \times \nabla \Gamma}{|\mathbf{B}|^2} (\mathbf{B} \bullet \nabla) \left(\frac{\xi |\mathbf{B}|}{|\nabla \Gamma|} \right). \qquad (3.0.3 - 19)$$

The next order in the expansion of the potential energy functional yields

$$\delta W_f = \frac{1}{2} \int \frac{|\mathbf{Q}_{\perp 0}|^2}{\mu_0} + \frac{|\mathbf{B}|^2}{\mu_0} |\nabla \bullet \xi_{\perp 0} + i\xi_{\perp 1} \bullet \nabla \Gamma + 2\xi_{\perp 0} \bullet \kappa|^2$$

$$- 2 \left(\xi^*_{\perp 0} \bullet \kappa \right) (\xi_{\perp 0} \bullet \nabla p) - \frac{\mathbf{J}_{\parallel}}{|\mathbf{B}|} \xi^*_{\perp 0} \times \mathbf{B} \bullet \mathbf{Q}_{\perp 0} \, dx + O(n^{-2}). \qquad (3.0.3 - 20)$$

At this order, $\xi_{\perp 1}$ can be chosen such that the magnetic compression term vanishes. Also, using (3.0.3 - 18), the kink term is identically zero since,

$$(\xi^*_{\perp 0} \times \mathbf{B}) \bullet (\mathbf{B} \times \nabla \Gamma) = 0 . \qquad (3.0.3 - 21)$$

The remaining terms give a balance between the stabilizing effect of field line bending, and the possibly destabilizing effect of unfavorable field line curvature,

$$\delta W_f = \frac{1}{2\mu_0}\int\left|\frac{\mathbf{B}\times\nabla\Gamma}{|\mathbf{B}|^2}(\mathbf{B}\cdot\nabla)\left(\frac{\xi|\mathbf{B}|}{|\nabla\Gamma|}\right)\right|^2$$

$$- 2\mu_0\frac{\mathbf{B}\times\nabla\Gamma}{|\mathbf{B}|\,|\nabla\Gamma|}\cdot\kappa\left[\frac{\mathbf{B}\times\nabla\Gamma}{|\mathbf{B}|\,|\nabla\Gamma|}\cdot\nabla p\right]|\xi|^2\,d\mathbf{x} + O(n^{-2})$$

$$= \frac{1}{2\mu_0}\int\frac{|\nabla\Gamma|^2}{|\mathbf{B}|^2}\,|(\mathbf{B}\cdot\nabla)\,\xi_n|^2$$

$$- \frac{2\mu_0\,p'(\psi)}{|\mathbf{B}|^2}(\nabla\Gamma\times\mathbf{B})\cdot\kappa\,|\xi_n|^2\,d\mathbf{x} + O(n^{-2}) \qquad (3.0.3 - 22)$$

with ξ_n defined as $\xi\,|\mathbf{B}|/|\nabla\Gamma|$.

Considering (2.0.1.2 - 10),

$$\omega^2 = \frac{\delta W}{\frac{1}{2}\int\rho_0\left(\frac{|\nabla\Gamma|}{|\mathbf{B}|}\right)^2|\xi|^2\,d\mathbf{x}}, \qquad (3.0.3 - 23)$$

the minimizing Euler-Lagrange equation is

$$\mathbf{B}\cdot\nabla\left(\frac{|\nabla\Gamma|^2}{|\mathbf{B}|^2}\mathbf{B}\cdot\nabla\xi_n\right) + \frac{2\mu_0\,p'(\psi)}{|\mathbf{B}|^2}(\nabla\Gamma\times\mathbf{B}\cdot\kappa)\xi_n$$

$$+ \rho\omega^2\left(\frac{|\nabla\Gamma|}{|\mathbf{B}|}\right)^2\xi_n = 0\,. \qquad (3.0.3 - 24)$$

This is the large-n ballooning equation for incompressible displacements. It is a second order ordinary differential equation (compressional displacements lead to a fourth order system; see Dewar and Glasser). It is one dimensional since only derivatives along the

field line appear. It is shown by CHT that the higher order n terms are stabilizing, therefore (3.0.3 - 24) is usually the order computed and understood as the most unstable. Also notice that ψ appears as a parameter in this equation, so that solution of the global mode with one eigenvalue breaks down into a solution of arbitrarily many equations, one for each flux surface, with separate "quasimode" eigenvalues.

The final step in deriving the ballooning equation is to transform variables into more familiar quantities, use axisymmetric flux coordinates, and specify the boundary conditions. A simple way to do this is to first decompose some vectors into components that are parallel and perpendicular to $\nabla\psi$,

$$\nabla\Gamma \equiv \Lambda_p \nabla\psi + \frac{\mathbf{B}\times\nabla\psi}{|\nabla\psi|^2}, \qquad (3.0.3 - 25)$$

where

$$\Lambda_p = \frac{\nabla\psi \bullet \nabla\Gamma}{|\nabla\psi|^2}, \qquad (3.0.3 - 26)$$

and

$$\kappa \equiv \frac{\kappa_n \nabla\psi}{|\nabla\psi|} + \kappa_g \frac{\mathbf{B}\times\nabla\psi}{|\mathbf{B}||\nabla\psi|}, \qquad (3.0.3 - 27)$$

where

$$\kappa_n = \frac{\kappa \bullet \nabla\psi}{|\nabla\psi|}\,;\ \kappa_g = \kappa \bullet \frac{\mathbf{B}\times\nabla\psi}{|\mathbf{B}||\nabla\psi|} \qquad (3.0.3 - 28)$$

are the normal and geodesic curvatures of the magnetic field line. An additional variable related to Λ_p is introduced,

$$\Lambda \equiv \frac{\Lambda_p |\nabla\psi|^2}{|\mathbf{B}|} = \frac{\nabla\psi \bullet \nabla\Gamma}{|\mathbf{B}|} . \qquad (3.0.3 - 29)$$

By taking the curl of (3.0.3 - 25) then dotting into $(\mathbf{B} \times \nabla\psi)$, notice that

$$\mathbf{B} \bullet \nabla\Lambda_p = \frac{\mathbf{B} \times \nabla\psi}{|\nabla\psi|^2} \bullet \nabla \times \frac{\mathbf{B} \times \nabla\psi}{|\nabla\psi|^2} \equiv S_{\text{local}} \qquad (3.0.3 - 30)$$

is the local shear. Therefore, Λ_p is identified as the integrated local shear. Also,

$$|\nabla\Gamma|^2 = (1 + \Lambda^2) \frac{|\mathbf{B}|^2}{|\nabla\psi|^2} , \qquad (3.0.3 - 31)$$

and

$$\nabla\Gamma \times \mathbf{B} \bullet \kappa = \frac{|\mathbf{B}|^2}{|\nabla\psi|} (\kappa_n - \Lambda\kappa_g) . \qquad (3.0.3 - 32)$$

substituting (3.0.3 - 3), (3.0.3 - 31), and (3.0.3 - 32) into (3.0.3 - 24), the large-n ballooning equation becomes

$$\frac{1}{\mathcal{J}\partial\theta}\left(\frac{1 + \Lambda^2}{\mathcal{J}|\nabla\psi|^2} \frac{\partial\xi_n}{\partial\theta}\right) + \frac{2\mu_0 p'(\psi)}{|\nabla\psi|} (\kappa_n - \Lambda\kappa_g)\, \xi_n + \rho\omega^2 \left(\frac{1 + \Lambda^2}{|\nabla\psi|^2}\right) \xi_n = 0 . \qquad (3.0.3 - 33)$$

The boundary conditions are that ξ_n be square integrable over the domain of the quasimode, which is $(-\infty \leq \theta \leq \infty)$.

In performing both analytic and computational study of (3.0.3 - 33), the following expressions for Λ, and the curvature terms are useful. Λ is easily derived from (3.0.3 - 29),

$$\Lambda = \frac{g^{11}\Gamma_\psi + g^{12}\Gamma_\theta}{|\mathbf{B}|} , \qquad (3.0.3 - 34)$$

where the derivatives of Γ are given by (3.0.3 - 6). The curvature terms can be computed, as derived by Phillips,[7]

$$\kappa_n = \kappa_{n\ \text{poloidal}} + \kappa_{n\ \text{toroidal}} \qquad (3.0.3 - 35)$$

where

$$\kappa_{n\ \text{poloidal}} \equiv \frac{R}{\mathcal{J}\nabla\psi|\mathbf{B}|^2}\left(\frac{Z_\theta R_{\theta\theta} - R_\theta Z_{\theta\theta}}{\mathcal{J}^2}\right) \qquad (3.0.3 - 36)$$

and

$$\kappa_{n\ \text{toroidal}} \equiv -\frac{g^2 Z_\theta}{\mathcal{J}\nabla\psi|\mathbf{B}|^2 R^2} , \qquad (3.0.3 - 37)$$

and

$$\kappa_g = \frac{g}{\mathcal{J}\nabla\psi|\mathbf{B}|^3}\frac{\partial}{\partial\theta}\left(\frac{|\mathbf{B}|^2}{2}\right). \qquad (3.0.3 - 38)$$

---

[1]Dewar, R.L., Glasser, A.H., Phys. Fluids **26** (1983) 3078.

[2]Greene, J.M., and Johnson, J.L., Phys. Fluids **5** (1962) 510.

[3]Greene, J.M., Chance, M.S., Nuclear Fusion **21** (1981) 453.

[4]Glasser, A.H., in Proceedings of the Finite Beta Theory Workshop, Varenna, edited by B. Coppi and W.L. Sadowski (US DOE, Washington, D.C., 1977), CONF-7709167 (1977) 55.

[5]Connor, J.W., Hastie, R.J., Taylor, J.B., Phys. Rev. Lett. **40** (1978) 396; Proc. R. Soc. (London) A **365** (1979) 1.

[6]Roberts, K.V., and Taylor, J.B., Phys. Fluids **8** (1965) 315.

[7]Phillips, M.W., *priv. comm.*

3.0.4 Local Shear Reversal

An unstable region to large-n ballooning modes forms in a finite β tokamak equilibrium because the destabilizing effect of unfavorable field line curvature can dominate the stabilizing effect of field line bending. These two conditions are satisfied when the local shear of the magnetic field lines is sufficiently weak in the bad curvature region of the tokamak. As a rule of thumb, a flux surface is usually unstable when the local shear has a null point in the unfavorable curvature region. Therefore, physical effects that increase the magnitude of the local shear in the tokamak are stabilizing. The origin of a second stability region can be explained in this context. In a low β tokamak, the field lines on the inner flux surfaces travel more quickly in the poloidal direction than the outer ones. As the pressure gradient is increased in a tokamak, the Shafranov shift and p′ driven Phirsch-Schluter currents increase, and the local shear can decrease in magnitude in the bad curvature region. This is caused by a strengthening of the poloidal field on the outboard side of the machine that causes the local wrapping of the

outer field lines to catch up and surpass the wrapping number of the inner ones. At some critical β, the local shear of the field lines will be small enough to allow the mode to be unstable. However, as β is increased further, the local shear reverses and therefore begins to increase in magnitude. The local shear null will then migrate toward the favorable curvature region and the large-n ballooning mode can regain stability. This process is described by Greene and Chance.[1]

While this description can be used as a physical picture of the shear reversal process and its influence on second stability, it is sometimes misused or needs additional physics to explain the stability of arbitrary, two-dimensional tokamak equilibria. For example, toroidal effects alter not only the global equilibrium but also the local shear. Since finite ε will generally tend to reverse the local shear, decreasing aspect ratio is thought to ease the establishment of second stability for all classes of equilibria.[2] However, it will be shown in Section 3.1.6.1 that enhanced stability is not always gained at low A. While toroidal effects can help reverse S_{local}, the point at which S_{local}=0 will sometimes need to move further into the favorable curvature region to gain second stability as A is decreased. This will lead to a destabilization of the second region boundary pressure gradient, and a higher β value needed to enter the second stability region. It will also be shown that reduced Shafranov shift can *increase* the plasma stability, a seemingly contrary result to that of the simple physical model. Modifications to the basic intuition are due to the coupling of effects of separate phenomena that are usually considered only independently in simple stability models.

---

[1]Greene, J.M., Chance, M.S., Nuclear Fusion 21 (1981) 453.

[2]Gerver, M.J., Kesner, J., Ramos, J.J., Phys. Fluids 31 (1988) 2674.

What I find tolerable in my own work is not so really and in itself, but only in comparison with other worse productions that I see well received.

Montaigne, *Essays*, (from "On Presumption")

3.1 SECOND REGION PARAMETERIZATION

The efficient operation of a tokamak reactor requires that the plasma figure of merit, β, be as large as possible. Unfortunately, experimental[1,2] studies of tokamak operation at high β show that pressure gradient and current driven plasma instabilities limit the stable operating β value. A recent empirical scaling for this β limit, given by Eq. (1.0.1 - 1) depends linearly on the plasma current and reproduces the limit found in present tokamaks. This scaling is in contrast to earlier scalings[3,4] based on high-n mode stability that were proportional to I^2. The success of the β_1 scaling has led to considerable effort to maximize β_1, primarily by increasing I through techniques such as shaping of the plasma cross-section.

There remains another alternative in obtaining high β operation in a tokamak. Theoretically, a "second region" of stability at β values greater than β_1 has been shown to exist[5-11]. This stability region exhibits a *threshold* β value, which must be exceeded before a plasma reaches second stability. Analytic models for the scaling of the second region pressure gradient threshold value, α_2, have been found for simple low $\beta \sim O(\varepsilon^2)$, high aspect ratio, circular cross-section models of equilibrium.[12,13] In order to attain an analytic solution, these models neglect important geometric effects of the equilibrium that can change the stability properties of the equilibrium. In the present study, the two-dimensional equilibria are calculated numerically, and are iterated to

marginal stability on the second region boundary. Therefore, all effects are retained in the present modeling, and coupling between effects such as large Shafranov shift and aspect ratio that affect stability are examined.

---

[1]Burrell, K.H., Stambaugh, R.D., Angel, T.R., et al., Nuclear Fusion **23** (1983) 536.

[2]Bol, K., Buchenauer, D., Chance, M., et al., Phys. Rev. Lett. **57** (1986) 1891.

[3]Todd, A.M.M., Chance, M.S., Greene, J.M., Grimm, R.C., Johnson, J.L., Manickam, J., Phys. Rev. Lett. **38** (1977) 826.

[4]Bateman, G., *MHD Instabilities*, MIT Press, Cambridge, Mass. (1978) 166.

[5]Coppi, B., Ferreira, A., Mark, J.W.-K., Ramos, J.J., Nuclear Fusion **19** (1979) 715.

[6]Coppi, B., Ferreira, A., Ramos, J.J., Phys. Rev. Lett. **44** (1980) 990.

[7]Greene, J.M., Chance, M.S., Nuclear Fusion **21** (1981) 453.

[8]Mercier, C., in Plasma Physics and Controlled Nuclear Fusion Research (Proc. 7th Int. Conf. Innsbruck, 1978) Vol. 1, IAEA, Vienna (1978) 701.

[9]Fielding, P.J., Haas, F.A., Phys. Rev. Lett. **41** (1978) 801.

[10]Lortz, D., Nuhrenberg, J., Phys. Lett. **68a** (1978) 49.; Nuclear Fusion **19** (1979) 1207.

[11]Strauss, H.R., Park, W., Monticello, D.A., White, R.B., Jardin, S.C., Chance, M.S., Todd, A.M.M., Glasser, A.H., Nuclear Fusion **20** (1980) 638.

[12]Llobet, X., Berk, H.L., Rosenbluth, M.N., Phys. Fluids **30** (1987) 2750.

[13]Chen, Liu, Bondeson, A., Chance, M.S., Nuclear Fusion **27** (1987) 1918.

3.1.1 Objective and Key Results

The objective of this study is to determine the behavior of the local pressure gradient and the global β variables that define the marginal second region threshold with respect to variations in q profile, A, and the plasma outer boundary shaping. The stability analysis is carried out on a collection of numerically computed, two-dimensional, finite A equilibria that have pressure profiles that are marginally stable at the second region boundary to large-n ballooning modes. A novel feature of this study

is that the stability is generated self-consistently with the equilibrium and that both finite A and finite β effects are entirely retained. The important characteristics of these equilibria are subsequently examined.

It is found that the second region boundary becomes more sensitive to variations in the q profile as A decreases. The second region boundary will stabilize or destabilize at conventional tokamak aspect ratio ($A \sim 3$) depending on the balance of higher order ε modifications of κ_n. Physically, these modifications can be described as a competition between the stabilizing toroidal field component of κ_n (geometric magnetic well), and the destabilizing poloidal field component of κ_n. The latter effect is normally ordered small and neglected in simpler analytic models, but appears when Shafranov shifts of the order of the minor radius are included in finite A equilibrium models. Because of this, increased values of q_0 or q_a improve stability, but for different physical reasons that will be discussed. This result leads to both a new explanation of how increasing q_0 increases the plasma stability, and a significant alteration of the standard connection length argument for enhanced plasma stability. Elongation alone destabilizes the second region boundary, while appropriate dee-shaping stabilizes the boundary. Also, direct access to the second region occurs on a flux surface when $S < S_{crit}$. The value of S_{crit} is well approximated by the value of S pertaining to the flux surface on which S_{local} reverses sign on the outboard midplane of the plasma. The sensitivity of the marginally stable equilibria to variations in the finite radial wavenumber is also shown to be greatly decreased when compared to calculations that are not self-consistent. This discrepancy is explained in the context of reduction of the pressure gradient driven modulation of the integrated local shear by geometric effects that are neglected in the (S,α) model.

3.1.2 Predictor and Response Variables

The global predictor variables used for the modeling of the marginal second region boundary are the basic variables that describe the plasma equilibrium. The plasma major and minor radii are contracted into the tokamak aspect ratio. The plasma current and toroidal field are combined in a "cylindrical" q variable, defined as

$$q^* \equiv 5 \frac{a(\mathrm{m})^2 B(\mathrm{T})}{R(\mathrm{m})\, I(\mathrm{MA})} \left[\frac{(1 + \kappa^2(1 + 2\delta^2))}{2} \right] . \qquad (3.1.2 - 1)$$

The q profile is used as one of the free functions that specifies the equilibrium and is defined in this analysis as

$$q(\psi) = q_0 + (q_a - q_0)\left((\psi - \psi_0)/(\psi_a - \psi_0) \right)^{\alpha_q} . \qquad (3.1.2 - 2)$$

Here, the subscripts 'a' and '0' correspond to the plasma edge and magnetic axis values, respectively. Therefore, three scalar variables are introduced that determine the safety factor, q_0, q_a, and α_q which is a profile shape parameter. Note that the other free function, $p(\psi)$, is determined by the second region marginal stability constraint and is not an independent variable. Finally, the outer boundary of the plasma is described by the transformation

$$x_b = R_0 + a \cos(\theta + \delta \sin(\theta)) , \qquad (3.1.2 - 3)$$

$$z_b = \kappa a \cos(\theta) \qquad (3.1.2 - 4)$$

where κ and δ are the elongation and triangularity of the plasma boundary.

Therefore, the set of global variables chosen to describe the equilibria reduces to $(A, q^*, q_0, q_a, \alpha_q, \kappa, \delta)$. Note that q^* and the remaining q variables are not independent, so that q^* can be eliminated by the results of the numerical equilibria, or by an analytic relation of q^* and q for a specific analytic equilibrium model. Therefore, the set of independent global predictor variables reduces to $(A, q_0, q_a, \alpha_q, \kappa, \delta)$. The range of the global tokamak equilibrium parameters considered in the present study is $1.5 \leq A \leq 15$, $1.01 \leq q_o \leq 3.0$, $1.1 \leq q_a \leq 20.1$, $1.1 \leq \alpha_q \leq 4.0$, and $0.5 \leq \kappa \leq 2.5$, and $0.0 \leq \delta \leq 1.0$.

In addition, the magnetic field shear $S(\psi)$ is used as a local (meaning, a function of ψ) predictor variable in this analysis. In the present study,

$$S \equiv \frac{r^2 B_0}{q^2} \left(\frac{dq}{d\psi}\right). \qquad (3.1.2 - 5)$$

This definition reduces to the standard definition

$$S = \frac{r}{q} \left(\frac{dq}{dr}\right) \qquad (3.1.2 - 6)$$

when considering the low β, or infinite A shifted circular model of equilibrium.

The primary global response variables defining the second region threshold are the plasma figures of merit,

$$\beta \equiv \frac{2\mu_0}{B_0{}^2} \int p dv \qquad (3.1.2 - 7)$$

and

$$\varepsilon\beta_p \equiv \frac{8\pi\,\varepsilon}{\mu_0 I^2}\int p\,ds\,. \qquad (3.1.2 - 8)$$

The local response variable is the normalized plasma pressure gradient,

$$\alpha \equiv \frac{-2\mu_0 R\, r\, q}{B_0}\left(\frac{dp}{d\psi}\right). \qquad (3.1.2 - 9)$$

This definition reduces to the standard definition

$$\alpha = \frac{-2\mu_0 R\, q^2}{B_0{}^2}\left(\frac{dp}{dr}\right) \qquad (3.1.2 - 10)$$

when considering the low β, or infinite $\tilde{A}$ shifted circular model of equilibrium.

3.1.3 Solution Techniques

Since the goal of the present study is to establish the behavior of the second region threshold with respect to variations of the tokamak parameters while retaining all stabilizing and destabilizing effects to all orders, the primary solution techniques used are computational. The algorithm that brings an initial equilibrium state to a marginal second stability region state (described in Section 3.1.4) has been created by a conjunction of two well established computer codes that calculate the axisymmetric equilibrium and large-n ballooning stability of a given plasma. These routines are summarized in the following sections. In addition, physical insight into the

computational results and model development for the second region threshold are gained by considering simple analytic models of the equilibrium and numerical fitting of the computational marginal second region stability results.

3.1.3.1 Computational

The two major computational tools used that form the basis of the marginal second region boundary calculations are the Grumman fixed boundary equilibrium solver, EQGRUM, and the Grumman large-n ballooning mode solver, STBAL. These have been used extensively as reconstructive tools to determine the equilibrium and stability of tokamak experiments from measured data, and as predictive tools to map out stable trajectories to high β that existing and proposed tokamak experiments might follow.

3.1.3.1.1 Two-dimensional, Flux Conserving Equilibrium

The two-dimensional equilibrium code, EQGRUM, is based on the iterative metric method of equilibrium computation derived by Delucia, Jardin, and Todd.[1] This reference provides a detailed and complete description of the algorithm and its implementation. A summary of the routine is provided here. Additional detail can be found in the reference. The code solves the two-dimensional Grad-Shafranov equation in axisymmetric flux coordinates (Eq. 2.0.1.1.2 - 9) on a computational mesh given $p(\psi)$ and $q(\psi)$ for a fixed boundary shape on which $\psi \equiv 0$. The solution is then

computed as the inverse mapping $\psi = \psi(R, Z)$. The equilibria are assumed to possess up-down symmetry with the number of meshpoints on the upper half plane typically being (ψ, θ):(50,65). The distribution of the grid points over the poloidal angle variable θ is determined by a prescribed Jacobian, typically chosen to produce equal arc length spacing between adjacent gridpoints (ψ_i, θ_j) and (ψ_i, θ_{j+1}). An initial guess is provided for $\psi(R, Z)$ and is iterated upon until both Eq. (2.0.1.1.2 - 9) and the Jacobian constraint are satisfied [see Ref. 1 for an excellent, detailed description of this process]. The derivatives that are contained in these two constraint equations are computed by finite difference approximations accurate to $O(h^2)$ in the mesh spacing parameter, h, and are considered satisfied when the residuals of these equations are less than some specified tolerance, typically 10^{-7} for the normalized ψ variable, $0 < \tilde{\psi} < 1$.

This routine additionally writes output files for use in computing the stability of the equilibrium by the PEST and STBAL ideal MHD stability codes. EQGRUM also accepts input data from $1^1/_2$ dimensional transport codes to compute equilibria for stability analysis.

---

[1]Delucia, J., Jardin, S.C., and Todd, A.M.M., J. Comp. Phys. 37 (1980) 83.

3.1.3.1.2 High-n Mode Marginal Second Region Solver

STBAL,[1] written by Mike Phillips, solves the large-n mode ballooning equation (3.0.3 - 33) as an eigenvalue problem on each ψ surface for ω^2 and ξ_n over the poloidal angle variable in the infinite "quasimode" space. In the present study, the equation is solved for the marginally stable quasimode. When solved with $\omega^2 = 0$,

$p'(\psi)$ becomes the eigenvalue in the ballooning equation. This $p'(\psi)$ then represents the critical value at which the ballooning modes are marginally stable. The input quantities for this equation ($\mathcal{J}$, $|\nabla\psi|$, Λ, κ_n, κ_g) are obtained directly from the equilibrium and are defined in Section 3.0.3. The equation is solved by integrating from infinity, prescribed as a certain number of poloidal circuits away from the integration origin, θ_0, (usually 20 periods in these calculations), to the origin by a shooting method. The boundary conditions are $\xi_n(-/+\infty) = 0$ and $\xi_n'(\theta_0) = 0$. By estimating the envelope of the quasimode by the trial function $\xi_{trial} \sim ((1 + (S(\theta - \theta_0))^2)^{-1/2}$, the mode amplitude is reduced to 2.5% of its peak value at the θ interval boundaries when $S = 0.3$. Therefore, resolution of the mode is reliable for $S > 0.3$. This value of S is used as a lower bound for the numerical fitting of $\alpha_2(S)$ in Section 3.1.7.2.

In addition, it is known that high β effects create a second stability region to high-n ballooning modes. This is caused by the effects of p' and the distortion of the equilibrium geometry on the local shear at high β. STBAL can predict the second region marginal pressure gradient, p_2', for a given equilibrium. The code approximates p_2' by keeping the geometry of the given equilibrium fixed and using an expansion of the Grad-Shafranov equation in terms of the normal distance from the flux surface to approximate the pressure gradient effects on Λ. Λ is linear in $p'(\psi)$, therefore, the resulting ballooning equation is quadratic in $p'(\psi)$. Depending on the coefficients of the ballooning equation, that are functions of the equilibrium geometry, there will be two roots, or fewer roots for $p'(\psi)$. When two roots exist, they represent the first and second region marginal stability gradients, p_1' and p_2'. When one root exists, these two values coalesce and when no (real) roots exist, there is no unstable region and the flux surface has direct access to the second region.

Therefore, the code computes p_2' by considering the effect of p' on Λ, however, the effect of the varying equilibrium geometry as p' varies is not taken into account. In order to account for this effect in the computation of p_2', the above process must be iterated. That is, once p_2' is computed, this pressure gradient must be fed back to the equilibrium. The equilibrium is recomputed with p_2' as the new p' input, and the resulting equilibrium will have the correct geometry. However, recomputing p_2' for this equilibrium will result in a new prediction for p_2'. By iterating this process, a self-consistent computation of p_2' is obtained. This technique is used to produce the second region equilibria using EQGRUM and STBAL as major components, and is described in more detail in Section 3.1.4.

---

[1]Phillips, M.W., Todd, A.M.M, Hughes, M.H., et al., Nuclear Fusion **28** (1988) 1499.

3.1.3.2 Analytical Flux Conserving Equilibrium

The analytic model of equilibria used to analyze the numerical results is the shifted flux surface equilibrium model. Flux surfaces are assumed to be circular in shape, each having a Shafranov shift, $\sigma(r)$. The direct mapping of the flux surfaces is given by

$$R = R_0 + \sigma(r) + r\cos(\theta)\,, \qquad (3.1.3.2 - 1)$$

$$Z = r\sin(\theta) \qquad (3.1.3.2 - 2)$$

This model is particularly useful in the present study since it is the simplest model that still retains the destabilizing effect of the poloidal field curvature drive enhanced by the large Shafranov shift when finite A effects are retained.

In general, the equilibrium solution $\psi(r)$ and $\sigma(r)$ can be determined by varying the Lagrangian function

$$L = \int\int\left[\frac{B^2}{2\mu_0} - p(\psi)\right] dv \qquad (3.1.3.2 - 3)$$

that can be written in axisymmetric flux coordinates as

$$L = \frac{\pi}{\mu_0}\int\int\left[\frac{Z_\theta{}^2 + R_\theta{}^2}{\jmath^2} - \frac{g(\psi)^2}{R^2} - 2\mu_0\, p(\psi)\right] \jmath\, d\theta\, d\psi \qquad (3.1.3.2 - 4)$$

The θ integration can be performed explicitly without an ε expansion, the result being

$$L = \frac{2\pi^2}{\mu_0}\int_0^a dr\, \frac{r\psi_r{}^2}{\sigma'(R_0 + \sigma) - r}\left(\frac{\sigma'}{\sqrt{1 - \sigma'^2}} - \frac{r}{\sqrt{(R_0 + \sigma)^2 - r^2}}\right)$$
$$- \psi_r\, g(\psi)\, q(\psi) - 2\mu_0\, r\, p(\psi)\left((R_0 + \sigma) + \frac{r\sigma'}{2}\right) \qquad (3.1.3.2 - 5)$$

with $\psi_r \equiv \partial\psi/\partial r$. The relation of q and g is

$$q(\psi) = \frac{rg(\psi)}{\psi_r}\,\frac{r}{\sqrt{(R_0 + \sigma)^2 - r^2}} \times$$
$$\left(1 + \frac{\sigma'}{r}\left(\sqrt{(R_0 + \sigma)^2 - r^2} - (R_0 + \sigma)\right)\right) \qquad (3.1.3.2 - 6)$$

and the current given in terms of q^* is given by (Eq. 2.0.1.1.2 - 10),

$$\frac{rB_0}{q^*\psi_r} = \frac{1}{\sigma'\left(1 + \frac{\sigma}{R_0}\right) - \varepsilon}\left(\frac{\sigma'}{\sqrt{1 - \sigma'^2}} - \frac{\varepsilon}{\sqrt{\left(1 + \frac{\sigma}{R_0}\right)^2 - \varepsilon^2}}\right). \quad (3.1.3.2 - 7)$$

The expressions used for this model in the present work require only ε expansions of the full result. Other than the ballooning mode coefficient functions, that will be stated when needed in the appropriate sections, the useful quantities are the lowest order estimate of ψ_r determined from Eq. (3.1.3.2 - 6)

$$\psi_r = \frac{rB_0}{q(\psi)} + O(\varepsilon) \quad (3.1.3.2 - 8)$$

and the subsequent relation of q^* and q, obtained from combining (3.1.3.2 - 7) and (3.1.3.2 - 8)

$$\frac{q}{q^*} = \left(\frac{1}{\sigma' - \varepsilon}\right)\left(\frac{\sigma'}{\sqrt{1 - \sigma'^2}} - \frac{\varepsilon}{\sqrt{1 - \varepsilon^2}}\right), \quad (3.1.3.2 - 9)$$

the lowest order result being

$$\left(\frac{q^*(r)}{q(r)}\right)^2 = 1 - \sigma'^2 \ . \quad (3.1.3.2 - 10)$$

3.1.4 Self-consistent, Marginally Stable, Second Region Equilibria

A database of two-dimensional equilibria that are marginally stable at the second region boundary to high-n ballooning modes has been compiled to determine the behavior of the threshold values of the global variables, β and $\varepsilon\beta_p$, and the local normalized pressure gradient, α, above which second stability is reached.

A significant feature of the present technique of computing marginally stable second region threshold values is that the calculation is *self-consistent*, that is, the result of the stability calculation is fed back to the equilibrium. By iterating this procedure to marginal stability, the coefficients in the ballooning equation, that are directly influenced by the high $\varepsilon\beta_p$ distortion of the magnetic geometry of the equilibrium, are calculated consistently with the equilibrium values on each flux surface. An additional advantage to this procedure is that the marginal second stability region constraint eliminates $p(\psi)$ as an independent profile. This greatly reduces the number of predictor variables in the stability analysis. Notice that while the pressure and safety factor profiles are constrained in this analysis, the current profile is unconstrained. Consequently, it is found that some equilibria require a large ratio of the edge current density to the central current density in order to meet the marginal second region constraint. These equilibria may not be experimentally feasible, and therefore, the edge current density is a consideration in the determination of favorable second stability region operating regimes. This topic, and its relation to local direct access at the plasma edge will be discussed in Section 3.1.4.2.

3.1.4.1 Second Region Marginal Stability Constraint

The marginally stable, second region equilibria have been computed by using a two-dimensional flux coordinate equilibrium code[1] that iterates with a high-n ballooning solver until marginal second region stability is attained on each flux surface. This procedure involves choosing an initial equilibrium, with pressure profile $p'_{t=0}(\psi)$, and computing the high-n mode stability boundaries by solving the ballooning equation (3.0.3 - 33) at marginal stability,

$$\frac{\partial}{\partial\theta}\left(\frac{1+\Lambda^2}{\jmath|\nabla\psi|^2}\frac{\partial\xi}{\partial\theta}\right)+\frac{2\jmath\mu_0 p'(\psi)\,(\kappa_n - \Lambda\kappa_g)}{|\nabla\psi|}\xi = 0. \qquad (3.1.4.1 - 1)$$

The method of solving for the first and second region boundary marginally stable pressure gradients is outlined in Section 3:1.3.1.2. Once the stability is determined, the equilibrium pressure profile is altered to match the computed marginal second region boundary pressure gradient, $p_2'(\psi)$, at each flux surface. Both the edge pressure and the pressure gradient at the magnetic axis are chosen to be zero, however, the edge pressure gradient is allowed to be finite, since an unstable range of $p'(\psi)$ is generally possible at the edge, and $p'(\psi)$ is chosen to equal the second region $p'(\psi)$. On flux surfaces that are computed to be stable to large-n modes for all values of $p'(\psi)$, the magnitude of the pressure gradient is reduced exponentially. Both $p'(\psi)$ and $p''(\psi)$ are matched on the flux surfaces that join these regions with regions that exhibit a band of unstable $p'(\psi)$. Since the newly generated pressure gradient $p'_{t=1}(\psi)$ will in general be different than $p'_{t=0}(\psi)$, the equilibrium is recomputed using the newly computed pressure gradient, and the process is iterated until

$$<|p'_{(t)} - p'_{(t-1)}|> < 1\%, \qquad (3.1.4.1 - 2)$$

where <...> is an average over all flux surfaces. When this condition is met, the equilibrium is considered marginally stable, and is included in the database. The resulting $p'(\psi)$ profile vs. the minor radial flux coordinate, $\sqrt{(\psi - \psi_0)/(\psi_a - \psi_0)}$, is shown in Fig. 3.1.4.1 - 1 for a typical marginally stable equilibrium with $\theta_0 = 0$. An unstable region is formed by the ballooning instability. The lower bound to the region corresponds to the first stability region boundary, while the upper bound corresponds to the second region boundary. If the equilibrium $p'(\psi)$ lies between these two boundaries, it is ballooning mode unstable. Notice that the equilibrium $p'(\psi)$ in Fig. 3.1.4.1 - 1 is seen to lie on the second region boundary.

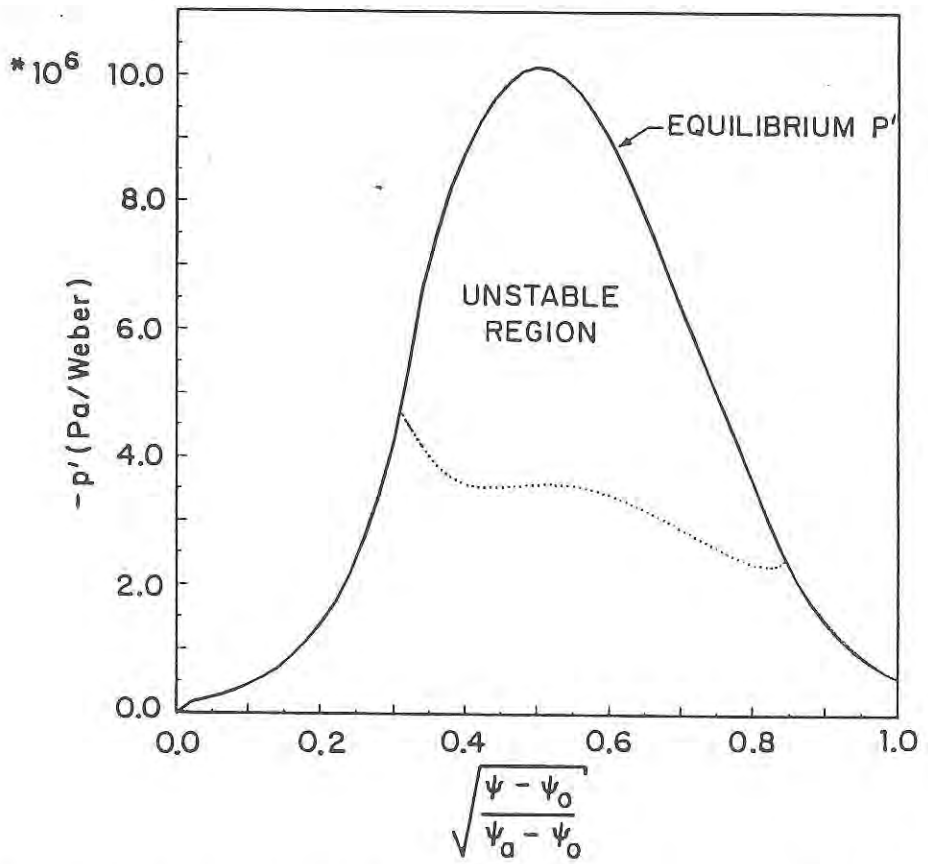

Fig. 3.1.4.1 - 1: Large-n instability region for A=7.5, q_0 =1.01, q_a =8.1, α_q =2.5, circular outer boundary equilibrium with θ_0 =0. The equilibrium pressure gradient lies on the second stability region boundary.

[1]Delucia, J., Jardin, S.C., and Todd, A.M.M., J. Comp. Phys. 37 (1980) 83.

3.1.4.2 Boundary Conditions and Edge Current Density

While iterating the equilibria to marginal second region stability, q is held constant and p is allowed to vary by matching the computed second region boundary. The current density is unconstrained in this procedure, and as expected, it is found that cases with large p' at the plasma edge also have a large current density at the plasma edge.

It is presently a matter of some controversy whether or not large pressure gradients and current densities can be sustained at the plasma edge in an actual tokamak. One problem is deciding where the "edge" of the plasma is actually located in a real machine. This is usually defined by a divertor or a limiter, while most MHD stability analyses, including the present one, assume that the edge is a rigid, perfectly conducting boundary. Another problem is that the current density is difficult to measure in a large tokamak experiment, so direct experimental verification is essentially nonexistent. Also, almost all tokamaks run with pressure gradients in the first stability region, and except for PBX, only recently have large tokamaks even considered operation at pressure gradients characteristic of the second stability region. Finally, H-mode plasma operation, for example in the DIII-D tokamak, displays very steep density gradients at the plasma edge. While this H-mode edge plasma is not in the second stability region, the gradients can occur on scale lengths that are too small to be described by ideal MHD.

Nonetheless, the general belief is that "large" edge pressure gradients and current densities cannot be supported in an actual tokamak. Since the magnitude of these quantities that can be supported is unknown, individual theories have been investigated. The work of Ramos[1] assumes that the current density at the plasma edge is identically zero, and this restriction leads to an equilibrium limit that scales as Eq. (1.0.1 - 1). The present study allows the pressure gradients and current densities to be large at the plasma edge. Equilibria of this kind are produced because local direct access does not appear in some cases, and the pressure gradient cannot be brought to zero at the edge, since it is constrained to lie on the second region boundary. Therefore, the appearance of a local direct access window at the plasma edge may be important in an actual second region tokamak to allow the pressure gradient to relax to zero at the edge. The conditions that produce an edge access window are described in the present work, and are considered favorable in producing a second region stable plasma in a tokamak experiment.

---

[1]Ramos, J.J., US-Japan Workshop on Kinetic Modifications of MHD Modes, Second Stability, and Alpha Particles in Toroidal Systems, Jan 9-13, PPPL, 1989.

3.1.4.3 Variation of Finite Radial Wavenumber

Previous work using the (S,α) model[1,2,3] to describe large toroidal mode number, n, stability correctly emphasizes the role of the finite radial wavenumber, θ_0, in calculating the marginal second region stability boundary to large-n modes. For this simple model, which is ordered in the inverse aspect ratio as $\beta \sim O(\varepsilon^2)$, and $\beta' \sim O(\varepsilon)$, it is found that $\theta_0=0$ is the most destabilizing choice for the first region boundary, but

that finite θ_0 is necessary in computing the eigenfunction that maximizes the destabilization of the second region boundary. In contrast, studies of the marginal second region boundary of fully two-dimensional equilibria[4,5,6] show that the destabilization of the second region boundary due to the variation of θ_0 is small and in most cases has a negligible effect on the pressure gradient above which second stability is attained. In fact, stabilization is seen on many unstable flux surfaces when θ_0 is taken to be finite. The discrepancy can be understood when the integrated local shear is examined in the (S,α) model and compared to more sophisticated numerical or analytic models. The pressure gradient driven modulation of the integrated local shear, which is responsible for the generation of the second stability region by reversal of the local shear,[7,8] is exaggerated in the (S,α) model. This leads to inflated values of the local shear and causes a stabilizing effect in the ballooning equation that must be compensated by finite θ_0 to yield the most unstable mode. However, in more complete models of equilibria and stability, the effect of geometry on the local shear decreases the role of the pressure gradient in the shear reversal process as the second region is approached. This effect greatly decreases the influence of finite θ_0 on the marginal second stability boundary.

The stabilizing effect of θ_0 can be understood by examining the large-n ballooning equation at marginal stability, Eq. (3.1.4.1 - 1). The arbitrary function θ_0 appears in Λ_p as an arbitrary constant of integration. This can be seen by combining Eqs. (3.0.3 - 26), (3.0.3 - 6), and the Grad-Shafranov equation (2.0.1.1.2 - 9), with the result,

$$\Lambda_p = \int_{\theta_0}^{\theta} \frac{\partial}{\partial \psi}\left(\frac{\mathcal{J} g}{R^2}\right) d\theta \,'$$

$$- \frac{g}{|\nabla \psi|^2} \int_{\theta_0}^{\theta} \left(\frac{\partial}{\partial \psi}\left(\frac{\mathcal{J}|\nabla \psi|^2}{R^2}\right) + \mathcal{J}\left(\mu_0 p'(\psi) + \frac{g g'(\psi)}{R^2}\right)\right) d\theta \,' . \quad (3.1.4.3 - 1)$$

Notice that the geodesic curvature term in the ballooning equation contains the integrated local shear. Assuming that $p'(\psi)$ is negative, the sign of this term is dependent on the product $\Lambda \kappa_g$. κ_g is an odd function of θ, so if Λ is also an odd function of θ with the opposite sign of κ_g, this term is destabilizing. Such a configuration is obtained for first region values of S and α when $\theta_0 = 0$. However, for larger values of α, the local shear can reverse sign near $\theta = 0$, causing Λ to be non-monotonic. The geodesic curvature term then becomes stabilizing in the region about $\theta = 0$ where $\Lambda \kappa_g$ is positive. This effect is well known and has been explained in the literature on second region stability.[2,3,8,9] The way to avoid this stabilizing effect is to choose θ_0 finite such that the result leads to the most unstable eigenfunction for the system. For the (S,α) model, this value of θ_0 corresponds to the value at which both Λ_p and S_{local} both vanish simultaneously.[2,3] This effect is shown schematically in Fig. 2 of Ref.[9]. Choosing θ_0 finite is then shown to have a large destabilizing effect on the marginal second region boundary in Ref.[2].

While finite θ_0 is clearly an important variable in the calculation of the most unstable second stability boundary for the (S,α) model of stability, its importance is exaggerated in comparison to the result obtained from large-n ballooning stability analysis of fully two dimensional, marginally stable, second region equilibria. The reason for this is that the (S,α) model overemphasizes the role of the pressure driven modulation of Λ_p that creates the second stability region. It does so primarily because

this modulation is the only feature that enables second stability to be produced in this model. However, geometry effects, such as the Shafranov shift, have a large effect on the modulation of Λ_p. Specifically, the pressure driven modulation is reduced by these effects in more sophisticated models of stability.

The destabilizing effect of θ_0 on the second region boundary for these equilibria is found to be much smaller than that expected by the simple (S,α) model. This can be seen in Fig. 3.1.4.3 - 1, where the equilibrium in Fig. 3.1.4.1 - 1 is tested for stability with finite values of θ_0 , varied in increments of $\pi/18$ from 0 to $\pi/2$ radians.

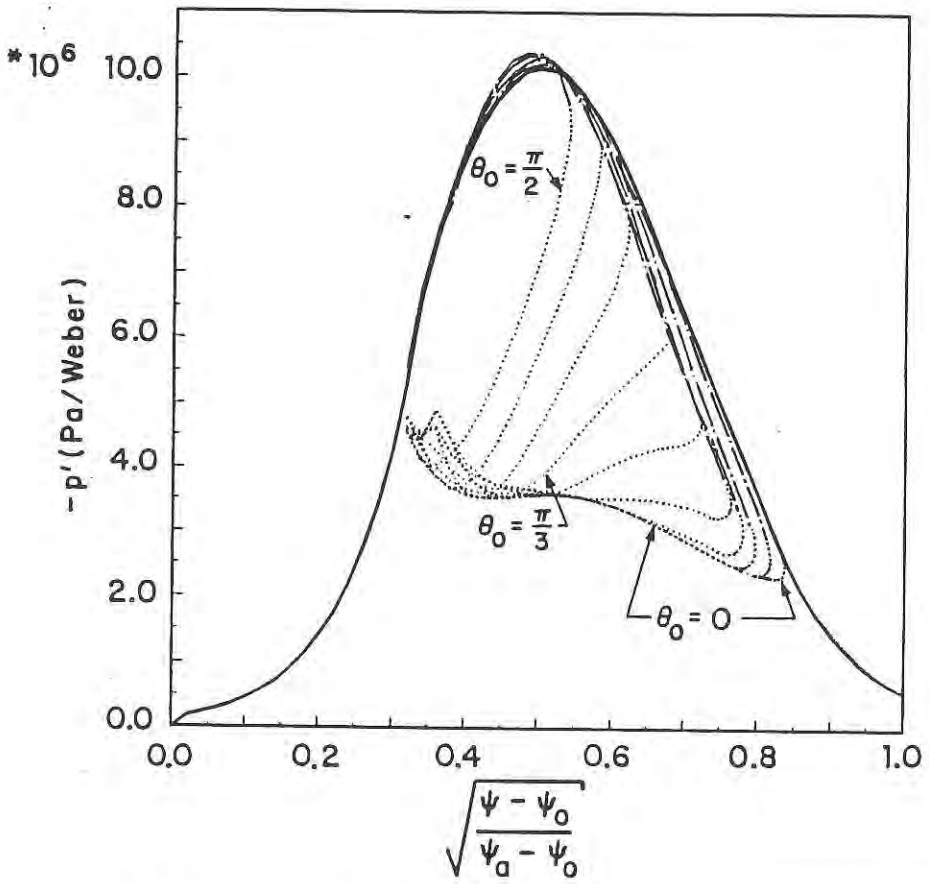

Fig. 3.1.4.3 - 1: Effect of θ_0 variation on the second stability region boundary for circular boundary equilibrium. *The equilibrium used is the same as in Fig. (3.1.4.1 - 1). The magnitude of the critical second region boundary pressure gradient is negligibly increased for finite values of θ_0.*

Note that in the two-dimensional calculations, θ_0 is specified on a scale θ_p where

$$\theta_p = 2\pi \left(\frac{\int_0^{\chi} \frac{J}{R^2} \, d\chi'}{\int_0^{2\pi} \frac{J}{R^2} \, d\chi'} \right), \qquad (3.1.4.3 - 2)$$

χ representing the poloidal angle coordinate used in the numerical computations. The unstable regions corresponding to $\pi/2 < \theta_0 \leq \pi$ were also computed, but are omitted for clarity. These regions are small, and are bounded by the regions with smaller θ_0 values. The maximum value of α for this equilibrium, $\alpha_{max} = 4.9$. Only a very small increase in the magnitude of the pressure gradient defining the second region boundary is noticed for finite θ_0 over the entire plasma. A more straightforward comparison to the (S,α) model can now be made by choosing a specific flux surface in this equilibrium and evaluating the ballooning equation coefficients locally. Treating S and α as parameters, a stability diagram similar to that found for the (S,α) model can be produced for various values of θ_0. Figs. 3.1.4.3 - 2a and 3.1.4.3 - 2b show these stability contours on the flux surface where $\alpha = \alpha_{max} = 4.9$ and Fig. 3.1.4.3 - 2c shows stability contours on the flux surface where $\alpha = 2.1$. Notice that finite θ_0 *enhances* stability on the flux surface shown in Figs. 3.1.4.3 - 2a and 3.1.4.3 - 2b. This is contrary to the intuition given by the (S,α) model result shown in Fig. 2 of Ref. 2, that indicates a large destabilization of the marginal second region boundary at finite θ_0. For the equilibrium shown in Fig. 3.1.4.1 - 1, the marginal stability curve is destabilized by finite θ_0 only on the flux surfaces $0.4 \leq \sqrt{(\psi - \psi_0)/(\psi_a - \psi_0)} \leq 0.5$. Local stability contours for a flux surface in this range are shown in Fig. 3.1.4.3 - 2c.

This figure contains the $\theta_0 = 0$ contour, and also the θ_0 contour that maximizes the destabilization of the second region boundary. Notice that the difference between the two contours increases as α increases, which is similar to the result found from the (S,α) model. However, the portions of the stability contours at large α are not calculated self-consistently, since only the local values of the ballooning equation coefficients at $\alpha = 2.1$ are used in this particular calculation. As shown in Figs. 3.1.4.3 - 2a and 3.1.4.3 - 2b, when a flux surface with a larger value of α is used, the destabilization seen in Fig 3.1.4.3 - 2c no longer exists. Fig. 3.1.4.3 - 3 shows results for an A=4.5, Dee shaped configuration to illustrate that the results are similar for finite aspect ratio, shaped configurations. The results are qualitatively the same for equilibria with larger maximum values of α.

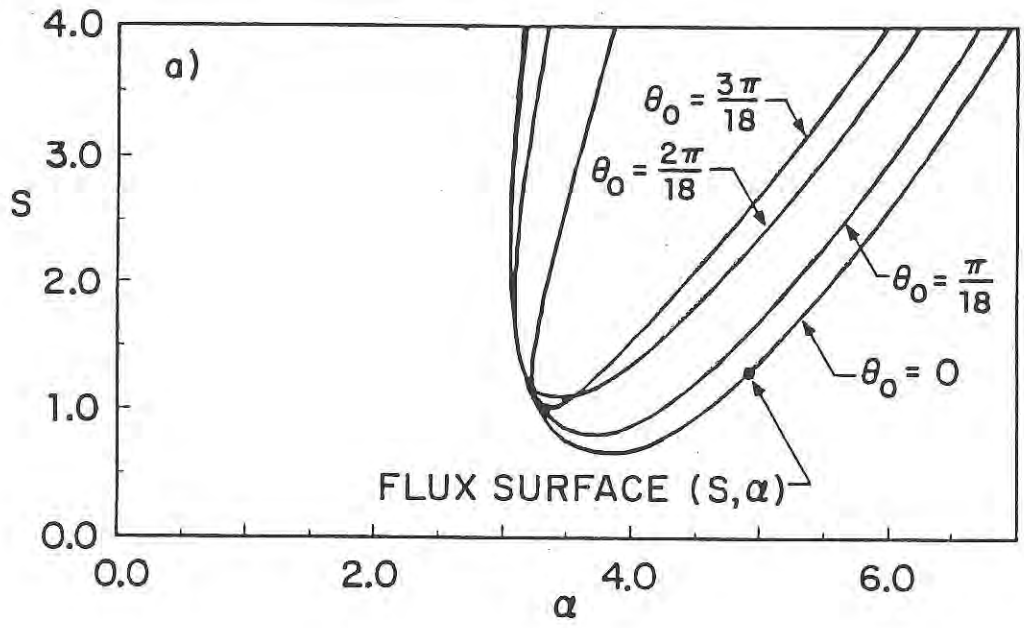

Fig 3.1.4.3 - 2: Effect of θ_0 variation on the local stability contours for circular boundary equilibrium.

a) Contours computed using flux surface with $S = 1.3$, $\alpha = \alpha_{max} = 4.9$, with θ_0 in the range $0 \le \theta_0 \le 3\pi/18$. Finite θ_0 enhances stability on this flux surface.

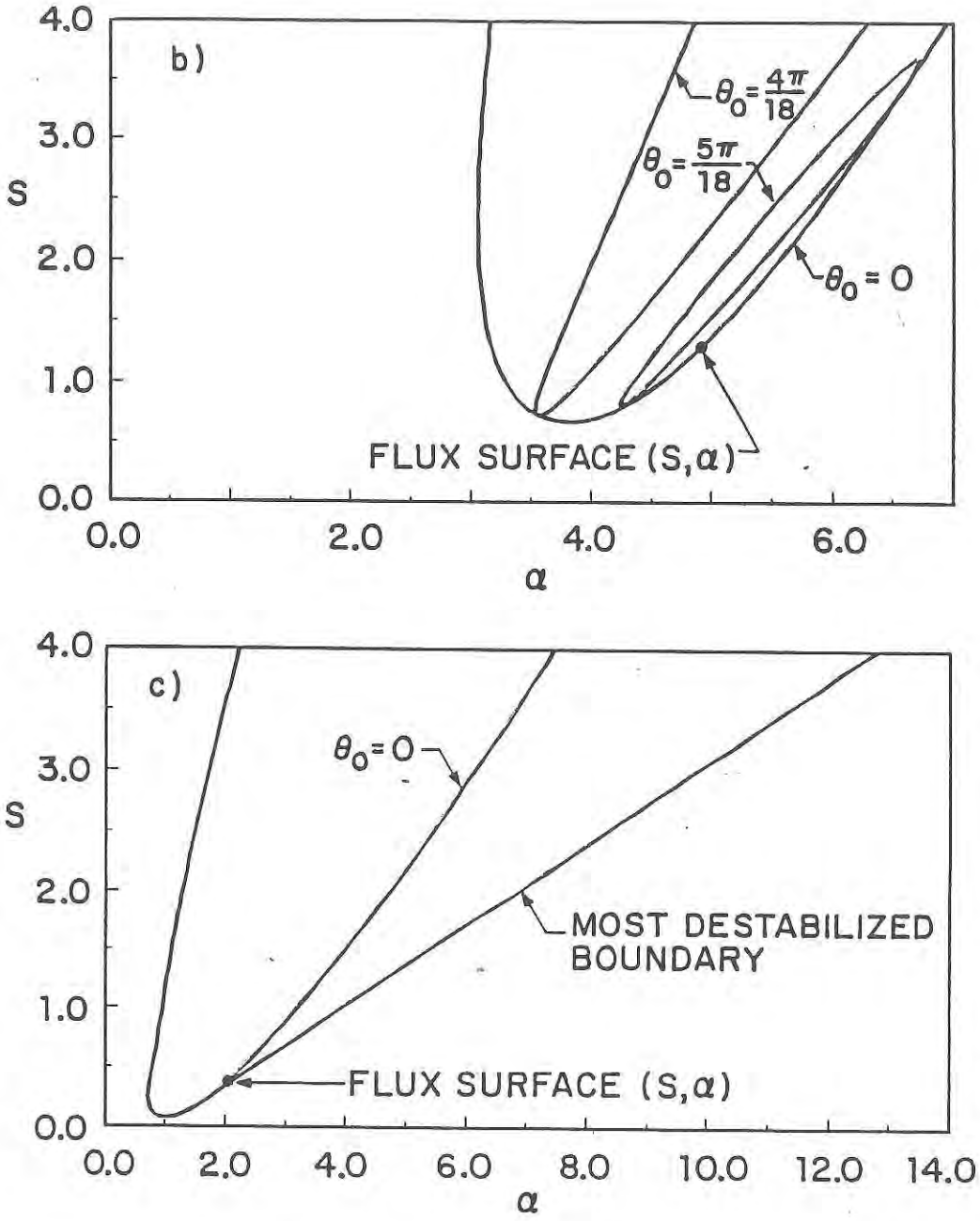

Fig 3.1.4.3 - 2: Effect of θ_0 variation on the local stability contours for circular boundary equilibrium.

b) ***Contours computed for the flux surface in a) with $4\pi/18 \leq \theta_0 \leq 5\pi/18$. The range $6\pi/18 \leq \theta_0 \leq \pi$ did not yield a region of instability for $0 \leq S \leq 4$. The surface $\theta_0 = 0$ is shown for comparison.***

c) ***Contours computed using flux surface with $S = 0.38$, $\alpha = 2.1$. Destabilization of the second region boundary for finite θ_0 is observed at large α, where the computation is not performed self-consistently.***

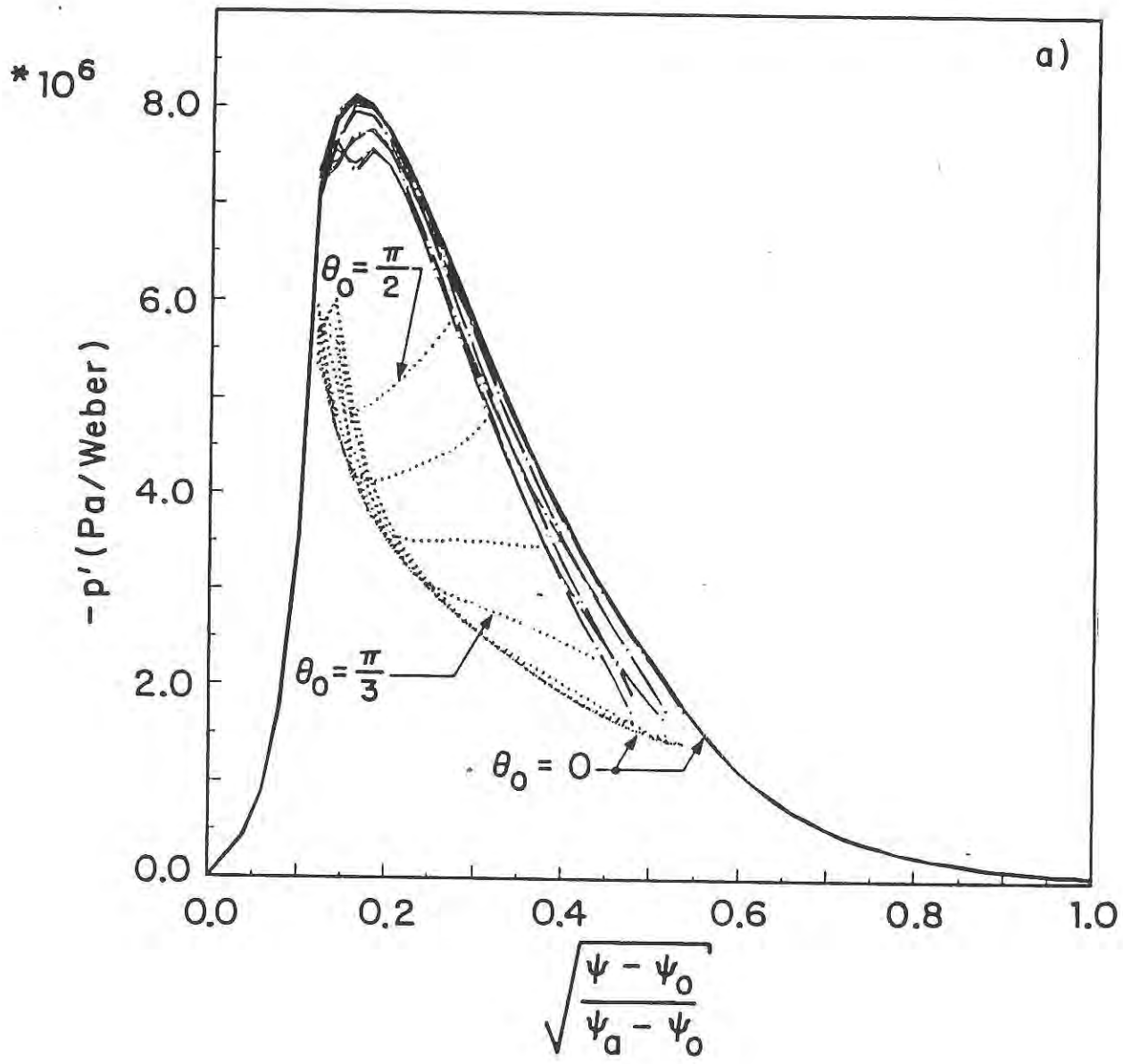

Fig 3.1.4.3 - 3: Effect of θ_0 variation on the second stability region boundary for Dee shaped equilibrium. *The equilibrium parameters are A=4.5, q_0 =1.01, q_a =8.1, α_q =1.1, elongation κ = 2.0, triangularity δ = 1.0.*

a) ***Global stability contours for $0 \leq \theta_0 \leq \pi/2$.***

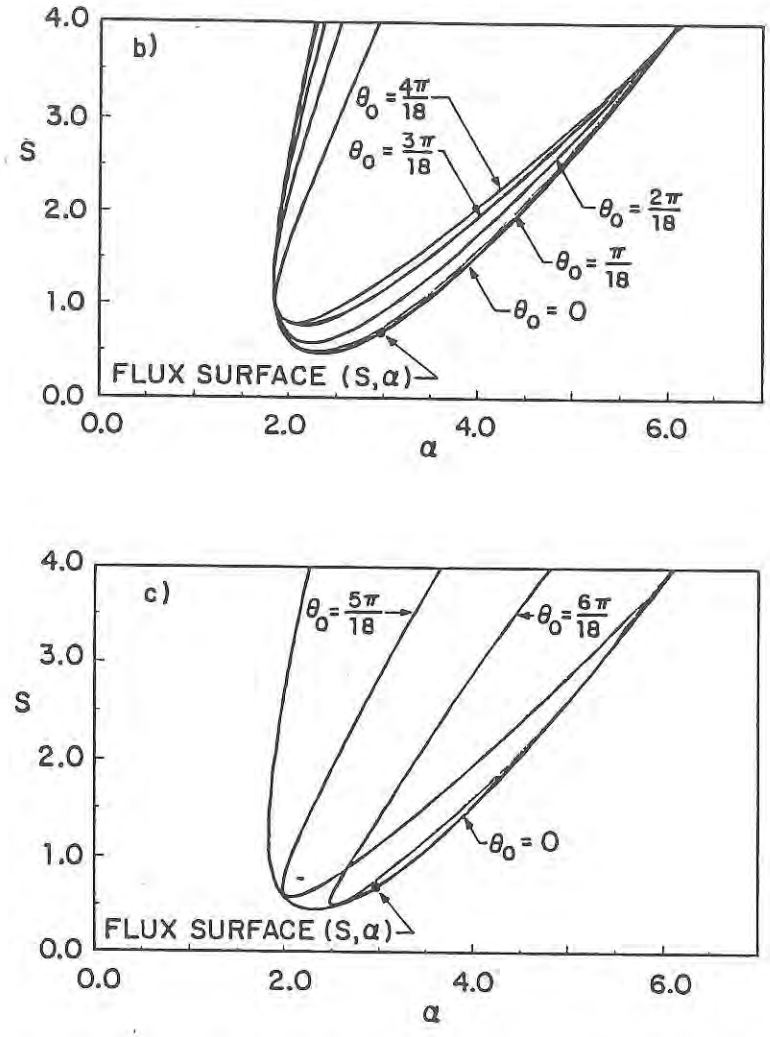

Fig 3.1.4.3 - 3: Effect of θ_0 variation on the second stability region boundary for Dee shaped equilibrium. *The equilibrium parameters are A=4.5, q_0 =1.01, q_a =8.1, α_q =1.1, elongation κ = 2.0, triangularity δ = 1.0.*

b) ***Local stability contours for θ_0 in the range $0 \leq \theta_0 \leq 4\pi/18$.*** *The flux surface used in the computation has $S = 0.70$ and $\alpha = \alpha_{max} = 3.0$.*

c) ***Local stability contours for $5\pi/18 \leq \theta_0 \leq 6\pi/18$.*** *The range $7\pi/18 \leq \theta_0 \leq \pi$ did not yield a region of instability for $0 \leq S \leq 4$. The surface $\theta_0 = 0$ is shown for comparison.*

The relative insensitivity of the second region boundary to variations in θ_0 for the two-dimensional, marginally stable equilibria can be explained by examining the integrated local shear. To examine how Λ_p is influenced by different physical effects in

the numerically generated equilibria, it is convenient to decompose it into geometric, pressure gradient, and magnetic field shear components as

$$\Lambda_p = \Lambda_p^{geom} + \Lambda_p^{p'} + \Lambda_p^{q'} \qquad (3.1.4.3 - 3)$$

where

$$\Lambda_p^{geom} = - \int_{\theta_0}^{\theta} \frac{\jmath B_t}{R^2 B_p} \left(2\kappa_p + \frac{2}{\jmath R B_p} \frac{\partial z}{\partial \theta'} \right) d\theta' + \frac{\int_{\theta_0}^{\theta} \frac{\jmath B^2}{R^2 B_p^2} d\theta'}{\int_0^{2\pi} \frac{\jmath B^2}{R^2 B_p^2} d\theta'} \int_0^{2\pi} \frac{\jmath B_t}{R^2 B_p} \left(2\kappa_p + \frac{2}{\jmath R B_p} \frac{\partial z}{\partial \theta'} \right) d\theta' , \quad (3.1.4.3 - 4)$$

$$\Lambda_p^{p'} = \mu_0 p'(\psi) \left(\int_{\theta_0}^{\theta} \frac{\jmath B_t}{R B_p^2} d\theta' - \frac{\int_{\theta_0}^{\theta} \frac{\jmath B^2}{R^2 B_p^2} d\theta'}{\int_0^{2\pi} \frac{\jmath B^2}{R^2 B_p^2} d\theta'} \int_0^{2\pi} \frac{\jmath B_t}{R B_p^2} d\theta' \right) , \quad (3.1.4.3 - 5)$$

$$\Lambda_p^{q'} = 2\pi q'(\psi) \frac{\int_{\theta_0}^{\theta} \frac{\jmath B^2}{R^2 B_p^2} d\theta'}{\int_0^{2\pi} \frac{\jmath B^2}{R^2 B_p^2} d\theta'} , \qquad (3.1.4.3 - 6)$$

$$\kappa_p \equiv \frac{\nabla\psi}{|\nabla\psi|} \cdot \left(\frac{\mathbf{B}_p}{B_p} \cdot \nabla\right)\frac{\mathbf{B}_p}{B_p}, \qquad (3.1.4.3 - 7)$$

z is the cylindrical coordinate parallel to the centerline of the torus, and B_p is the poloidal field. The $q'(\psi)$ component is further reduced by separating the periodic and secular components

$$\Lambda_p^{q' \, periodic} = \Lambda_p^{q'} - q'(\psi)(\theta - \theta_0). \qquad (3.1.4.3 - 8)$$

To simplify comparison between the numerical and analytic stability models, Λ_p and its components can be normalized as

$$\Lambda_n = \frac{r^2 B_0}{q^2}\Lambda_p, \qquad (3.1.4.3 - 9)$$

the subscript "n" denoting the normalized quantities. Note that for the (S,α) model

$$\Lambda_n = S\left(\theta - \theta_0\right) - \alpha\left(\sin(\theta) - \sin(\theta_0)\right), \qquad (3.1.4.3 - 10)$$

therefore, $\Lambda_n^{q' \, periodic}$ and Λ_n^{geom} vanish identically. Terms that are due to the effects of geometry alone are absent from this model. Only terms that are explicitly dependent on the pressure gradient and the magnetic field shear appear. Shown in Fig. 3.1.4.3 - 4 are Λ_n and its components for the flux surface with the largest value of α in the equilibrium shown in Fig. 3.1.4.1 - 1. Superimposed in Fig. 3.1.4.3 - 4b is Λ_n calculated by the (S,α) model. Notice that for the two dimensional marginally stable equilibrium, Λ_n^{geom} is finite and of the same order as $\Lambda_n^{p'}$, but of opposite sign. The geometric effects on Λ_n associated with flux surface distortion counteract the pressure gradient effect. When comparing these results to the (S,α) model in Fig. 3.1.4.3 - 4b, it is clear that the simpler model exaggerates the pressure gradient modulation of Λ_n, which leads to the

sensitivity of the second stability boundary with respect to θ_0 as described earlier. The complete self-consistent minimization of ξ performed in the two dimensional equilibria causes a large region in θ where Λ_n and $\partial\Lambda_n/\partial\theta$, both of which are responsible for the stabilizing effects of field line bending, are nearly zero. This behavior is responsible for the greatly decreased sensitivity of the second region boundary to the variation of θ_0.

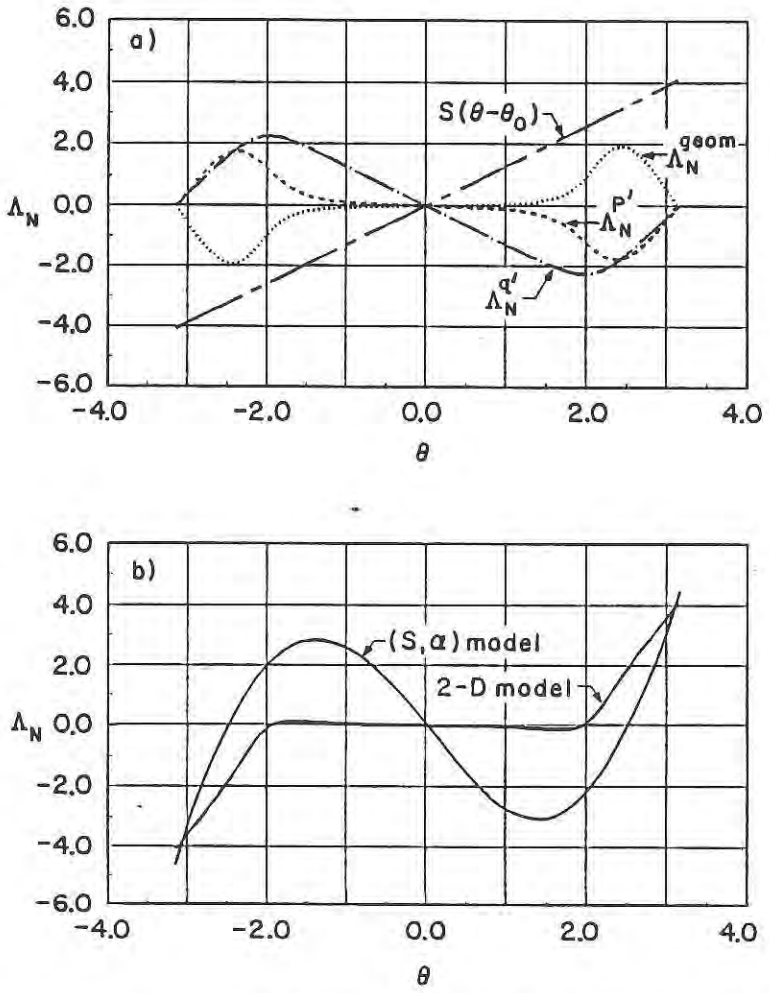

Fig. 3.1.4.3 - 4: Normalized integrated local shear as a function of θ. The flux surface, chosen for this analysis of Λ_n from the equilibrium shown in Fig. 3.1.4.1 - 1, has S = 1.3, α = 4.9.

*a) **Components of** Λ_n **vs.** θ. Geometric effects not related to q'(ψ) reduce the local shear reversal caused by p'(ψ) effect.*

*b) **Total** Λ_n **for two dimensional equilibrium and (S,α) model.** The modulation of Λ_n that leads to local shear reversal is greatly exaggerated in the simpler model.*

The physical mechanisms responsible for this behavior are included in another simple analytic model, that of shifted circular equilibria.[10,11] It is found that distortion of the concentric circular flux surface geometry, accomplished by shifting the circular flux surfaces outward, reduces the modulation of the integrated local shear. Notice that this reduction is still realized in this model even though the toroidal field assumes the vacuum value and all other ε effects vanish identically. For the shifted circular flux surface model,

$$\Lambda_n = S\left(\theta-\theta_0\right) + \left(\not{F}\ \sigma' + \eta\right)\sin(\theta) - \eta\sin(\theta_0)\,, \qquad (3.1.4.3\text{ - }11)$$

$$\eta \equiv \frac{3\sigma'\left(S\text{-}1+\sigma'^2\right) - \alpha\left(1-\sigma'^2\right)^{\frac{5}{2}}}{\left(1+2\sigma'^2\right)}\,,$$

$$\not{F} \equiv \left(1+\sigma'\cos(\theta)\right)\,.$$

Λ_n then reduces to the standard (S,α) model result when the derivative of the Shafranov shift, $\sigma'(r) = 0$. In Fig. 3.1.4.3 - 5, Λ_n vs. θ is plotted for two different values of σ', zero corresponding to the (S,α) model, and the finite value corresponding to the flux surface shown in Fig. 3.1.4.3 - 4. This value of $\sigma'(r)$ is computed using the relation

$$\left(\sigma'(r)\right)^2 + \left(\frac{q^*(r)}{q(r)}\right)^2 = 1\,. \qquad (3.1.4.3\text{ - }12)$$

It is clear that for $\sigma' = 0$, there is a large pressure driven modulation, of amplitude α, which leads to the stabilizing effect described previously. However, with finite σ', the modulation of Λ_n is reduced by a factor $\left(1-\sigma'^2\right)^{\frac{5}{2}}$ due to the non-concentric geometry.

As α increases to cause the reversal of S_{local}, σ' subsequently increases to maintain equilibrium, and the stabilizing effect is reduced. As $|\sigma'|$ approaches its limiting value of unity, the effect of geometry on the modulation of Λ_n dominates over the effect of the local pressure gradient. Therefore, if any decrease in the stability of the second region boundary is found, it is seen at small ψ where α can be greater than S, yet σ' is still small. This occurs only near the magnetic axis in the two dimensional marginally stable elongated equilibria with no triangularity, that exhibit the largest threshold values of α needed to reach second stability.[4]

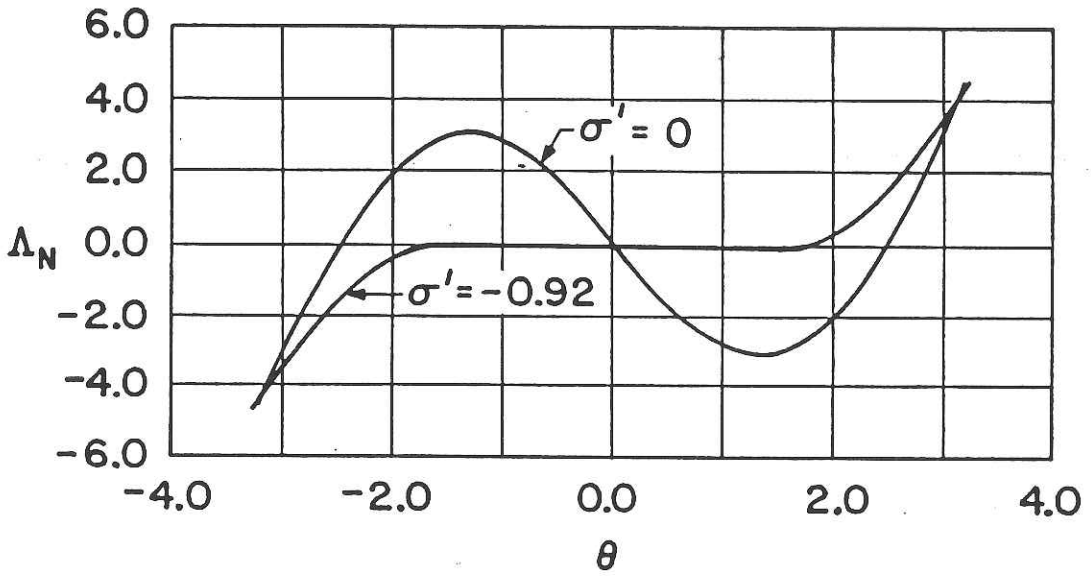

Fig. 3.1.4.3 - 5: Normalized integrated local shear for (S,α) and shifted circular flux surface stability models; $S = 1.3$, $\alpha = 4.9$.

---

[1]Connor, J.W., Hastie, R.J., Taylor, J.B., Phys. Rev. Lett. 40 (1978) 398; Proc. R. Soc. London Ser. A 365 (1979) 1.

[2]Chen, Liu, Bondeson, A., Chance, M.S., Nuclear Fusion 27 (1987) 1918.

[3]Llobet, X., Berk, H.L., Rosenbluth, M.N., Phys. Fluids 30 (1987) 2750.

[4]Sabbagh, S.A., Mauel, M.E., Navratil, G.A., Hughes, M.H., Phillips, M.W., Todd, A.M.M., Fu, G.Y., Van Dam, J.W., and Rosenbluth, M.N.,in *Plasma Physics and Controlled Nuclear Fusion Research* (Proc. 12th Int. Conf. Nice, 1988) Vol. 2, IAEA, Vienna (1989) 319.

[5]Sabbagh, S.A., Hughes, M.H., Phillips, M.W., Todd. A.M.M., Navratil, G.A., Nuclear Fusion 29 (1989) 423.

[6]Sabbagh, S.A., Phillips, M.W., Todd. A.M.M., Navratil, G.A., Bull. Am. Phys. Soc. 33 (1988) 1929.

[7]Coppi, B., Phys. Rev. Lett. 39 (1977) 939.

[8]Greene, J. M., and Chance, M.S., Nuclear Fusion 21 (1981) 453.

[9]Gerver, M.J., Kesner, J., Ramos, J.J., Phys. Fluids 31 (1988) 2674.

[10]Clarke, J.F., and Sigmar, D.J., Phys. Rev. Lett. 38 (1977) 70.

[11]Choe, W.H., and Friedberg, J.P., Phys. Fluids 29 (1986) 1766.

3.1.5 Global Stability Diagrams

Several numerical and analytical studies using simple equilibrium models[1-7] have investigated the relation of α and S at both low and high values of shear. However, because stability is determined locally, that is, on each flux surface in the present study, a more general diagram showing the relation of α to S is needed. For example, Fig. 3.1.5 - 1 shows a generalization of the standard (S,α) diagram for a marginal second region equilibrium. Notice that each flux surface is represented by a point (S_i,α_i) on this diagram. A separate marginal stability contour is traced out on each flux surface by solving the ballooning equation for α while varying S using the geometry of the flux surface at the point (S_i,α_i). Therefore, while marginal stability contours can be determined on each flux surface, they are only extrapolations away from the point (S_i,α_i), since the equilibrium geometry only applies to this point. The points that self-consistently describe the marginal second region boundary are the locus

of intersections between the points (S_i,α_i) and the computed marginal stability boundary. The other important feature of Fig. 3.1.5 - 1 is point 3, where the value S_i, falls below the value S_{crit}, and no intersection is possible. When $S < S_{crit}$, no unstable mode is found for any value of α, and the flux surface is said to have *local direct access* to the second stability region.

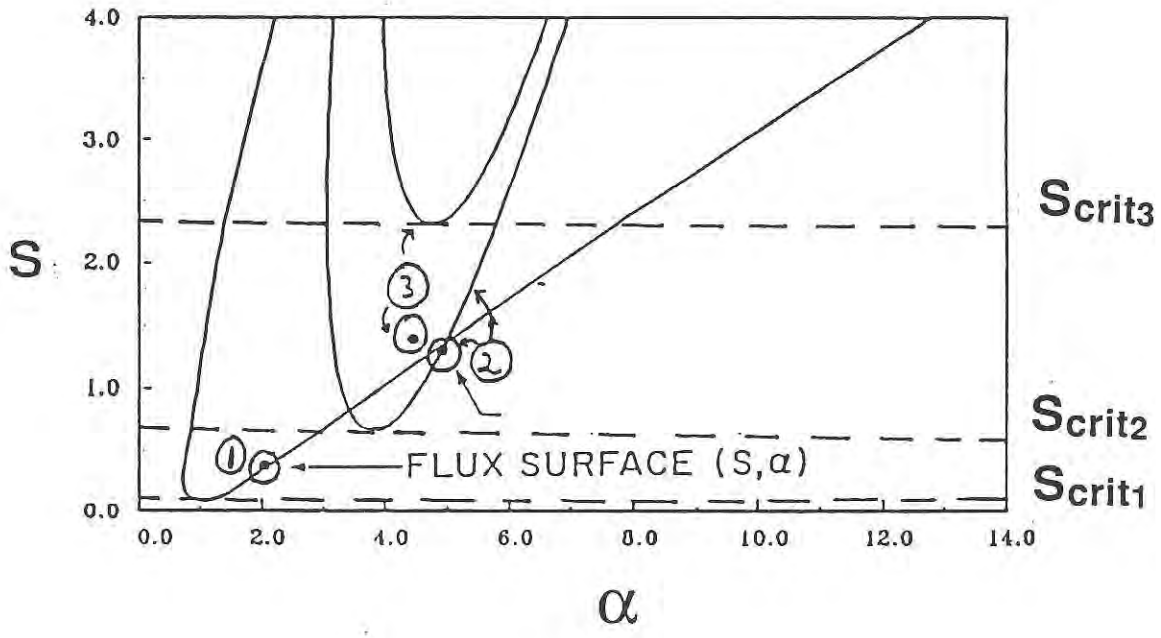

Fig. 3.1.5 - 1: Generalization of standard (S,α) diagram for numerically computed, marginally stable second region equilibrium. *Each flux surface produces a separate marginal stability contour. Notice that for the flux surfaces denoted by 1 and 2, $S > S_{crit}$, and the equilibrium flux surface "point" lies on the second region boundary. However, point 3 has $S < S_{crit}$, therefore the flux surface has direct access between the first and second stability region.*

If a contour diagram such as Fig. 3.1.5 - 1 is represented three-dimensionally, a generalized stability diagram is obtained. Such a diagram has been used by Chance, et al.[8,9] and is shown schematically in Fig. 3.1.5 - 2. Data describing the unstable region for a given equilibrium can be neatly extracted from this diagram in the following way. By varying α at constant S from a particular flux surface (S_i,α_i), a maximum of two intersections with a "local" (S,α) stability curve is encountered (see Fig. 3.1.5 - 2). A two-dimensional "global" (S,α) diagram illustrating the behavior of the unstable region that includes the effects of the distortion of the magnetic geometry in the stability calculation is obtained by considering the locus of intersection points projected upon the (α,S) plane. This diagram was first showed schematically by Coppi, et al.[10]. By projecting the unstable region upon the (α,ψ) plane, a similar global stability diagram is obtained, and was first shown by Phillips.

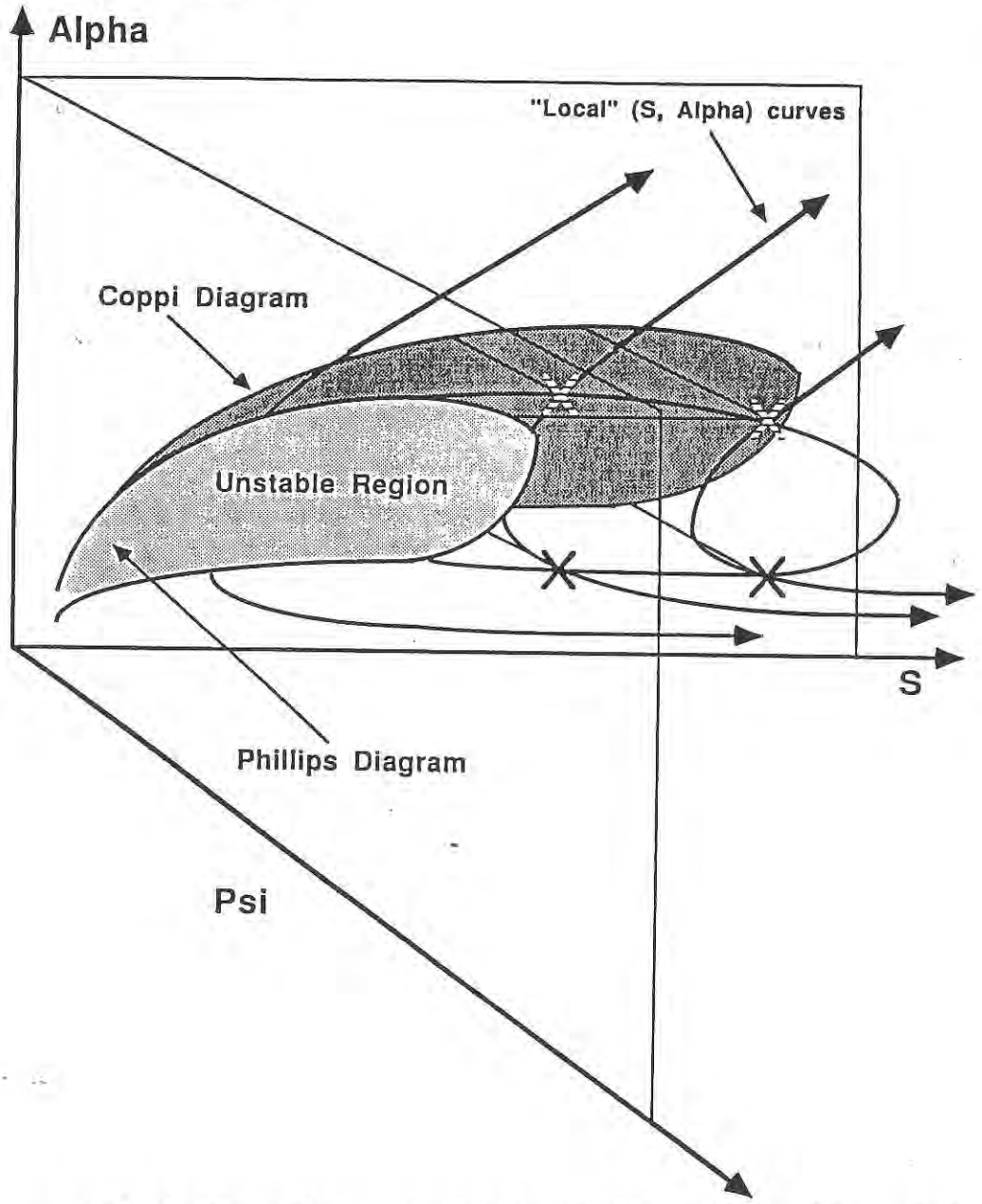

Fig. 3.1.5 - 2: Chance Diagram: the three dimensional generalization of the standard (S,α) diagram. *By varying α for a given equilibrium S(ψ), the local (S,α) marginal stability curve can be crossed. The crossed points form the periphery of the large-n unstable region. Two-dimensional global stability diagrams are produced by projecting the unstable region in the 3-d space on the (α,ψ) and (α,S) planes.*

The global (S,α) diagram clearly and concisely illustrates the relation of α_2 to S for a given marginally second stable equilibrium. Fig. 3.1.5 - 3 shows the important features of such a diagram. Note that in this figure, α and S have been transposed from

the local (S,α) diagrams, so that α is the ordinate and S is the abscissa. In general, an equilibrium will exhibit first and second stability boundaries. Notice that for marginally stable second region equilibria, the equilibrium α lies on the second region boundary. Another feature shown is the opening of a local direct access window between the first and second stability regions near the plasma edge. As shown before in Fig. 3.1.5 - 1, this happens when the equilibrium $S(\psi) < S_{crit}(\psi)$, and α is not constrained by an unstable region. The scaling of the second region boundary expressed in the local variables $S(\psi)$ and $\alpha(\psi)$ will then in general consist of a relation between α_2 and S, when α_2 is constrained. When unconstrained, α_2 is arbitrary and $S(\psi) < S_{crit}(\psi)$ determines the portion of the plasma where local direct access is possible.

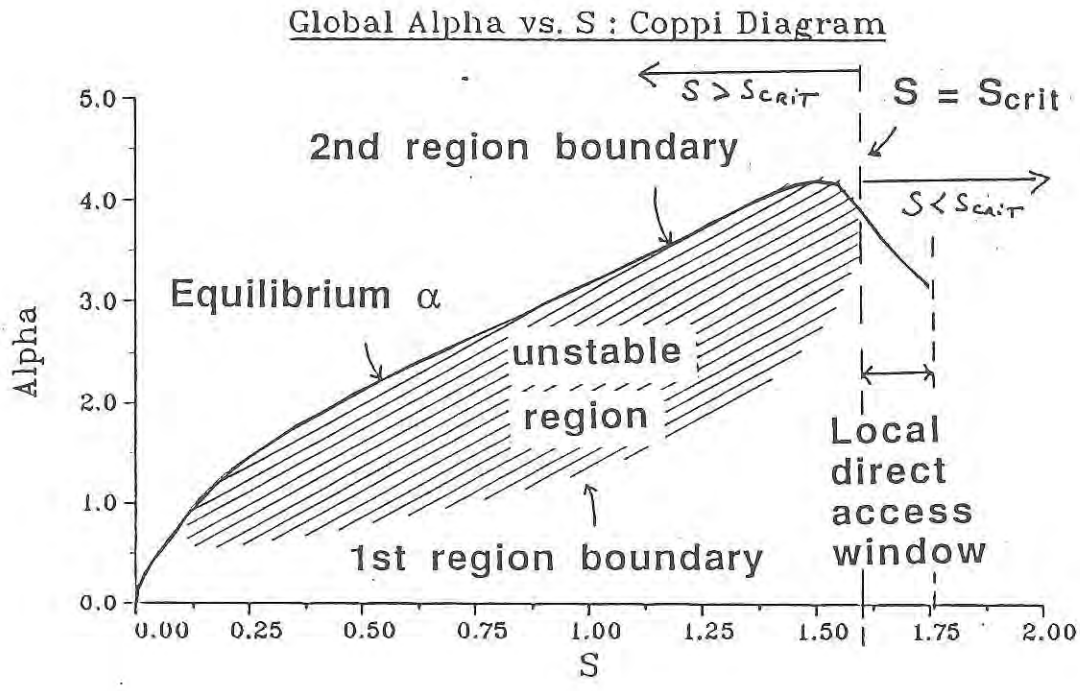

Fig. 3.1.5 - 3: Anatomy of the global (S,α) stability diagram (Coppi diagram). A large-n unstable region exists separating the first and second stability regions for $0.1 < S < 1.6$. For larger values of S, no unstable region exists and a local direct access window is formed.

[1]Connor, J.W., Hastie, R.J., Taylor, J.B., Phys. Rev. Lett. 40 (1978) 398; Proc. R. Soc. London Ser. A 365 (1979) 1.

[2]Pogutse, O.P, Chudin, N.V., Yurchenko, E.I., Sov. J. Plasma Phys. 6 (1980) 341.

[3]Pogutse, O.P., and Yurchenko, E.I., JETP Lett. 28 (1978) 318.

[4]Lortz, D., Nuhrenberg, J., Phys. Lett. 68a (1978) 49.; Nuclear Fusion 19 (1979) 1207.

[5]Llobet, X., Berk, H.L., Rosenbluth, M.N., Phys. Fluids 30 (1987) 2750.

[6]Chen, Liu, Bondeson, A., Chance, M.S., Nuclear Fusion 27 (1987) 1918.

[7]Choe, W.H., and Friedberg, J.P., Phys. Fluids 29 (1986) 1766.

[8]Chance, M.S., in Theory of Fusion Plasmas (Proceedings of the Varenna Workshop, Varenna, Italy, 1987) Vol. 1, Editrice Compositori, Bologna (1987).

[9]Simonen, T.S., et al., Phys. Rev. Lett. 61 (1988) 1720.

[10]Coppi, B., Crew, G.B., and Ramos, J.J. Comments on Plasma Physics and Controlled Fusion 8 (1983) 11.

3.1.6 Second Stability β, $\varepsilon\beta_p$, and Pressure Gradient Thresholds

In this section, the behavior of the second region threshold values of β, $\varepsilon\beta_p$ and α is reviewed as a function of the tokamak aspect ratio, the three q profile parameters q_0, q_a, α_q, and the outer boundary shape parameters κ and δ. Physical explanations for the characteristics of the β, $\varepsilon\beta_p$ and α curves will be given directly following the general summary of the results in each subsection.

3.1.6.1 Aspect Ratio and q_0 Effects

Shown in Fig. 3.1.6.1 - 1 are the β_2 and $\varepsilon\beta_{p2}$ curves as a function of A for various values of q_0 in a circular cross section plasma. Consider the behavior of β_2 for conventional tokamak operation at q_0 ~1. There is a dramatic increase in β_2 as A is decreased at q_0 = 1.01. The reason for this behavior is apparent when examining the global (S,α) stability diagrams for this curve in Fig. 3.1.6.1 - 2. At A = 3, there is basically a linear relationship of α_2 to S in the inner part of the plasma at small S. However, α_2 increases non-linearly at the edge of the plasma at large S . Notice that there is no direct access window at the plasma edge in this case, and that α_2 is largest at the edge. This not only leads to the large value of β_2, but also a large ratio of the average edge toroidal current density to the central current density, which is 65% in this case. This configuration is therefore a poor choice for the operating point of a second region experiment. As A is increased at q_0 = 1.01, there are two important changes in the behavior of α_2 . First, there is a large decrease in the slope of α_2 near the plasma edge. Second, a local direct access window appears at the plasma edge. Both of these effects reduce β_2 as A is increased. Recall that a direct access window appears when $S(\psi) < S_{crit}(\psi)$, and since the edge value of S is approximately the same as A is varied (Fig. 3.1.6.1 - 2), the direct access window occurs because S_{crit} increases rather than S decreasing. Therefore, there is a genuine enhancement of stability at high A that leads to the formation of the edge access window. Edge access also occurs for $q_0 > 1$ at low A in the A=2, q_0 =2 case.

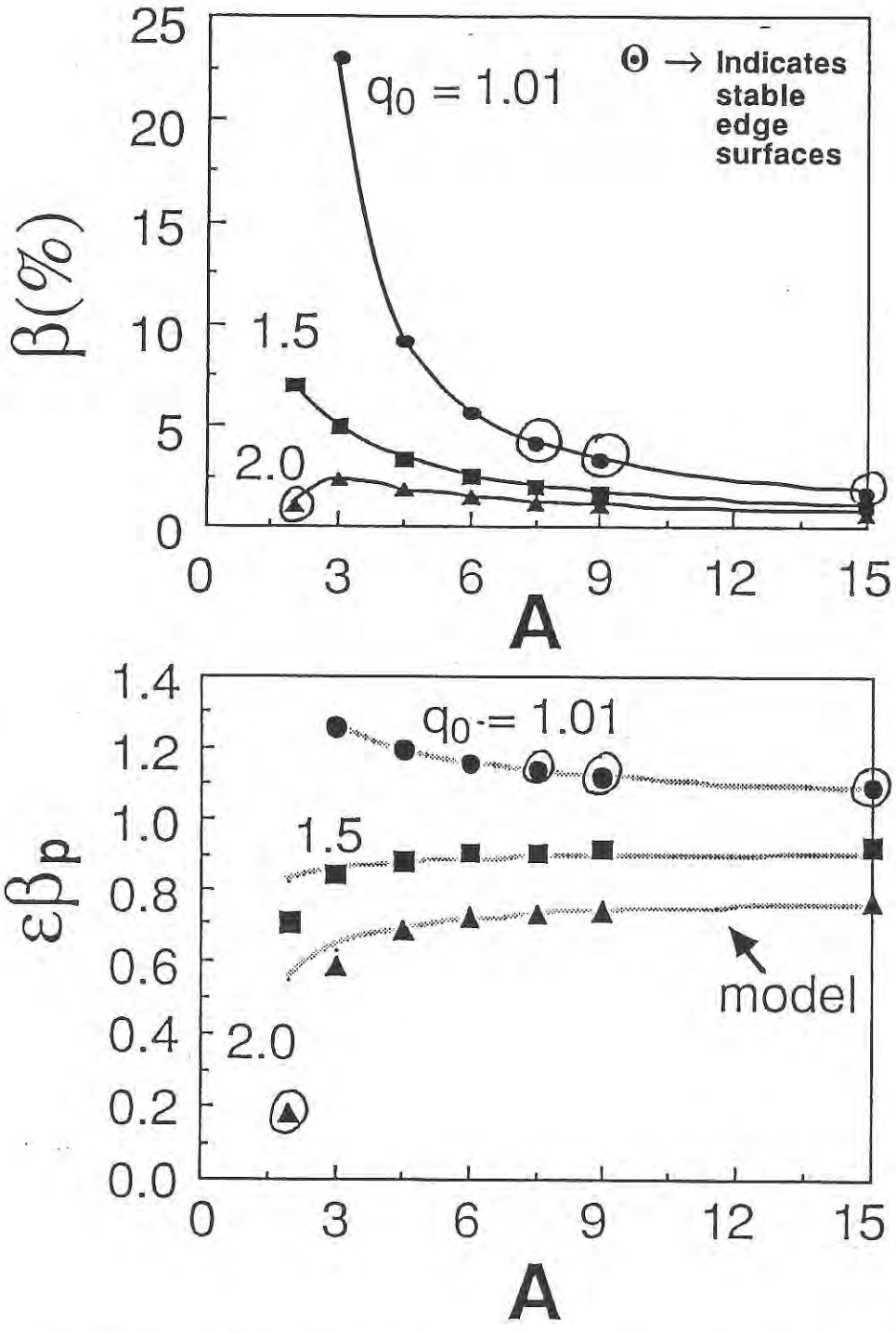

Fig. 3.1.6.1 - 1: β_2 and $\varepsilon\beta_{p2}$ vs. A and q_0 for circular boundary equilibria: $\alpha_q = 2.5$, $q_a = 4.1$. There is a marked increase in these second region threshold values at low A and $q_0 \sim 1$. Local access at the plasma edge, marked by circled points, occur at high A for $q_0 \sim 1$ and low A for $q_0 \geq 2$.

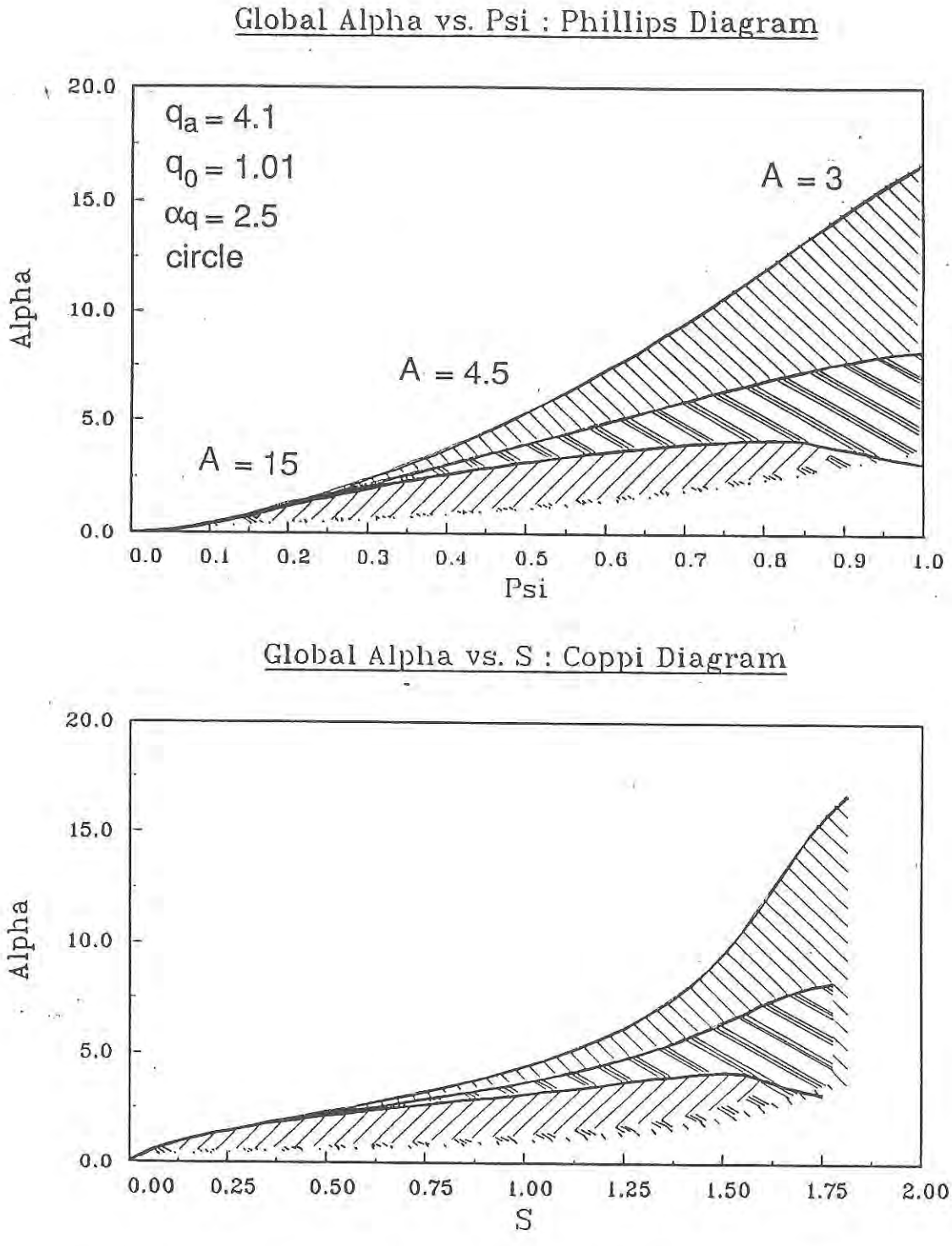

Fig. 3.1.6.1 - 2: Global stability diagrams for q_0 = 1 cases of Fig 3.1.6.1-1: A=3, 4.5, 15. Note that α_2 increases non-linearly as a function of S for A=3 and local direct access occurs at the plasma edge for A=15.

When $q_0 > 1$, the large increase in β_2 as A is decreased is no longer apparent. In fact, for sufficiently low A and sufficiently high q_0, β_2 *decreases* as A decreases (Fig. 3.1.6.1 - 1). Fig. 3.1.6.1 - 3 shows that when $q_0 = 2.0$ at $A \leq 4.5$, for equilibria with $\alpha_q = 1.1$, there is local direct access on all surfaces (global access), and $\beta_2 \equiv 0$. The global (S,α) diagram for the α_q =2.5 case (Fig. 3.1.6.1 - 4) shows that the slope of α_2 is greatly reduced for $q_0 > 1$, and that the linear relationship between α_2 and S returns. Notice however that a direct access window does not appear at the edge as q_0 is increased. Therefore, the reduction of the slope of α_2, and not the appearance of a local direct access window at the plasma edge, is responsible for the reduction of β_2 at low A and high q_0. Global direct access occurs suddenly as q_0 is increased, and occurs first in lower A configurations. Fig. 3.1.6.1 - 3 also shows that at high A, the sensitivity of β_2 to variations in q_0 is reduced. Increasing q_0 decreases $\varepsilon\beta_{p2}$ at all A. $\varepsilon\beta_{p2}$ is shown to be insensitive to A at low A, but there is a marked decrease of $\varepsilon\beta_{p2}$ toward zero as global direct access is approached at low A and high q_0.

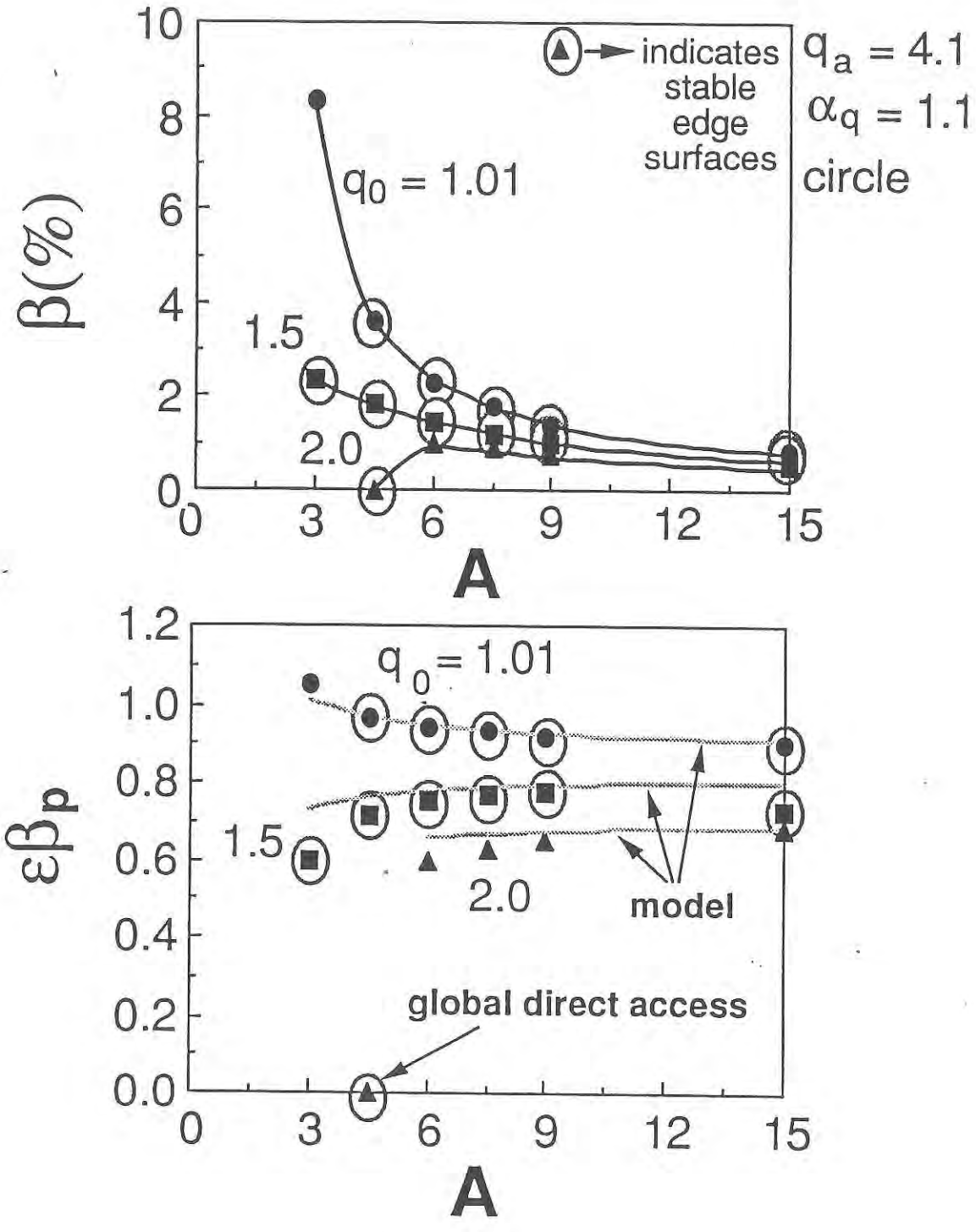

Fig. 3.1.6.1 - 3: *β_2 and $\varepsilon\beta_{p2}$ vs. A and q_0 for circular boundary equilibria: $\alpha_q = 1.1$, $q_a = 4.1$. At $A \leq 4.5$ and $q_0 \geq 2$, global direct access to the second region occurs.*

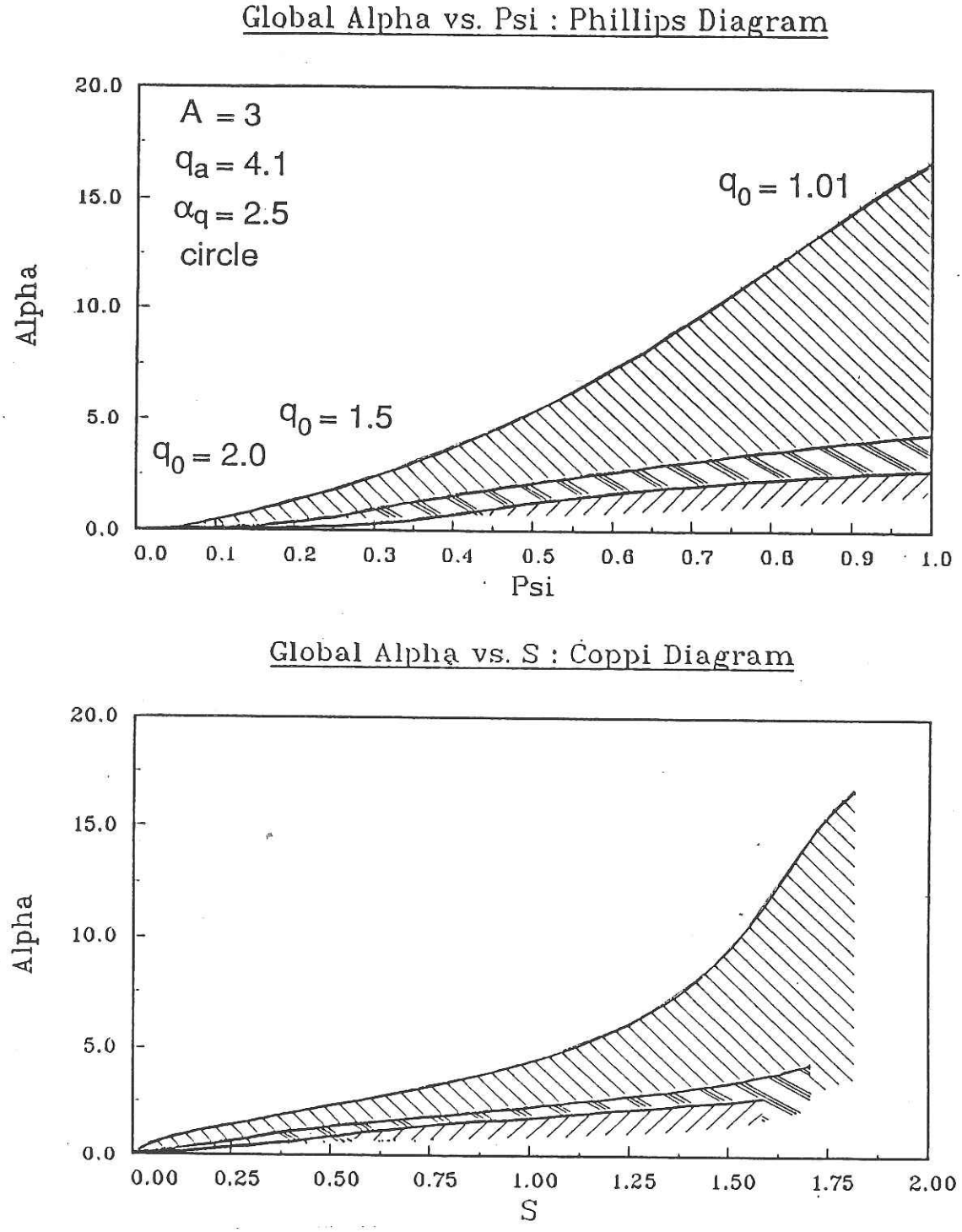

Fig. 3.1.6.1 - 4: Global stability diagrams for A=3 cases of Fig 3.1.6.1-1: q_0=1.01, 1.5, 2.0, α_q = 2.5. Note that the linear relation of α_2 to S returns as q_0 increases.

The stabilization or destabilization of the second region boundary, and the formation of the direct access window at the plasma edge are determined by the relative strength of the poloidal field component of κ_n to that of the toroidal field component of κ_n . Examining each effect separately, first consider the case A=15 and $\alpha_q = 2.5$, while varying q_0. Global (S,α) diagrams for this case are shown in Fig. 3.1.6.1 - 5. Notice that α and S are linearly related, except at the plasma edge for q_0 = 1.01, where an access window exists. This behavior agrees with the results obtained by Choe, et al.[1] for the stability of the infinite A, shifted flux surface model of plasma equilibrium.[2]

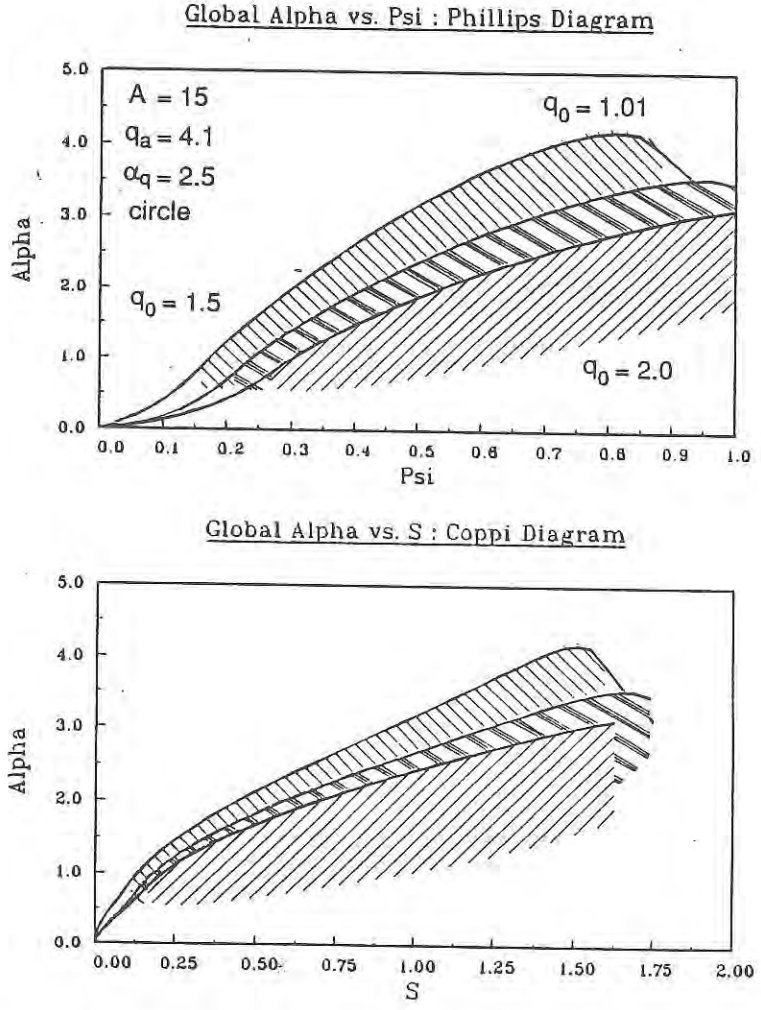

Fig. 3.1.6.1 - 5: Global stability diagrams for A=15 cases of Fig 3.1.6.1-1: q_0=1.01, 1.5, 2.0. Note that the edge access window is lost for the higher q_0 cases.

As a guide to the origins of the stabilizing effect, consider the ballooning equation (3.1.4.1 - 1) for the shifted circular flux surface model of equilibrium (Section 3.1.3.2) which yields

$$\frac{\partial}{\partial\theta}\left(\frac{\mathcal{F}\left(1+\frac{\mathcal{A}^2}{\mathcal{F}^4}\right)}{R\,r\,\Psi_r}\frac{\partial\xi}{\partial\theta}\right)-\left(\frac{rB_0}{q\psi_r}\right)\alpha\,\mathcal{F}^2 R\left(\kappa_n-\frac{\mathcal{A}\,\kappa_g}{\mathcal{F}^2}\right)\xi=0 \qquad (3.1.6.1\text{ - }1)$$

with no ε ordering, and

$$\mathcal{A}=S\left(\theta-\theta_0\right)+\left(\mathcal{F}\;\sigma'+\eta\right)\sin(\theta)-\eta\sin(\theta_0)+O(\varepsilon)\,. \qquad (3.1.6.1\text{ - }2)$$

See Eqs. (3.1.4.3 - 11) and (3.1.4.3 - 12) for the definitions of $\mathcal{F}$, η, and σ'. As $|\sigma'|$ increases, S_{crit} increases, thereby making local direct access easier. This enhanced stability is caused by the shortening of the connection length between the good and bad curvature regions of κ_n in the tokamak[3] and is expressed mathematically by the $\mathcal{F}^2$ factor that multiplies κ_n in Eq. (3.1.6.1 - 1), reducing the instability drive as $|\sigma'|$ increases. For $q_0 \sim 1$ in the marginally stable equilibria (Fig. 3.1.6.1 - 5), $|\sigma'|$ is sufficiently large at the plasma edge such that $S < S_{crit}$ and an access window forms. However, as q_0 increases, the shift of the flux surfaces decreases. In so doing, S_{crit} decreases more quickly than S, and the edge access window is lost. The other key aspect that is noticeable in this model is the reduction of the pressure gradient modulation in the integrated local shear as discussed in Section (3.1.4.2). Specifically, the α component is reduced by the factor $\left(1-\sigma'^2\right)^{(5/2)}$. Therefore, although the $\mathcal{A}$ stabilizing terms are increased by factors of $(1/\mathcal{F}^2)$, $\mathcal{A}$ is similarly decreased, and the strong stabilizing effect is reduced.

As q_0 increases, there is also a decrease in the slope of α_2 versus S that is especially prominent at low A (Fig. 3.1.6.1 - 2). This effect is caused by the $O(\varepsilon^2)$ corrections to κ_n. The stabilizing effect, sometimes referred to as the "geometric magnetic well" has been illustrated in finite ε, low $\beta \sim O(\varepsilon^2)$ models of equilibrium.[4-6] However, the strong destabilizing effect evident at low A and $q_0 \sim 1$ (Fig. 3.1.6.1 - 2) is not detected in the low β model or infinite A models since it involves a coupling of the toroidal effects in the equilibrium and the shift of the flux surfaces. This coupling is the increased poloidal field that is created on the outboard side of the torus as the flux surface shift increases. Consider the normal curvature in the shifted circle model. Including terms to $O(\varepsilon^2)$,

$$\mathcal{F}^2 \kappa_n = \mathcal{F}^2 \left(\frac{-\cos(\theta)}{R_0} + \frac{\varepsilon^2}{r} \left(\cos(\theta) \left(\frac{\sigma}{r} + \cos(\theta) \right) - \frac{1}{q^2 \mathcal{F}^2} \right) \right) + O(\varepsilon^3). \tag{3.1.6.1 - 3}$$

The first three terms are due to the toroidal field, the second and third being the geometric magnetic well for this model, and are stabilizing. The fourth is due to the poloidal field and is destabilizing. κ_n for this model differs from the low β model by including an $O(\varepsilon^2)$ stabilizing correction due to the shift, and more importantly, a factor of $(1/\mathcal{F}^2)$ increase in the destabilizing poloidal field term. Notice that while the toroidal field normal curvature drive is reduced by the connection length factor, $\mathcal{F}^2$, the poloidal field term is independent of $\mathcal{F}$, reflecting the fact that the poloidal field portion has no "connection length" and is always destabilizing over the poloidal angle. It is the balance of these higher order terms that determines whether the second region threshold pressure gradient increases or decreases with respect to the lowest order estimate of α.

The physical interpretation of the higher order effects is as follows. The stabilizing geometric magnetic well term comes from the fact that at larger values of R,

the magnitude of the toroidal field component of κ_n is reduced in a system of finite A. Therefore, this magnitude is reduced in the bad curvature region and increased in the good curvature region, and is therefore stabilizing. This is not dependent on the shift, and leads to the third term of Eq. 3.1.6.1 - 3. The shift will also place the field line at a greater R, thereby reducing the magnitude of the curvature in both the good and bad curvature regions. This is the cause of the second term in Eq. 3.1.6.1 - 3. Finally, the destabilizing poloidal field component of κ_n can be competitive with the other components in this model due to the allowance of a large Shafranov shift that is responsible for the $(1/\mathcal{F}^2)$ increase of this term. The shift increases the poloidal field on the outboard side of the torus, so that the field line wraps around the outboard side more quickly. Notice also that the poloidal curvature of a flux surface is $O(1/r)$ and is greater than the toroidal curvature that is $O(1/R)$. Therefore, in cases with very large flux surface shift, the poloidal field curvature can be larger than the toroidal field curvature in a region about the poloidal midplane on the outboard side of the tokamak.

Although not discussed in Ref. 6, this destabilization of the second region boundary has been observed, although mentioned only briefly, in previous second region computational studies[7,8]. Shown in Fig. 3.1.6.1 - 6 is the balance of the $O(\varepsilon^2)$ and higher terms in κ_n on the poloidal midplane at the outboard side of the torus for the equilibrium shown in Fig. 3.1.6.1 - 1. Note that the $O(\varepsilon^2)$ and higher order terms for $\theta = 0$ are given by $\kappa_{n\ \text{poloidal}}$ (Eq. 3.0.3 - 36) for the poloidal field component, and $(\kappa_{n\ \text{toroidal}} + 1/R_0)$ for the toroidal field component. The ratio of the poloidal to the $O(\varepsilon^2)$ toroidal component is defined as $\kappa_{n\ \text{ratio}}$. It is shown that for A=3 at q_0~1, the destabilizing poloidal field drive term dominates the stabilizing geometric magnetic well near the plasma edge (i.e. $|\kappa_{n\ \text{ratio}}| > 1$ on the outer flux surfaces). In this particular case, $|\kappa_{n\ \text{poloidal}}|$ is greater than $|\kappa_{n\ \text{toroidal}}|$, even though the former is one order smaller in ε. This dominance remains true as the aspect ratio increases, (Fig. 3.1.6.1 - 7)

however, the destabilizing effect on the second region threshold pressure gradient is reduced since the effect is one order larger in ε than the lowest order toroidal field κ_n component.

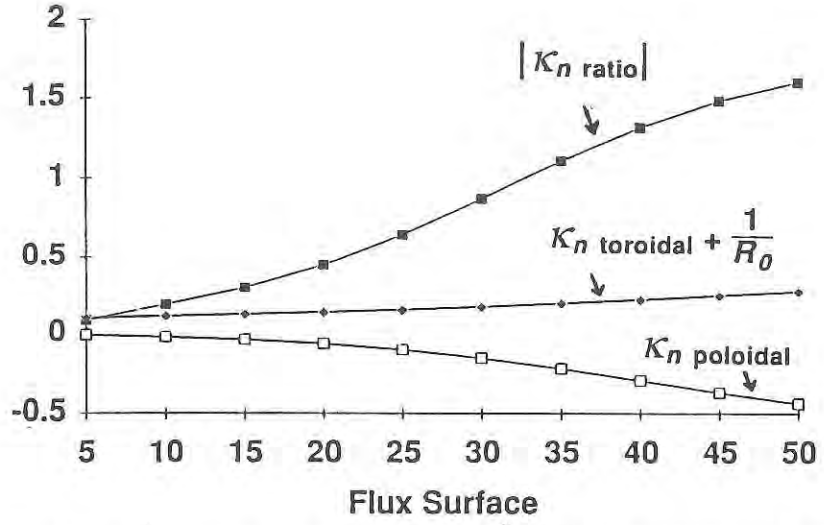

Fig. 3.1.6.1 - 6: Dominance of the destabilizing poloidal field component of κ_n over the stabilizing geometric magnetic well at $\theta = 0$ for the A=3, q_0~1 equilibrium of Fig. 3.1.6.1 - 1. $|\kappa_{n\ poloidal}|$ increases near the plasma edge and flux surfaces outside of surface 32 (surface 50 is the plasma edge) are destabilized by the $O(\varepsilon^2)$ effects, indicated by $|\kappa_{n\ ratio}| > 1$.

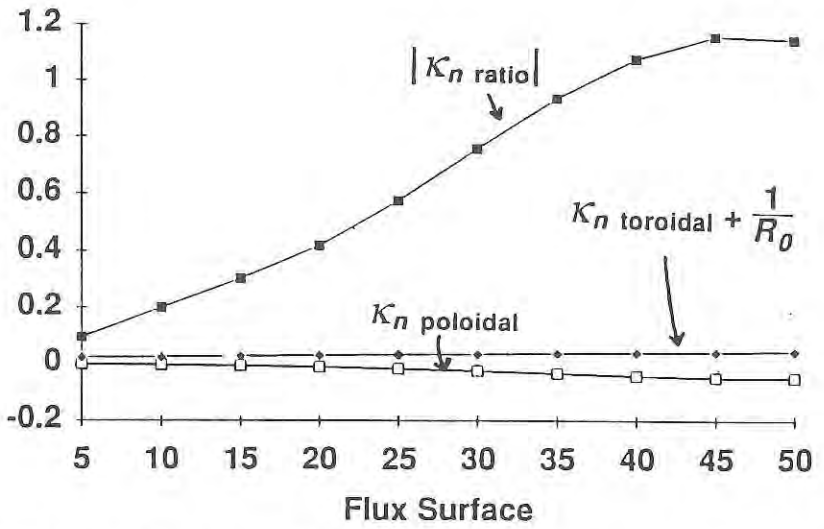

Fig. 3.1.6.1 - 7: $|\kappa_{n\ ratio}|$ and $O(\varepsilon^2)$ poloidal and toroidal field components of κ_n at θ=0 vs. flux surface number for A=15, q_0~1 equilibrium of Fig. 3.1.6.1 - 1. Notice that although the absolute values of the components are reduced at the larger A, $|\kappa_{n\ ratio}|$ still exceeds one near the plasma edge.

This analysis reveals a new physical interpretation of the stabilizing effect of increasing q_0 in a tokamak. Consider the ratio of the $O(\varepsilon^2)$ components of κ_n for the shifted circle model:

$$\frac{\kappa_{n\ \text{toroidal}}}{\kappa_{n\ \text{poloidal}}} = \cos(\theta)\left(\frac{\sigma}{r} + \cos(\theta)\right)(q^2 \mathcal{F}^2). \qquad (3.1.6.1 - 4)$$

As the ratio increases, the stabilizing geometric magnetic well will dominate over the destabilizing poloidal field curvature drive. Since the factor $\mathcal{F}^2$ does not appear in the analytic low β stability models, the standard interpretation of stability at elevated q is that the unfavorable poloidal field contribution to κ_n is reduced, and stability is thereby enhanced, that is, by increasing the q^2 term in Eq. 3.1.6.1 - 4. However, this equation is local, so that stability and instability of the edge plasma would then only be dependent on q_a if only the q^2 factor was important. This is the cause of the enhanced stability of the edge plasma observed in the numerical results as q_a is increased. However, when considering the equilibrium model with both shifted flux surfaces and finite ε, the extra factor $\mathcal{F}^2$ appears. As q_0 is increased, the extreme shift of the flux surfaces is reduced, thereby reducing the poloidal field curvature drive on the outer flux surfaces. This effect produces an increase in the $\mathcal{F}^2$ factor of Eq. 3.1.6.1 - 4, rather than affecting the q^2 factor. Therefore, the increased stability of the edge plasma at elevated q_0 is due to a *global* change in the equilibrium. This enhanced stability reduces $|\kappa_{n\ \text{ratio}}|$ to < 0.4 over the entire plasma for the A=3, q_0 = 2 case, shown in Fig. 3.1.6.1 - 8.

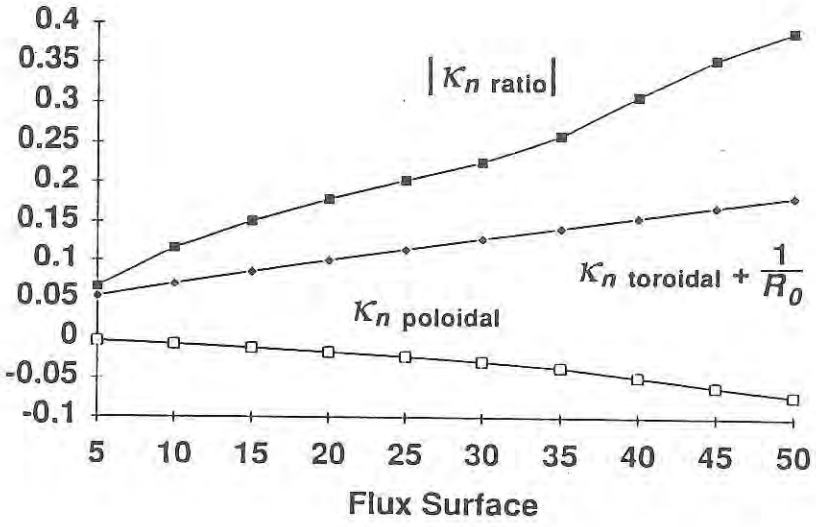

Fig. 3.1.6.1 - 8: *$|\kappa_{n\ ratio}|$ and $O(\varepsilon^2)$ poloidal and toroidal field components of κ_n at $\theta=0$ vs. flux surface number for A=3, q_0=2.0 equilibrium of Fig. 3.1.6.1 - 1. Increasing q_0 has reduced σ',thereby decreasing $|\kappa_{n\ poloidal}|$. $|\kappa_{n\ ratio}| < 0.4$ indicates the dominance of the stabilizing geometric magnetic well.*

By this illustration, it is evident that the standard connection length idea of high-n mode stability must also be revised. For a finite ε plasma, increasing the Shafranov shift will help stabilize the plasma by increasing the poloidal field in the unfavorable toroidal field normal curvature region, and thereby by decreasing the connection length, but only to a certain degree. Once the shift becomes sufficiently large for fixed q , the poloidal field component of κ_n will be strong enough to drive the mode unstable. This destabilization can then be suppressed by an increase in q_a. Notice also that the destabilization at large Shafranov shift is not seen in the simple infinite A, shifted circle model, since it is an $O(\varepsilon)$ effect, and therefore omitted from this model.

The primary cause for a second region of stability to large-n ballooning modes is the reversal of the local shear by pressure gradient driven Phirsch-Schluter currents. As the local shear reverses in the unfavorable curvature region, the point on a flux surface where $S_{local}= 0$ migrates toward the favorable curvature region, and second stability is achieved.[3] Therefore, geometric effects such as reduced A that help reverse the local shear in low β equilibrium models are thought to enhance the large-n stability of the plasma.[6] However, it is clear from the prior discussion that this is not necessarily true. The dilemma is resolved when both the shift and aspect ratio effects on the local shear are considered in the marginally stable second region equilibria.

Specifically, as discussed in Section 3.1.4.3, the effect of including a Shafranov shift $\sigma/a \sim O(1)$ reduces the magnitude of S_{local} in the unfavorable curvature region, in comparison to simpler models that neglect geometric effects. This also occurs when two-dimensional numerical calculations extrapolate the marginal second region boundary using flux surface geometry that is significantly different than the corresponding self-consistent equilibrium flux surface. Recall that the integrated local shear as a function of θ at the plasma edge for a marginally stable second region equilibrium with A=7.5, and that computed from the CHT (S,α) model of stability that neglects geometric effects in the equilibrium (Fig. 3.1.4.3 - 4b). The (S,α) model overestimates the pressure driven modulation of Λ_n, and neglects modifications due to the shift of the flux surfaces. Computing Λ_n with the infinite A, shifted flux surface model, Eq. (3.1.4.3 - 11) provides a more accurate representation of the two-dimensional model (Fig. 3.1.4.3 - 6). Examination of Λ_n in (3.1.4.2 - 11) shows that the reduction of the magnitude of S_{local} is due to the reduction of the pressure gradient driven modulation by the factor $\left(1-\sigma'^2\right)^{(5/2)}$ and the addition of geometric terms that tend to cancel the S and α terms in the unfavorable curvature region. As A is decreased, the reversal of S_{local} is enhanced, but mostly in the good curvature region. This is

shown in Fig. 3.1.6.1 - 9, where Λ_n is plotted as a function of θ at the plasma edge for the A=15 and A=3 equilibria of Fig. 3.1.6.1 - 1. Consequently, cases that exhibit a destabilization of the second region boundary need to have the point of S_{local}=0 further into the favorable curvature region. This is illustrated in Fig. 3.1.6.1 - 10, where the contours of constant S_{local} are shown for the A=3 and A=15 equilibria of Fig. 3.1.6.1 - 1. Notice that for A=3, the S_{local}=0 contour is further into the favorable curvature region than the A=15 case near the plasma edge. Therefore, even though the aspect ratio effects aid in the shear reversal process, they do not fully compensate for the reduction in S_{local} in the unfavorable curvature region due to the increase in $|\sigma'|$ in the lower A equilibrium. Instead, α must increase to reverse the shear, that results in the destabilized second region boundary. Also notice that for the A=15 case, the S_{local}=0 contour closes off just near the edge of the plasma. This condition signals the appearance of a local direct access window, and is discussed more fully in Section 3.1.6.4.

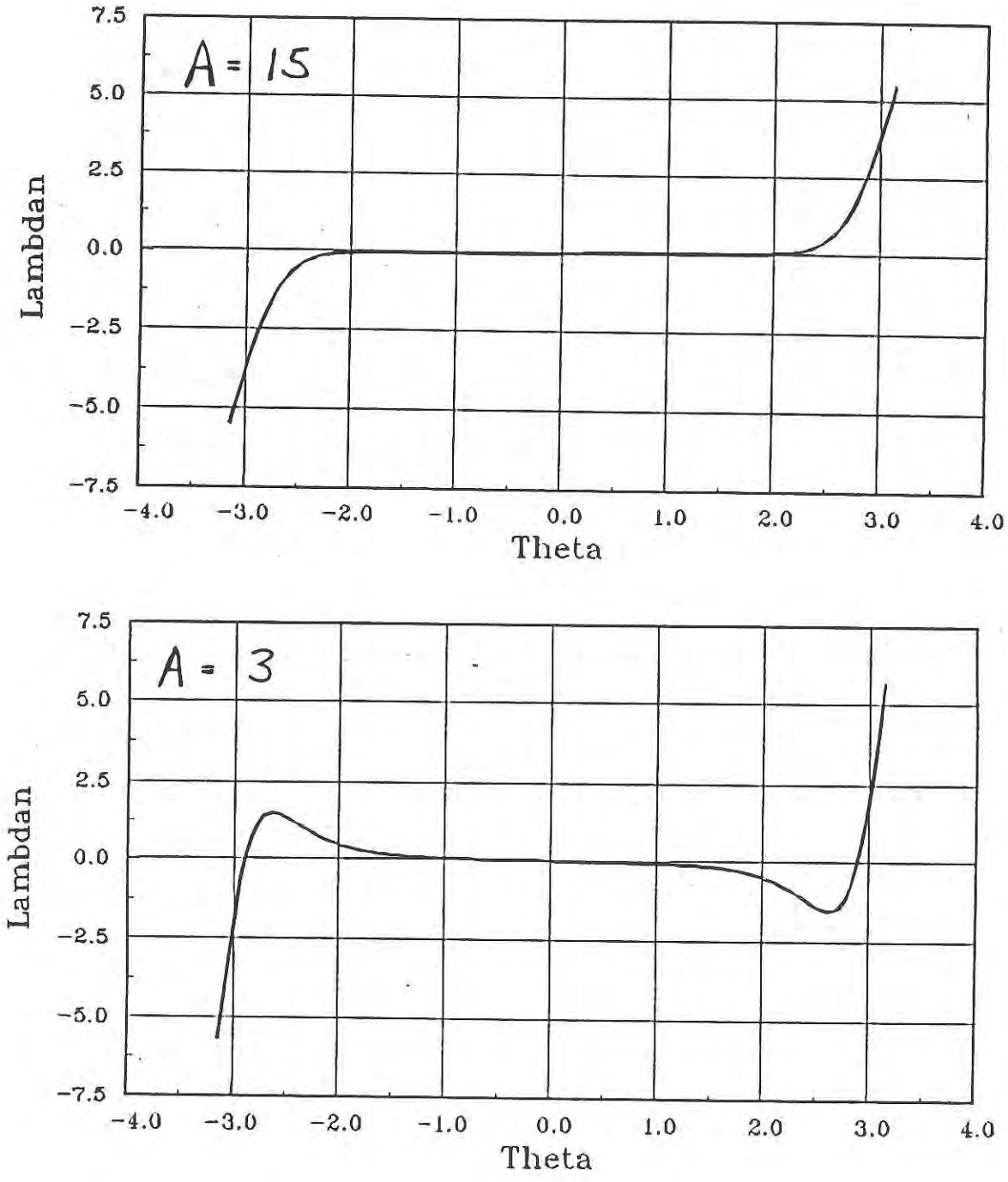

Fig. 3.1.6.1 - 9: *Λ_n vs.θ for the edge flux surface in the A=15 and A=3, q_0~1 equilibria of Fig. 3.1.6.1 - 2. Notice that the local shear reversal is most pronounced (A=3 case) in the favorable curvature region.*

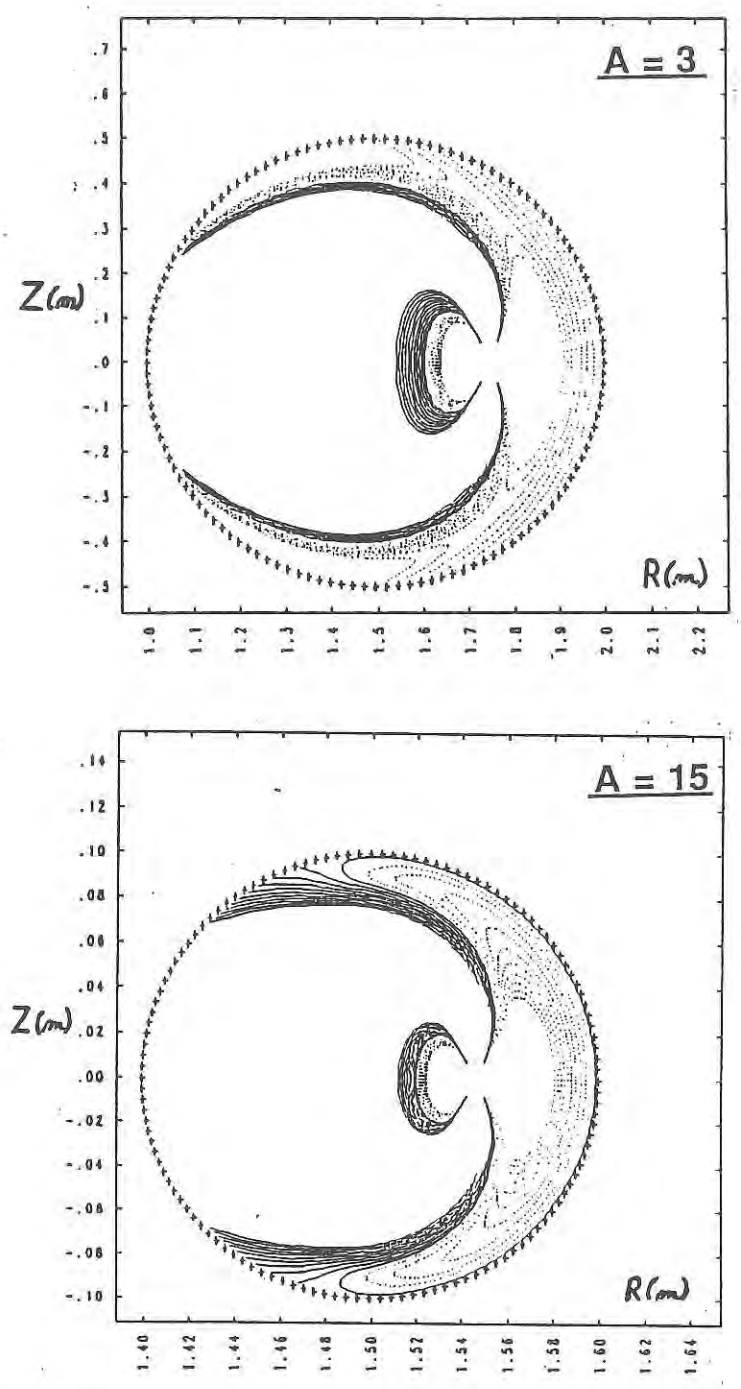

Fig. 3.1.6.1 - 10: Contours of S_{local} for the A=3 and A=15 equilibria. *The dotted contours indicate $S_{local}<0$ and the solid contours indicate $S_{local}>0$. Note that the boundary contour, $S_{local}=0$, separating these two regions curves further back into the favorable curvature region for the A=3 case. The $S_{local}=0$ contour closes off near the plasma edge for the A=15 case, signalling the onset of an edge access window.*

[1]Choe, W.H., and Friedberg, J.P., Phys. Fluids **29** (1986) 1766.

[2]Clarke, J.F., and Sigmar, D.J., Phys. Rev. Lett. **38** (1977) 70.

[3]Greene, J. M., and Chance, M.S., Nuclear Fusion **21** (1981) 453.

[4]Pogutse, O.P., and Yurchenko, E.I., JETP Lett. **28** (1978) 318.

[5]Pogutse, O.P, Chudin, N.V., Yurchenko, E.I., Sov. J. Plasma Phys. **6** (1980) 341.

[6]Gerver, M.J., Kesner, J., Ramos, J.J., Phys. Fluids **31** (1988) 2674.

[7]Monticello, D.A., in Plasma Physics and Controlled Nuclear Fusion Research (Proc. 8th Int. Conf. Brussels, 1980) Vol. 1, IAEA, Vienna (1980) 227.

[8]Sugiyama, L., and Mark, J.W.-K., Phys. Letters **84A** (1981) 123.

3.1.6.2 Edge q and Profile Effects

Shown in Fig. 3.1.6.2 - 1 are the β_2 and $\varepsilon\beta_{p2}$ curves as a function of A for various values of q_a in a circular cross section plasma. As expected, there is an increase in β_2 as A decreases. β_2 also decreases as q_a is increased at all A. Fig. 3.1.6.2 - 2 illustrates that this decrease is due to the opening of a local direct access window at the edge of the plasma, and not from a decrease in the slope of α_2. Also interesting is the result that *S decreases* as q_a increases for these cases. This apparent inconsistency is caused by the flux-conserving equilibrium model, and will be shown mathematically in Section 3.1.7.3. In fact, there is a slight increase in the slope as q_a is increased. Also, due to the lower current at large q_a, $\varepsilon\beta_{p2}$ increases as q_a increases.

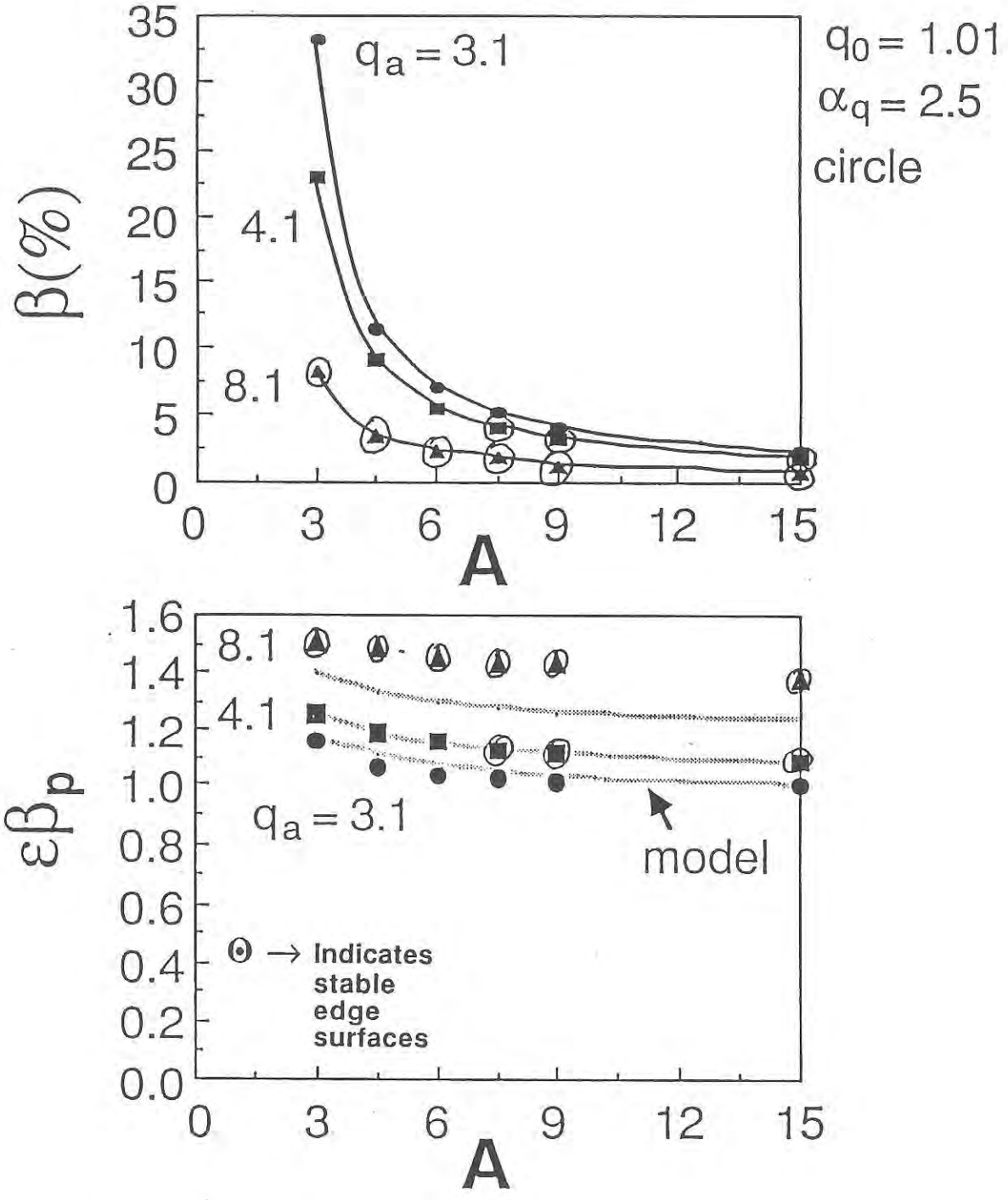

Fig. 3.1.6.2 - 1: β_2 and $\varepsilon\beta_{p2}$ vs. A and q_a for circular boundary equilibria: $\alpha_q = 2.5$.

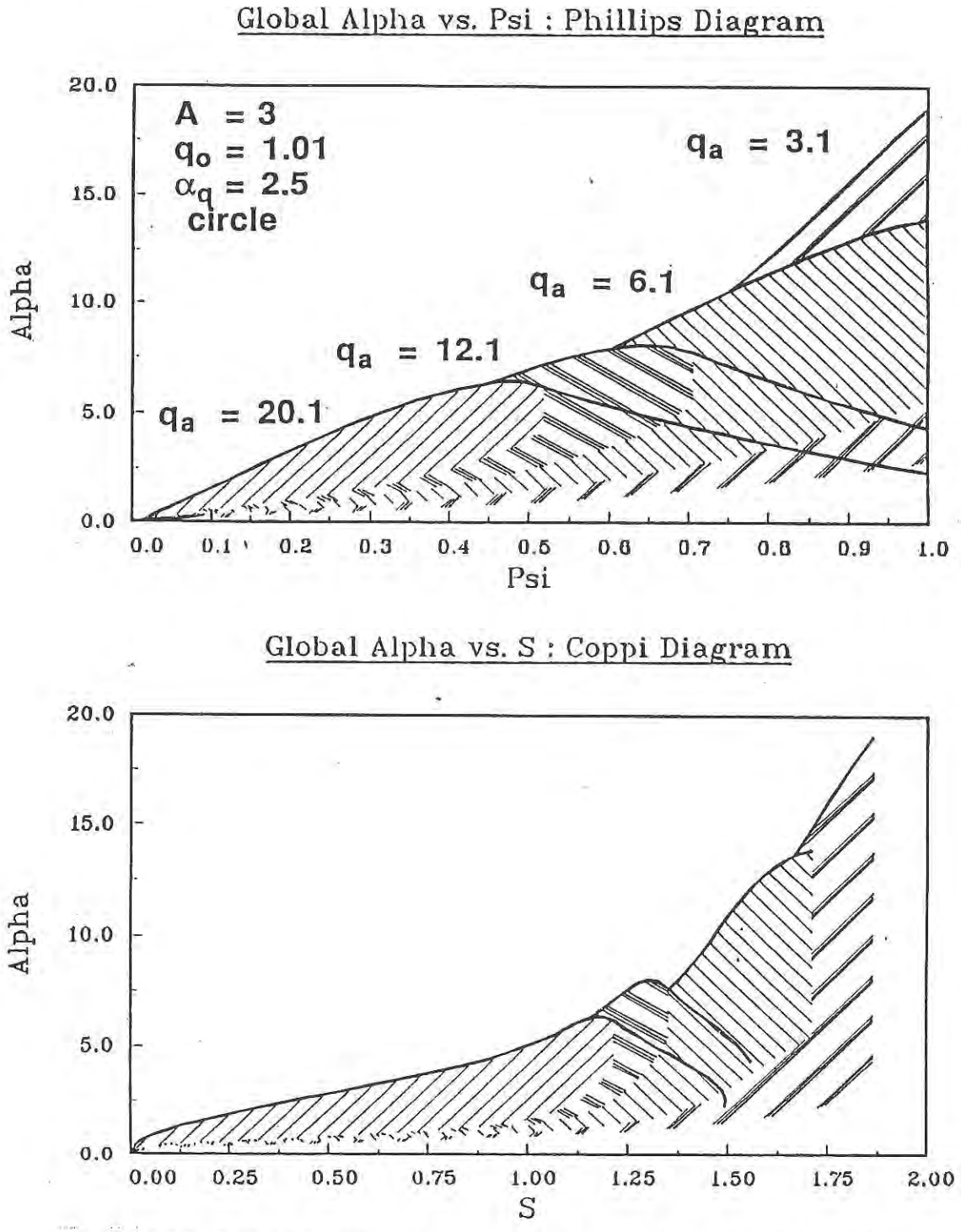

Fig. 3.1.6.2 - 2: Global stability diagrams for A=3 cases of Fig 3.1.6.2-1: q_a =3.1, 6.1, 12.1, 20.1. Note that the reduction of β_2 at large q_a comes from the reduction of α_2 near the plasma edge.

The increased value of q_a reduces the destabilizing effect of $\kappa_{n\ \text{poloidal}}$ near the plasma edge as discussed in Section 3.1.6.1. Fig 3.1.6.2 - 3 shows the $O(\varepsilon^2)$ terms of κ_n for the A=3, q_a = 12.1 equilibrium of Fig 3.1.6.2 - 2. Notice that for this case, the large q_a reduces $|\kappa_{n\ \text{ratio}}|$ at the plasma edge as compared to the equivalent A=3, q_a =4.1 equilibrium shown in Fig. 3.1.6.1 - 6. In this case, $|\kappa_{n\ \text{ratio}}| < 0.8$, illustrating that the stabilizing geometric magnetic well dominates the destabilizing terms of κ_n. This increased stability allows the formation of the edge access window.

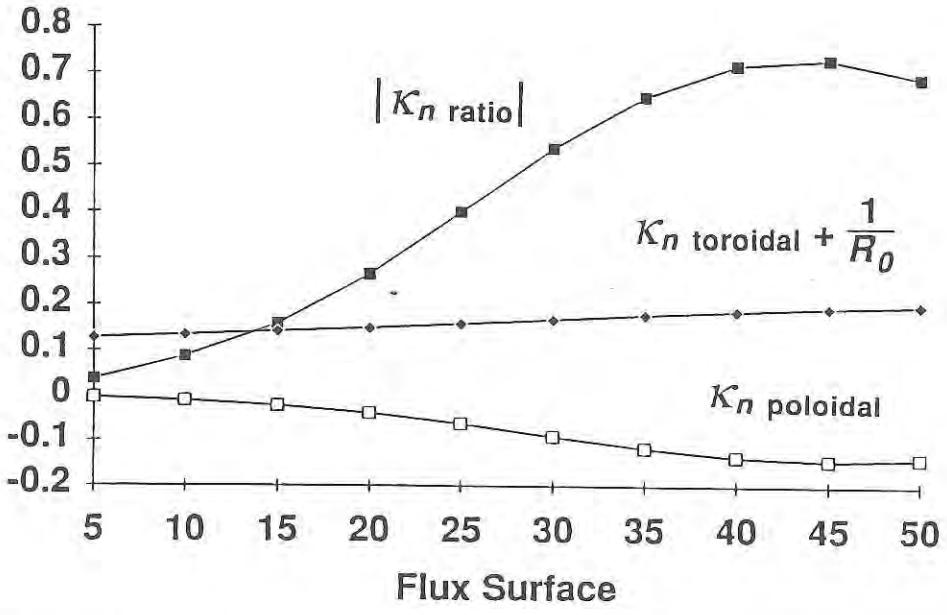

Fig. 3.1.6.2 - 3: Reduction of $|\kappa_{n\ ratio}|$ for A=3, q_a = 12.1 circular boundary equilibrium of Fig. 3.1.6.2 - 2. Note that $|\kappa_{n\ ratio}| < 0.8$ due to the increased q_a (compare with Fig. 3.1.6.1 - 6).

β_2 decreases as α_q decreases (Fig. 3.1.6.2 - 4). Examination of this behavior from the global (S,α) diagram is a bit more complicated, since varying α_q causes S to change significantly. Therefore, consider both the the global (S,ψ) and (S,α) diagrams in Fig. 3.1.6.2 - 5. The global (S,ψ) diagram (Fig. 3.1.6.2 - 5a) shows that a local direct access window increases in size at the plasma edge as α_q decreases. The unstable

region migrates to lower values of ψ as α_q decreases. This is due to the rearrangement of the shear as α_q is changed. At low α_q, there is more global shear near the magnetic axis, and less shear at the plasma edge. The global (S,α) diagram (Fig. 3.1.6.2 - 5b) shows that the slope of α_2 remains essentially the same, while the value of $S = S_{crit}$ decreases as α_q decreases.

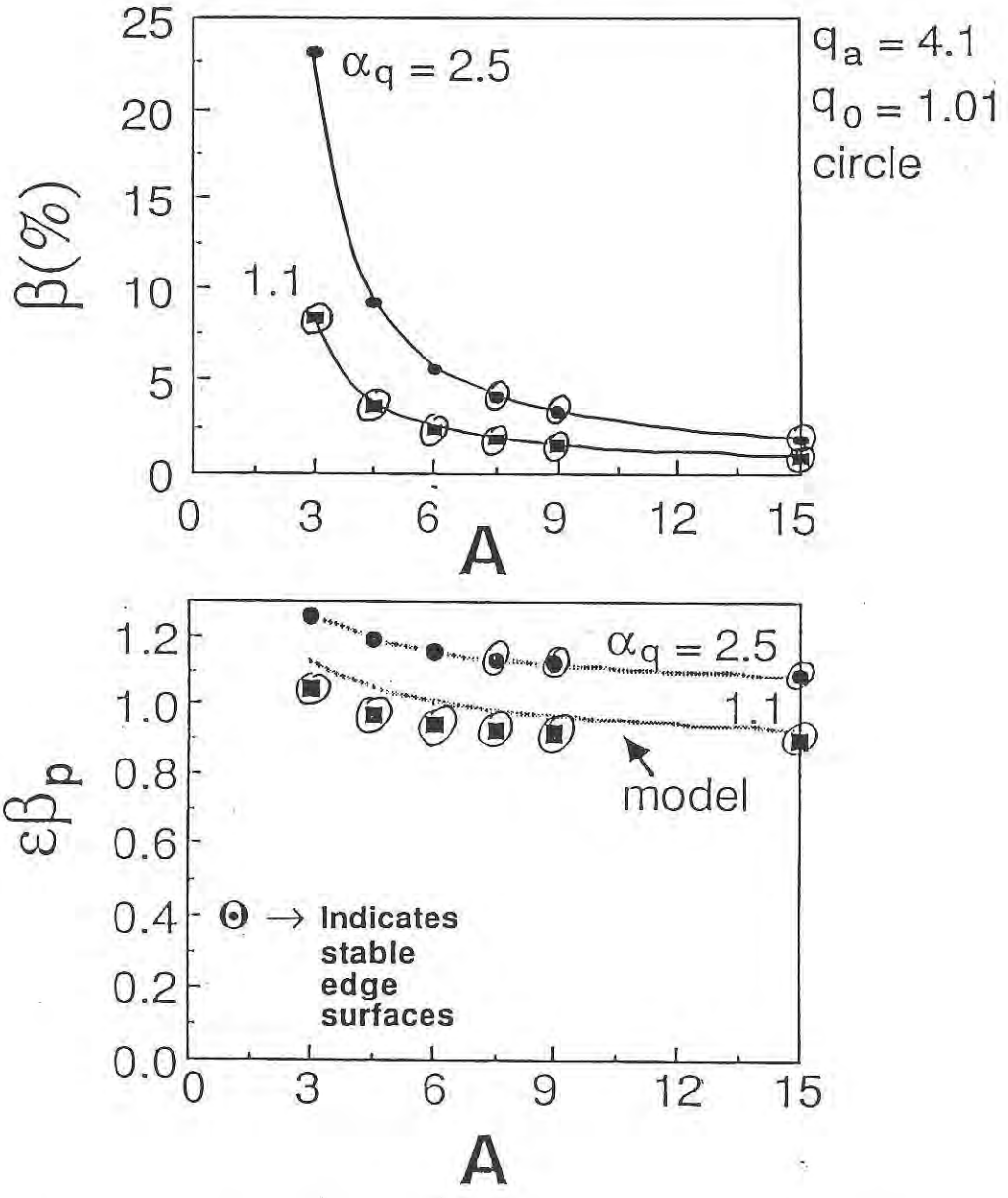

Fig. 3.1.6.2 - 4: *β_2 and $\varepsilon\beta_{p2}$ vs. A and α_q for circular boundary equilibria: $q_a = 4.1$, $q_0 = 1.01$.*

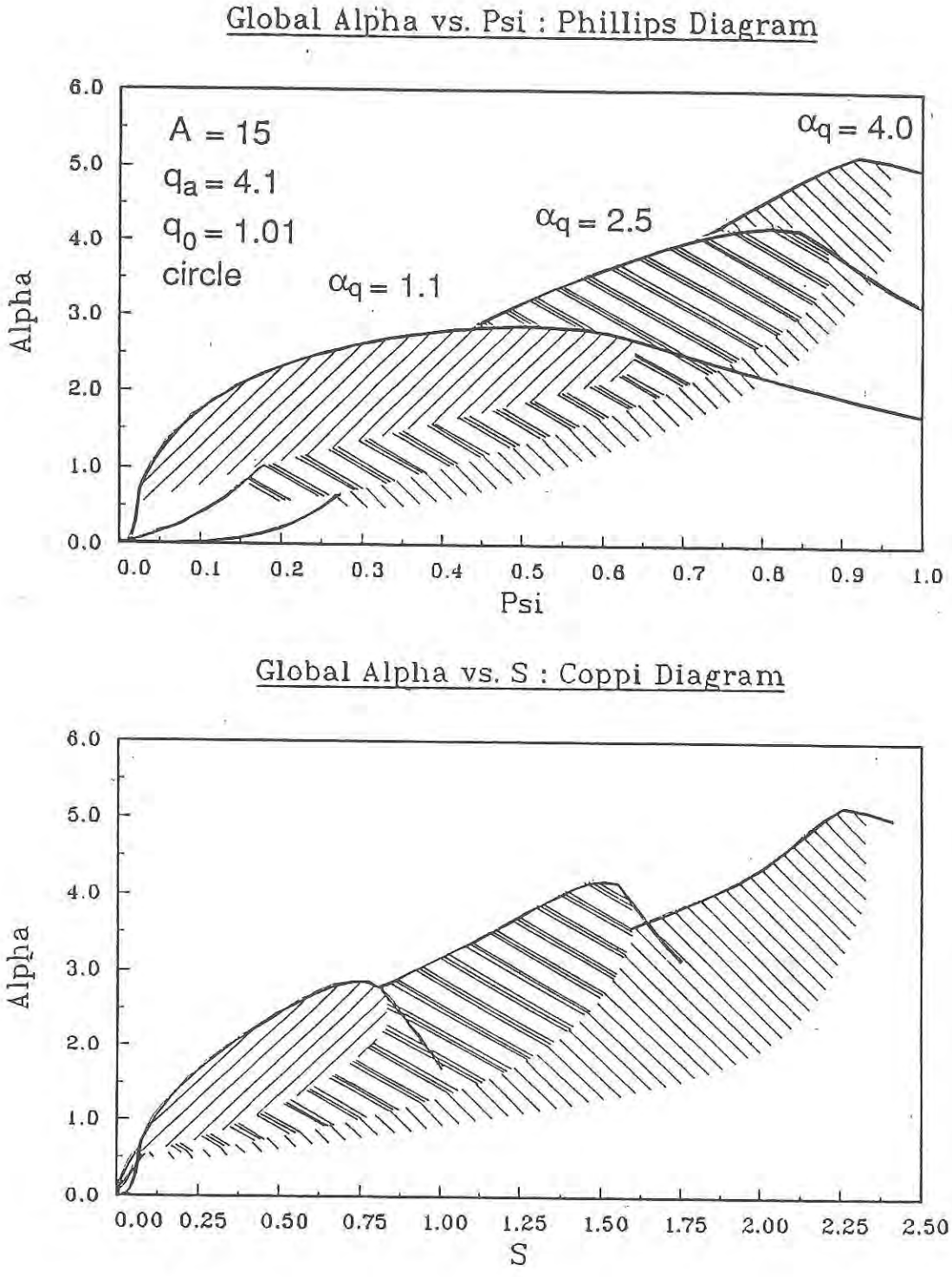

Fig. 3.1.6.2 - 5: Global stability diagrams for A = 15 equilibria of Fig 3.1.6.2-4: α_q=1.1, 2.5, 4.0.

3.1.6.3 Plasma Shaping Effects

Elongation without triangularity increases β_2 (Fig. 3.1.6.3 - 1.). The global (S,α) diagram shows that the slope of α_2 increases as a function of S as κ increases and that there is no longer a direct access window at the edge. Consequently, the edge current density is a large fraction of the central current density. These negative characteristics show that increasing κ at $\delta = 0$ is unfavorable in attaining second region operation.

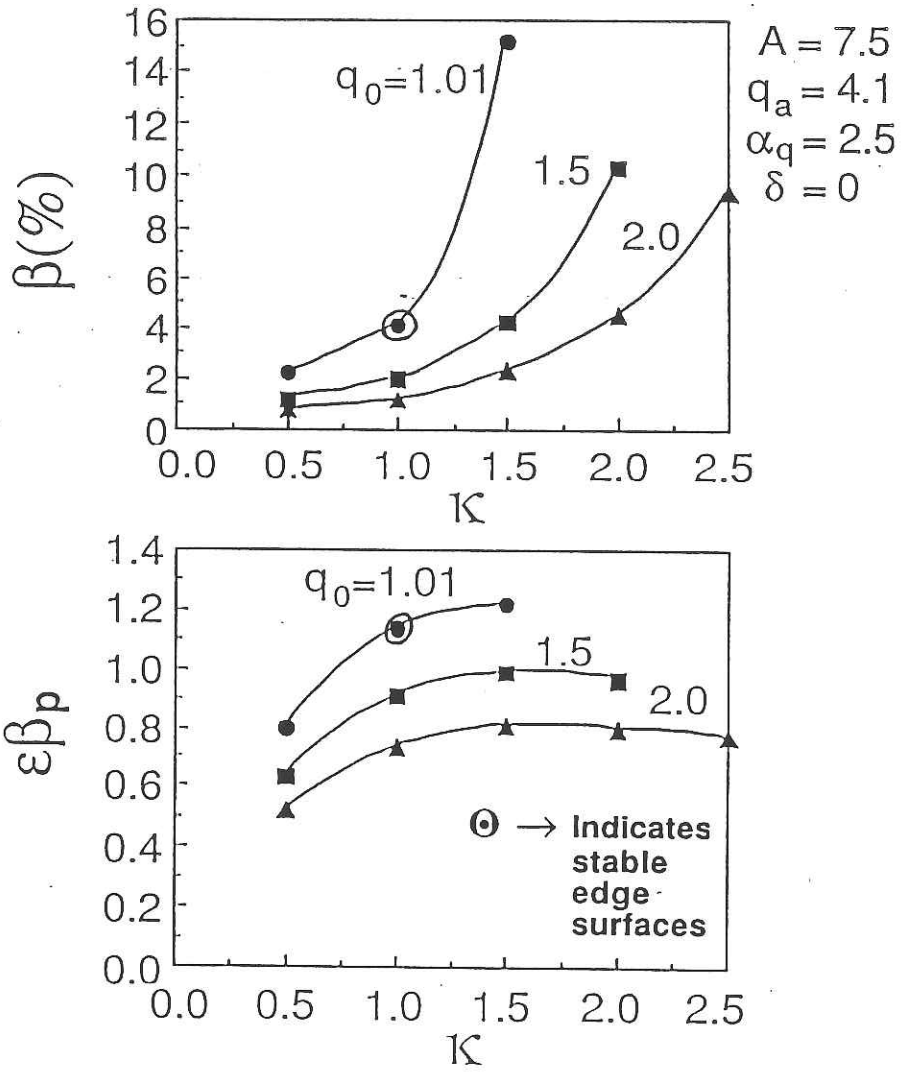

Fig. 3.1.6.3 - 1: β_2 and $\varepsilon\beta_{p2}$ vs. κ and q_0 for elliptical boundary equilibria: A= 7.5, q_a= 4.1, α_q = 2.5, δ =0.

Dee-shaped plasmas reduce β_2 (Fig. 3.1.6.3 - 2). Examination of the global (S,α) diagram (Fig. 3.1.6.3 - 3) shows that the decrease in β_2 is achieved in the Dee-shape in much the same way as in the $q_0 > 1$, circular plasma. As δ increases, the slope of α_2 decreases, yet a local direct access window does not appear at the edge (until δ is large).

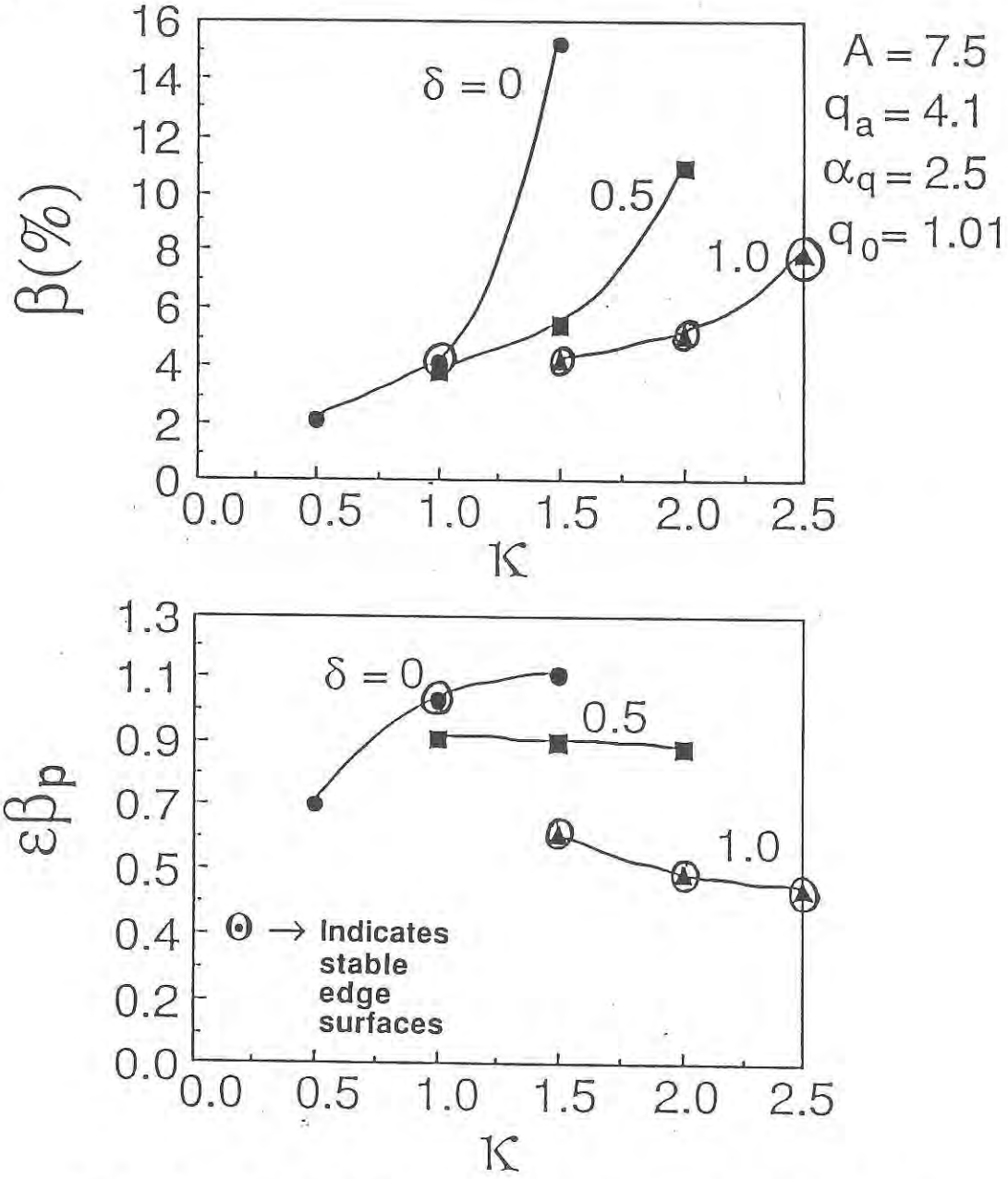

Fig. 3.1.6.3 - 2: β_2 and $\varepsilon\beta_{p2}$ vs. δ and κ for dee-shaped equilibria: A= 7.5, q_a= 4.1, α_q = 2.5.

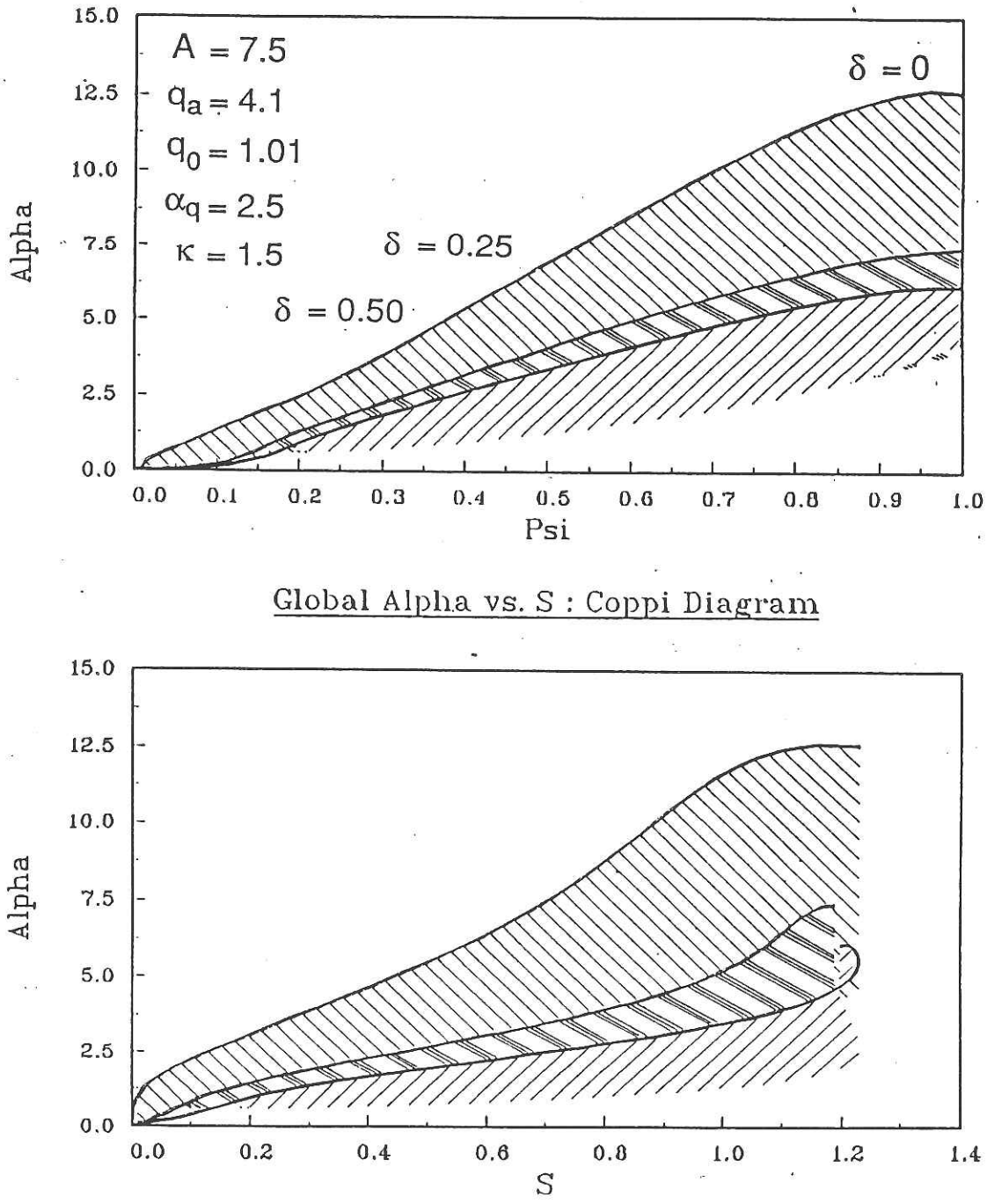

Fig. 3.1.6.3 - 3: Global stability diagrams for dee-shaped equilibria of Fig 3.1.6.3-2: δ =0, 0.25, 0.5.

Combining the favorable effects of the global equilibrium parameters produces the smallest values of β_2 and $\varepsilon\beta_{p2}$ (Fig. 3.1.6.3 - 4). All of these equilibria have edge access windows and considerably lower β_2 and $\varepsilon\beta_{p2}$ threshold values than the more standard equilibrium configuration with A=3, q_a = 4.1, and circular boundary shape (Fig. 3.1.6.1 - 1).

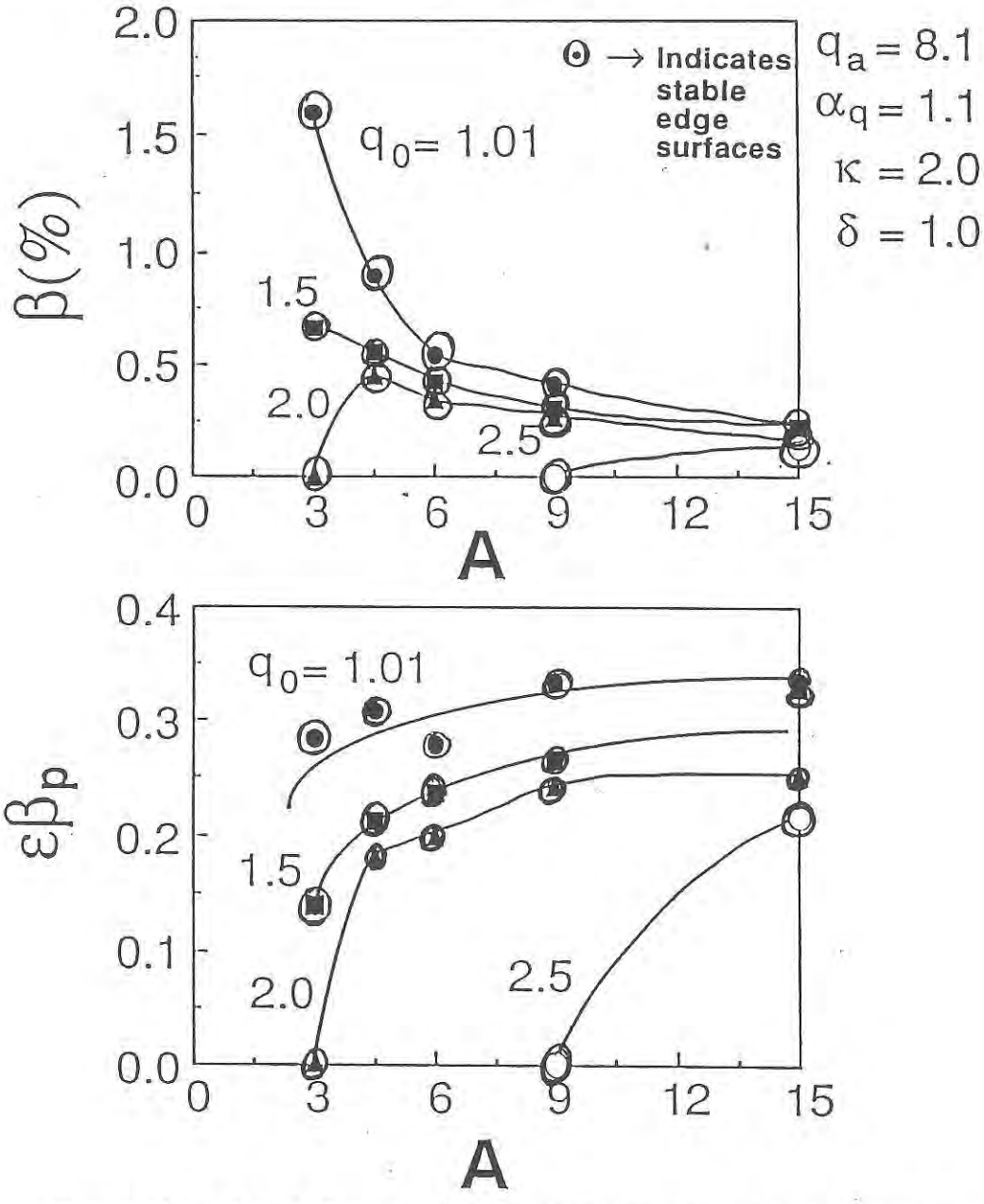

Fig. 3.1.6.3 - 4: *β_2 and $\varepsilon\beta_{p2}$ vs. A and q_0 for dee-shaped equilibria: q_a= 8.1, α_q = 1.1, κ = 2.0,δ =1.0 .*

3.1.6.4 Local Direct Access to the Second Region

Although seen numerically and analytically in previous second region studies,[1-4] the local direct access window has been studied analytically using low β models of equilibria that do not include important geometric effects such as magnetic shift at high $\varepsilon\beta_p$. One of the key results of the present study is the illustration of the stabilization and destabilization of the second region boundary on the outer flux surfaces in different regions of the tokamak operating space. The importance of operating a plasma that exhibits a local direct access window to high-n modes at the plasma edge is already being shown in DIII-D, where giant ELMs are suppressed in such plasmas.[5,6] As remarked in Section 3.1.4.2, an edge access window may be necessary in a second region plasma to allow the pressure gradient to be reduced to zero in a stable manner at the plasma edge.

As noted in Section 3.1.5, a local direct access window occurs on flux surfaces where

$$S(\psi) < S_{crit}(\psi). \qquad (3.1.6.4 - 1)$$

This is the general criterion that must be met to have local direct access to the second stability region. Other conditions for direct access, such as having q_0 sufficiently larger than one, are merely prescriptions of the global parameters of the equilibrium chosen to satisfy (3.1.6.4 - 1). Therefore, local direct access is most easily obtained for an equilibrium by reducing the global magnetic field shear, $S(\psi)$, or by increasing the stability of the equilibrium itself by increasing $S_{crit}(\psi)$. For the simplest models of stability, these requirements would seem trivial to satisfy, for example, by keeping q_a

and q_0 small to decrease $S(\psi)$, and reducing A to increase the stability effect of the geometric magnetic well, thus increasing $S_{crit}(\psi)$. However, as shown in the previous sections, the coupling of terms in the present self-consistent stability model introduces significant alteration to the intuition given by simpler models. Examination of the present database reveals an interesting and useful criterion for local access to the second region for marginally stable second region equilibria.

Reconsider the stability diagrams of Fig. 3.1.6.1 - 2 and the contours of S_{local} for the A=15 and A=3 equilibria (Fig. 3.1.6.1 - 10). Notice that the A=15 case exhibits a local direct access window near the plasma edge. Notice also that for this case, the contour S_{local} =0 closes off near the plasma edge. The A=3 equilibrium displays neither of these characteristics. As q_0 is increased to 2.0 in the A=3 case, the S_{local} =0 contour moves toward the unfavorable curvature region (Fig 3.1.6.4 - 1), but does not close off near the plasma edge, and consequently, direct access at the plasma edge is not achieved.

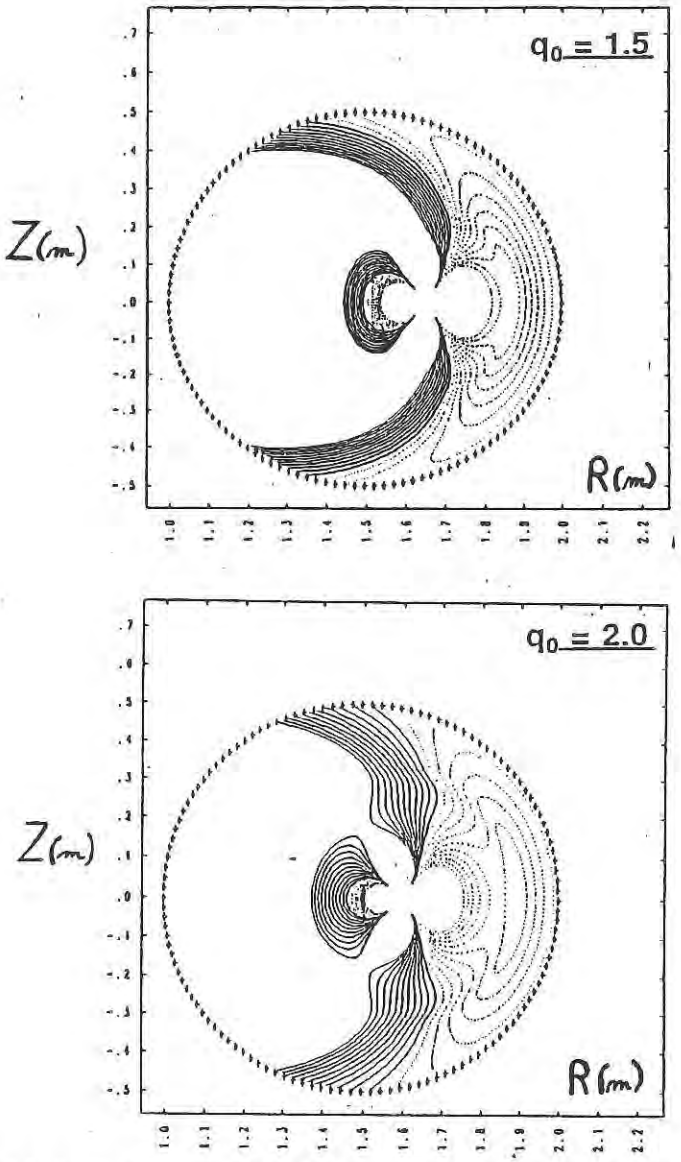

Fig. 3.1.6.4 - 1: S_{local} contours for A=3 circular boundary equilibria with q_0 = 1.5, 2.0. The S_{local} =0 contour does not close off inside the plasma.

For all of the equilibria computed in the present study, there is a correlation between attaining a local direct access window and having the S_{local} =0 contour close off in the plasma. In particular, the value of S required for local direct access corresponds to the value $S(\psi)$ at which S_{local} =0 at the outboard side of the plasma midplane (θ =0). This is illustrated in Fig. 3.1.6.4 - 2, where the value of S at the flux surface on which S_{local} = 0 at θ =0 is plotted versus the values of S at which the local

direct access window occurs in the equilibrium ($S_{window} = S_{crit}$). Notice that for both circular and shaped equilibria of arbitrary A, these values are essentially equal. Therefore, by computing these quantities for a given analytic representation of the equilibrium and using the relation of α_2 to S, the value of S_{crit} can be determined analytically. This is performed in Section 3.1.7.3 for the shifted circular equilibrium model.

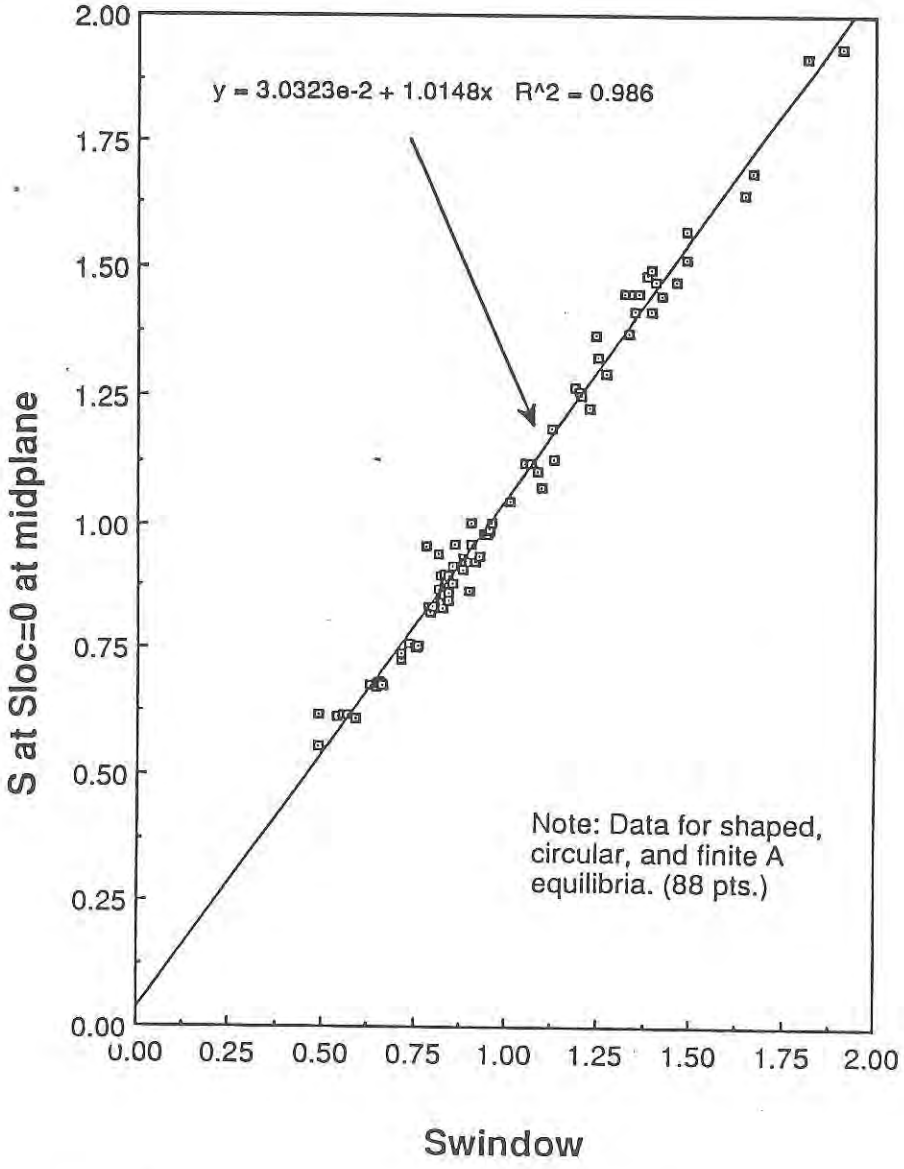

Fig. 3.1.6.4 - 2: Global S at S_{local}=0 and θ=0 vs. S_{window} for all marginally stable equilibria that have local direct access to the second region at the plasma edge.

Note that the stability calculations of Choe, et al.[7] for the infinite A, shifted circular equilibrium model also confirm this finding. Consider the local (S,α) marginal stability contours for this model as a function of $\sigma'(r)$, reprinted in Fig. 3.1.6.4 - 3. Superimposed on this diagram are the curves of $S_{local}=0$ at $\theta=0$ for this model. The expression defining these curves is

$$S+\left(\frac{3\sigma'(S-1+\sigma^2)\ -\ \alpha(1-\sigma^2)^{\frac{5}{2}}}{(1+2\sigma^2)}+\ \sigma'\right)+\sigma^2=0\,. \qquad (3.1.6.4\ -\ 2)$$

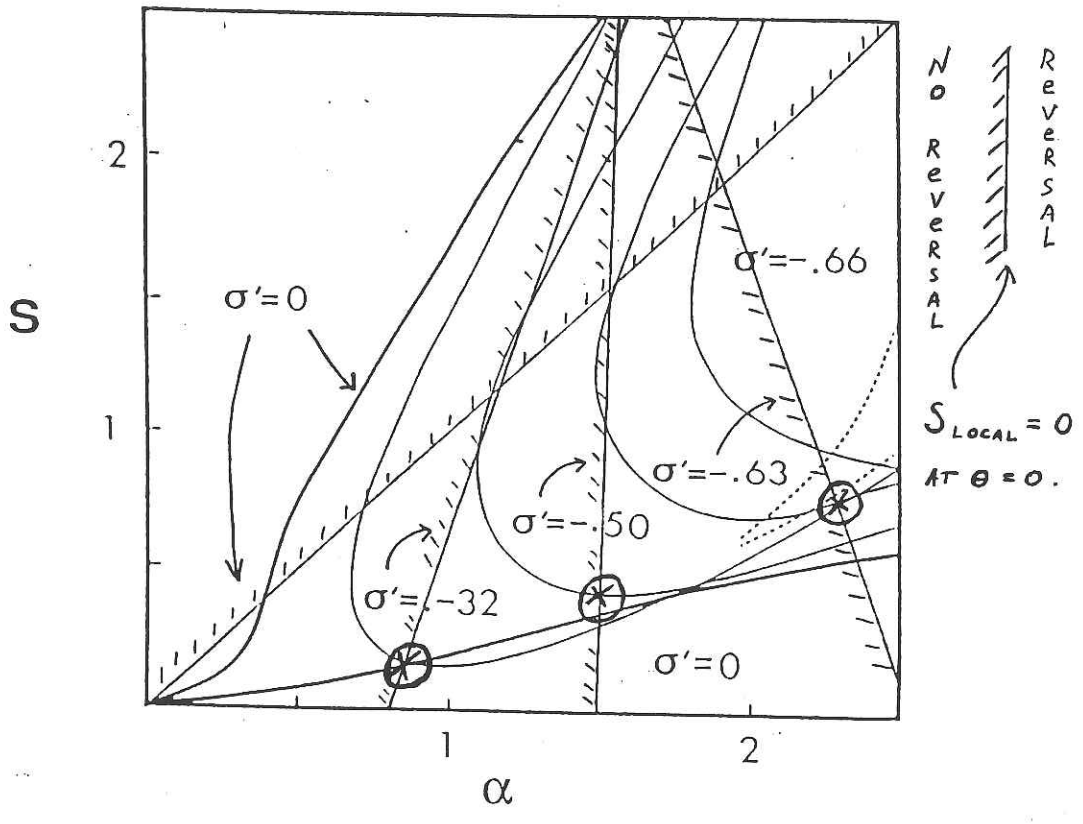

Fig. 3.1.6.4 - 3: Local (S,α) marginal stability contours for the infinite A, shifted circular equilibrium model. *Superimposed are the lines $S_{local}=0$ at $\theta=0$. Intersections of these lines and the marginal stability contours yield a good approximation for S_{crit}.*

There are two interesting features of this plot. First is the verification of the correspondence between $S_{local} = 0$ at $\theta = 0$ and S_{crit}. Notice that for $\sigma' \neq 0$, the intersection between the marginal stability contours and the lines of $S_{local} = 0$ at $\theta = 0$ occur at values of S that are close to S_{crit}. For $\sigma' = 0$, $S_{crit} = 0$ (no access), and correspondingly, $S = 0$ at $S_{local} = 0$ and $\theta = 0$. The second interesting feature is the modification of the standard intuition concerning shear reversal in a plasma with large Shafranov shift. The "standard" (S,α) stability model corresponds to the curves with $\sigma' = 0$. The local shear for this case is

$$S_{local} = S - \alpha \cos(\theta). \qquad (3.1.6.4 - 3)$$

The first term is the global shear and the second is the residual, pressure driven shear that reverses S_{local}. The standard intuition is that as S is increased, S_{local} becomes more positive and as α is increased, $-S_{local}$ becomes more negative. However, Eq. (3.1.6.4 - 2) shows that for $|\sigma'| > 0$, geometric effects also alter S_{local}. In particular, when $|\sigma'| > 0.5$, S_{local} *decreases* as S is increased, in contrast to intuition. This is another example of how more complex equilibrium models introduce results that contradict the expectations taken from simpler models.

---

[1]Choe, W.H., and Friedberg, J.P., Phys. Fluids 29 (1986) 1766.

[2]Pogutse, O.P., and Yurchenko, E.I., JETP Lett. 28 (1978) 318.

[3]Pogutse, O.P, Chudin, N.V., Yurchenko, E.I., Sov. J. Plasma Phys. 6 (1980) 341.

[4]Greene, J. M., and Chance, M.S., Nuclear Fusion 21 (1981) 453.

[5]Gohil, et al., Phys. Rev. Lett 61 (1988) 1603.

[6]Ozeki, T., Chu, M.S., Lao, L.L., Taylor, T.S., Chance, M.S., Kinoshita, S., Burrell, K.H., Stambaugh, R.D., "*Plasma Shaping, Edge Ballooning Stability, and ELM behavior in DIII-D*", General Atomics report GA-A19495, June 1989.

[7]Choe, W.H., and Friedberg, J.P., Phys. Fluids 29 (1986) 1766.

3.1.7 Equations Defining the Second Region Stability Threshold

In this section, models for the second region boundary threshold values of $\varepsilon\beta_{p2}$ and α_2, and the local direct access criterion $S(\psi) < S_{crit}(\psi)$, are considered for the marginally stable, circular boundary equilibria.

3.1.7.1 $\varepsilon\beta_p$ Threshold

β_p can be expressed in terms of an integral of α by combining Eqs. (3.1.2 - 8) and (3.1.2 - 9). In general, the integral cannot be solved analytically for an arbitrary two-dimensional equilibrium. Even the simple case of the shifted circular equilibrium model (no ε expansion) yields the form

$$\beta_{p2} = \left(\frac{2\pi B_0}{\mu_0 I}\right)^2 \int_{q_0}^{q_a} \frac{\alpha_2 r^3}{S R q^3} dq , \qquad (3.1.7.1 - 1)$$

the difficulty of the solution being primarily the specification of α_2 when a direct access window appears at the plasma edge. For instance, if only one access window appears near the edge and $\alpha_2 \equiv 0$ when $S(\psi) < S_{crit}(\psi)$, the appropriate integral form would be

$$\beta_{p2} = \left(\frac{2\pi B_0}{\mu_0 I}\right)^2 \int_{q_0}^{q_{crit}} \frac{\alpha_2 r^3}{S R q^3} dq . \qquad (3.1.7.1 - 2)$$

The difficulty is the specification of the upper limit, q_{crit}, defined as the q value where $S(\psi) = S_{crit}(\psi)$.

A simple empirical scaling of $\varepsilon\beta_{p2}$ that includes the effect of A to first order in ε has been fit to the data set for circular boundary equilibria. At large A, the results of Section 3.1.6.1 show that $\varepsilon\beta_{p2}$ is independent of A, whereas finite ε corrections cause $\varepsilon\beta_{p2}$ to increase or decrease at low A, depending on the value of q_0. The model

$$(\varepsilon\beta_{p2})^2 + \left(\frac{q^*}{q_a}\right)^2 = D_1(q_0)\,\varepsilon + D_0(q_0) \qquad (3.1.7.2 - 3)$$

with D_1 = 1.09, -0.66, and -0.92, and D_0 = 1.37, 1.28, and 1.17 for q = 1.01, 1.5, and 2.0 respectively, reproduces all circular outer boundary equilibrium values with $A \geq 3$ (110 equilibria) with an average absolute error of 10%. A shortcoming of the model is that it does not accurately reproduce the global access condition $\varepsilon\beta_{p2} \equiv 0$. The condition that describes local access on a flux surface is considered in Section 3.1.7.3.

3.1.7.2 Pressure Gradient Threshold

As observed in Section 3.1.6.1, the normalized marginal second region threshold pressure gradient, α_2, can be approximated for the large A, circular outer boundary equilibria by considering a linear model in S,

$$\alpha_2 = C_0 + C_1 S \qquad (3.1.7.2 - 1)$$

when $S > S_{crit}$ and $S > S_{min}$. Here, S_{min} is the value of the global shear below which the ballooning stability calculation may be considered inaccurate. This inaccuracy is due to the form of the quasimode at low S, which extends over a greater number of poloidal periods as S decreases. Here, S_{min} is taken to be 0.3, which is a conservative estimate. Also, the linear model is only valid for $S > S_{crit}$, since α_2 is arbitrary when $S < S_{crit}$. A minimizing prescription would model $\alpha_2 = 0$ when $S < S_{crit}$.

This simple model was used to fit the appropriate data using a least squares fitting procedure. All A=15 circular boundary cases were used (36 equilibria). The computed coefficients and their standard deviations are

$$C_0 = 1.15 \text{ (+/-) } 0.18 , \qquad (3.1.7.2 - 2)$$

and

$$C_1 = 2.06 \text{ (+/-) } 0.42 . \qquad (3.1.7.2 - 3)$$

A model of α_2 using half integer powers of S was fitted to the data and the resultant fit produced larger standard deviations of the coefficients.

3.1.7.3 Local Direct Access Criterion

Using the result that S_{crit} is well approximated by the value of S where S_{local} =0 at θ =0 (Section 3.1.6.4) and the marginal second stability threshold pressure gradient for infinite A, circular boundary equilibria given in the previous section, an

expression for S_{crit} as a function of σ' can be derived. Combining Eq. (3.1.6.4 - 2) and Eq. (3.1.7.2 - 1) yields,

$$S_{crit} = m(\sigma')\,\alpha_2 + b(\sigma'), \qquad (3.1.7.3 - 1)$$

where

$$m(\sigma') = \frac{\left(1-\sigma'^2\right)^{\frac{5}{2}}}{\left(1 + 3\sigma' + 2\sigma'^2\right)}, \qquad (3.1.7.3 - 2)$$

and

$$b(\sigma') = \frac{-\sigma'\left(-2 + \sigma' + 5\sigma'^2 + 2\sigma'^3\right)}{\left(1 + 3\sigma' + 2\sigma'^2\right)}. \qquad (3.1.7.3 - 3)$$

After plugging in for α_2, the result is

$$S_{crit}(\psi) = \frac{1.15(1-\sigma'^2)^{2.5} - \sigma'(-2+\sigma'+5\sigma'^2+2\sigma'^3)}{(1+3\sigma'+2\sigma'^2) - 2.06(1-\sigma'^2)^{2.5}}, \qquad (3.1.7.3 - 4)$$

that is plotted over the domain $0.5 < |\sigma| < 1.0$ in Fig 3.1.7.3 - 1.

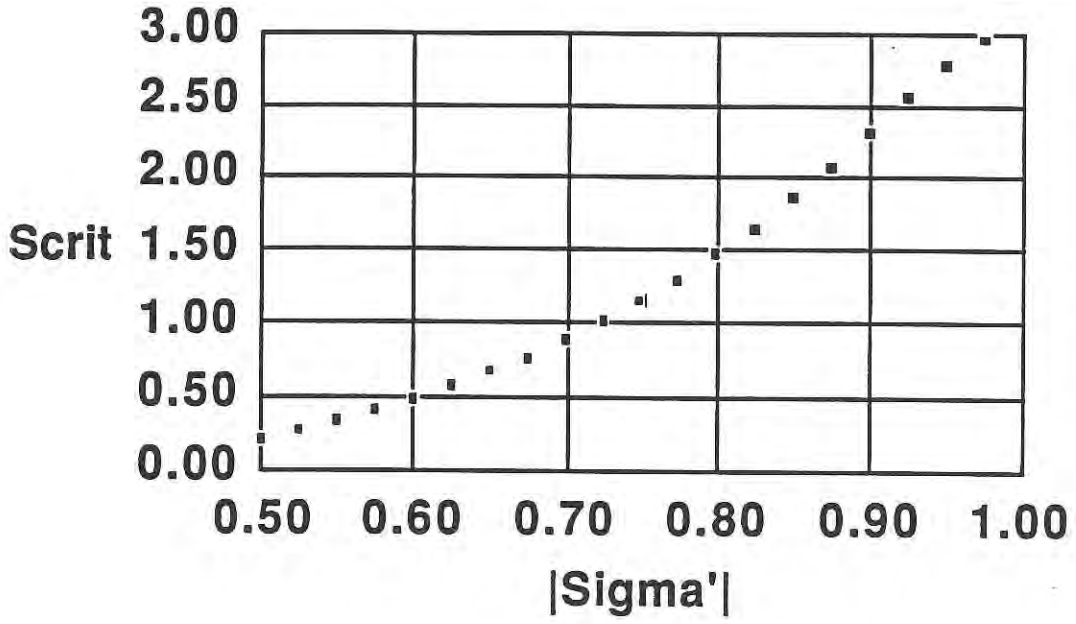

Fig. 3.1.7.3 - 1: S_{crit} vs. σ' for the infinite A, shifted circular flux surface model of plasma equilibrium over the domain $0.5 < |\sigma'| < 1.0$.

From this expression, the criterion $S < S_{crit}$ can be tested for the large A, marginally second region stable equilibria as a function of the global predictor variables. First, σ' is determined by the expression relating q^* and $q(\psi)$ for the shifted circle model, neglecting ε effects,

$$\sigma'(r) = -\sqrt{1 - \left(\frac{q^*(r)}{q(r)}\right)^2} \; . \qquad (3.1.7.3 - 5)$$

Second, an expression for $S(\psi)$ is computed as a function of the global parameters. This involves a short calculation whose steps are outlined below. The definition of $S(\psi)$ for the infinite A, shifted circle equilibrium model is given by (3.1.2 - 6). The poloidal flux for the model is given by the differential equation

$$\frac{\partial \psi}{\partial r} = \frac{rB_0}{q} . \qquad (3.1.7.3 - 6)$$

ψ as a function of q is determined by inverting (3.1.2 - 2),

$$\left(\frac{\psi - \psi_0}{\psi_a - \psi_0}\right) = \left(\frac{q - q_0}{q_a - q_0}\right)^{1/\alpha_q} . \qquad (3.1.7.3 - 7)$$

Eqs. (3.1.7.3 - 6) and (3.1.7.3 - 7) are combined to form the differential equation

$$\left(\frac{B_0\, \alpha_q\, (q_a - q_0)}{\psi_a - \psi_0}\right) r\, dr = q\left(\frac{q - q_0}{q_a - q_0}\right)^{(1 - \alpha_q)/\alpha_q} . \qquad (3.1.7.3 - 8)$$

This equation is integrated yielding an explicit expression for r as a function of q,

$$r^2 = \frac{2(\psi_a - \psi_0)}{B_0}\left(\frac{q - q_0}{q_a - q_0}\right)^{1/\alpha_q}\left\{\frac{q + q_0\, \alpha_q}{1 + \alpha_q}\right\} . \qquad (3.1.7.3 - 9)$$

dq/dr is evaluated using (3.1.7.3 - 8), and after plugging in r^2 from (3.1.7.3 - 9), the result is

$$S(\psi) = \frac{2\alpha_q}{1 + \alpha_q}\left(\frac{(q(\psi) + q_0\, \alpha_q)(q(\psi) - q_0)}{q^2}\right) . \qquad (3.1.7.3 - 10)$$

Note that while this expression is only appropriate for infinite A, it does well in reproducing S for finite A equilibria in the marginally second region stable equilibria.

This expression for $S(\psi)$ is important since it clarifies some of the non-intuitive behavior of S as a function of q_0 and q_a observed in Section 3.1.6. First, consider q_a.

In Section 3.1.6.2, S was shown to decrease as q_a. increased, which is non-intuitive. However, it is clear from Eq. (3.1.7.3 -10) that this can occur. This is due to the inverse q dependence of the poloidal flux gradient for this equilibrium model. Therefore, variations in q change S through both changes in the local derivative of the q profile and also by changing the global equilibrium itself. Using (3.1.7.3 - 10),

$$\frac{dS}{dq} = \frac{2\alpha_q}{1+ \alpha_q} \frac{q_0}{q^3} \left[q\ (1 - \alpha_q) + 2\ q_0\ \alpha_q\right] \qquad (3.1.7.3 - 11)$$

so that whenever

$$q > \frac{2\ q_0\ \alpha_q}{\alpha_q - 1}, \qquad (3.1.7.3 - 12)$$

the shear will decrease as q increases. Therefore, q_a can be raised and produce favorable large-n stability properties by reducing S. Similarly, increasing q_0 can *increase* S. Whenever

$$q_0 < \frac{q\ (\alpha_q - 1)}{2\alpha_q}, \qquad (3.1.7.3 - 13)$$

increasing q_0 will increase S. It can be easily shown that increasing α_q will always increase S, and therefore its variation shows no surprises with regard to changing S.

Equations (3.1.7.3 - 4) and (3.1.7.3 - 10) comprise the local direct access condition (3.1.6.4 - 1) for the infinite A, shifted circular equilibrium model. The condition is illustrated to test whether or not the edge of the plasma has direct access for

some of the database equilibria with A = 15 in Table (3.1.7.3 - 1). This criterion predicts edge access correctly in these cases.

2-D Marginal Equilibria					Model	
q_0	q_a	α_q	$-\sqrt{1-(q^*/q_a)^2}$	Access	S_{edge}	S_{crit}
1.01	4.1	2.5	-0.861	yes	1.74	1.95
1.50	4.1	2.5	-0.788		1.73	1.38
2.00	4.1	2.5	-0.705		1.62	0.90
1.01	3.1	2.5	-0.826		1.75	1.66
1.01	8.1	2.5	-0.892	yes	1.64	2.23
1.01	20.1	2.5	-0.892	yes	1.53	2.23
1.01	4.1	1.1	-0.735	yes	1.00	1.06
1.01	4.1	2.0	-0.840	yes	1.50	1.77
1.01	4.1	4.0	-0.893		2.39	2.24

Table 3.1.7.3 - 1: Prediction of access window at the plasma edge for some marginally second region stable, A=15 equilibria using large A shifted circular equilibrium model.

This table briefly summarizes the relative increase or decrease of $S(\psi)$ and S_{crit} (ψ) in determining the cause of the local direct access window at the plasma edge when ε effects are small. For the q_0 variation, there is a decrease in S as q_0 increases, but in the range of q_0 shown, this decrease is small. However, the increase in q_0 reduces the stabilizing effect of the large Shafranov shift and S_{crit} decreases rapidly, more so than $S(\psi)$, and the edge access is lost. However, as q_0 increases further, the factor $(q - q_0)$ in (3.1.7.3 - 10) will dominate, and local direct access will be regained at low S. This usually occurs across the plasma when the edge stabilizes, and global access is attained (see Section 3.1.6.1). When ε effects are large, as shown in Section 3.1.6.1, the additional destabilizing effect of the large poloidal field component of the normal curvature eliminates the edge access window at $q_0 \sim 1$. Since this destabilizing effect is due to a coupling of ε and σ' effects, it disappears in large A models and is reduced

when $|\sigma'|$ is reduced. Therefore, the edge access window is still evident at $q_0 \sim 1$ when $|\sigma'|$ is decreased in the finite A equilibria. The q_a variation shows that as q_a is increased, $S(\psi)$ is decreased and $S_{crit}(\psi)$ is increased. These are both favorable with regard to attaining local direct access. This characteristic makes raising q_a a very effective method of achieving edge access. The effect is retained at finite A since increasing q_a increases $|\sigma'|$ but also decreases the destabilizing poloidal field curvature drive through the q^2 term in (3.1.6.1 - 4). Finally, as α_q is decreased, both $S(\psi)$ and $S_{crit}(\psi)$ decrease at about the same rate. Therefore, while decreasing α_q does lead to an edge access window, it is not as effective as increasing q_a in creating local direct access to the second region.

All this I will bring to pass for him, if he changes from his anger. Let him give way. For Hades gives not way, and is pitiless, and therefore he among all the gods is most hateful to mortals.

Homer, *The Iliad*, (Book 9, l 157-159).

3.2 TRANSITION TO THE SECOND REGION

In this section, transition to the second stability region is studied by analyzing sequences of equilibria generated by a $1^1/_2$ dimensional transport calculation. In this prescription, large-n ballooning stability is checked during the equilibrium evolution to high β, and the result is self-consistently fed back in the calculation by changing the local transport properties of the plasma. Self-consistent transport calculations that analyze first region tokamak operation at small aspect ratio have been performed previously.[1] These calculations produce pressure profiles which are marginally first region stable, and generate maximum first region β values. Empirical scaling laws for energy confinement time have been derived using similar methods.[2] In the present work, transition to the second region of ideal MHD stability is addressed. The large aspect ratio configuration was found to be favorable, since the β required to reach second stability and the separation of the first and second stability boundaries in β decreases with aspect ratio when q_0~1.[3] A large aspect ratio, second region device also has desirable reactor characteristics. At large A, toroidal field utilization is increased and machine access is improved. Furthermore, the plasma current at fixed q_a decreases with increasing A, reducing current drive requirements and disruption damage. The engineering advantages and reactor relevance of the large aspect ratio approach to high β tokamaks are discussed in refs. [4,5,6].

[1]Azumi, M., Tsumenatsu, T., Itoh, K., et al., in Plasma Physics and Controlled Nuclear Fusion Research (Proc. 8th Int. Conf. Brussels, 1980) Vol. 1, IAEA, Vienna (1980) 293.

[2]Connor, J.W., Taylor, J.B., and Turner, M.F., Nuclear Fusion 24 (1984) 642.

[3]Monticello, D.A., in Plasma Physics and Controlled Nuclear Fusion Research (Proc. 8th Int. Conf. Brussels, 1980) Vol. 1, IAEA, Vienna (1980) 227.

[4]Navratil, G.A. and Marshall, T.C., Comments Plasma Phys. Controlled Fusion 10 (1986) 185.

[5]Mauel, M.E., Nuclear Fusion 27 (1987) 313.

[6]Ehst, D., Baker, C., Billone, M, et al., Tokamak Power Systems Studies - FY 1986: A Second Stability Power Reactor, ANL-FPP-86-1, Argonne National Laboratory, Argonne Illinois (1987).

3.2.1 Computational Transport Study

The MHD stability study of the previous section is useful for determining the behavior of $<\beta>_2$ and $(\varepsilon\beta_p)_2$ while prescribing the pressure and safety factor profiles independently. In an actual experiment, precise measurement and control of these profiles is difficult. Therefore, while certain areas of parameter space may seem optimal for operation of a tokamak in the second stability region, the necessary parameters may not be experimentally obtained or sustained. A less restrictive approach in modeling transition to the second region is to allow the equilibrium profiles to evolve toward second stability by the solution of density, energy, and magnetic field transport equations, while maintaining equilibrium quasi-statically. In the present work, all plasma profiles, including the beam deposition profile, evolve self-consistently in this manner.

The vehicle used for these calculations is a variant of the $1^1/_2$ dimensional BALDUR transport code.[1] This algorithm solves the flux surface averaged transport equations derived in Section 2.0.2. by a Crank-Nicholson method of finite differences. The code contains algorithms that simulate many different sources and sinks of particles, energy, and current including a Monte Carlo calculation of neutral beam deposition, heating, and current drive and bootstrap current. The code also allows several different prescriptions of the transport coefficients. The transport model used in the present analysis is given in the next section.

---

[1]Bateman, G., Spring College on Plasma Physics, Charged Particle Transport in Plasmas, Int. Centre for Theoretical Physics, Trieste, (1985).

3.2.2 Transport Coefficients

The transport model adopted here includes neoclassical diffusion supplemented by a model of anomalous transport developed by Tang.[1] In this model, the anomalous heat diffusion is driven by low frequency drift instabilities; for the parameters of interest here, the dominant mechanism is the toroidal ion temperature gradient mode (η_i mode). A fundamental feature of the model is that local thermal diffusion coefficients are derived which are constrained to satisfy the empirical notion of "profile consistency". This model has been used successfully to simulate details of both TFTR[2] and PBX[3] discharges. A complete description of this transport model can be found in Ref. [2]. In the calculations described here the confinement times predicted by the model are comparable, for example, with the widely quoted Kaye-Goldston "L-mode" scaling formula.[4]

At sufficiently high $<\beta>$ ballooning modes appear and the electrostatic model of anomalous transport is no longer applicable. Since the transport code can detect infinite-n ballooning instability at any flux surface we model the onset of these modes by locally enhancing diffusion.[5] Thus, at an unstable surface we simply increase the local transport coefficients by a large factor dependent on the ratio p'/p'_c whenever this ratio exceeds unity; here p' is the local pressure gradient and p'_c is the critical value for high-n ballooning. These "ballooning enhanced" transport coefficients were limited to values comparable to the local Bohm diffusion values. Stabilizing FLR effects are not assumed in the derivation of p'_c. This transport model provides a barrier to direct access of the second stability region. The extent of this barrier is governed by the pressure and safety factor profile evolution. Depending on the input conditions of the simulation, the plasma parameters can either saturate at marginal first region values, or make a transition to second stable region values. In this way, the present prescription need not necessarily result in marginally stable first region profiles with $<\beta>$ limited to a value comparable to $<\beta>_1$. This transition has also recently been studied using analytic models to define the high-n unstable region.[6,7]

---

[1]Tang, W.M., in *Plasma Physics and Controlled Nuclear Fusion Research* (Proc. 11th Int. Conf. Kyoto, 1986) Vol. 1, IAEA, Vienna (1986) 337; Nuclear Fusion **26** (1986) 1605.

[2]Redi, M.,Tang, W.M., Efthimion, P.C., Mikkelsen, D.R., Schmidt, G.L., Nuclear Fusion **27** (1987) 2001.

[3]Jardin, S.C., Delucia, J., Okabayashi, M, Pomphrey, N., Reusch, M., Kaye, S., Takahashi, H., *Post Distruptive Plasma Loss in the Princeton Beta Experiment (PBX)*, PPPL-2358, Princeton, New Jersey (1986).

[4]Kaye, S.M. and Goldston, R.J., Nuclear Fusion **25** (1985) 65.

[5]Houlberg, W.A., Hogan, J.T., Nuclear Technology/Fusion **3** (1983) 244.

[6]Capes, H., Mercier, C., Morera, J.P., Nuclear Fusion, **27** (1987) 149.

[7]Fu, G.Y., Van Dam, J.W., Rosenbluth, M.N., in *Theory of Fusion Plasmas* (Proceedings of the Varenna Workshop, Varenna, Italy, 1987) Vol. 1, Editrice Compositori, Bologna (1987) 153.

3.2.3 Simulation of Transition to Second Stability Region

The calculations described in this section refer to a circular cross section tokamak with aspect ratio 9 (major radius R = 1.5m), toroidal field B = 1T, plasma current I = 30-45KA, and heated by high energy neutral injection. Variation of the injection angle and the beam parameters also permits some control of the q profile through the effect of beam induced current drive.[1] The existence of this current has now been documented in several experiments: DITE,[2] TFTR,[3] and DIII-D.[4] Here, a 3MW hydrogen neutral beam with a primary energy of 30 keV is co-injected such that the tangent radius is halfway between the geometric center and the large major radius boundary.

The computational procedure involves first establishing an ohmic target plasma whose density is close to the Murakami value; subsequently the beam is switched on at full power and the density is increased by a factor of two to exploit the weak, but favorable dependence of confinement with density. This procedure is illustrated in Fig. 3.2.3 - 1 which shows the evolution of the average electron density, temperature, $<\beta>$, and energy confinement time, τ_e. The beam is switched on at 50 ms. The total $<\beta>$ in this case increases to 3% of which 0.8% is contributed by beam particles. For reference, values of τ_e calculated from the Kaye-Goldston L-mode formula are indicated in the figure during the beam heating phase. The intense heating results in a dramatic change of the equilibrium configuration. The magnetic axis suffers a large displacement, the flux surfaces become distorted, and the edge q value increases rapidly. It is necessary to limit this behavior by ramping the total current to prevent β_p from becoming too large. Although not modeled here, this characteristic could be exploited to produce an inboard divertor configuration, which theoretically exhibits

favorable stability properties to high-n modes.[5] In the present example, the current was increased linearly from 30kA to 45kA in 50 ms from the start of beam heating. During the evolution, the MHD equilibrium was recalculated at frequent intervals and each state saved for subsequent analysis.

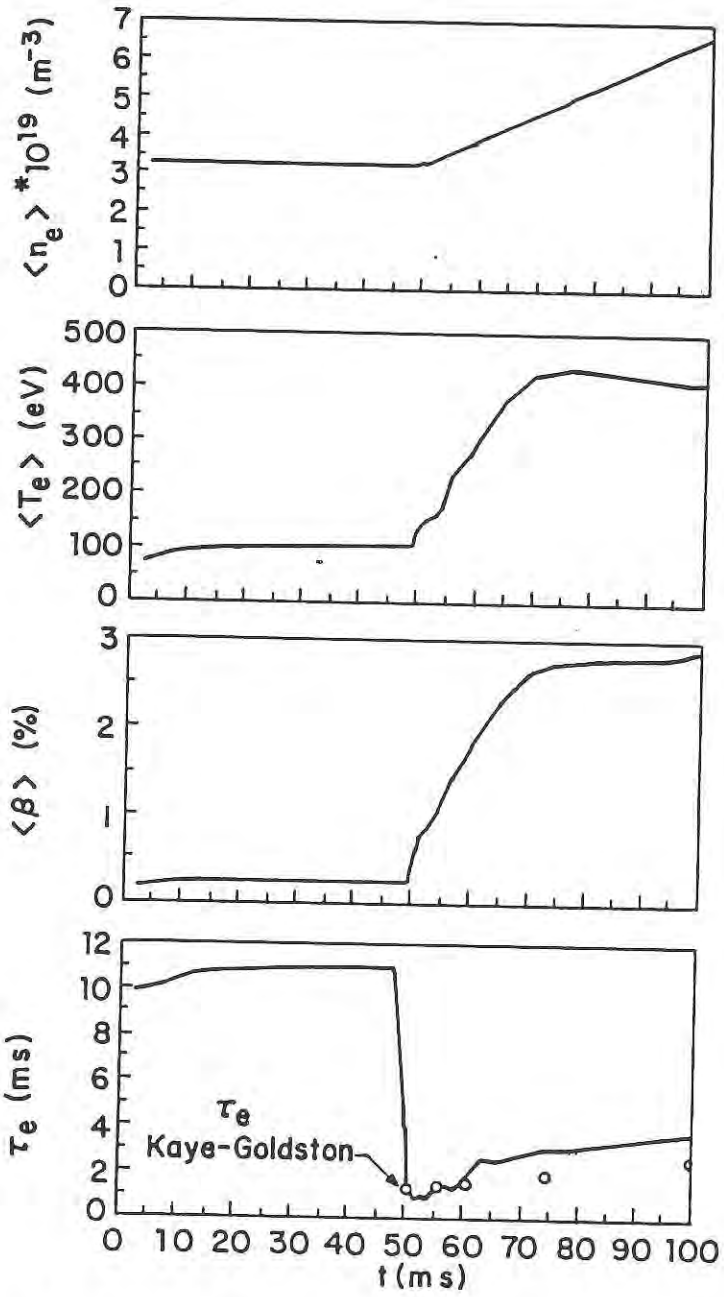

Fig. 3.2.3 - 1: Evolution of global parameters for A=9 transition case. Beams are switched on at 50 ms.

While MHD stability studies show that completely stable access paths to the second region exist,[6,7] our transport generated equilibrium profiles have always shown a region of residual high-n ballooning instability. The q profile is not independently prescribed and frozen in time in the transport calculations. Instead, it evolves from an ordinary ohmic profile with $q_0 \sim 1$, to a second stable profile with $q_0 > 1$, satisfying the magnetic field diffusion equation as the transition is made. For all aspect ratios, the high-n instability occurs before the stabilizing effects of magnetic axis shift and raising q_0 take full effect. It is a general feature of the simulation that global second stability is obtained when the size of the high-n unstable region is sufficiently reduced, which allows the plasma core to heat and the plasma edge to stabilize during beam heating. The size of the unstable region refers to the area covered in (p', ψ) space by the instability. This reduction is provided by suitable q profile modification by neutral beam driven current. Figs. 3.2.3 - 2 and 3.2.3 - 3, showing the evolution of $<\beta>$ and the dynamics of the high-n unstable region, illustrate transition to the second region.

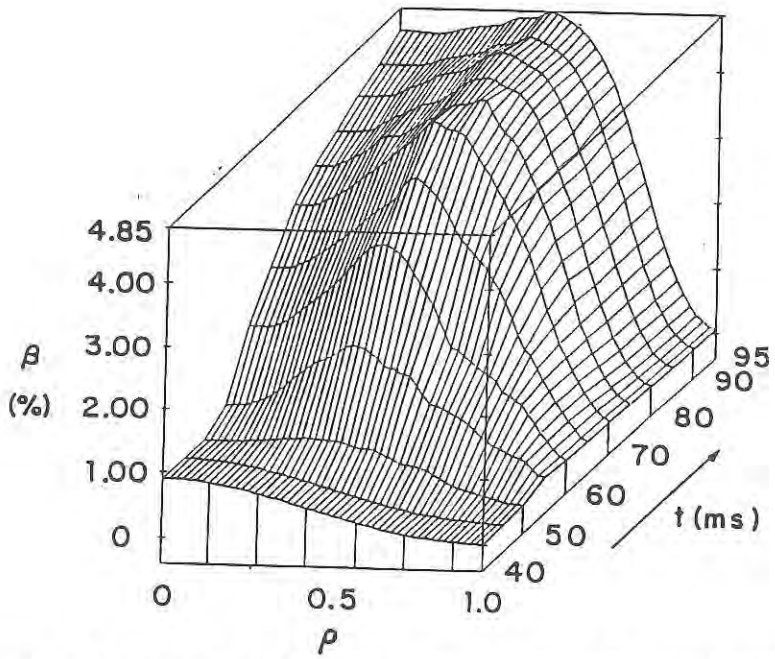

Fig. 3.2.3 - 2: Evolution of β profile during transition to second stability. *The normalized flux coordinate* $\rho = ((\psi - \psi_0)/(\psi_a - \psi_0))^{0.5}$. *The pressure includes the contribution from the beam.*

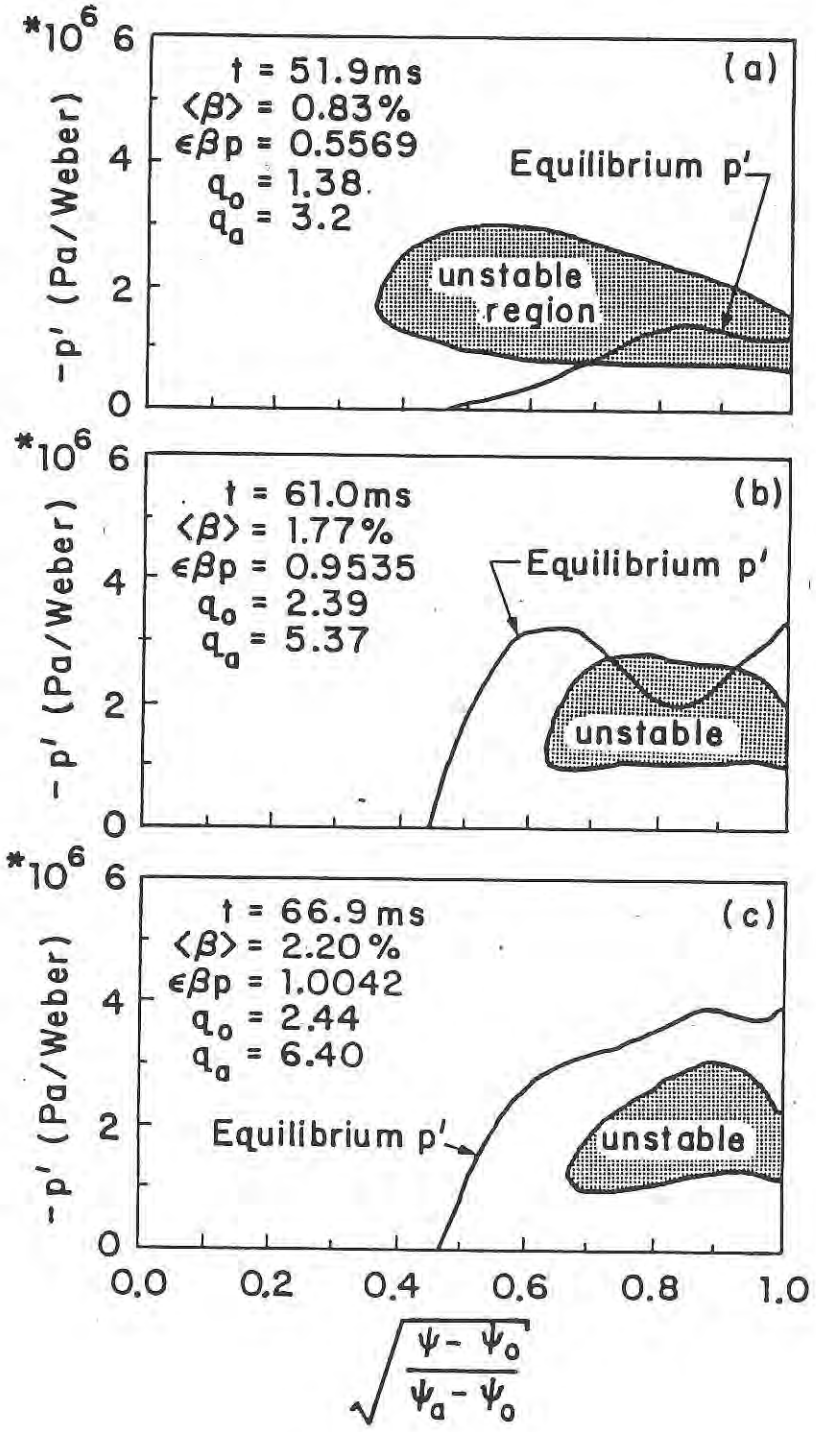

Fig. 3.2.3 - 3: Dynamics of the unstable region during transition. *Second region transition occurs when the outer flux surfaces become second region stable, thereby isolating the unstable surfaces from the plasma edge.*

At the early stages of the beam heating phase (~2 msec), the marginal first region stability boundary covers 65% of the plasma minor radius (Fig 3.2.3 - 3a). High-n modes appear on some flux surfaces, and the pressure profile is subsequently driven toward marginal first region stability caused by the enhanced transport losses due to the instability. As the heating proceeds, the beam driven current flattens the current profile and raises q_0 above unity. This reshaping of the q profile enhances the plasma stability (Section 3.2.4.1). Fig. 3.2.3 - 3b shows that the unstable region has been reduced in size, covering only the outer 40% of the flux surfaces 11 msec into the beam phase. The pressure gradient is limited on these surfaces while the pressure increases steadily in the high-n stable core (Fig. 3.2.3 - 2). The core plasma establishes a rising pressure pedestal, which increases p' on the unstable surfaces. At sufficient beam power, the outermost flux surfaces bridge the small unstable gap in p' (Fig 3.2.3 - 3b), and restabilize in the second region. The remaining unstable surfaces are thermally isolated from the plasma edge as ballooning enhanced transport ceases on the stable edge surfaces. The pressure on this unstable "plateau" is subsequently raised by beam heating and the local unstable region shrinks in size. Eventually, the plasma reaches global second stability when the unstable surfaces restabilize in the second stability region (Fig. 3.2.3 - 3c), 17 msec after the beam turns on. Fig. 3.2.3 - 4 shows the high-n second region stable poloidal flux contours with $<\beta> = 2.2\%$, $\varepsilon\beta_p = 1.00$; also shown are the pressure and q profiles used to generate this equilibrium.

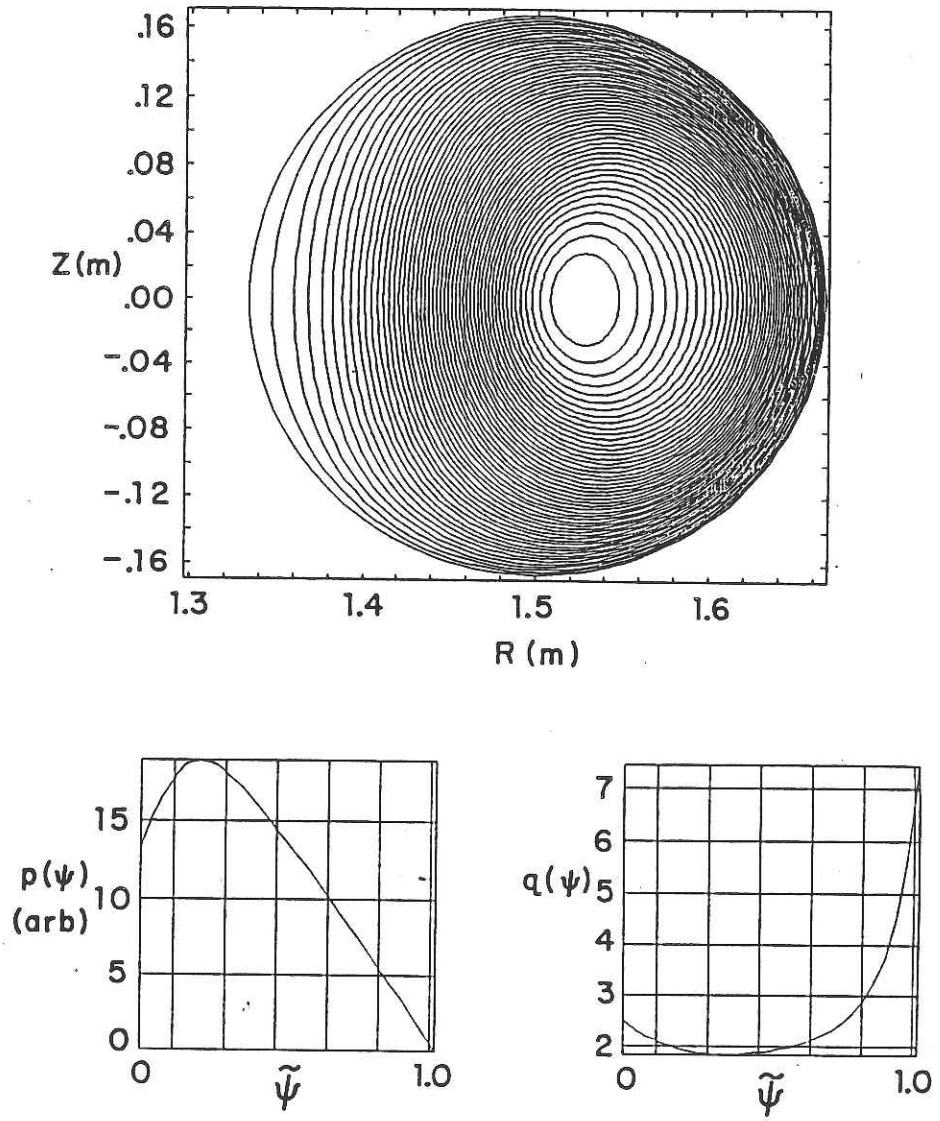

Fig. 3.2.3 - 4: Second stable region equilibrium flux contours, pressure and safety factor profiles. $<\beta>=2.2\%$, $\varepsilon\beta_p=1.00$. *The normalized flux coordinate* $\Psi = (\psi - \psi_0)/(\psi_a - \psi_0)$.

---

[1]Fisch, N., Reviews of Modern Physics, **59** (1987) 175.

[2]Clark, W.H.M., Cordey, J.G., Cox, M., Gill, R.D., Hugill, J., Paul, J.W.M., and Start, D.F.H., Phys. Rev. Lett. **45** (1980) 1101.

[3]Hawryluk, R.J., and TFTR Group, in *Plasma Physics and Controlled Nuclear Fusion Research* (Proc. 11th Int. Conf. Kyoto, 1986) Vol. 1, IAEA, Vienna (1986) 51.

[4]Simonen, T.C., Bhadra, D.K., Groebner, R.J., Harvey, R.W., Kim, J., Lao, L., Matsuoka, M., and St. John, H., Bull. Am. Phys. Soc. **32** (1987) 1900.

[5]Bishop, C.M., Nuclear Fusion, **26** (1986) 1063.

[6]Todd, A.M.M., Phillips, M.W., Chance, M.S., Manickam, J., and Pomphrey, N., in *Plasma Physics and Controlled Nuclear Fusion Research* (Proc. 11th Int. Conf. Kyoto, 1986) Vol. 2, IAEA, Vienna (1986) 37.

[7]Yamazaki, K., Naitou, H., Amano, T., Hamada, Y., Matsuoka, K., Midzuno, Y., Nakayama, Y., Sato, T., Tsunematsu, T., Tuda, T., Seki, S., Azumi, M., Tokuda, S., Ozeki, T., Nemoto, T., Kishimoto, Y., Takeda, T., in *Plasma Physics and Controlled Nuclear Fusion Research* (Proc. 11th Int. Conf. Kyoto, 1986) Vol. 2, IAEA, Vienna (1986) 27.

3.2.4 Effects of Parameters on Transition

The following three sections discuss the effects that q_0, outer boundary shaping, aspect ratio, and the large-n instability transport enhancement factor, on the transition to the second region. It is found that increasing q_0 and A reduces the auxiliary power requirements to successfully cross into the second region. As expected, increasing the transport enhancement factor increases the power requirement, and dee-shaping of the plasma outer boundary reduces the required auxiliary power.

3.2.4.1 Current Programming

The substantial reduction of the size of the high-n unstable region needed to allow access to second stability is obtained with current programming. Since the neutral beam driven current is comparable in magnitude to the plasma current for the transition case of Section 4, beam injection is an effective means of current programming. We wish to reduce the current density near the magnetic axis, which in turn increases the value of q_0. This reshaping of the q profile enhances the plasma stability.[1-3] Shown in

Fig. 3.2.4.1 - 1 is the effect of the neutral beam on the flux surface averaged current density profile defined as $<J\varphi B\varphi>/(RB\varphi <1/R>)$.

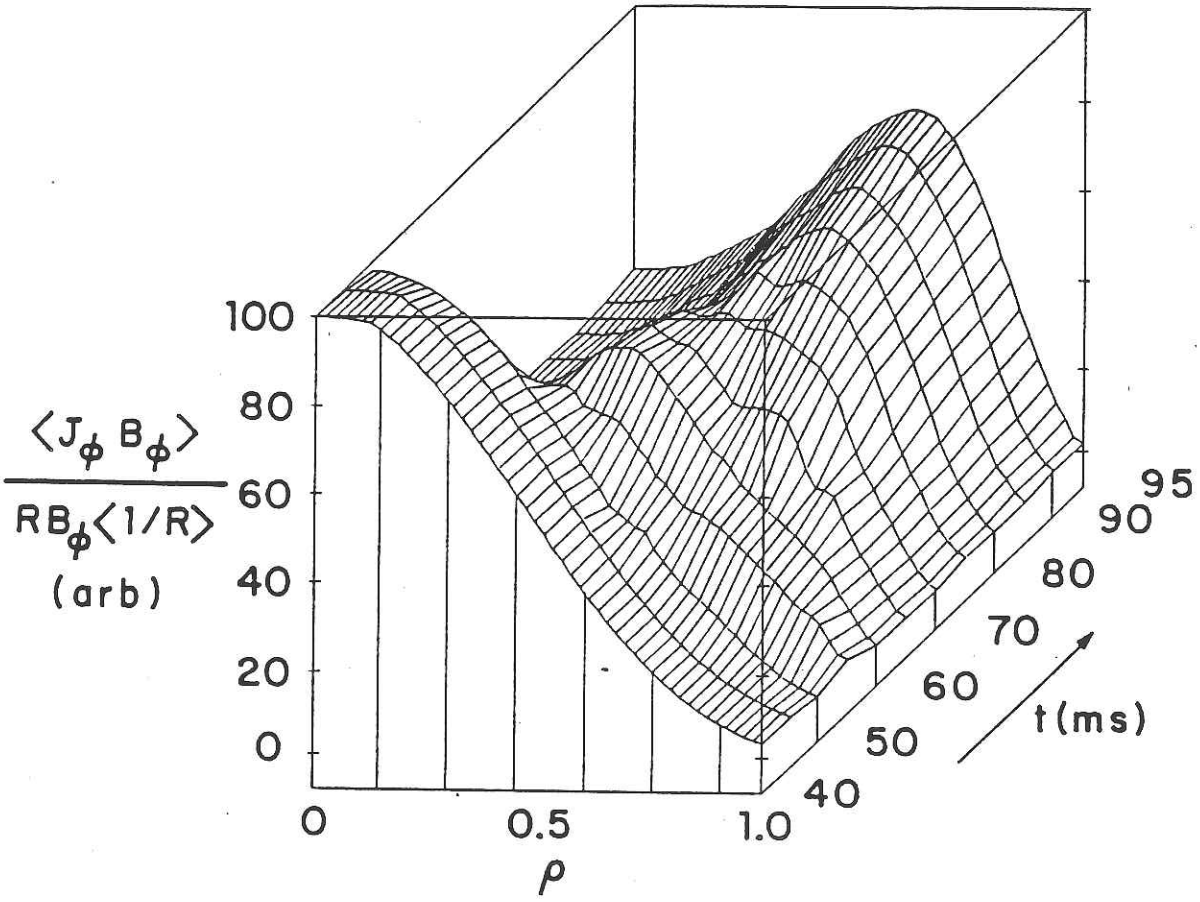

Fig. 3.2.4.1 - 1: Effect of neutral beam on current density, q_0=2.45 case. The current density is plotted as a flux surface averaged quantity $<J\varphi B\varphi>/(RB\varphi <1/R>)$. The current profile flattens and becomes hollow as the off-axis beam heating begins.

The point of tangency of the beam centerline is shifted off-axis, toward the outboard side of the plasma, in order to broaden the current profile thus raising q_0. At the start of the simulation, the current density profile relaxes to an ohmic shape. However, shortly after the beam turns on, half of the plasma current is driven by the beam. Since q is greater than one throughout the plasma, there is no sawtooth activity. Fig. 3.2.4.1 - 2 shows the evolution of the q profile.

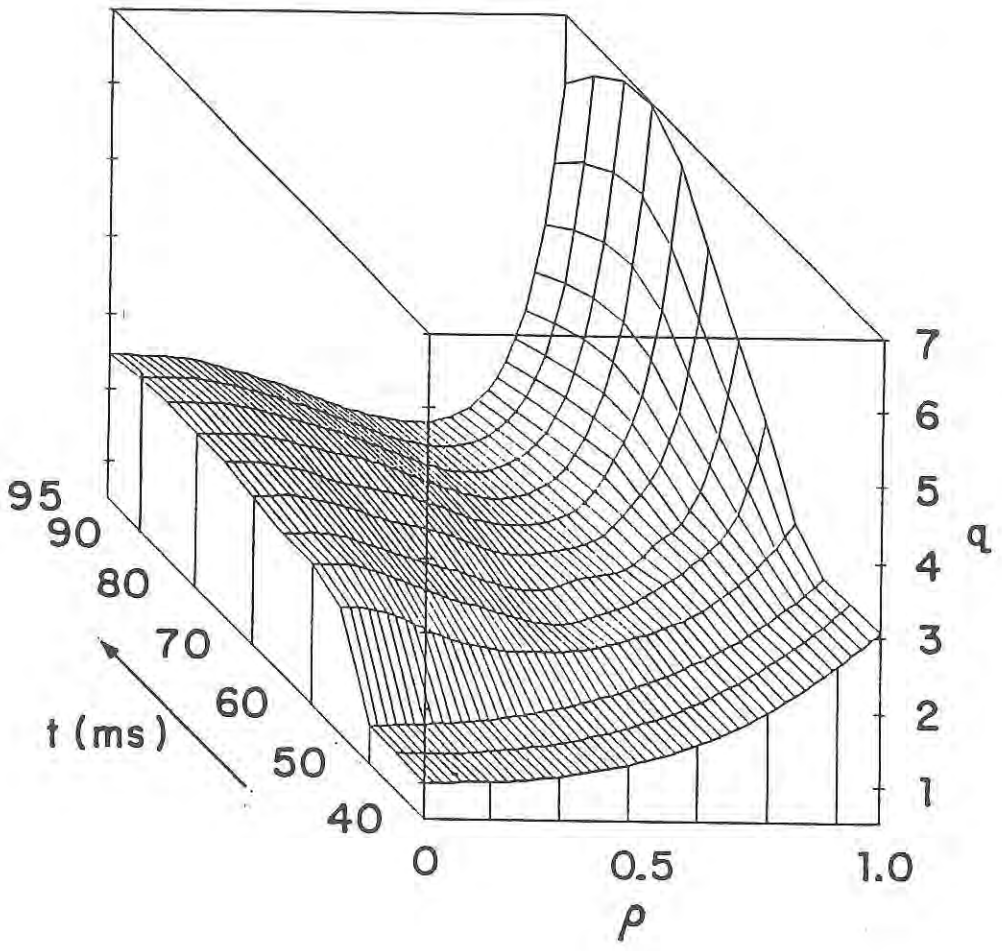

Fig. 3.2.4.1 - 2: Safety factor profile, q_0=2.45 case.

In this particular case, q_0 reaches a peak value of 2.45 and a hollow current profile develops. Second region transition is also obtained for smaller values of q_0 and flatter current profiles. Fig. 3.2.4.1 - 3 illustrates the current and q profiles for a second stable region transition with peak q_0=1.55.

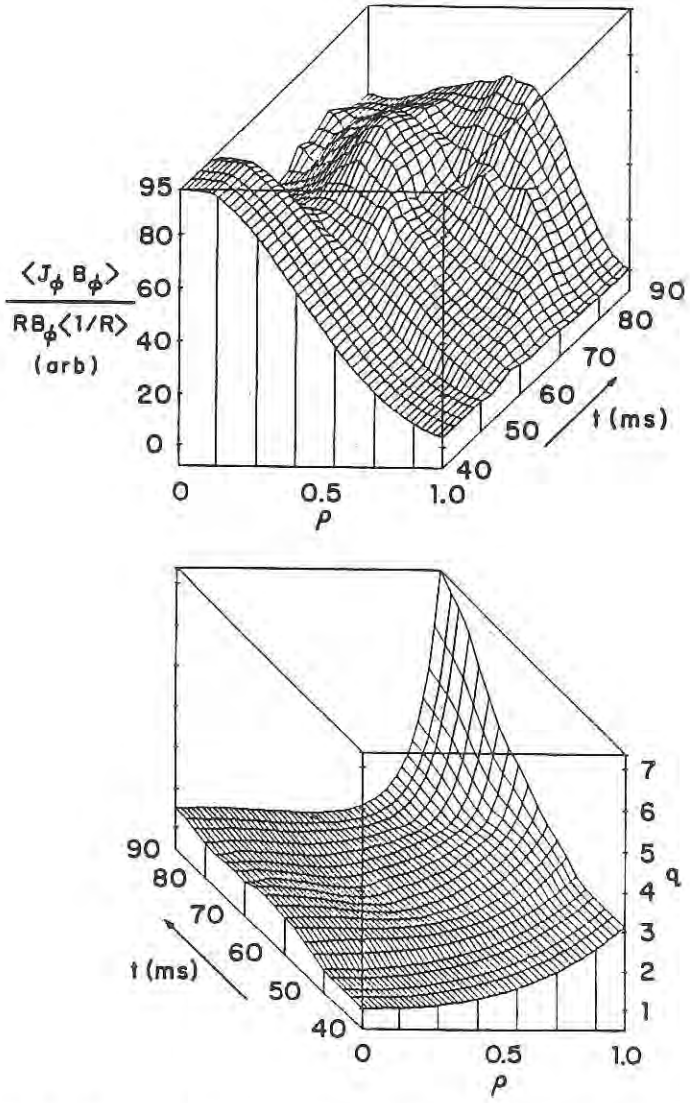

Fig. 3.2.4.1 - 3: Current density and safety factor profiles, q_0=1.55 case.

Increasing q_0 typically decreases the size of the unstable region. This is illustrated in Fig. 3.2.4.1 - 4 where the unstable region of two equilibria with q_0>1 are compared to an equivalent case in which q_0~1. This sequence exhibits a reduction in the spatial extent of the unstable region from a maximum of 85% (Fig. 3.2.4.1 - 4a) to a minimum of 25% (Fig. 3.2.4.1 - 4c) of the plasma minor radius.

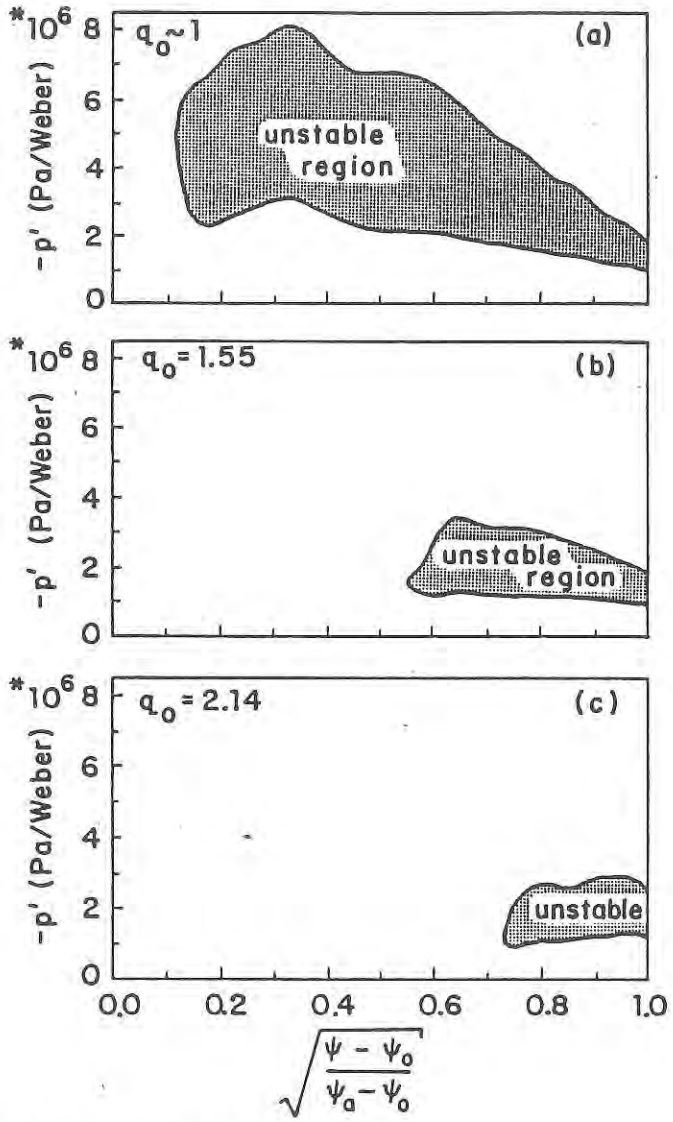

***Fig. 3.2.4.1 - 4:** Reduction in size of the unstable zone with increasing q_0. In case a) $q_0 \sim 1$, b) $q_0 = 1.55$, c) $q_0 \sim 2.14$. This reduction allows transition to the second region.*

Transition to the second region is not observed in simulations where q_0 remains near unity. Consider case a) of Fig. 3.2.4.1 - 4. where the beam is injected tangentially to the inboard edge of the plasma. The evolution of p for this case is shown in Fig. 3.2.4.1 - 5. The unstable region initially covers more than 85% of the plasma, including the edge region, so that the absorbed power is quickly transported away. As the simulation proceeds in time, the outer flux surfaces remain marginally stable to the

first region boundary. Ultimately, $<\beta>$ is limited to a maximum value of 1.04%, which occurs 10 ms after the beam turns on. The constant C_t for this case is 3.9. This result is consistent with previous calculations exhibiting marginally first region stable pressure profiles.[4,5]

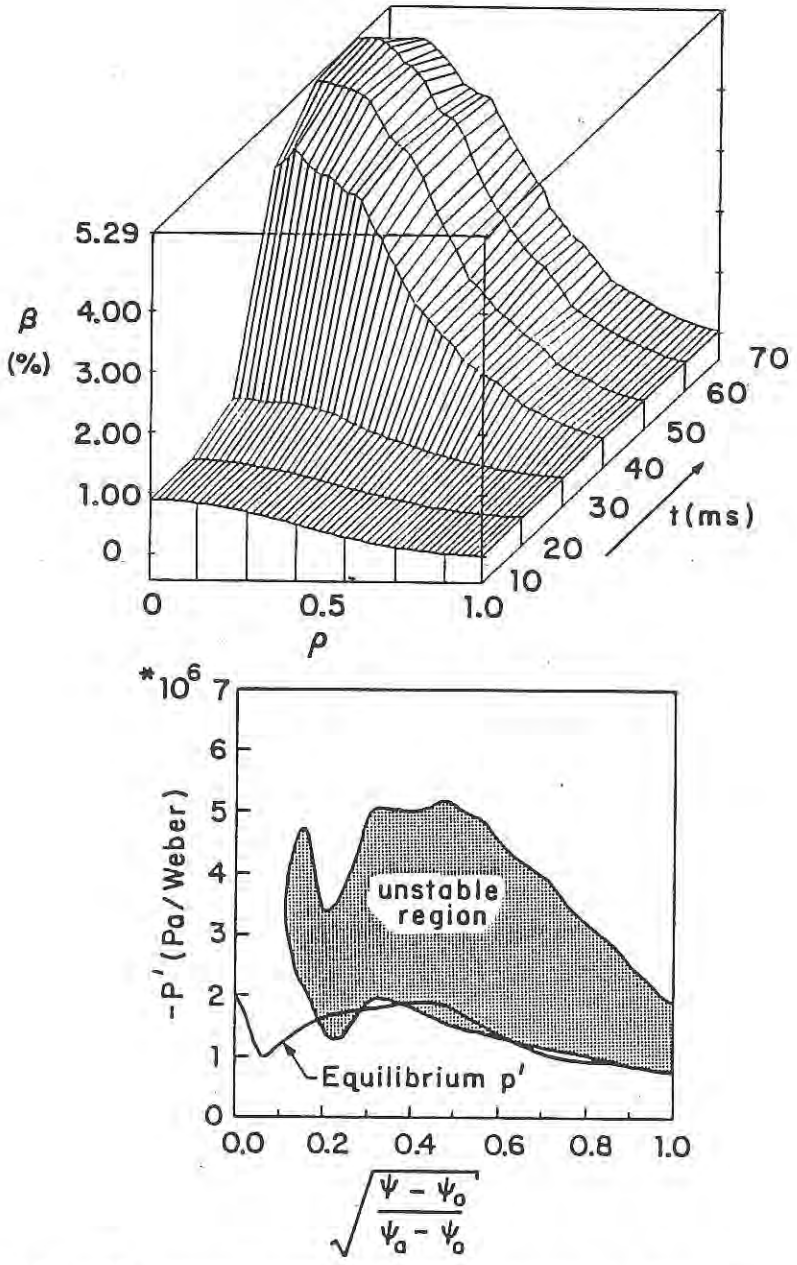

Fig. 3.2.4.1 - 5: Pressure profile and critical pressure gradients $q_0 \sim 1$ case. Equilibrium p' values closely match marginally stable first region values.

The bootstrap current, which has been theoretically associated with current related $<\beta>$ limits in tokamaks[6,7] is not important here since the plasmas considered are collisional. For the modeled parameters, ν_e^*, the ratio of the electron collision frequency to the bounce frequency, is large during transition. The value of $\nu_e^* \sim 40$ in the large pressure gradient region of the A=9 case of Section 4. In principle, the bootstrap current would help increase q_0, since the pressure gradient that drives the current is large in the outer flux surfaces. In banana regime plasmas, the bootstrap current may need to be counteracted by the beam driven current to insure that the local q value remain above unity where the bootstrap effect is largest.

---

[1]Sykes, A., Turner, M.F., in *Controlled Fusion and Plasma Physics* (Proc. 9th Europ. Conf., Oxford, 1979), UKAEA, Culham Lab., Abingdon (1979) 161.

[2]Coppi, B., Crew, G.B., and Ramos, J.J. Comments on Plasma Physics and Controlled Fusion 8 (1983) 11.

[3]Todd, A.M.M., Manickam, J., Okabayashi, M., Chance, M.S., Grimm, R.C., Greene, J.M., Johnson, J.L., Nuclear Fusion 19 (1979) 743.

[4]Azumi, M., Tsumenatsu, T., Itoh, K., et al., in *Plasma Physics and Controlled Nuclear Fusion Research* (Proc. 8th Int. Conf. Brussels, 1980) Vol. 1, IAEA, Vienna (1980) 293.

[5]Connor, J.W., Taylor, J.B., and Turner, M.F., Nuclear Fusion 24 (1984) 642.

[6]Kadomtsev, B.B., and Shafranov, V.D., in *Plasma Physics and Controlled Nuclear Fusion Research* (Proc. 4th Int. Conf. Madison, 1971) Vol. 2, IAEA, Vienna (1971) 479.

[7]Bickerton, R.J., Connor, J.W., and Taylor, J.B., Nature Physical Science 229 (1971) 110.

3.2.4.2 Outer Boundary Shaping

Dee-shaped outer boundary plasmas were examined in addition to the circular boundary shape and an improvement in performance was observed with respect to the requirements needed to make transition to the second region. As a comparison, an A=9,

dee-shaped plasma with R = 1.5m, a =0.17m, κ = 1.5, and δ = 0.23 was considered as a transition case. While a high-n unstable region was encountered near the plasma edge during the start of the beam heating phase, the time required to make the transition to the second region was reduced as compared to the circular boundary cases. In addition, the minimum power required was reduced to 2MW for the dee-shape, constituting as 23% reduction in the required power to make the transition. This reduction is due to the reduced size of the unstable region created by the inclusion of the plasma shaping and the increased value of q_0 that this case displayed. The value of q_0 was greater than one during the ohmic phase of the discharge simulation, in this case, $q_0 \sim 1.5$ as the beams turned on.

3.2.4.3 Power Requirements for Transition

There is a critical auxiliary power level, P_{crit} , below which the transition to second stability does not occur. Since the beam driven current scales as $P\,T_e/(n_e\,R)$, where T_e and n_e are the electron plasma temperature and density, and P is the beam power[1], a reduction of the beam power and the accompanying decrease in T_e both conspire to reduce the magnitude of the beam driven current. When the auxiliary power is less than P_{crit} , the current profile is flattened, but the edge flux surfaces do not cross into second stability. This behavior limits T_e on the high-n unstable surfaces near the plasma edge, thus reducing the beam driven current locally. This reduces q_0 and the profiles are again driven toward marginal first region stability.

The minimum power density, $P_{crit}\,/\,V$, needed to accomplish transition to the second stability region is found to decrease with increasing A. Here, V represents the

plasma volume. This critical power density as a function of A is shown in Fig. 3.2.4.3 - 1. In these calculations, aspect ratio was varied by fixing the minor radius at 0.167m and allowing the major radius to change between cases. Alternatively, R or V could be held constant while varying minor radius. However, we find that constant minor radius is necessary to keep the q profiles of the same shape for various aspect ratios, so that the cases can be more readily compared. The ohmic density is kept at the Murakami value, which depends explicitly on R, and therefore is changed for each A. This prescription for the density eliminates the explicit R^{-1} dependence of the beam driven current, allowing q_0 to be similar for each case. The beam injection angle was varied to keep the beam deposition approximately constant. The edge and axis q values were kept approximately constant for various ε by altering the total plasma current appropriately. For all cases, $q_{o\ \text{beam}}$ ranged from 1.5 to 1.7, $q_{a\ \text{ohmic}}$ ~3 and $q_{a\ \text{beam}}$ ~ 4 where the subscripts refer to the steady state values during the ohmic and beam phases of the simulation.

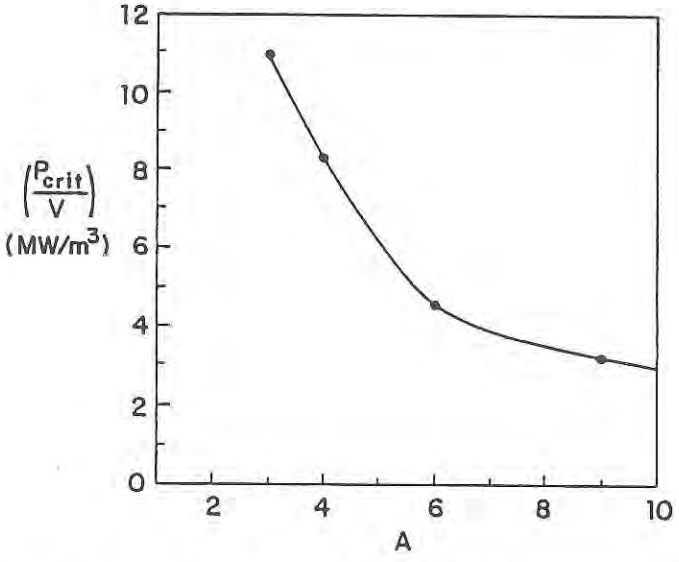

Fig. 3.2.4.3 - 1: Critical power density for second region transition as a function of A.

Since the transport generated equilibria encounter a region of instability during transition, P_{crit} / V depends on the magnitude of the diffusion enhancement in the

unstable region. Fig. 3.2.4.3 - 2 shows the relation of P_{crit}/V to the enhanced thermal diffusivity, χ_{max}, normalized to the Bohm diffusion value, for two different values of A. The ratio of these coefficients pertains to the flux surface located at the center of the unstable region. Except for the data in Fig. 3.2.4.3 - 2, all the results presented in this paper have $\chi_{max}/(kT_e/16eB_0) \sim 3$. This enhancement corresponds to approximately a factor of ten increase in the coefficients obtained from the η_i mode anomalous transport model. The flux surface averaged description of transport breaks down if the coefficients are large enough to cause the timestep of the calculation to be comparable to the Alfvén time. This happens for our calculations when $\chi_{max}/(kT_e/16eB_0) \sim 20$. The power estimate for the A=9 case is in rough agreement with a large A, analytic model of P_{crit} derived by Fu, et al..[2]

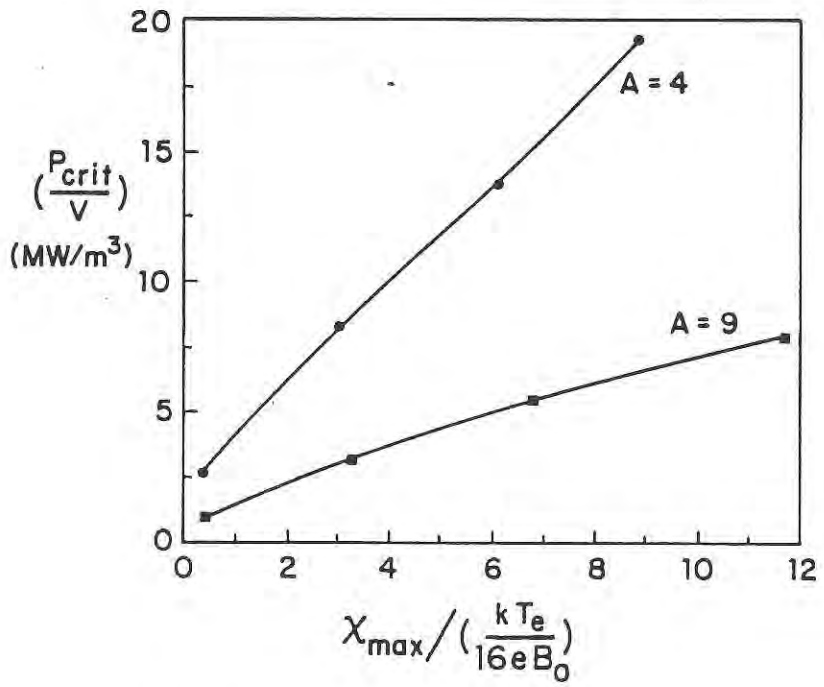

Fig. 3.2.4.3 - 2: Critical power density for second region transition as a function of diffusivity enhancement. Curves shown are for A=4 and A=9 cases.

The ratio of the time required to make the transition to the second region, to the ohmic energy confinement time, $\tau_{trans}/\tau_{e\ \text{ohmic}}$, maintains an essentially constant

value of 2.3 for each aspect ratio at the critical power density. Also, it should be noted that if the auxiliary power is increased above P_{crit}, the ratio τ_{trans}/τ_e ohmic is reduced. For example, at A=9 we find that this ratio is reduced from 2.3 to 0.9 as the beam power density is increased from P_{crit}/V = 3.16 MW/m^3 to 4.26 MW/m^3. The unstable gap in $<\beta>$ is shown in Fig. 3.2.4.3 - 3 with values generated by the transport code. The curve labeled $<\beta>_2$ corresponds to the $<\beta>$ values at the critical power density. The curve labeled $<\beta>_1$ corresponds to the $<\beta>$ values obtained for cases which did not transition to the second region at slightly lower power density. The difference in power density between the cases represented by $<\beta>_2$ and $<\beta>_1$ is small; about 7% for all aspect ratios. Therefore, as P/V is raised from zero to a value greater than P_{crit}/V, $<\beta>$ rises until the plasma becomes high-n mode unstable and the transport losses increase Fig. 3.2.4.3 - 4. At this point, $<\beta>$ saturates at a value near $<\beta>_1$ until the power density reaches P_{crit}/V. The $<\beta>$ then increases abruptly to $<\beta>_2$ as transition to the second region is made.

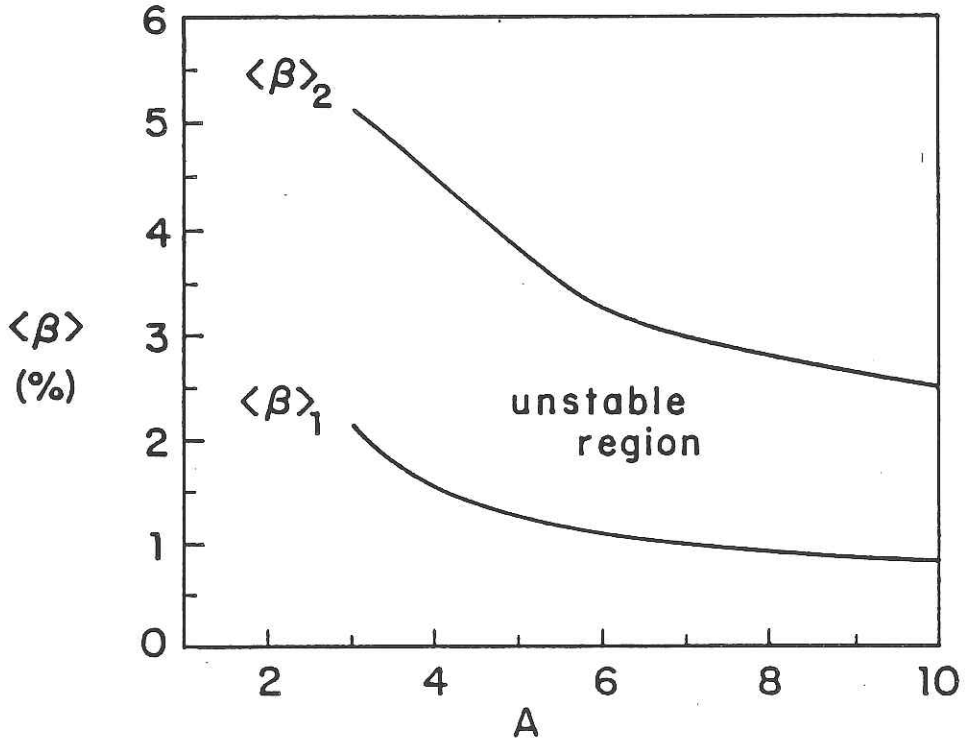

Fig. 3.2.4.3 - 3: Unstable gap in <β> as a function of A for transport generated equilibria; q_0~1.6.

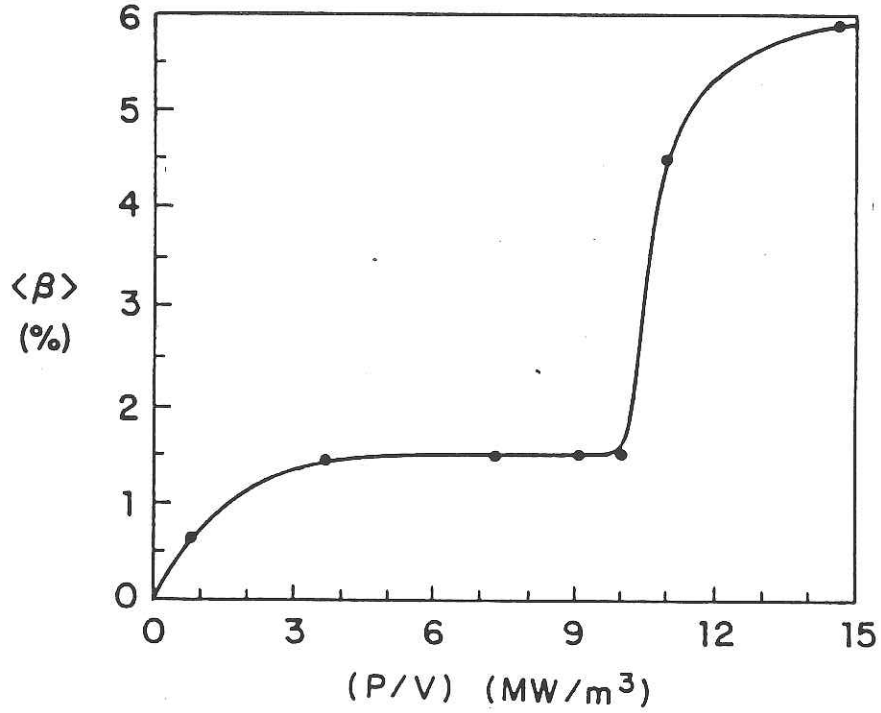

Fig. 3.2.4.3 - 4: <β> as a function of power density for A=4. As P/V increases, <β> saturates at $<\beta>_1$, and increases abruptly to $<\beta>_2$ when P/V reaches P_{crit}/V.

[1]Fisch, N., Reviews of Modern Physics, 59 (1987) 175.

[2]Fu, G.Y., Van Dam, J.W., Rosenbluth, M.N., in *Theory of Fusion Plasmas* (Proceedings of the Varenna Workshop, Varenna, Italy, 1987) Vol. 1, Editrice Compositori, Bologna (1987) 153.

3.2.5 Low-n Analysis of Transition Equilibria

Analysis of low-n modes for the transport generated equilibria considered here is consistent with previous MHD studies in which both external and internal mode stability is shown to improve as $\varepsilon\beta_p$ approaches and exceeds unity.[1] Internal mode stability of the transition equilibria analysed in Section 3.2.3 is shown in Fig. 3.2.5 - 1. At 2ms after the beam phase starts (Fig. 3.2.5 - 1a), an unstable mode is found which exhibits a monotonic increase in growth rate for n above 2.3 and oscillatory "infernal" mode behavior for smaller n values, indicating a breakdown of the conventional ballooning theory in low shear regions.[2,3] Note that n is treated as a continuous variable. This is necessary for a complete analysis since stability depends on the product (nq), and modest changes in q can shift non-integer n unstable infernal peaks to integer values of n. As $\varepsilon\beta_p$ increases however, we see the unstable mode move to larger values of n, and the infernal oscillations vanish (Fig. 3.2.5 - 1b). Finally, within a resolution of $\Delta n = 0.1$, the high-n mode, second stable equilibrium is also stable to low-n internal modes.

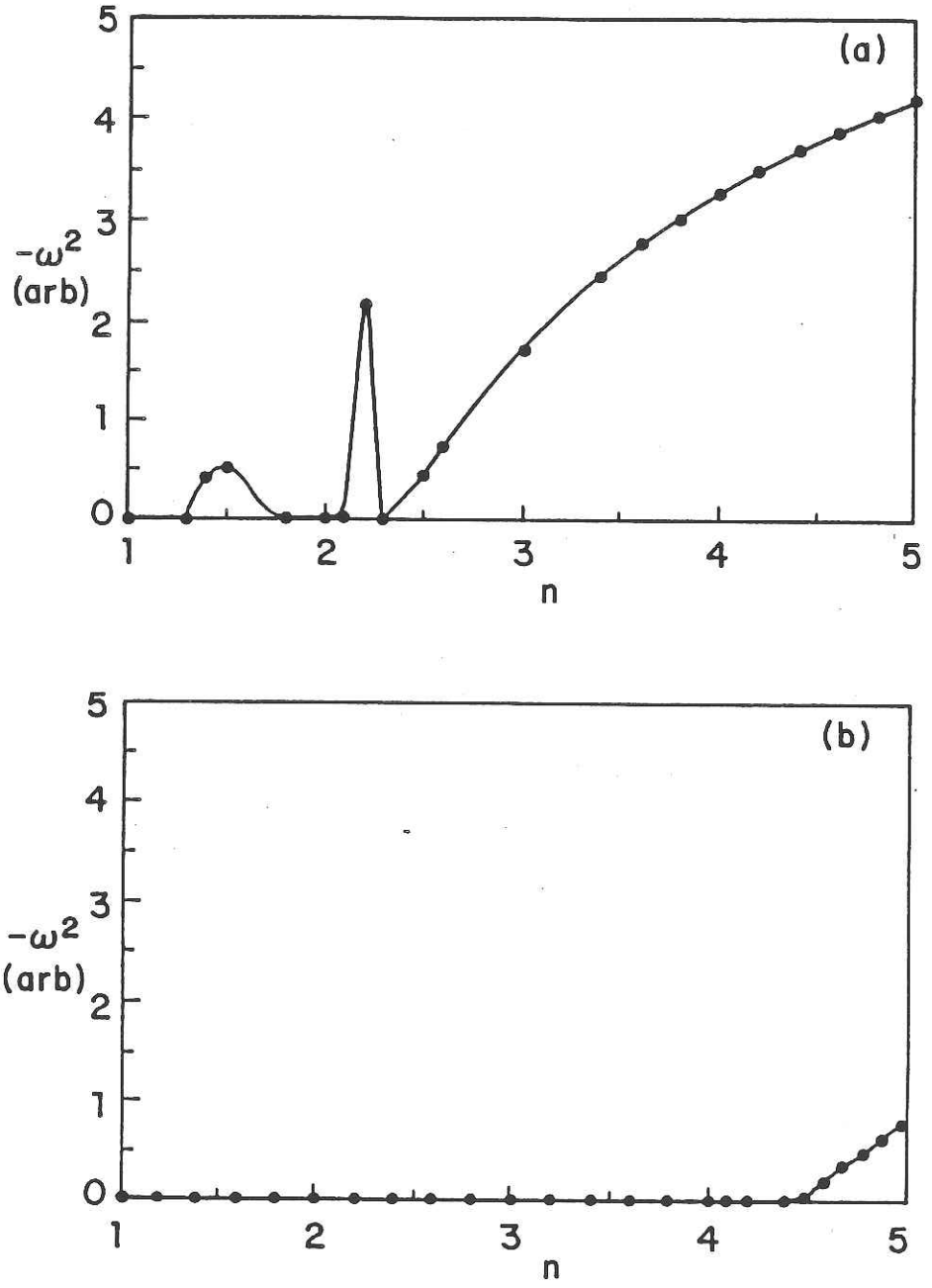

Fig. 3.2.5 - 1: Internal mode stability of A=9 transition equilibria. *The cases shown have a conducting wall on the plasma surface. a) $\varepsilon\beta_p$ = 0.56; n≥3 ballooning modes are unstable and infernal behavior is evident for n<2.5. b) $\varepsilon\beta_p$ = 0.95; shows a restabilization of these modes as $\varepsilon\beta_p$ increases toward unity. The second stable equilibrium with $\varepsilon\beta_p$ = 1 is stable to low n modes with n ≤5.*

Low-*n* infernal modes have not yet been identified in tokamak experiments, so their effect on the plasma is unclear. The stability of these internal modes is sensitive to

the profile details, as well as the value of $\varepsilon\beta_p$. In particular, moving large pressure gradients out of low shear regions increases stability. Again, since independent control of the pressure and q profile is not possible for the transport equilibria, a transition path completely stable to low-n modes has not yet been observed, in contrast to MHD calculations using analytic profiles in which stable access to all ideal modes has been found.[1] This situation is likely to also be the case in experiments where independent control of the pressure and safety factor profiles may not be possible. For the equilibrium shown in Fig 3.2.5 - 1a, the mode localizes in the region of high-n instability. This is shown in Figs. 3.2.5 - 2 and 3.2.5 - 3 which show the Fourier decomposition of the mode and a poloidal projection of the unstable eigenvectors.

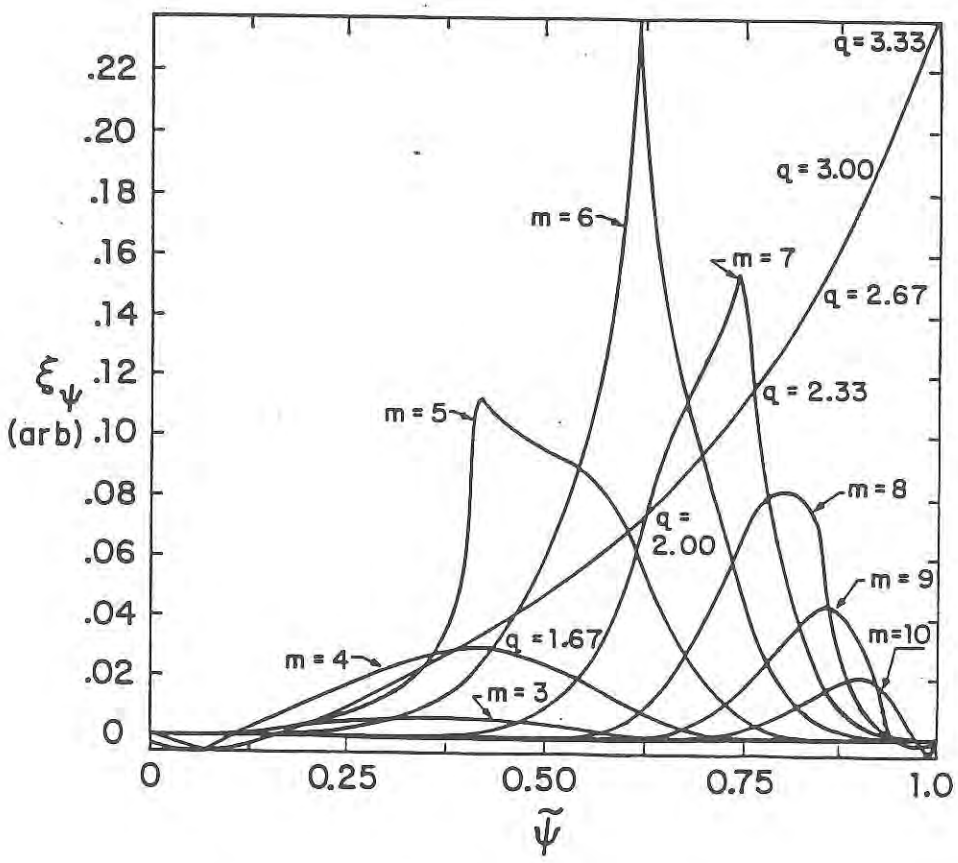

Fig. 3.2.5 - 2: Fourier decomposition of n=3 ballooning mode.

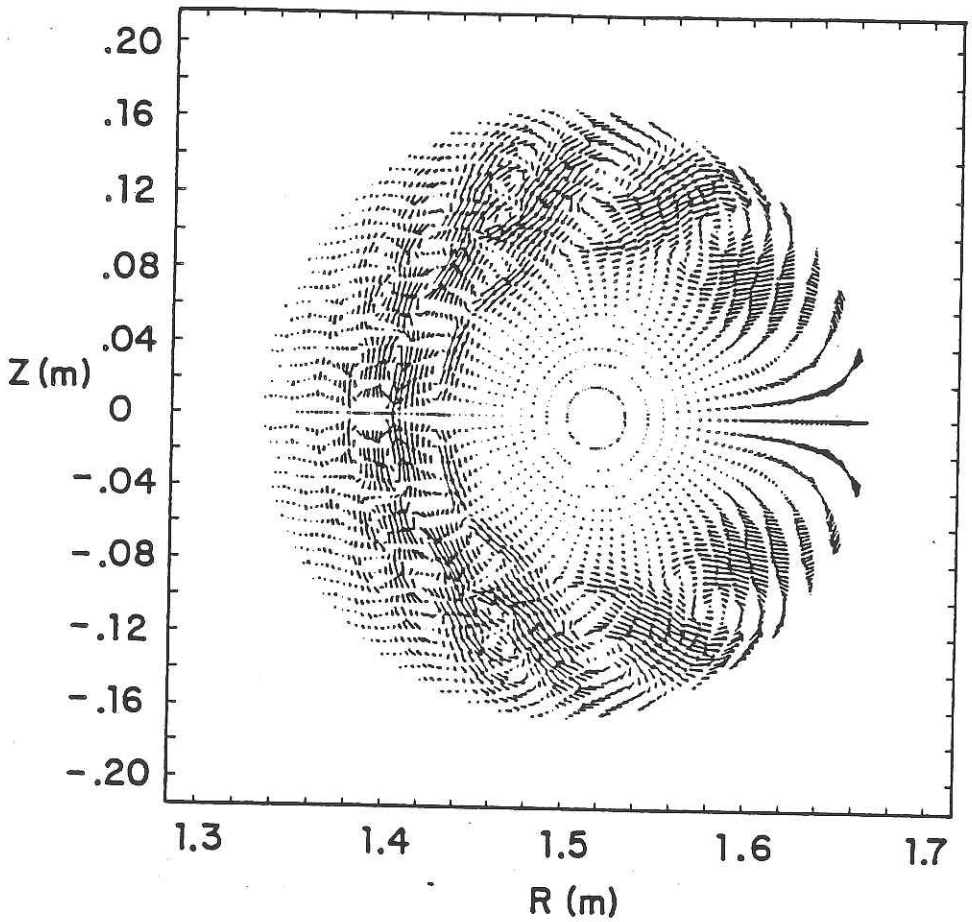

Fig. 3.2.5 - 3: Poloidal projection of unstable eigenvectors for n=3 ballooning mode. The mode localizes on the outer flux surfaces which are high-n unstable.

A low-n external kink mode has also been studied for these equilibria, which is found to be stabilized by a close fitting conducting wall. Fig. 3.2.5 - 4 shows the growth rate as a function of wall position for the transition equilibria shown in Fig. 3.2.3 - 3. The n=1 and 2 unstable modes at $\varepsilon\beta_p$ = 0.5569 contain both pressure gradient and current driven components, the latter being stabilized as the wall is brought closer to the plasma. The pressure gradient contribution is strongly unstable in this external kink-ballooning mode. This is reflected in the extremely small wall-plasma separation needed to stabilize the n=2 component. The wall radius, (b+a), must have a value that is 5% larger than the plasma radius (b/a=5%). This restriction is relaxed substantially as $\varepsilon\beta_p$ increases and the second region is reached. The most restrictive

wall position for the intermediate transition case (Fig. 3.2.5 - 1b) has a radius 15% larger that the plasma minor radius (b/a=15%). For the stable equilibrium in the second region, only n=1 and 2 modes are found to be unstable without a conducting wall, and these are stabilized by a wall with b/a=35%.

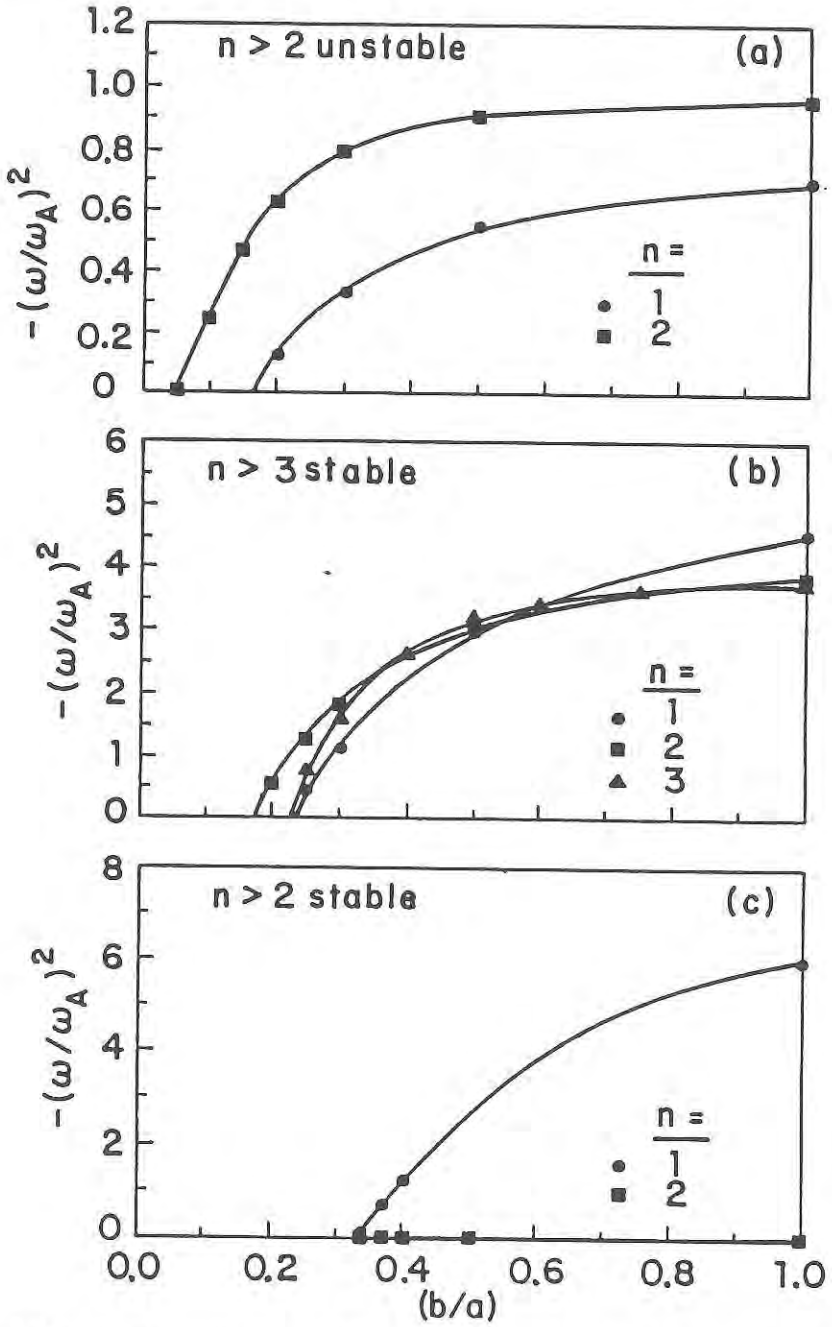

Fig. 3.2.5 - 4: External mode stability of A=9 transition equilibria. ω is normalized to the Alfvén frequency, ω_A. Conducting wall restrictions are mitigated as $\varepsilon\beta_p$ increases toward unity.

---

[1]Todd, A.M.M., Phillips, M.W., Chance, M.S., Manickam, J., and Pomphrey, N., in *Plasma Physics and Controlled Nuclear Fusion Research* (Proc. 11th Int. Conf. Kyoto, 1986) Vol. 2, IAEA, Vienna (1986) 37.

[2]Hastie, R.J., and Taylor, J.B., Nuclear Fusion 21 (1981) 187.

[3]Manickam, J., Pomphrey, N., and Todd, A.M.M., Nuclear Fusion 27 (1987) 1461.

Therefore, when the same wind that happens to accumulate them (the clouds) in some one particular spot has squeezed out many seeds of heat and in so doing has itself become intermingled with that fire, the imprisoned eddy spins in a cramped space and there in a glowing furnace forges a thunderbolt.

Lucretius (c. 100 - 55 B.C.) *On the Nature of Things*, 1 274-279.

4.0 APPLICATION TO EXISTING AND PROPOSED TOKAMAKS

The large contemporary tokamak experiments have been designed to optimize performance in the first stability region. One difficulty of the operation of these devices, and the subsequent reactor designs based on them, is the large plasma current needed to obtain adequate confinement and plasma pressure (by raising the Troyon-Sykes β limit) to produce fusion-relevant values of P_{fusion}. Recently, many experimental programs, including the large first region plasma tokamaks have considered trying to produce plasma equilibria that exist with pressure gradients within the second stability region. A major hope of these studies is to be able to produce a new tokamak operating regime in which a large β can be obtained at lower current and, as theoretically conjectured[1,2], possibly uncover an enhanced confinement regime at high β.

While the large tokamaks possess large amounts of auxiliary heating power, and are more than capable of producing the low plasma currents characteristic of high β_p equilibria, they are not optimally designed to produce second region plasmas. However, they are adequately suited to run experiments that attempt to access the second region to investigate its reality and whether or not improved confinement can be

observed. In this section, the consequences of the results of the present work are discussed in the context of a proposed second region experiment at Columbia University, SRX, and the two large tokamak experiments in the U.S., TFTR at the Princeton Plasma Physics Laboratory, and DIII-D at General Atomics.

---

[1]Bhattacharjee, A., Iacono, R., Marshall, T.C., Mauel, M.E., Navratil, G.A., Paranicas, C., Sabbagh, S.A., Sen, A.K., Van Dam, J.W., Wang, X.-H., Hughes, M.H., Phillips, M.W., Todd, A.M.M., "Second Regime Tokamak Operation at Large Aspect Ratio", Columbia University report #109, June 1987.

[2]Kesner, J., Nuclear Fusion 29 (1989) 1397.

4.1.1 SRX

The Second Regime Experiment (SRX) is a tokamak experiment proposed by Columbia University whose purpose is to operate a plasma in the second stability region. The present work grew from a design study for SRX,[1] the transition to the second region (Chapter 3.2) being a generalization of the original $A = 9$ study to include conventional aspect ratios of $A \geq 3$. With regard to large-n modes, SRX was designed as a high A device to avoid the destabilization of the second region boundary at low A and $q_0 \sim 1$. The method of accessing the second stability region was to increase q_0 by driving plasma current non-inductively through neutral beam injection. The beamlines were oriented tangentially to the magnetic axis to maximize driven currents on the outer flux surfaces and produce the largest values of q_0. The beam injection angles could be made more tangential than present devices since the larger A allowed the additional advantage of greater accessibility to the machine itself. The large A design also permitted operation of a lower plasma current for a given value of q,

thereby allowing the beams to drive a greater percentage of the current and further enhance the ability of the machine to create a larger q_0. With the second region plasma established, maintaining $q_0 > 1$ would no longer be important since β_2 and $\varepsilon\beta_{p2}$ are much less sensitive to the value of q_0 at high A. Recall, for instance, in Fig. 3.1.6.1 - 1, that at A=9, $\beta_2 < 5\%$ at $q_0 \sim 1$ while at A=3, $\beta_2 > 23\%$. The high A design avoids the problem of maintaining $q_0 > 1$ throughout the plasma steady state and still maintains a small value of β_2 by reducing the destabilizing poloidal field curvature drive, that appears in $O(\varepsilon^2)$, by reducing ε. As shown in Sections 3.1.6.1 and 3.1.6.4, the large A configuration also eases the production of an edge access window at $q_0 \sim 1$. This may be necessary to allow the pressure gradient to relax to zero at the edge once a second region equilibrium is established.

When making the transition from the first to the second region, it was found (Section 3.2.3) that through current programming, q_0 could be made greater than one by the beam driven current and that the high-n unstable region could subsequently be reduced in size. However, as the plasma heated, the pressure profile would encounter an unstable region so that additional auxiliary power would be needed to overcome the enhanced transport losses caused by the unstable large-n mode. This process required less auxiliary power for the large A cases. Also, SRX was designed as a small device, so that the auxiliary heating power to plasma volume ratio is much larger than in present day, large tokamak experiments. This was an additional advantage in providing the requirements for second region transition (Fig. 3.2.4.3 - 2).

The low-n kink/ballooning mode was calculated as being unstable during the transition to the second region for the transport generated equilibria, and a conducting shell was used to stabilize the external modes in the calculation. This shell was considered an integral component in the SRX design for this reason. Recent results on

PBX-M have shown that the external mode can be suppressed on the resisitive time of the conducting structure, but that the low-n internal modes were basically unaffected. Internal modes were calculated as being transiently unstable in the A=9 equilibrium (Section 3.2.5). Fortunately, the stability of the modes improved as the second region of stability to high-n modes was attained. Therefore, although additional schemes to stabilize the low-n modes would probably be needed in SRX, the conducting shell is an additional design feature, favorable for second region access, that most optimized first region experiments lack.

---

[1]Bhattacharjee, A., Iacono, R., Marshall, T.C., Mauel, M.E., Navratil, G.A., Paranicas, C., Sabbagh, S.A., Sen, A.K., Van Dam, J.W., Wang, X.-H., Hughes, M.H., Phillips, M.W., Todd, A.M.M., "Second Regime Tokamak Operation at Large Aspect Ratio", Columbia University report #109, June 1987.

4.1.2 TFTR

The TFTR tokamak at Princeton, while being one of the largest contemporary devices designed to operate a first region stable plasma at large values of P_{fusion}, could explore operation of α in excess of the first stability boundary to large-n modes and perhaps achieve second stability values of α.

By examining Fig 3.2.4.3 - 2 and taking nominal TFTR equilibrium parameters of P_{inj} =25MW, A=3 and a plasma volume of about 30 m^3, the injected auxiliary power to volume ratio is too small to heat a plasma through the high-n mode unstable region in TFTR unless the region could be kept sufficiently small, or could be eradicated completely. Using the results of the present work, an operational strategy

would be to minimize the size of the high-n unstable region by taking advantage of the enhanced stability obtained at low A and $q_0 > 1$. Since the beam orientation was not optimized to drive non-inductive current in the TFTR design, q_0 might not be raised sufficiently high to provide global access to the second region. However, while raising q_0 lowers α_2 substantially, unless q_0 is sufficiently large and global access is obtained, the first region boundary is not greatly affected. This is shown in Fig. 3.1.6.1 - 2. Therefore, the plasma may encounter an equivalent first region obstacle, even though the second region boundary has been altered. In this way, transition to the second region might be equally inhibited. A method of avoiding this is to increase q_a. Running at lower plasma current would increase q_a, thereby increasing β_p and creating a local direct access window at the plasma edge (Fig. 3.1.6.2 - 2). At large values of q_a the edge access window exists at $q_0 = 1$, so that as the pressure is raised, the profile may not encounter an unstable region at the edge. Therefore, if the large-n mode is responsible for limiting the pressure gradient, the profile should be able to exceed the limitations of the first region boundary, at least near the plasma edge, even though q_0 may not be sufficiently large to provide global access to the second region.

A Columbia University proposal to extend the operating regime of supershots in TFTR in this manner has been approved, and the initial results are positive. Previous TFTR supershots operated with $\varepsilon\beta_p$ below an apparent limiting value of 0.7 (Fig. 4.1.2 - 1). By operating plasmas at a plasma current of 300kA and a total injected neutral beam power of about 20MW, values of $\varepsilon\beta_p > 1.3$ were attained. The plasmas were started up by first using the co-injected beams only in an effort to raise the value of q_0 in a similar fashion to that described in Section 3.2.4.1. The total beam power was maximized by subsequently supplementing the heating with the counter-injected beams. A natural inboard poloidal field null was measured by Mirnov coils on many of the highest β_p shots. The separatrix created by the high β_p effects of the plasma

equilibrium was also observed clearly by a tangential viewing video camera. Also, a confinement enhancement of a factor of 2.5 times greater than the benchmark Goldston "L-mode" scaling was calculated. The cause of the enhanced confinement is presently unknown, but may be due to the high β_p effects of the equilibrium.

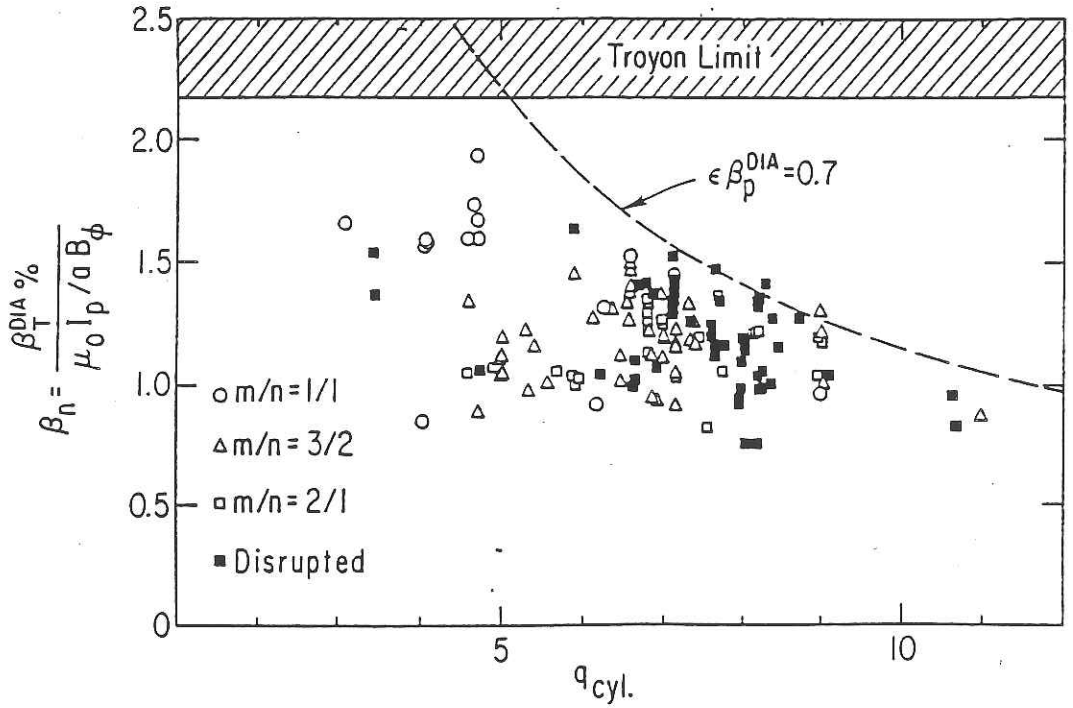

Fig. 4.1.2 - 1: Supershot operating regime in TFTR. *The various point markers indicate the MHD activity observed in the discharges. The data seems to be limited to values of $\epsilon\beta_{p\ dia} \leq 0.7$, although the region of $q^* > 10$ is basically unexplored.*

The initial stability results support the findings of the present work. A free boundary equilibrium solver[1] was used to reconstruct the TFTR high β_p equilibrium. The routine uses magnetic flux loops and also internal poloidal field measurements taken from a diagnostic that uses the injection of lithium pellets to determine the field.[2] The global equilibrium parameters for this case were A= 3.06, I_p = 265kA, q_0 = 1.5, q_a = 58, κ = 0.75, β = 0.14%, $\varepsilon\beta_p$ = 1.20, β/β_l = 0.5. The global stability diagrams for this equilibrium are shown in Fig. 4.1.2 - 2. The q_0 value is not large enough to totally

remove the unstable region, however, a local direct access window at the plasma edge is present and the equilibrium profile curves around the unstable region in the Coppi diagram. Although this is not a second region equilibrium as defined by the marginal stability prescription of Section 3.1.4.1, this equilibrium has obtained values of (α, S) greater than those thought obtainable from the standard CHT (S, α) stability model. This indicates that the effects of low A and high β_p (i.e. large Shafranov shift) at high q_a and $q_0 > 1$ are producing an experimental plasma with enhanced stability properties.

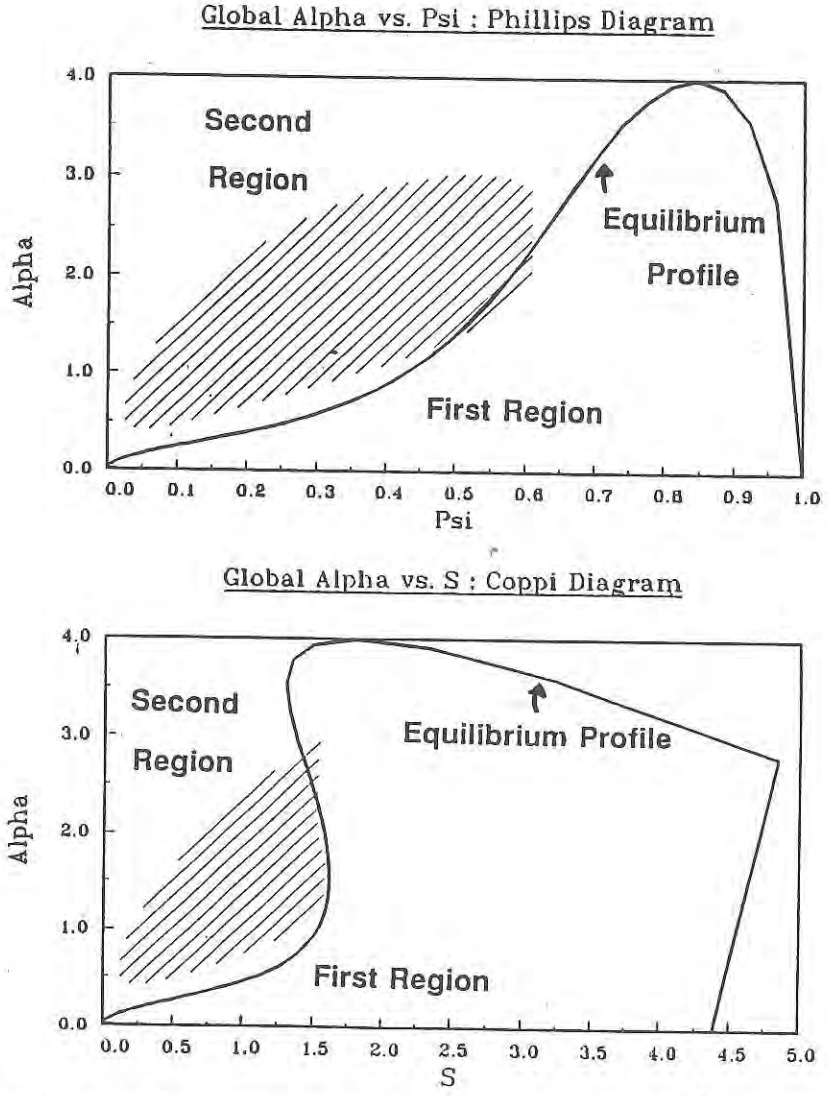

Fig. 4.1.2 - 2: Global stability diagrams for $\varepsilon\beta_p$ = 1.2 equilibrium in TFTR. A local direct access window is evident at the plasma edge and the equilibrium profile is locally unconstrained by an unstable region.

The local (S, α) stability contours are shown in Fig. 4.1.2 - 3 for the flux surfaces with the largest values of α. These three points clearly have $S < S_{crit}$ and have α values that are slightly greater than the α value corresponding to $\partial S/\partial\alpha = 0$ on the corresponding marginal stability contour. Since α changes from about 0.5 to 4.0 while $S \sim 1.5$, it is clear that the profile trajectory would normally enter the unstable region predicted by the standard (S, α) model of stability. Future stability analysis of the present experimental data as well as future experimental runs will aim to uncover plasma equilibria with more enhanced stability properties and greater (α, S) values than those presently known.

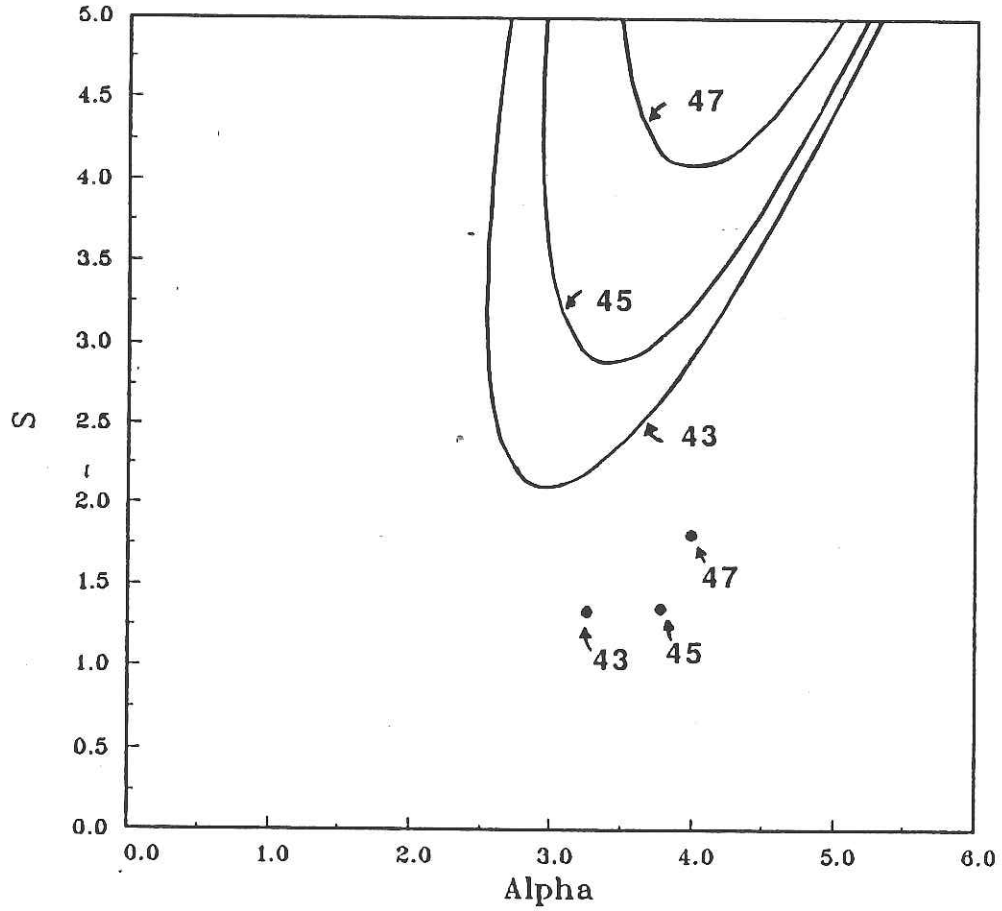

Fig. 4.1.2 - 3: Local stability diagrams for $\varepsilon\beta_p$ = 1.2 equilibrium in TFTR. *The marginal stability contours for the flux surfaces with the largest values of α are plotted. For these surfaces, $S < S_{crit}$ and the surfaces are entering the second stability region.*

[1]Mauel, M.E., et al., in *Plasma Phys and Controlled Nuclear Fusion Research* 1 (1988) 415.

[2]Marmar, E.S., Terry, J., et al., Rev. Sci. Instrum. 60 (1989) 3739.

4.1.3 DIII-D

The DIII-D tokamak at General Atomics is another large tokamak that has already begun to study access to the second stability region. Important initial experiments that have begun this investigation have already been performed. By driving the plasma current by neutral beam current drive alone, DIII-D has produced MHD stable plasmas of high $\varepsilon\beta_p \sim 1.5$ that exhibited enhanced confinement properties.[1] If q_0 was taken to be about three, the flux surfaces were located near the first and second region coalescence point. Due to the small, non-inductively driven plasma current of 340 kA, q_a was large in these plasmas (≥ 60) and an edge access window to the second region may have been achieved. The low current also reduced the beam deposition and further investigation of this mode of operation could probably be enhanced by introducing ohmic drive, sacrificing the very large q_a for more efficient beam heating. As shown on Section 3.1.6.3, equilibria with $q_a \geq 8$ can still exhibit an edge access window so that beam shine through and first orbit losses could be reduced, producing a higher β plasma with larger pressure gradients. These plasmas may provide the extra margin needed to exceed the second region boundary on some flux surfaces. With a nominal volume of $18m^3$ and auxiliary heating power of 15MW, DIII-D probably would not have enough power to burn through a high-n unstable region into second stability even with a 25% power saving due to the dee-shaping, as shown in Section 3.2.4.2. Therefore, it is important that the unstable region be studied in the DIII-D

geometry so that an operating scenario might be found to eliminate the high-n unstable region.

A recent set of experiments on DIII-D has produced interesting results concerning the establishment of a local direct access window to large-n modes at the plasma edge.[2] The goal is to investigate the conditions under which an edge access window can be produced in DIII-D with respect to boundary shape variations. The onset of bursts of MHD activity at the plasma edge in DIII-D, so named giant ELM's (edge localized modes) have been correlated to the plasma pressure gradient reaching the first region boundary to large-n ballooning modes.[3] Therefore, if the first stable region boundary could be eliminated at the plasma edge, for example, by establishing an edge access window to the second region, then the giant ELM should be suppressed by removing the "trigger" of the instability. In this way, the giant ELM could provide a diagnostic for locating the onset of the edge access window. Initial experiments of this type have varied the outer boundary shaping to bring the plasma from a configuration that theoretically lacked an edge access window, to an equilibrium that theoretically possessed an edge access window. This was performed by increasing the dee-shaping of the plasma discharge. The results show that this change in the equilibrium outer boundary shape successfully suppressed the giant ELM. Time traces of the various plasma parameters for this type of discharge are reprinted from Ref. [2] in Fig. 4.1.3 - 1.

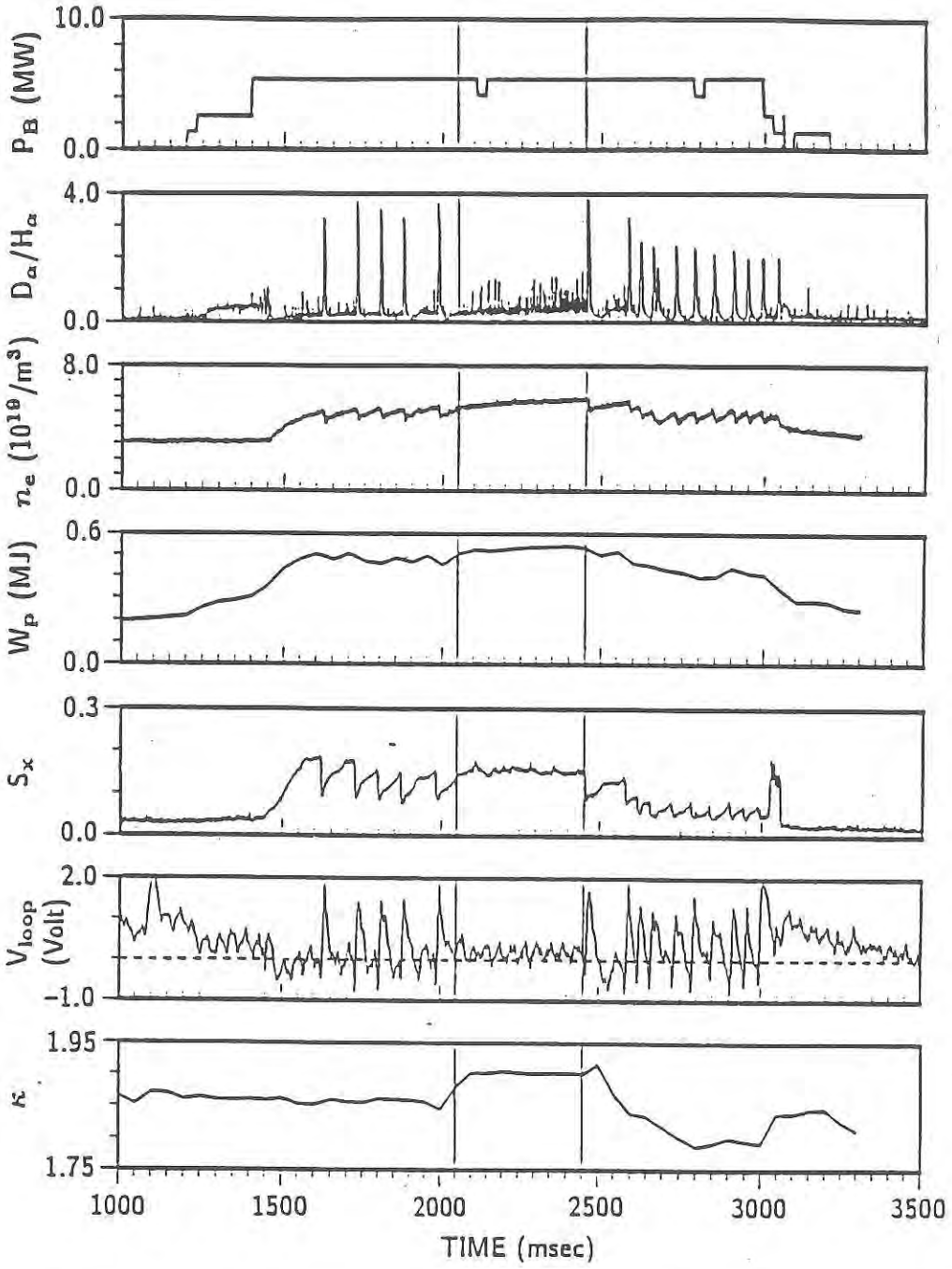

Fig. 4.1.3 - 1: Time traces of various plasma parameters for an elongation scan during an H-mode discharge in DIII-D, I_p = 1.0 MA, B_0 = 2.1 T. The traces show neutral beam injection power, P_b, D_α/H_α radiation in the divertor region, line averaged electron density, n_e, plasma stored energy, W_p, edge soft X-ray emission, S_x, loop voltage, V_{loop}, and elongation, κ. Notice that as κ is increased, the giant ELM (indicated by the D_α/H_α bursts) are suppressed.

This experiment not only discovered a method of controlling the giant ELM, but also suggests a series of experiments that could be performed on DIII-D that could map out the onset of the edge access window with respect to varying additional plasma parameters. Varying q_a by ramping the current down during the discharge, the edge access window could be made to appear (see Section 3.1.6.2) and could be used to further corroborate the boundary shaping results by suppressing the giant ELM. A similar experiment could be performed, varying the q_0 by changing the ratio of co- to counter-injected neutral beam heating during the discharge. Although this experiment may not be as conclusive as the q_a variation (since q_0 is more difficult to approximate from the experimental measurements), it may also manifest the ability to suppress the giant ELM and reveal the effect of the beam orientation on achieving an edge access window.

---

[1]Simonen, T.S., et al., Phys. Rev. Lett. **61** (1988) 1720.

[2]Ozeki, T., Chu, M.S., Lao, L.L., Taylor, T.S., Chance, M.S., Kinoshita, S., Burrell, K.H., Stambaugh, R.D., "*Plasma Shaping, Edge Ballooning Stability, and ELM behavior in DIII-D*", General Atomics report GA-A19495, June 1989.

[3]Gohil, et al., Phys. Rev. Lett **61** (1988) 1603.

'Justice, therefore, we may say, is a principle of this kind; its real concern is not with external actions, but with a man's inward self, his true concern and interest. The just man will not allow the three elements which make up his inward self to trespass on each other's functions or interfere with each other, but by keeping all three in tune, like the notes of a scale, will in the truest sense set his house to rights, attain self-mastery and order, and live on good terms with himself.'

Plato, *The Republic*, p 443 d.

5.0 MINIMIZATION OF REQUIREMENTS TO REACH SECOND REGION THRESHOLD

The establishment of an experimental tokamak equilibrium with pressure gradients in the second stability region will require the suppression of disruptive ideal MHD instabilities and possibly the ability to overcome enhanced transport losses due to non-disruptive instabilities. By understanding the behavior of the self-consistently calculated, high-n mode marginal second region threshold values of α, β, and $\varepsilon\beta_p$, with respect to variations in the tokamak parameters, minimum requirements for attaining second stability can be defined.

The general prescription for avoiding an encounter with a large-n mode unstable region is to insure that $S(\psi) < S_{crit}(\psi)$ over all plasma flux surfaces. This condition defines global access to the second stability region so that large-n ballooning instabilities would be irrelevant. However, this condition can not always be satisfied, and unstable regions should subsequently be reduced in size. The second region threshold quantities, α_2, β_2, and $\varepsilon\beta_{p2}$, can all be reduced by considering the large A configuration for $q_0 \sim 1$. The large A, marginally stable second region equilibria also

display an edge access window to the second region. The transport generated sequences of equilibria also show that the auxiliary input power to plasma volume ratio required to cross over to the second region is reduced at larger A when a small enhanced transport region due to large-n instabilities is encountered. The ability of the large A configuration in reducing the second region threshold comes from the reduction of the poloidal field component of the normal curvature drive, that is one order smaller in ε than the dominant toroidal field curvature. This term appears and destabilizes the second region threshold for low A, $q_0 \sim 1$ equilibria. However, this effect can also be reduced in the small A configuration when q_0 is sufficiently large. In this case, the stabilizing geometric magnetic well of the toroidal field can balance or overcome the destabilizing poloidal field normal curvature drive. The stabilizing effect of the increased q_0 is caused by the reduction of the latter destabilizing effect by changing the *global* stability properties of the plasma. Specifically, raising q_0 reduces the large Shafranov shift in the marginally stable second region plasmas, which in turn reduces the destabilizing effect. Without this coupling, a local variable such as q_0 could not affect the stability of the outer flux surfaces on which it clearly has a large effect. Also, while raising q_0 has a large effect in reducing the second region threshold values, it also makes the large-n unstable region migrate to the outer flux surfaces and generally creates global access to the second region at a critical value of q_0, approximately when local access appears at the edge. Therefore, an experiment that is unable to raise q_0 sufficiently may fail to show any improvement over $q_0 \sim 1$ first region performance, since the first region boundary across the entire plasma would still be encountered. However, raising q_a creates a local direct access window at the plasma edge, so that a pressure profile evolving toward the second stability region would not be limited on these flux surfaces regardless of the value of q_0, and gains produced toward achieving a second region profile should be evident. This stabilizing effect is not caused by a reduction in the Shafranov shift, as with $q_0 > 1$, since raising q_a also increases σ'.

Instead, the increase in q_a decreases the poloidal field strength, that in turn decreases the destabilizing poloidal field component of κ_n *locally* near the plasma edge. The reduction of β_2 at increased q_a is due to the opening of the edge access window and not a reduction of the slope of α_2 vs. S, as produced by increasing q_0. The reduction in current at increased q_a causes $\varepsilon\beta_{p2}$ to increase. It is also shown (Section 3.1.7.3) that at high q_a, the global shear *decreases* as q_a increases due to the effect that this variation has on the equilibrium ψ. This helps provide local direct access since S is reduced. In addition, global access can be achieved by reducing S by keeping $(q_a - q_0)/q_a$ sufficiently small. However, it is also shown that raising q_0 for certain values of α_q and q_0 can actually cause S to *increase*. Therefore, it is important to avoid the parameter regime in which this occurs (see Eqs. 3.1.7.3-12, -13).

β_2, $\varepsilon\beta_{p2}$, and S all decrease as α_q decreases. However, this also reduces S_{crit}, so that a large increase or decrease in the size of the edge access window is not observed as α_q is varied. Elongation without triangularity causes the field line to spend more time in the unfavorable curvature region and therefore creates a large increase in α_2 and β_2 as κ is increased in an elliptical plasma. Oblate shaping ($\kappa < 1$) correspondingly shows a reduction in β_2. Dee-shaping can significantly reduce the size of the unstable region, basically by reducing α_2. The dee-shape also shows a reduction of the power requirements needed to cross a residual large-n unstable region in the transport generated transition equilibria. It is shown that when combining all of the favorable effects, no additional destabilizing coupling between the global variables is found, allowing β_2 and $\varepsilon\beta_{p2}$ to be reduced substantially. Edge access windows are obtained for all aspect ratios when q is sufficiently large (~ 8.1 in sample cases). In the transport generated sequences of equilibria, small-n kink/ballooning modes appear and the external modes can be suppressed by a conducting shell. However, early in the beam heating phase, small-n internal modes appear transiently. Therefore, an externally

applied stabilization scheme will probably be required experimentally during the transition to suppress the instability and allow second region access. These modes restabilize as the equilibria attain second stability to the large-n ballooning mode.